UNIVERSIDAD DE CHILE
FACULTAD DE CIENCIAS FÍSICAS Y MATEMÁTICAS
DEPARTAMENTO DE FÍSICA

PARTICLE-LIKE SOLUTIONS IN NONEQUILIBRIUM SYSTEMS: COUPLED OSCILLATORS, VEGETATION, AND OPTICS

TESIS PARA OPTAR AL GRADO DE MAGÍSTER EN CIENCIAS, MENCIÓN FÍSICA

ERNESTO ANTONIO BERRÍOS CARO

PROFESOR GUÍA:
MARCEL G. CLERC GAVILÁN

MIEMBROS DE LA COMISIÓN:
SERGIO RICA MERY
MUSTAPHA TLIDI
ALEJANDRO VALDIVIA HEPP

Este trabajo ha sido principalmente financiado por Becas Conicyt Magíster Nacional 2015,
Folio No. 22151824

SANTIAGO DE CHILE
2017

RESUMEN DE LA MEMORIA PARA OPTAR
AL GRADO DE MAGÍSTER EN CIENCIAS, MENCIÓN FÍSICA
POR: ERNESTO ANTONIO BERRÍOS CARO
FECHA: 2017
PROF. GUÍA: SR. MARCEL G. CLERC GAVILÁN

PARTICLE-LIKE SOLUTIONS IN NONEQUILIBRIUM SYSTEMS: COUPLED OSCILLATORS, VEGETATION, AND OPTICS

Las soluciones tipo partícula se encuentran presentes en muchos campos de la física, incluyendo simples sistemas mecánicos, como osciladores acoplados, así como en sistemas más complejos tales como magnetismo, vegetación, superconductores, entre otros. Su importancia radica en el modelamiento de fenómenos fuera del equilibrio en sistemas disipativos, donde la inyección y disipación de energía juega un importante rol. En este trabajo estamos particularmente interesados en estudiar estas soluciones en tres distintos contextos: osciladores acoplados, vegetación y óptica, los cuales serán tratados separadamente.

Esta tesis está compuesta por seis capítulos y cuatro apéndices, los cuales contienen los artículos publicados durante este trabajo. Los primeros dos capítulos sirven como introducción: En el Capítulo 1 presentamos las motivaciones y objetivos generales de esta tesis y en el Capítulo 2 los conceptos y herramientas necesarias para la comprensión del estudio.

El primer contexto en el que estudiaremos soluciones tipo partículas es tratado en el Capítulo 3 y en los Apéndices A y B. En ellos estudiaremos osciladores acoplados sometidos a forzamiento paramétrico, particularmente enfocados en estudiar el efecto de este forzamiento en soluciones *kinks* de la ecuación *sine-Gordon* y de la ecuación escalar ϕ^4. Presentaremos un nuevo tipo de *kinks*, los cuales hemos denominados como *flaming kinks*, los cuales se caracterizan por emitir ondas desde su posición central. Mostraremos cómo la interacción de estas soluciones permite la formación de estructuras localizadas estables, caracterizando la dinámica de esta interacción analíticamente. Además, aplicaremos nuestros resultados a un hilo magnético, puesto que en cierto límite se describe por la ecuación *sine-Gordon*.

El segundo contexto bajo estudio es vegetación, donde estudiaremos un mecanismo de formación de patrones a través de la interacción de estructuras localizadas rodeadas por suelo descubierto. El Capítulo 4 y el Apéndice C están dedicado a este tópico. En ellos trataremos los casos uni y bi dimensionales, derivando en cada uno la dinámica de interacción entre las estructuras. Mostraremos cómo esta interacción permite la formación de *redes de estructuras localizadas*, y cómo éstas se reorganizan para formar configuraciones estables.

El último contexto de nuestro estudio es un experimento que consiste en la red de difracción producida al aplicar un rayo láser a una inestabilidad tipo zigzag, producida en una celda de cristal líquido tipo *in-plane switching* (IPS) conectada a un generador. Esta inestabilidad zigzag no es más que una extensión natural de soluciones tipo partícula a dos dimensiones. Discutiremos este tema en el Capítulo 5 y en el Apéndice D. En ellos propondremos un modelo teórico para explicar los diferentes perfiles de difracción observados al variar la frecuencia y amplitud de la señal del generador. Este modelo está basado en la difracción de Fraunhofer.

Finalmente, en el Capítulo 6 presentamos las conclusiones de este trabajo.

THESIS ABSTRACT
DEGREE: MASTER IN PHYSICS
MASTER CANDIDATE: ERNESTO ANTONIO BERRÍOS CARO
DATE: 2017
THESIS ADVISOR: MARCEL G. CLERC GAVILÁN

PARTICLE-LIKE SOLUTIONS IN NONEQUILIBRIUM SYSTEMS: COUPLED OSCILLATORS, VEGETATION, AND OPTICS

Particle-like solutions are present in many fields in physics, including simple mechanical systems, like coupled oscillators, as well as in more complex systems such as magnetism, vegetation, superconductors, among others. Their importance lies in the modeling of non equilibrium phenomena in dissipative systems, where the injection and dissipation of energy plays an important role. In this work, we are particularly interested in studying these solutions in three different contexts: coupled oscillators, vegetation, and optics, which will be treated separately.

This thesis is composed of six chapters and four appendices that contain the articles published during this work. The first two chapters serve as an introduction: In Chapter 1 we present the motivations and general objectives for this thesis and in Chapter 2 useful concepts and tools.

The first context where we study particle-like solutions is treated in Chapter 3 and Appendices A and B. There we study coupled oscillators submitted to a parametric forcing, particularly focused on studying the effect of this forcing in kink solutions from the sine-Gordon equation and from the ϕ^4 scalar field equation. We present a new type of kinks named as *flaming kinks*, characterized by emitting waves from their center position. We show how the interaction of these solutions allows the formation of stable localized structures, characterizing the dynamics of this interaction analytically. Moreover, we apply our results to a magnetic wire, since in certain limit this system is described by the sine-Gordon equation.

The second context under study is vegetation, where we study a mechanism of pattern formation through the interaction of localized structures of vegetation surrounded by bare soil. Chapter 4 and Appendix C are devoted to this topic. There we treat both one and two dimensional cases, deriving in each one the interaction dynamics between the structures. We show that this interaction allows the formation of stable *localized structure lattices*, and how they reorganize to form stable configurations.

The last context of our study is an experiment consisting of a diffraction grating produced by applying a laser beam to a zigzag instability, produced in a in-plane switching (IPS) liquid crystal cell connected to a generator. This zigzag instability is nothing but the natural extension of particle-like solutions to two dimensions. We discuss this subject in Chapter 5 and Appendix D. There we propose a theoretical model to explain the different diffraction profiles observed as the frequency and amplitude of the generator signal is varied. This model is based on Fraunhofer diffraction theory.

Finally, in Chapter 6 we present the conclusions of this work.

Dedicado a mis padres

Agradecimientos

Quiero agradecer profundamente al profesor Marcel Clerc por su dedicación, pasión y compromiso en el desarrollo de este trabajo. Su energía y motivación fueron esenciales para concluir esta etapa académica. Estaré siempre agradecido por el apoyo mostrado y por su confianza en cada paso que di. Agradezco también al profesor Vincent Odent, por su guía y paciencia en mi primeros pasos como investigador, y por su disposición a recibirme en mi visita a la *Université de Lille*. Agradezco también la preocupación y guía del profesor Mustapha Tlidi, y por su disposición para realizar una pasantía en la *Université Libre de Bruxelles*, la cual me entregó valiosas experiencias. Agradezco también a los profesores del departamento que de alguna u otra forma me inspiraron a seguir adelante, especialmente a Gonzalo Palma, María Luisa Cordero, Domenico Sapone, Raúl Muñoz y Nicolás Mujica.

Fuera del ámbito académico, quiero dar gracias a mis padres, Patricia y Marco, por su apoyo incondicional en cada paso que he dado, por confiar en mí y animarme a dar lo mejor. A Anariky por estar siempre presente, por escuchar mis alegrías y quejas, por creer siempre en mí y darle a mi vida un toque mágico. También a mi hermana Jessica y mis abuelos por estar siempre pendientes de cada paso.

Me gustaría también agradecer a mis amigos del departamento, especialmente a Cristóbal Lledó y Daniel Feliú, por su amistad, compañía y apoyo a lo largo de mi magíster. También a Pablo Cabello (especialmente por su acogida en mi visita a Delft), Alfredo García y Fabián Sepúlveda. Agradezco también el apoyo de los integrantes de los *Lunch Meetings*, en especial a Alejandro León por sus muy buenas observaciones en mis trabajos. A Ignacio Andrade, Alejandro Álvarez, Gregorio González, Nicolás Perinet y Pablo Gutiérrez.

Agradezco también a quienes me han brindado su apoyo fuera del ámbito universitario. A Juan Pablo Paulsen por las tardes de videojuegos que compartimos. A Valentina Torres por compartir su alegría en mis victorias y su confianza. A Misheel y Valeria por su apoyo y los buenos momentos que compartimos. Gracias también a la gente de mi iglesia Malaquías Concha que me ha mostrado su apoyo. También quisiera mencionar a quienes han estado de alguna forma presente (sin ningún orden en particular): a Nicole, Jóse, Mani, Eliezer, Baru, Mauri, Lizi, Pía, Angie y Dani.

Finalmente, agradezco el financiamiento de Conicyt mediante su Beca de Magíster Nacional, Convocatoria 2015, Folio No. 22151824.

Contents

List of Figures

Chapter 1

Introduction

Spatially localized structures are a fascinating element of nature, whose relevance has been appreciated over the past decades, given its presence in various fields, ranging from physical, biological, geological or even chemical systems. Which has captured their attention is the similarity of different structures observed in multiple contexts, suggesting the existence of general principles behind their formation. Their main feature is that they allow the confinement of energy, chemical concentration, phytomass density, fluid, depending on context [64, 91], that offers a short spatial range correlations in comparison to long-range correlations, e.g., *periodic patterns*, characterized by occupying the whole available space [10, 65, 80]. This confinement can have a wide range of applications, as the case of light confinement used in fibre optics or spectroscopy [5, 99].

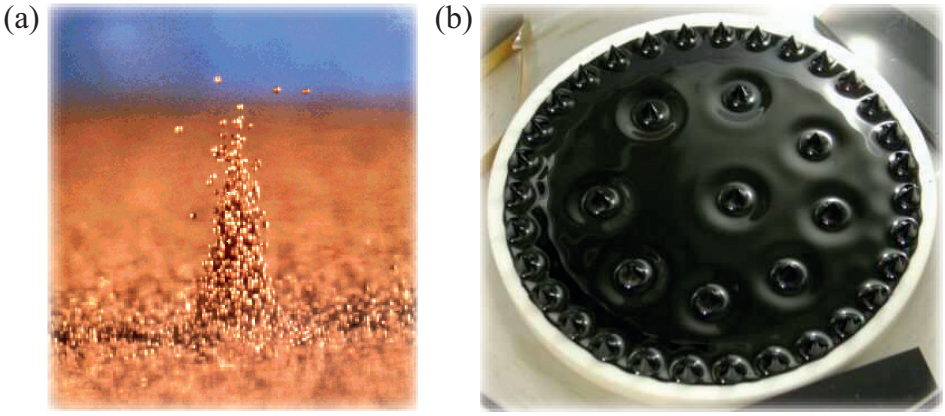

Figure 1.1: (a) Oscillon formed by vibrating vertically granular layers [93]. (b) Two-dimensional localized structures on the surface of a ferrofluid, under a uniform magnetic field normal to the surface [84].

Localized structures can be found in several non-equilibrium systems, where the injection and dissipation of energy play an important role [30, 31]. They can appear as patches, spikes, interfaces, dissipative solitons, among others forms. In some cases these structures are time-dependent, as the case of particle-like localized excitations created by vibrating vertically

granular layers in evacuated containers, known as *oscillons* [93] (see Fig. 1.1 (a)); or can be stationary in time, as the solitons formed in a ferrofluid (suspension of magnetic dipoles) submitted to a uniform magnetic field applied in the normal direction to the surface [84] (see Fig. 1.1 (b)). In general, the formation of localized structures is due to a balance between a positive feedback balance that tends to amplify the spatial homogeneities and a transport process that tends to restore the homogeneity [91]. They can also arise as the coexistence between two stable states, not necessarily homogeneous [24].

This thesis is not intended to provide a general description of the formation of localized structures, but in studying properties that arise from the interaction between them or with an external factor. Given the wide variety of physical systems where localized structures appear, we will not restrict ourselves to one physical system. We study in this work separately three different contexts: coupled oscillators, vegetation, and optics, focusing on localized structures with particle-like properties, that is, structures defined by a finite set of parameters, such as width, momentum, charge, etc. In the next section, we present the main objectives and results of this thesis.

1.1 Objectives and main results

The main purpose of this work is to study particle-like localized structures in different physical systems, using theoretical, numerical and experimental tools. In particular, our goals are:

Coupled oscillators:

1. Study the effect of dissipation and an external oscillatory parametric forcing in particle-like solutions in coupled oscillators, particularly focused on *kink* solutions from the *sine-Gordon equation*. As a result of this study, we have found a new type of kinks, which we have named as *flaming kinks*. We have also found these solutions in the parametrically driven and damped ϕ^4 *scalar field equation*.
2. Study the interaction between a flaming kink and a flaming antikink, using theoretical nonlinear tools to characterize their dynamics, and compare with numerical data. We have found that this interaction allows the formation of a family of stable localized structures.
3. Apply our results to a magnetic wire submitted to external oscillatory magnetic fields, which in some limit is described by the sine-Gordon equation.
4. Extend our study to two dimensions. Study in this directions is still in progress.

Vegetation:

1. Study particle-like localized structures in vegetation by using numerical simulations of a mathematical model based on facilitation and competition growth rate process. Our characterization includes both one and two dimensions.

2. Study the interaction of these localized structures, deriving theoretically the interaction law of the distance of separation between them. We have demonstrated that this interaction is repulsive, which agrees with numerical observations.
3. Characterize numerically the stable equilibrium configurations that arise when several localized structures are placed in arbitrary configurations. We study the reorganization of these configurations when a single localized structure is removed.

Optics:

1. Study experimentally the diffraction grating produced by applying a laser beam in a zigzag interface instability, formed in an in-plane switching cell filled with nematic liquid crystal. This cell is connected to a generator, which modifies the interface as the signal is varied. We consider this zigzag instability as a transverse particle-like solution.
2. Characterize theoretically the different diffraction profiles observed, by proposing a model based on the Fraunhofer diffraction theory. Our findings are in good agreement with the experimental data.

Chapter 2

Theoretical background

In this section, we will briefly introduce the tools, methods, and concepts useful for this thesis, as well as the physical models on which it will be based.

2.1 Elementary concepts

A *dynamical system* is a system whose configuration is described by a *phase space* (or state space), where its evolution in time is specified by a mathematical rule [56, 87]. If the time is continuous, the rule of evolution might be in general a differential equation, or if it is discrete, a map from the phase space to itself.

A phase space corresponds to a space $U \subseteq \mathbb{R}^n$ composed by states $\mathbf{u} \in U$ which depend on space $\mathbf{r}$ and time t. In the continuous case the evolution of the states will be given by

$$\frac{\mathrm{d}\mathbf{u}}{\mathrm{d}t} = \mathbf{f}(\mathbf{u}, t), \tag{2.1}$$

where $\mathbf{f} : U \times \mathbb{R} \to U$ is a vector field. The system will be of order n and if $\frac{\partial f}{\partial t} = 0$ will be called *autonomous*. Notice that every system with n temporal variables can be written as in (2.1) through a change of variables. For instance, the second order equation $\ddot{x} + \dot{x} + x = 0$ can be expressed as $\dot{x} = y$, $\dot{y} = -x - y$.

The interest of dynamical systems not only includes physics but also biology, economics, ecology, among others fields, where the notion of time evolution is relevant. A well known example of a dynamical system is the $Lotka - Volterra$ model of competition [12] between two species (e.g. r =rabbits and s =sheeps)

$$\dot{r} = r(a - br - cs), \quad \dot{s} = s(\mathrm{d} - \mathrm{e}r - fs), \tag{2.2}$$

where $a, b, c, \mathrm{d}, \mathrm{e}, f$ are positive constants. These positive constants are parameters that characterize the different temporal evolution exhibited by the above model. This is a second order and autonomous system, which lives in the phase space $(r, s) \in [0, \infty) \times [0, \infty)$.

The solutions of a dynamical system follow particular curves in the phase space called *trajectories*. A dynamical system is said to describe the *flow* in the phase space, the motion of a particular point (an initial condition) along one of these curves. The pattern of solution curves or trajectories is called *phase portrait*, like the one shown in Fig. 2.1 for Eq. (2.2) for the case $a = 3, b = \mathrm{e} = f = 1$ and $c = \mathrm{d} = 2$. Here the arrows represent the directions of the flow and the dots the *fixed points*, i.e., the points that satisfy $f = 0$. The solid black dots represent the *stable* fixed points (also known as *attractors*, since the flow is toward them), the open circle $(0, 0)$ is an *unstable* fixed point (or *repeller*), while the point $(1, 1)$ corresponds to a *saddle point*, which is a point that can attract or repel in different directions.

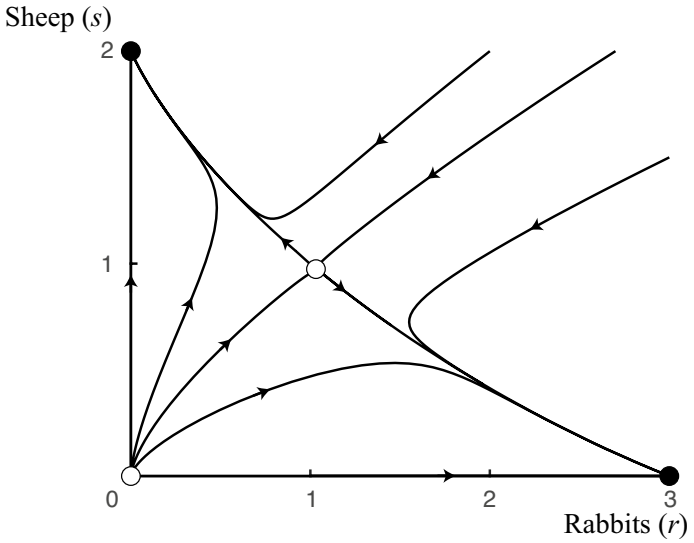

Figure 2.1: Phase portrait of Lotka-Volterra model (Eq. (2.2)) for $a = 3, b = \mathrm{e} = f = 1$ and $c = \mathrm{d} = 2$.

The advantage of studying a phase portrait is that it allows analyzing the system in a clear and simple way, without having the analytical solution. Indeed, this representation corresponds to a geometrical characterization of the solutions. For the previous case, we can interpret that the system will evolve in such a way that one species will drive the other to extinction. This situation also occurs in other models of competition, which has led the biologists to formulate the *principle of competitive exclusion*, or *Gause's law* [41].

The parameters on which the system depends can change the stability of fixed points and the nature of phase portraits. In the Lotka-Volterra system, there are three different qualitatively phase portraits.

2.2 Bifurcation theory

2.2.1 Linear analysis

The change in the qualitative character of a solution (stable, unstable, etc.) as a control parameter is varied is known as *instability* [56,87], concept introduced by Henri Poincaré [81].

The instability generates a qualitative change of phase portrait, known as *bifurcation*. To analyze the nature of the bifurcation it is necessary to perform a linear stability analysis. Let us consider then the following autonomous dynamical system

$$\frac{\mathrm{d}\mathbf{u}}{\mathrm{d}t} = \mathbf{f}(\mathbf{u}; r), \tag{2.3}$$

where r is a control parameter that we will vary. Suppose that $\mathbf{u} = \mathbf{u_0}$ is a fixed point (or *steady state solution*)

$$\mathbf{f}(\mathbf{u_0}; r) = 0.$$

To characterize its stability as the parameter r changes, we study the dynamics of a small perturbation $\delta\mathbf{u}$ around the equilibrium. Therefore, proposing $\mathbf{u} = \mathbf{u_0} + \delta\mathbf{u}$, replacing into Eq. (2.3) and linearizing in $\delta\mathbf{u}$, one gets

$$\delta\dot{u}^{\mathrm{i}} = \sum_j K_{\mathrm{i}j}\delta u^j, \quad K_{\mathrm{i}j} = \frac{\partial f_{\mathrm{i}}}{\partial u^j}(\mathbf{u} = \mathbf{u_0}). \tag{2.4}$$

Since $\mathbf{u_0}$ is a time-independent state, the matrix $K_{\mathrm{i}j}$ does not depend on time. This matrix corresponds to the Jacobian of $\mathbf{f}$ evaluated in $\mathbf{u_0}$. Its eigenvalues λ_σ determine how the system evolves under a perturbation [87] because

$$\delta\mathbf{u} = \sum_\sigma A_\sigma \mathrm{e}^{\lambda_\sigma t}\mathbf{v}^\sigma,$$

where A_σ is a set of initial amplitudes and $\mathbf{v}^\sigma$ the eigenvectors associated with the corresponding eigenvalues λ_σ.

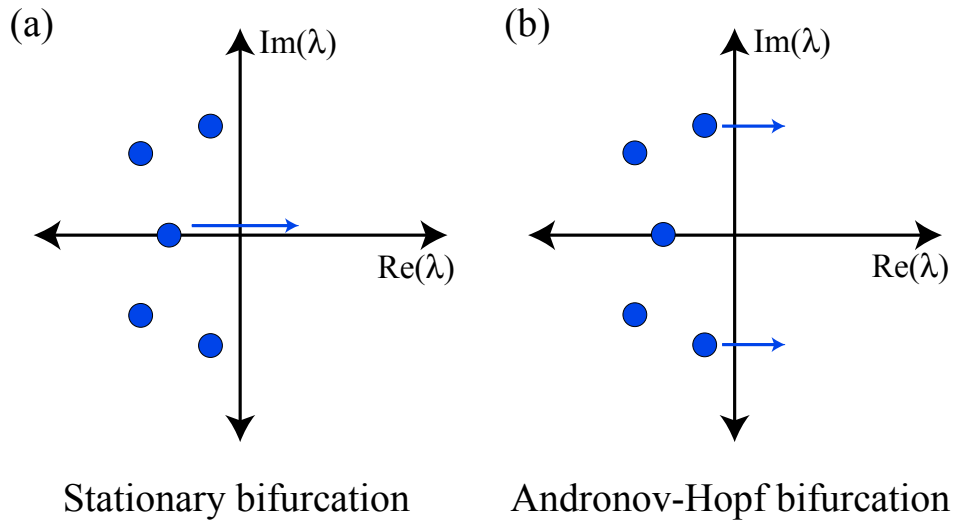

Figure 2.2: Two possible generic behaviors of how the eigenvalues of the system evolves when the control parameter r crosses its critical point r_c. (a) Stationary bifurcation. (b) Andronov-Hopf bifurcation.

The stability of the system is determined by the real part of λ_σ. The condition for being stable is that the real part of *all* eigenvalues be negative, i.e., Re $(\lambda_\sigma) < 0$. As r changes, the onset of instability occurs when it is fulfilled that Re $(\lambda_\sigma) = 0$, for some σ, at certain critical $r = r_c$. As this parameter is varied, based on the fact that the differential equations are real, there are two possible generic behaviors that the system can perform:

1. *Stationary bifurcation*: When only one real eigenvalue crosses the origin in the complex λ plane.
2. *Andronov-Hopf bifurcation*: A complex conjugate pair of eigenvalues crosses the imaginary axis in the complex λ plane. In this case, the imaginary part of them gives an oscillating component in time.

Both classes of bifurcations are illustrated in Fig. 2.2.

2.2.2 Nonlinear analysis

When $r > r_c$ there is at least one eigenvalue that grows exponentially in time in the linearized equation (2.4). However, the nonlinear terms of the dynamical system will clearly affect the evolution, either saturating the growth or further enhancing it.

The way that the system will behave after crossing the critical point $r = r_c$ falls into some possibilities, given by the form of dynamical equations for the amplitudes of unstable eigenvectors [56]. In general, the procedure to determine the type of bifurcation is to put these equations, after suitable nonlinear methods, into standard forms. The symmetries of these standard form equations and the sign of their coefficients will be crucial for the subsequent behavior. These equations are known as *normal forms* [20, 33, 53, 56, 87].

In what follows we will study some normal forms for stationary bifurcations, which will play an important role in future discussions.

2.2.3 Pitchfork bifurcation

Since this is a stationary bifurcation with reflection symmetry, there is a single growing eigenvector with amplitude $X(t)$. The normal form of this bifurcation is

$$\frac{\mathrm{d}X}{\mathrm{d}t} = \varepsilon X \pm X^3, \tag{2.5}$$

where $\varepsilon = r - r_c$ is the *bifurcation parameter* (or *control parameter*). Namely, it is the parameter that controls the stability of the equilibrium under study. Notice that the critical point occurs when $\varepsilon = 0$. Depending on the sign, we distinguish two different cases:

1. *Supercritical* (negative sign)[1]: In this case, the nonlinear term is saturating. The equilibriums of this equation are $X = 0$ and $X = \pm\sqrt{\varepsilon}$. For $\varepsilon < 0$ only $X = 0$ is stable and no other real solutions exist. For $\varepsilon > 0$, when it crosses the critical point, $X = 0$ becomes unstable and two stables equilibriums emerge, $X = \pm\sqrt{\varepsilon}$. The *bifurcation diagram*, that is, a schematic representation of the bifurcation, is shown in Fig. 2.3 (a). A well-known example of this bifurcation is the Andronov pendulum [7].

[1]This equation was first introduced by Landau (1944) to describe the effect of nonlinearities on linear hydrodynamic instability. A similar model with a constant term that breaks reflexion symmetry was introducing to study combustion process by Zeldovich and Frank-kemeneskii.

2. *Subcritical* (positive sign): Here the nonlinear term is destabilizing. The equilibriums are $X = 0$ and $X = \pm\sqrt{-\varepsilon}$. For $\varepsilon < 0$ the solution $X = 0$ is stable, and the two other unstable. For $\varepsilon > 0$ the solution $X = 0$ destabilizes and there are no other solutions. The respective bifurcation diagram is shown in Fig. 2.3 (b).

   If we add a quintic term to this equation of the form

$$\frac{\mathrm{d}X}{\mathrm{d}t} = \varepsilon X + X^3 - gX^5, \tag{2.6}$$

   with $g > 0$, the bifurcation diagram evolves as shown in Fig. 2.3 (c). The arrows show the path that the solution follows when ε is increased or decreased, allowing the possibility of *jumps* and *hysteresis* [87].

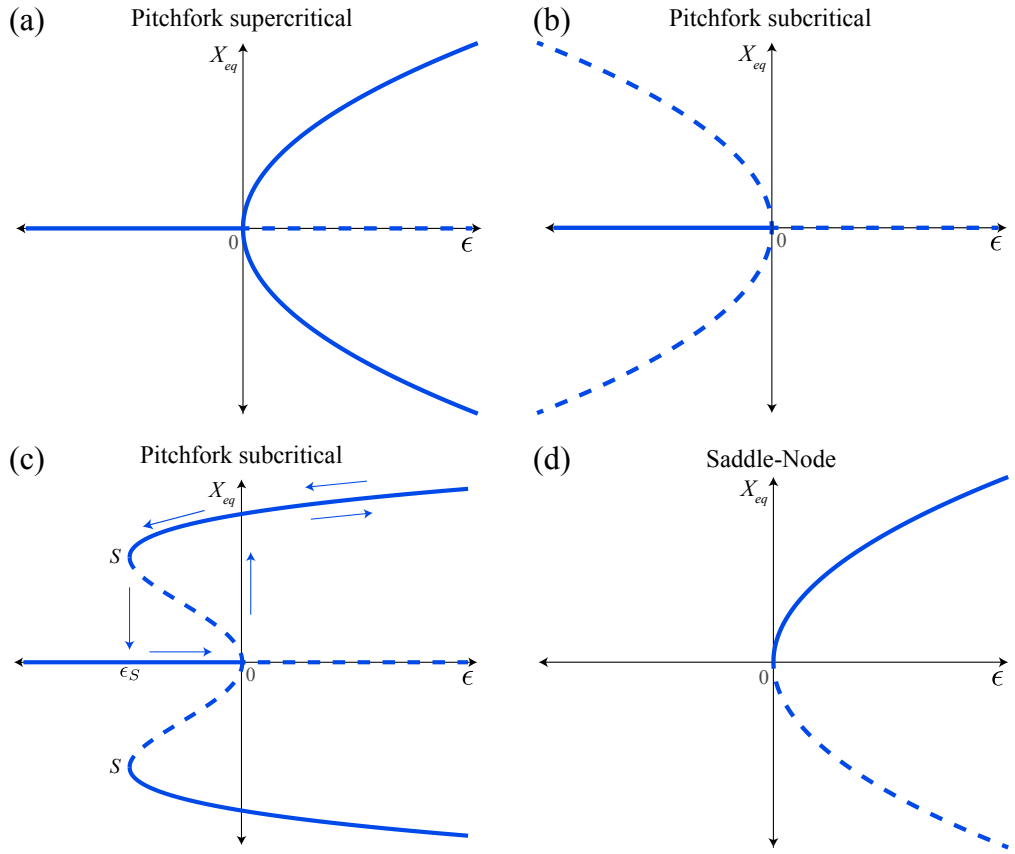

Figure 2.3: Bifurcation diagram for different kinds of Pitchfork bifurcations: (a) Supercritical. (b) Subcritical. (c) Subcritical with a quintic term (Eq. (2.6)). The plots show the evolution of the steady stable and unstable states in function of the bifurcation parameter ε. The full (dotted) lines represent the stable (unstable) states. The arrows in (c) account for the path that the equilibrium solution follows when the bifurcation parameter ε is increased or decreased. Notice that there is a jump in $\varepsilon = 0$ and in ε_s.

2.2.4 Saddle-Node bifurcation

The saddle-node bifurcation is characterized because fixed points are created and destroyed as the control parameter is varied. Following the same notation as the previous case, the

prototypical equation for this bifurcation writes

$$\frac{\mathrm{d}X}{\mathrm{d}t} = \varepsilon - X^2, \tag{2.7}$$

which has fixed points $\pm\sqrt{\varepsilon}$. Then, for $\varepsilon < 0$ there are not equilibrium points. Nevertheless, when $\varepsilon = 0$ the system has only one equilibrium $X = 0$, which is a *saddle-node fixed point*. This means that the point is stable for perturbations in one direction, but unstable in the opposite direction [87]. The interesting feature of this bifurcation occurs when $\varepsilon > 0$. In this case, two new equilibriums emerge: $+\sqrt{\varepsilon}$, which is stable, and $-\sqrt{\varepsilon}$, unstable. The corresponding bifurcation diagram is presented in Fig. 2.3 (d). A simple mechanical example that exhibits this bifurcation is the *Shilnikov particle* [21].

The same bifurcation can also be obtained from the equation

$$\frac{\mathrm{d}X}{\mathrm{d}t} = \varepsilon + X^2,$$

where now there is no equilibrium for $\varepsilon > 0$.

Note that in the subcritical Pitchfork with a quintic term (Eq. (2.6)) there are two saddle-node bifurcations in the positions marked as S as it is shown in Fig. 2.3 (c). It is important to note that although the mechanisms described above accounts for fixed point instabilities, these mechanisms are fundamental for understanding the emergence of extended solutions, particularly particle-like solutions [29].

2.3 Spatial instabilities

Until now we have been considering systems like Eq. (2.3), which are described by *ordinary differential equations* with derivatives in time. However, in most cases in physics (and other fields of course) are described by spatiotemporal fields, hence their dynamics is described by *partial differential equations*, with derivatives in space and time. In those cases, it is possible to find the emergence of *spatial instabilities*, depending on the parameters of the system. To illustrate this let us consider the following model

$$\partial_t u = \varepsilon u - u^3 - (\partial_{xx} + q^2)^2 u, \tag{2.8}$$

which is the so-called *Swift-Hohenberg* equation, named after Jack B. Swift and Pierre Hohenberg [88], derived to explain convecting rolls in the Rayleigh-Bénard experiment. The relevance of this equation lies in its *pattern formation* mechanism, which is present in fields like nonlinear optics and vegetation [25,61,89], among others. To analyze this mechanism let us first find the *homogeneous* and *stationary* equilibriums of this equation, i.e., equilibriums constant in space and time, respectively. These are

$$u_0 = 0, \quad u_\pm = \pm\sqrt{\varepsilon - q^4}.$$

The eigenvalues associated to u_0 can be obtained by means of a linear stability analysis as in Sec. 2.2.1, that is $u = u_0 + \delta u$, but now proposing $\delta u \propto \mathrm{e}^{\lambda t + \mathrm{i}kx}$. Thus, replacing in the

linearized equation, we can derive a relation between the growth rate and the wavenumber of the instability, which is

$$\lambda_k = \varepsilon - (q^2 - k^2)^2.$$

With this relation, we can analyze the region of parameters where the spatial instabilities take place. In Fig. 2.4 is sketched this expression for some values of ε. Notice that since ε is the maximum of this equation, λ is negative for every value of k for $\varepsilon < 0$, implying that the perturbations decay exponentially to zero, that is, u_0 is stable. On the other hand, for $\varepsilon > 0$ we see that λ is positive for some values of k, which means that u_0 destabilizes. In this case, it evolves to a periodic profile, known as *pattern*. This kind of instability is usually referred as *Turing instability*, in honor to the English mathematician Alan Turing who derived a similar equation to the Swift-Hohenberg equation 25 years before, in one of his unpublished works [27].

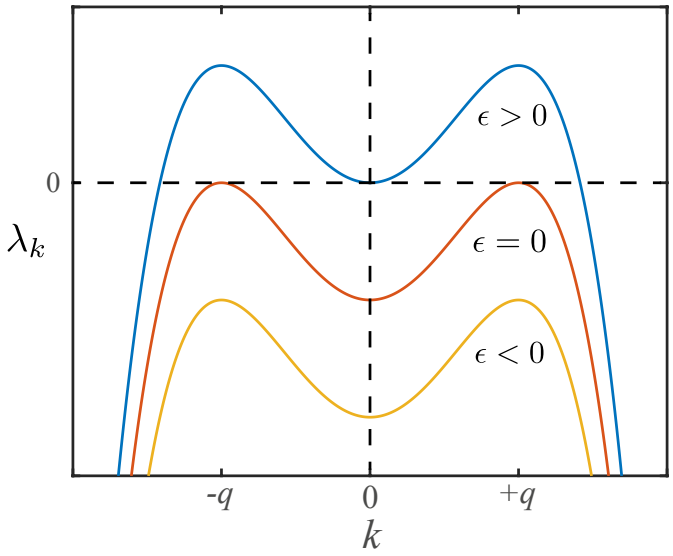

Figure 2.4: λ_k profile in function of the wavenumber k for different values of ε. The maximum value is ε and is obtained evaluating in $\pm q$. The critical case $\varepsilon = 0$ is usually referred as the *marginal case*.

In what follow we will derive the *amplitude equation* of this system that describes the envelope of the pattern, but first we need a useful tool called the *Fredholm solvability condition*.

2.4 Fredholm solvability condition

The Fredholm solvability condition (or *Fredholm alternative*) is named after the Swedish mathematician Erik Fredholm [38]. This is a useful result often used in nonlinear problems. It establishes, in an elementary way, that for a linear problem

$$\mathcal{L}W = b,$$

where $\mathcal{L}$ is a linear operator and W an unknown variable, one of the following conditions must be held:

1. Either: $\mathcal{L}W = b$ has solution W.
2. Or: $\mathcal{L}^\dagger v = 0$ has solution v, with $\langle v|b\rangle \neq 0$, where $\langle\cdot|\cdot\rangle$ is a given inner product and $\mathcal{L}^\dagger$ the adjoint operator under this product, that is,

$$\left\langle \mathcal{L}^\dagger f \middle| g \right\rangle = \langle f|\mathcal{L}g\rangle\,,$$

for every f and g.

In a more simpler way, this condition establishes that the system $\mathcal{L}W = b$ has solution if only if for $v \in \mathrm{Ker}\{\mathcal{L}^\dagger\}$ it fulfills that $\langle v|b\rangle = 0$, i.e., b must be orthogonal to v.

2.5 Amplitude equations

As we have seen in Sec. 2.3, in the Swift-Hohenberg equation the critical mode occurs when $\varepsilon = 0$. When this condition fulfills the critical mode is $k = q$, since $\lambda_k(k = q) = 0$ is the maximum value. To analyze the behavior of the system near this critical mode we propose as *ansatz*

$$u(x,t) = A(t)\mathrm{e}^{\mathrm{i}qx} + A^*(t)\mathrm{e}^{-\mathrm{i}qx} + W(x, A, A^*), \tag{2.9}$$

where A is the envelope of the pattern, A^* its complex conjugate and W is a small correction caused by nonlinear terms. It will be considered that A is a small variable and ε a small parameter, in the sense that terms proportional to AW and εW will be neglected. Moreover, it will be assumed that A is a slow variable, implying that its temporal derivative $\partial_t A$ is small. So that, $\partial_t A W$ will be neglected. It is straightforward that all the previous assumptions also applies to A^*.

Replacing Eq. (2.9) in Eq. (2.8) and linearizing in W, since is a small correction, we obtain

$$\mathcal{L}W = b, \tag{2.10}$$

where the linear operator is

$$\mathcal{L} = (\partial_{xx} + q^2)^2,$$

and

$$b = \left(-\partial_t A + \varepsilon A - 3|A|^2 A\right)\mathrm{e}^{\mathrm{i}qx} - A^3\mathrm{e}^{3\mathrm{i}qx} + c.c.,$$

where $c.c.$ refer to the complex conjugate terms. If we define the following inner product

$$\langle f|g\rangle = \frac{q}{2\pi}\int_{-\pi/q}^{\pi/q} f\cdot q\,\mathrm{d}x,$$

the linear operator turns out to be self-adjoint, that is, $\mathcal{L}^\dagger = \mathcal{L}$. Therefore, the elements of the Kernel of $\mathcal{L}^\dagger$ are

$$\mathrm{Ker}\{\mathcal{L}^\dagger\} = \{\mathrm{e}^{\mathrm{i}qx}, \mathrm{e}^{-\mathrm{i}qx}\}. \tag{2.11}$$

The Fredholm solvability condition states that the linear system (2.10) has solution if b is orthogonal to the elements in (2.11). Therefore, we need to impose that

$$\left\langle \mathrm{e}^{\mathrm{i}qx} \middle| b \right\rangle = 0 \quad \text{and} \quad \left\langle \mathrm{e}^{-\mathrm{i}qx} \middle| b \right\rangle = 0.$$

These two equations give the dynamical equations for $A(t)$ and $A^*(t)$:

$$\partial_t A = \varepsilon A - 3|A|^2 A$$

and

$$\partial_t A^* = \varepsilon A^* - 3|A|^2 A^*.$$

The equation that A satisfies (and also A^*) is known as the *Ginzburg-Landau equation* with real coefficients. Notice that they have the form of the normal form a supercritical Pitchfork bifurcation is a slow variable and epsilon a small parameter (see Eq. (2.5)). Moreover, the steady states have the form $A = (\varepsilon/3)^{1/2} e^{i\phi_0}$, where ϕ_0 is arbitrary. Then, according to Eq. (2.9), the steady states $u_s(x)$ evolves with ε like

$$u_s(x) = 2\sqrt{\frac{\varepsilon}{3}} \cos(qx + \phi_0) + \mathcal{O}(\varepsilon^{3/2}),$$

which is a periodic profile with wavelength $2\pi/q$. This profile is the pattern solution from the Swift-Hohenberg equation. Its wavelength depends on the parameters of the system and not in its size. Indeed, if we remove a wavelength of this profile, another wavelength will emerge and the system will return to its original form.

2.6 Time-dependent forcing

Let us analyze now the effects in a system under a *time-dependent* forcing, particularly the role played by the *forcing frequency*.

2.6.1 Resonance

Forced oscillators have been studied since the dawn of mechanics. During the study of the dynamics of the pendulum, Galileo observes the resonance phenomenon [40]. However, based on a linear forced oscillator, Euler was the first to explain this phenomenon [34]. Add forcing corresponds to add energy to a system. The simplest case is the driven oscillator, in which an external driving force varying harmonically is applied [59,68], like a driven simple pendulum. In presence of dissipation, the equation of motion writes

$$\ddot{\theta} + \mu\dot{\theta} + \omega_0^2\theta = a\cos\omega t,$$

with μ the damping coefficient, ω_0 the natural frequency of the system, a the forcing amplitude and ω the forcing frequency. Since the forcing is oscillatory, the system is gaining and losing energy. The response of the system consists in two parts: a *transient* effect, i.e., that die out, and an oscillatory *steady-state*, which is relevant for times larger than $2/\mu$. The amplitude A of this steady-state is given by [68]

$$A = \frac{a}{\sqrt{(\omega^2 - \omega_0^2)^2 + \omega^2\mu^2}}. \tag{2.12}$$

When the forcing frequency ω gets closer to the natural frequency ω_0, this amplitude reaches its maximum value. This phenomenon is called *resonance*. In this case, the periodic forcing generates a response that increases in time.

When the damping increases, the maximum amplitude A is reached in a frequency lower than ω_0, as illustrated in Fig. 2.5.

One important property of this kind of forcing, that is, when it is applied directly to the system, is that the response will be at the same frequency of the forcing. The situation is different in the case of *parametric forcing*.

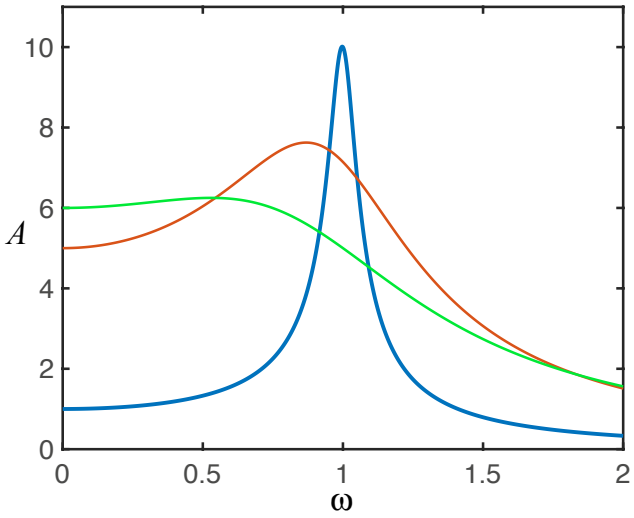

Figure 2.5: Amplitude of the steady-state solution (Eq. (2.12)) in function of the forcing frequency ω for different values of the damping coefficient μ, for $\omega_0 = 1$. For the blue line we have used $a = 1$ and $\mu = 0.1$, for the red $a = 5$ and $\mu = 0.7$, and for the green $a = 6$ and $\mu = 1.2$.

2.6.2 Parametric forcing

The previous case is not the only one that generates a response that increases with time. Let us consider the case when the injection of energy is applied to a *parameter* of the system, namely when the system is under a parametric forcing. One simple mechanical example of this is the simple driven pendulum with a vertical oscillatory point of support or pivot (see Fig. 2.6). In presence of dissipation, the equation of motion that satisfies the vertical deviation angle $\theta(t)$ of this system is [59]

$$\ddot{\theta} = -(\omega_0^2 + \gamma \sin \omega t) \sin \theta - \mu \dot{\theta},$$

with

$$\gamma = \frac{a\omega^2}{L},$$

where ω_0 and L are the natural frequency and length of the pendulum, a and ω the amplitude and frequency of the forcing, respectively, and μ the damping coefficient. It is interesting

to mention that this phenomenon was already used in the tenth century to perfume a Spain cathedral, of course, without their respective understanding [85]. This system has two stationary solutions, $\theta = 0$ and $\theta = \pi$. In absence of forcing these equilibriums are stable and unstable, respectively. However, vertical parametric forcing can change stability into instability and vice versa.

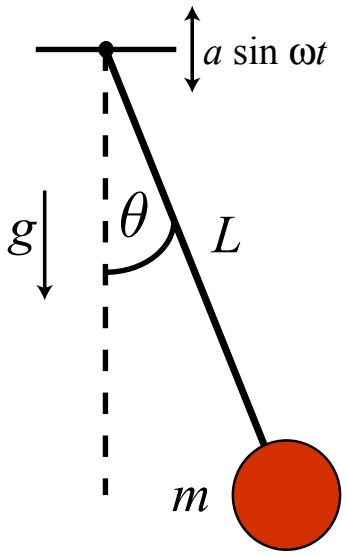

Figure 2.6: Driven simple pendulum with a vertical oscillatory pivot at frequency ω and amplitude a.

Linear stability analysis of $\theta = 0$

Let us analyze the stability of the $\theta = 0$ solution. Performing a linear analysis in θ we get

$$\ddot{\theta} = -(\omega_0^2 + \gamma \sin \omega t)\theta - \mu\dot{\theta}, \tag{2.13}$$

which is usually referred as the *Mathieu equation*, a special case of the Hill equation [36,59,70]. Even though the Mathieu equation is an ordinary differential equation, it has not analytical solutions due to the time-dependence in one of its coefficients [2]. Nevertheless, since this coefficient is *periodic in time*, we can apply the *Floquet theorem*. This theorem states that this equation has solutions of the form

$$\mathrm{e}^{\lambda_j t}\psi_j(t), \tag{2.14}$$

where λ_j, called the *Floquet exponents*, are functions of the parameters ω, γ and μ. The functions $\psi_j(t)$ are periodic in time [77], that is $\psi_j(t + 2\pi/\omega) = \psi_j(t)$. We are not interested in studying these functions, but in the λ_j exponents. Notice that they define the region where the solutions are stable or unstable, depending if their real parts are negative or positive. Stability requires that all the real parts be negative, implying that if one these exponents is positive the solution is unstable. Therefore, the *stability boundaries* in the space of parameters

[2]The solutions, in fact, corresponds to special functions named *Mathieu functions*, introduced by Émile Mathieu (1868) to analyze the motion of elliptical membranes.

are determined where all the real parts of these exponents vanish[3]. The stability chart that specifies these regions is called the *Ince-Strutt diagram* [96]. As we will see, the dissipation plays an important role on these regions.

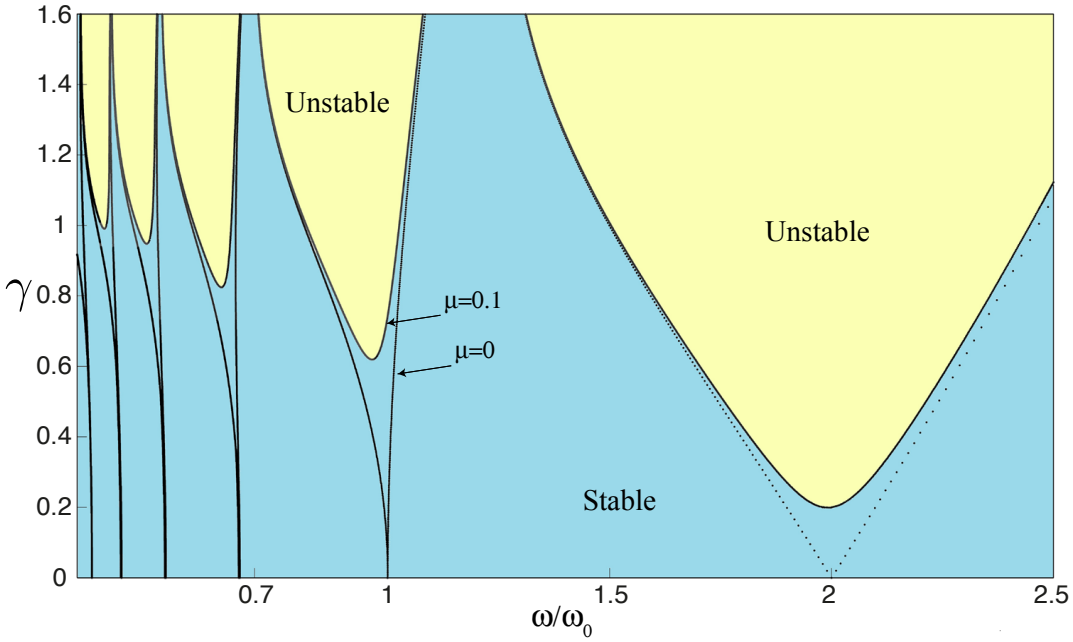

Figure 2.7: Stability chart of the damped Mathieu equation, known as Ince-Strutt diagram. The yellow part represents the unstable regions, while the blue part the stable regions. For $\mu = 0$ the boundary curves reach the horizontal axis in $\omega = 2\omega_0/n$. The unstable regions around these frequencies are usually called the Arnold Tongues. As μ grows these tongues rise.

Stability chart: Ince-Strutt diagram

To establish the stability boundary regions we consider the solution of the Mathieu equation as an expansion in Fourier series,

$$\theta(t) = \sum_{n=0}^{\infty} a_n \cos\left(\frac{nt\omega}{2}\right) + b_n \sin\left(\frac{nt\omega}{2}\right), \tag{2.15}$$

where a_n and b_n are the Fourier coefficients. Introducing this ansatz into the Mathieu equation (2.13) we derive a set of an infinite number of equations. Nonetheless, according to the principle of harmonic balance [32, 75], every coefficient proportional to every sine or cosine term is to be equated to zero. This yields to a linear system in a_n and b_n of infinite order.

[3]Notice that the Floquet theorem corresponds to the *Bloch theorem* in solid-state physics, applied to determine the bands in the energy spectrum.

Truncating until $n = 3$, this system writes in matrix form

$$\begin{pmatrix} \frac{4\omega_0^2}{\omega^2} & \frac{2\gamma}{\omega^2} & 0 & 0 & 0 & 0 & 0 \\ \frac{4\gamma}{\omega^2} & \frac{4\omega_0^2}{\omega^2} - 4 & \frac{4\mu}{\omega} & 0 & 0 & 0 & 0 \\ 0 & -\frac{4\mu}{\omega} & \frac{4\omega_0^2}{\omega^2} - 4 & 0 & 0 & 0 & 0 \\ 0 & 0 & 0 & \frac{4\omega_0^2}{\omega^2} + \frac{2\gamma}{\omega^2} - 1 & \frac{2\gamma}{\omega^2} & \frac{2\mu}{\omega} & 0 \\ 0 & 0 & 0 & \frac{2\gamma}{\omega^2} & \frac{4\omega_0^2}{\omega^2} - 9 & 0 & \frac{6\mu}{\omega} \\ 0 & 0 & 0 & -\frac{2\mu}{\omega} & 0 & \frac{4\omega_0^2}{\omega^2} - \frac{2\gamma}{\omega^2} - 1 & \frac{2\gamma}{\omega^2} \\ 0 & 0 & 0 & 0 & -\frac{6\mu}{\omega} & \frac{2\gamma}{\omega^2} & \frac{4\omega_0^2}{\omega^2} - 9 \end{pmatrix} \begin{pmatrix} a_0 \\ a_2 \\ b_2 \\ a_1 \\ a_3 \\ b_1 \\ b_3 \end{pmatrix} = \begin{pmatrix} 0 \\ 0 \\ 0 \\ 0 \\ 0 \\ 0 \\ 0 \end{pmatrix},$$

where the square matrix only has elements in the center diagonals. In fact, in absence of dissipation ($\mu = 0$) this matrix is tridiagonal.

In order to determine the boundary regions of stability, we need to impose that determinant of this square matrix is zero, which is equivalent to impose that the real part of the Floquet exponents λ_j from Eq. (2.14) vanish. From this condition, we can derive numerically the boundary stability regions in functions of the parameters of the system. However, since this matrix is of infinite order it is necessary to truncate the Fourier expansion, depending on the desired accuracy of the boundary.

In Fig. 2.7 it is shown the stability chart in the $\gamma - \omega$ plane, obtained by truncating the Fourier expansion until $n = 20$. It is important to note that when one consider more modes, critical curves do not change significantly in shape. As it is shown, for $\mu = 0$ the boundary curves reach the horizontal axis in certain values of the forcing frequency ω. These values in fact are

$$\omega = \frac{2}{n}\omega_0,$$

with n an integer number. They correspond to the frequencies where the $\theta = 0$ solution destabilizes, that is, they define the *parametric resonance condition*. Thus, the parametric forcing allows the possibility to have resonance not only at the natural frequency ω_0. The unstable regions around these critical frequencies are usually referred as *Arnold tongues* [82]. Notice that as μ grows the minimum value of these tongues raises.

Analytical approximation of 2:1 Arnold Tongue

The tongue located around $\omega = 2\omega_0$ is usually called the *2:1 tongue*, since it corresponds to the region where the system needs to be forced twice the natural frequency to resonate. This tongue has been largely studied in different physical contexts, e.g., in Faraday instability in fluids [55].

There is a way to approximate analytically this tongue, which is useful to predict the system behavior when the parameters cross the tongue boundary. To do that, based on the work of Eugene Butikov [16, 17], we should propose as ansatz in the Mathieu Eq. (2.13) the following expansion

$$\theta(t) = A_1 e^{i\frac{\omega}{2}t} + A_1^* e^{-i\frac{\omega}{2}t}, \tag{2.16}$$

where A_1^* denote the conjugate complex of A_1. Notice that this is nothing but to consider the term $n = 1$ in ansatz (2.15). Then, introducing it into the Mathieu equation, it yields to an expression with terms proportional to $e^{\pm i\frac{\omega}{2}t}$. Following the same procedure as before, these terms have to be equated to zero. Thus, we obtain a linear system, which in matrix form is represented as

$$\begin{pmatrix} -\frac{\omega^2}{4} + \frac{i\mu\omega}{2} + \omega_0^2 & -\frac{i\gamma}{2} \\ \frac{i\gamma}{2} & -\frac{\omega^2}{4} - \frac{i\mu\omega}{2} + \omega_0^2 \end{pmatrix} \begin{pmatrix} A_1 \\ A_1^* \end{pmatrix} = \begin{pmatrix} 0 \\ 0 \end{pmatrix},$$

and imposing that the determinant of this system be zero, we derive the following expressions for the boundary stability curve

$$\gamma_\pm = \pm\frac{1}{2}\sqrt{4\mu^2\omega^2 + \omega^4 - 8\omega_0^2\omega^2 + 16\omega_0^4}.$$

Since the forcing amplitude is positive, γ_+ is the solution with physical meaning. In Fig. 2.8 we compare this analytical approximation with the 2:1 tongue obtained in the previous section. Notice that the approximation fits better for frequencies $\omega > 2\omega_0$.

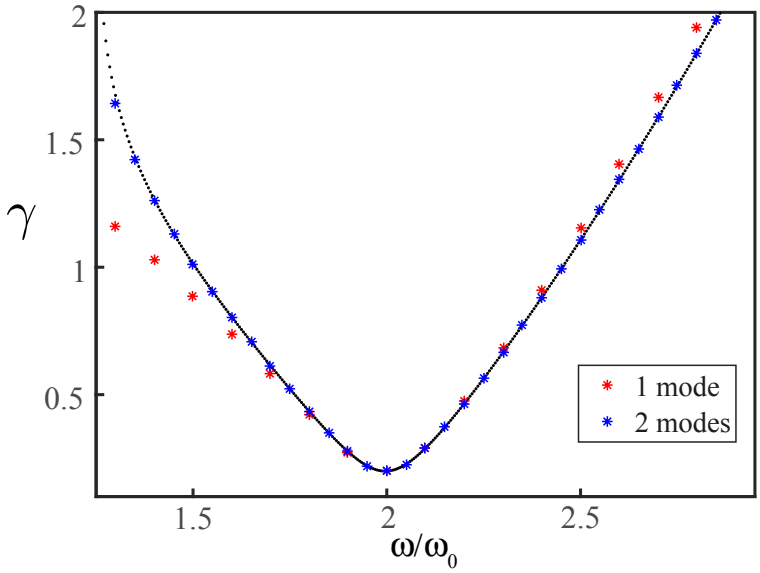

Figure 2.8: $2:1$ tongue for $\mu = 0.1$, with its analytical approximations using 1 and 2 modes as ansatz, expressed in Eqs. (2.16) and (2.17), respectively.

If we now consider an ansatz of the form

$$\theta(t) = A_1 e^{i\frac{\omega}{2}t} + A_3 e^{-i\frac{3\omega}{2}t} + c.c, \tag{2.17}$$

and perform the same analysis, the approximation fits even better as it is shown in Fig. 2.8. Therefore, one may conclude that some Arnold tongues can be described in a few modes, which makes it possible to obtain analytical formulas.

2.6.3 Kapitza effect

One interesting feature of this parametric forcing is the stabilization of the $\theta = \pi$ steady state (upside-down pendulum) in the vertically driven pendulum. As we have discussed in the previous section, the dynamical equation of this system is given by

$$\ddot{\theta} = -(\omega_0^2 + \gamma \sin \omega t) \sin \theta - \mu \dot{\theta}. \tag{2.18}$$

In what follows we will apply a method developed by the Russian physicist Pyotr Leonidovich Kapitsa (or Peter Kapitza) [48], in order to treat analytically dynamical systems with a natural time scale much larger than the time scale of the forcing. To illustrate the time-scale separation in this system, in Fig. 2.9 is shown the temporal evolution for a forcing frequency $\omega = 20\omega_0$, without dissipation.

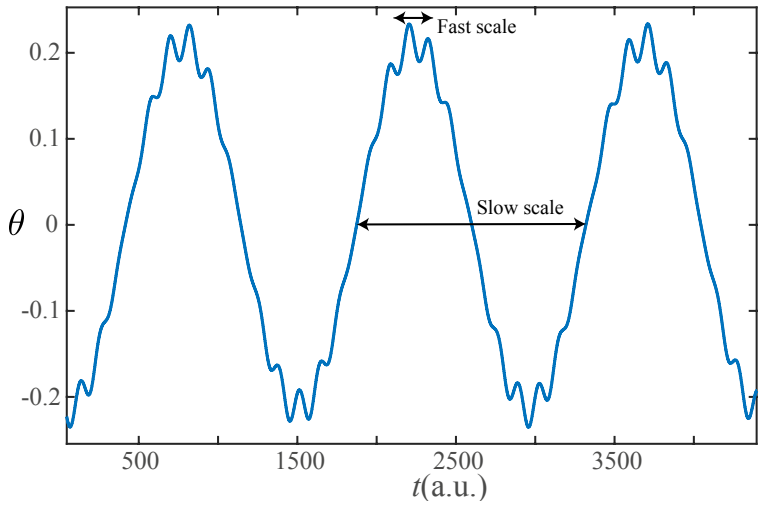

Figure 2.9: Temporal evolution obtained by integrating numerically the Eq. (2.18), with $\omega_0 = 1$, $\gamma = 40$, $\omega = 20$ and $\mu = 0$.

To apply this strategy we propose the following ansatz

$$\theta(t) = \theta_{\text{slow}}(t) + \theta_{\text{fast}}(t),$$

where $\theta_{\text{slow}}(t)$ accounts for the slowly part, that is, the envelop of the temporal profile, and $\theta_{\text{fast}}(t)$ stands for the fast one, representing the small amplitude traveling waves (see Fig. 2.9). In addition, the $\theta_{\text{fast}}(t)$ variable will be considered small compared to $\theta_{\text{slow}}(t)$,

$$\theta_{\text{fast}}(t) \ll \theta_{\text{slow}}(t).$$

Then, introducing this ansatz into Eq. (2.18) and linearizing in θ_{fast}, we get

$$\ddot{\theta}_{\text{slow}} + \ddot{\theta}_{\text{fast}} = -(\omega_0^2 + \gamma \sin \omega t)(\sin \theta_{\text{slow}} + \theta_{\text{fast}} \cos \theta_{\text{slow}}) - \mu(\dot{\theta}_{\text{slow}} + \dot{\theta}_{\text{fast}}). \tag{2.19}$$

From this equation we can extract the equation for the rapid motion, by collecting the terms that vary in the fast time scale ($T = 2\pi/\omega$). These are

$$\ddot{\theta}_{\text{fast}} = -\gamma \sin \omega t \sin \theta_{\text{slow}} - (\omega_0^2 + \gamma \sin \omega t)\theta_{\text{fast}} \cos \theta_{\text{slow}} - \mu \dot{\theta}_{\text{fast}}.$$

However, to simplify our analysis let us consider the limit of high frequencies, particularly when $\mu \ll \omega$. Since $\gamma \propto \omega^2$ the dominant terms in this limit are

$$\ddot{\theta}_{\text{fast}} \approx -\gamma \sin \omega t \sin \theta_{\text{slow}},$$

where we have considered the fact that θ_{fast} is small. Here the time dependence of θ_{slow} can be neglected if we take into account that the two time scales are well separated. Thus, the integration yields

$$\theta_{\text{fast}} \approx \frac{\gamma}{\omega^2} \sin \omega t \sin \theta_{\text{slow}}.$$

Likewise, this result can be obtained by using the method of the stationary phase for the integral of Laplace [9]. Then, replacing this solution in Eq. (2.19) and taking the temporal average on the fast time scale, i.e.,

$$\langle f(t) \rangle = \frac{\omega}{2\pi} \int_0^{2\pi/\omega} f(t) \mathrm{d}t,$$

we get

$$\ddot{\theta}_{\text{slow}} = -\omega_0^2 \sin \theta_{\text{slow}} - \gamma \langle \sin \omega t \, \theta_{\text{fast}} \rangle \cos \theta_{\text{slow}} - \mu \dot{\theta}_{\text{slow}},$$

since the variable θ_{slow} does not vary on this time scale and $\langle \sin \omega t \rangle = 0$. On the other hand,

$$\langle \sin \omega t \, \theta_{\text{fast}} \rangle \approx \frac{\gamma}{\omega^2} \langle \sin^2 \omega t \rangle \sin \theta_{\text{slow}} = \frac{\gamma}{2\omega^2} \sin \theta_{\text{slow}},$$

which finally yields to an effective equation for the slow variable

$$\ddot{\theta}_{\text{slow}} = -\omega_0^2 \sin \theta_{\text{slow}} - \frac{\gamma^2}{4\omega^2} \sin 2\theta_{\text{slow}} - \mu \dot{\theta}_{\text{slow}}.$$

From this equation is possible to establish the stability condition for the $\theta_{\text{slow}} = \pi$ solution. Stability requires that the potential energy has a local minimum at this solution. This condition is indeed

$$\frac{\gamma^2}{2\omega^2} > \omega_0^2,$$

and since $\gamma = a\omega^2/l$, this condition writes

$$\omega > \sqrt{2} \frac{\omega_0 l}{a}.$$

Therefore, for frequencies that fulfill this condition the upside-down position becomes stable.

2.7 Particle-like solutions in coupled oscillators

Let us turn now to study an important aspect of this thesis, the *particle-like solutions*. These solutions are particle-like states for classical field equations, that is, they are solutions that can be characterized by to be localized and be described by a finite number of parameters

such as position, width, charge, and so forth. The study of the particle-like solutions is in the structural pillar of the nonlineal physics, from the discovery of solitons. The study of these solutions involves nonlinear wave equations, scalar field theory [42, 45, 100], to name a few.

In what concerns this thesis, we are interested in studying the effect of parametric forcing in the so-called *kink soliton solutions*. We will discuss this effect in Chapter 3. In this section we will introduce the main aspects of kink solutions of the *sine-Gordon equation*, as well as in the ϕ^4 scalar field equation, where we will study the *kink-antikink* interaction.

2.7.1 Sine-Gordon equation

The sine-Gordon equation was first introduced in 1862 by the French engineer Edmond Bour in his work on deformation of surfaces [14]. It was rediscovered in 1939 by Frenkel and Kontorova in the study of crystal dislocations [54].

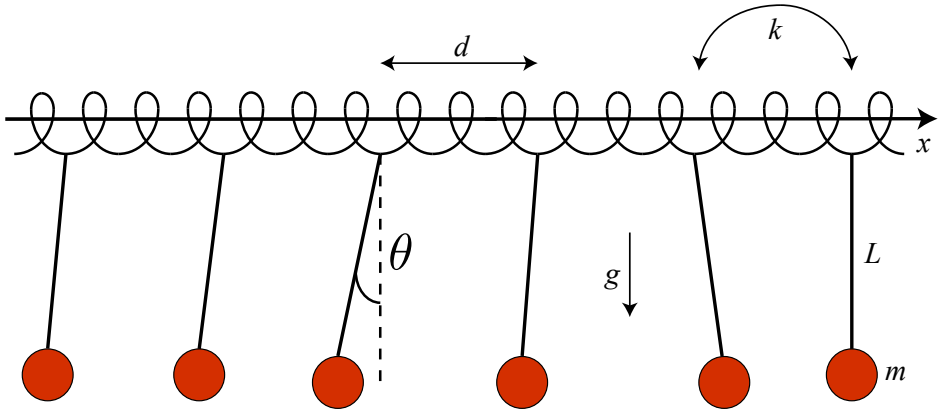

Figure 2.10: Schematic representation of a chain of coupled pendulums by springs.

To introduce this equation let us consider a simple and pedagogical mechanical model composed of a chain of simple pendulums, with each pendulum connected by linear springs to its nearest neighbors as it is depicted in Fig. 2.10. Here k is the torque constant of the springs, d the distance of separation between the pendulums, m and L their mass and length, respectively. Defining

$$\omega_0^2 = g/l \quad \text{and} \quad \kappa^2 = \frac{k\,\mathrm{d}^2}{mL^2},$$

the equation that describes the dynamics of the vertical deviation angle $\theta(x,t)$ in the continuous limit, that is, when $\omega_0/\kappa \gg \mathrm{d}$, is [83]

$$\partial_{tt}\theta = -\omega_0^2 \sin\theta + \kappa^2 \partial_{xx}\theta,$$

which is the so-called *sine-Gordon equation*[4]. The importance of this equation lies on its modeling of many fields of physics, like dislocations in crystals, domain walls in ferromagnets,

[4]The name of this equation is a word play on the well known *Klein-Gordon equation*, which has the form $\partial_{tt}\theta = -\omega_0^2\theta + \kappa^2\partial_{xx}\theta$.

flux in Josephson transmission lines, among others [15, 26]. Notice that under the following transformations

$$t \to \omega_0 t \quad \text{and} \quad x \to \frac{\omega_0}{\kappa} x,$$

the SG equation can be written as

$$\partial_{tt}\theta = -\sin\theta + \partial_{xx}\theta, \tag{2.20}$$

where it is easy to appreciate its *Lorentz invariance*, since it includes the d'Alembert operator $\Box \equiv \partial_{tt} - \partial_{xx}$.

One important property of the SG equation is that admits analytical solutions of *soliton* solutions, such as kinks or breathers[5], introduced by Seeger and co-workers more than sixty years ago [15]. In addition, it is important to note that this equation is integrable.

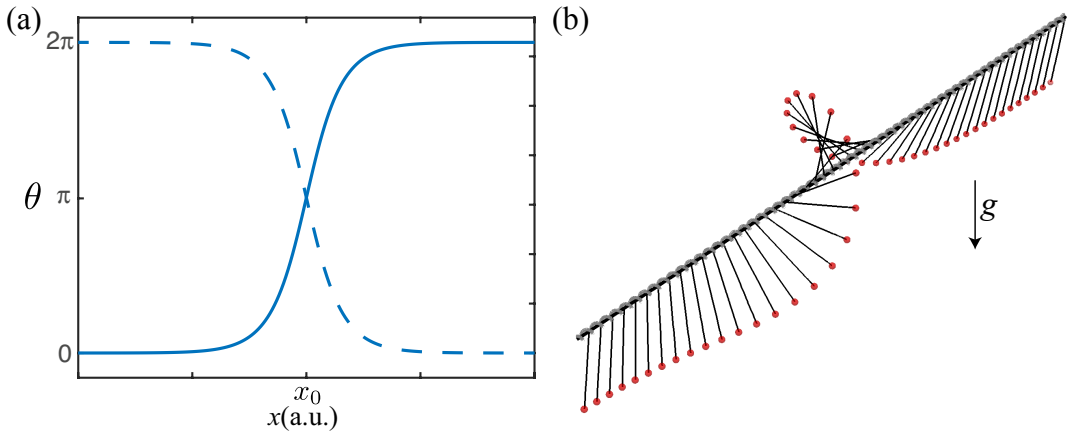

Figure 2.11: (a) Spatial profile of kink and antikink solution in function of the variable $s = x - vt$ (see Eq. (2.21)). The full (dotted) line corresponds to the kink (antikink) solution. (b) Representation of the kink solution in the chain of pendulums.

Kinks

The kinks are due to the degeneracy of the system in the $\theta = 0$ solution. They correspond to solutions that connect two symmetric states, or minima of the (periodic) potential energy [66, 95]. In the case of the chain of pendulums the kinks correspond to a localized rotation in 2π, connecting the states $\theta = 0$ and $\theta = 2\pi$ (see Fig. 2.11). Since the SG is Lorentz invariant, it is expected that traveling solutions also exist. Their analytical expression from Eq. (2.20) writes

$$\theta(x,t) = 4\arctan\left(\exp\{-\sigma\gamma(v)(x - x_0 - vt)\}\right), \tag{2.21}$$

with

$$\gamma(v) = \frac{1}{\sqrt{1-v^2}},$$

[5]The original German name for kinks and breathers were *translatorische and oszillatorische Eigenbewegungen.*

where v is the kink speed, which can not exceed the value 1. The value x_0 is the center position at $t = 0$. The factor $\gamma(v)$ can be treated as the Lorentz contraction of the kink width. The parameter $\sigma = \pm 1$ is usually referred as the *topological charge*. When $\sigma = 1$ we call the solution as *kink*, while for $\sigma = -1$ as *antikink*. In the chain of pendulums, when $s = x - vt$ increases from $-\infty$ to $+\infty$, the pendulums rotate from 0 to 2π for the kink, and from 2π to 0 for the antikink. Their respective spatial profile is plotted in Fig. 2.11.

Kink-kink and kink-antikink collisions

It is possible to show that Eq. (2.20) admits further solutions [57, 58] of the form

$$\theta(x,t) = 4 \arctan\left(\frac{F(x)}{G(t)}\right), \tag{2.22}$$

where $F(x)$ and $G(t)$ are arbitrary functions. Introducing this expression into the SG equation one can obtain analytical expressions for *kink-kink* and *kink-antikink* collisions.

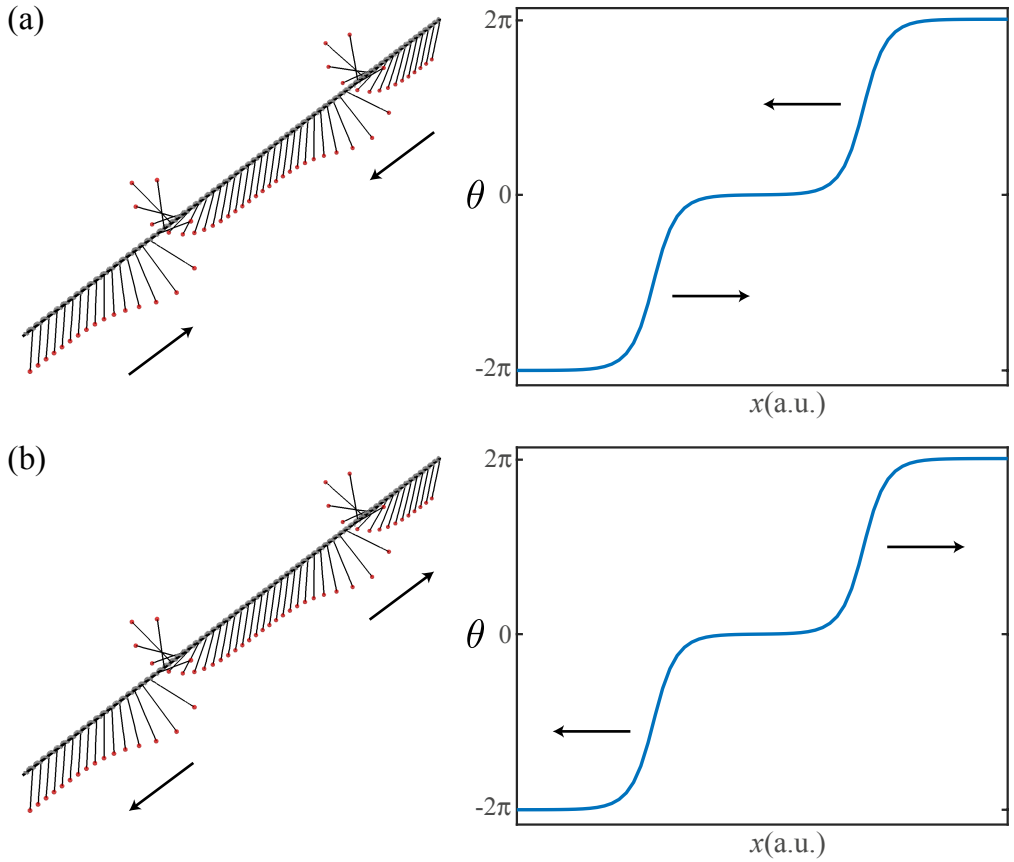

Figure 2.12: Initial and final instant of the kink-kink collision. (a) Two kinks travel with the same velocity in opposite directions. (b) After the collision, the each kink changes its velocity direction. Then, the kink-kink interaction is repulsive.

The kink-kink collision has the form

$$\theta(x,t) = 4\arctan\left(\frac{v\sinh\left(\frac{x}{\sqrt{1-v^2}}\right)}{\cosh\left(\frac{vt}{\sqrt{1-v^2}}\right)}\right),$$

and describes the collision between two kinks traveling with respective velocities $+v$ and $-v$ to the origin. As it shown in Fig. 2.12, the kink-kink collision is *repulsive*, that is, it results in a change of the direction of each kink.

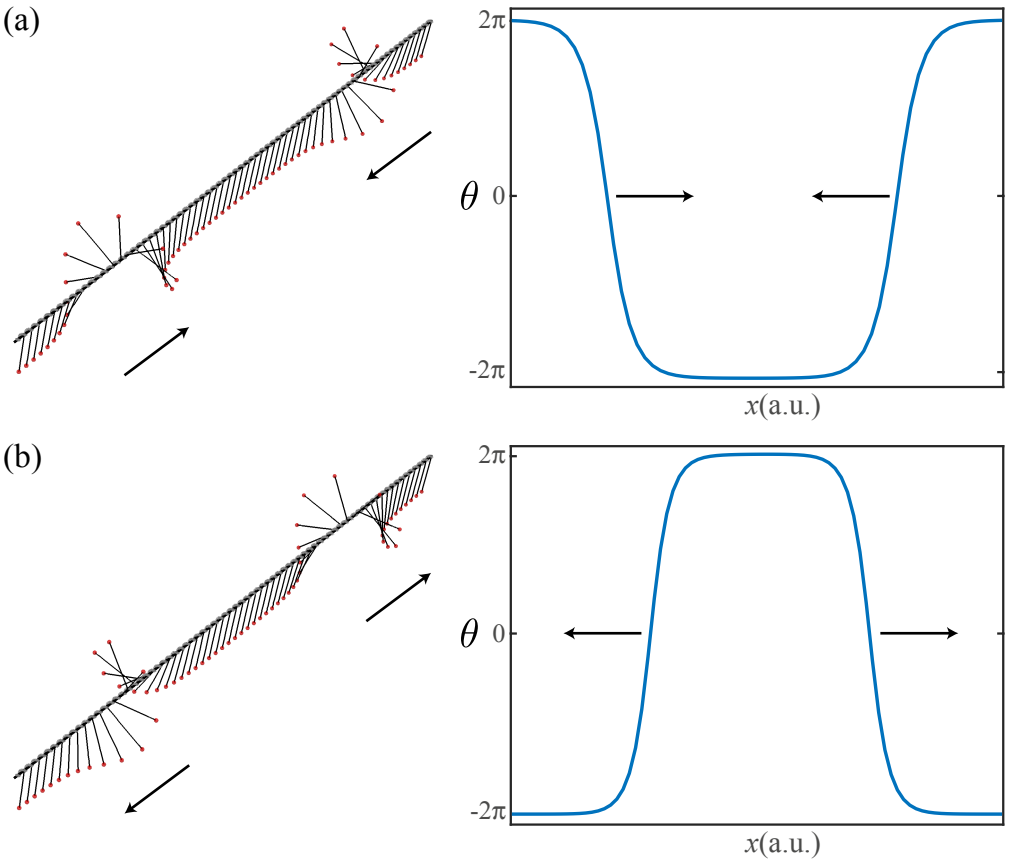

Figure 2.13: Initial and final instant of the kink-antikink collision. (a) One kink and an antikink travel with the same velocity in opposite directions. (b) After the collision, the each kink passes through each other. Then, the kink-antikink interaction is permeable.

In a similar way, the kink-antikink collision writes

$$\theta(x,t) = 4\arctan\left(\frac{\sinh\left(\frac{vt}{\sqrt{1-v^2}}\right)}{v\cosh\left(\frac{x}{\sqrt{1-v^2}}\right)}\right),$$

and shows that the kink-antikink collision is perfectly permeable since they pass through each other. Their temporal evolution is shown in Fig. 2.13.

Breathers

The *breather* solutions correspond to localized solutions characterized by oscillations in their amplitude. This solution can also be obtained from Eq. (2.22). Their analytical solution reads

$$\theta(x,t) = 4\arctan\left(\frac{\sqrt{1-\Omega^2}}{\Omega}\,\mathrm{sech}\left(\sqrt{1-\Omega^2}x\right)\sin\Omega t\right),$$

and represents an oscillating state where its envelope is modulated at frequency Ω. Its temporal evolution is shown in Fig. 2.14.

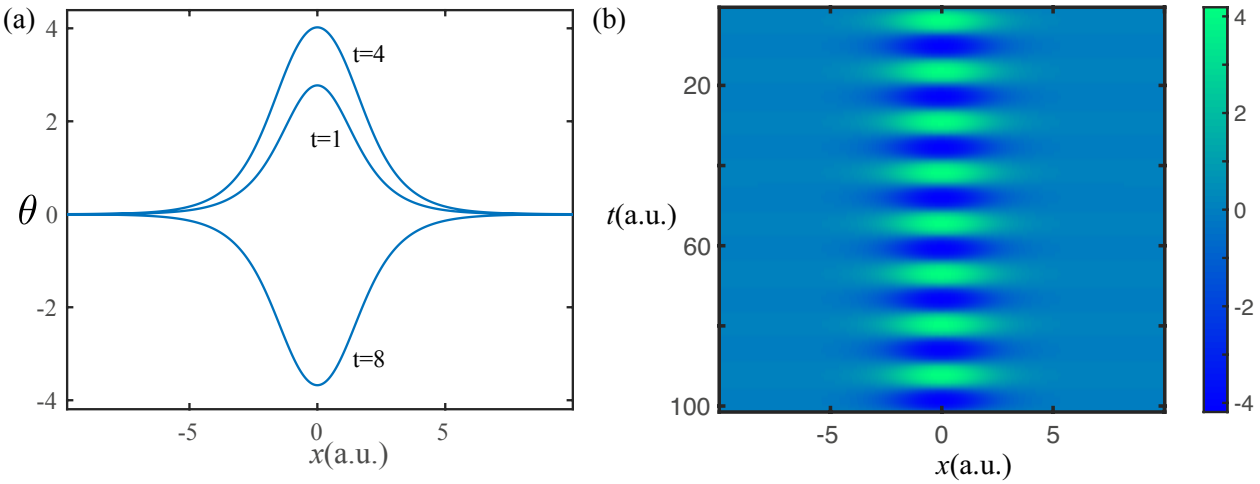

Figure 2.14: Temporal evolution of breather solution. (a) Spatial profile evolution for different times. (b) Corresponding spacetime diagram. We have used $\Omega = 0.5$.

2.7.2 ϕ^4 scalar field equation

Let us turn now to the study of kink solutions in the ϕ^4 scalar field theory equation. The ϕ^4 scalar theory is the simplest model that describe spontaneous symmetry breaking, widely used to describe phase transitions. This field theory is called ϕ^4 since the Lagrangian contains a fourth power in $\phi(x,t)$. It appears in different physical contexts, such as quantum physics, particle physics and cosmology [79, 95, 97, 98]. The equation of this model reads

$$\partial_{tt}\phi = \varepsilon\phi - \phi^3 + \partial_{xx}\phi,$$

where ε controls the size of the kink solution, which has the analytical form

$$\phi(x,t) = \sigma\sqrt{\varepsilon}\tanh\left(\sqrt{\frac{\varepsilon}{2\sqrt{1-v^2}}}(x - vt - x_0)\right), \tag{2.23}$$

where $-1 < v < 1$ is the kink velocity and x_0 the center position at $t = 0$. The topological charge σ follows the same rules as in sine-Gordon kinks, i.e., for $\sigma = 1$ the solution is called kink and for $\sigma = -1$, antikink. The spatial profile of these solutions is similar to those of sine-Gordon equation. However, the maximum and minimum values in this case are $\sqrt{\varepsilon}$ and $-\sqrt{\varepsilon}$, respectively, as it is shown in Fig. 2.15.

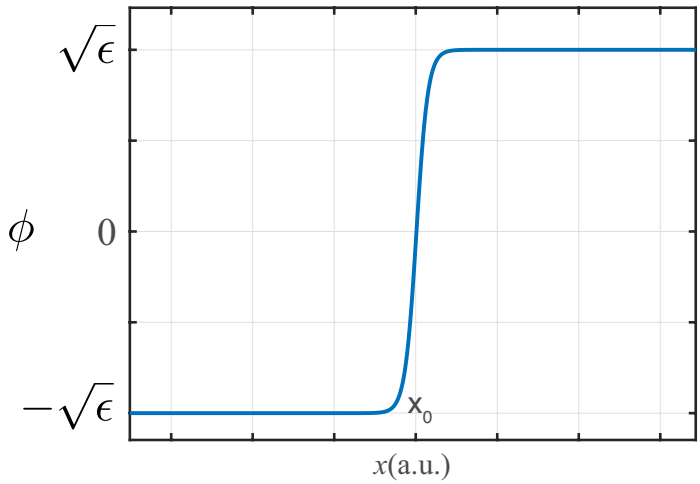

Figure 2.15: Spatial profile of the analytical kink solution of the ϕ^4 equation expressed in Eq. (2.23), with $x_0 = 0$, $v = 0$ and $\varepsilon = 1$.

Unlike the sine-Gordon equation, there are not analytical expressions for the kink-kink and kink-antikink collision. In fact, depending on the initial velocities of the kinks, there are different possible configurations. In a different range of velocities the kink-antikink collision could be repulsive, or lead to the mutual capture of the pair, or lead to a phenomenon called *two bounce resonance* [18, 43], where the kinks first coalesce and then escape, with a very regular pattern governing the behaviors.

In what concern this thesis, we are interested in studying the dissipative effects on kinks solutions. In the next section, we will analyze the kink-antikink interaction in the dissipative ϕ^4 equation.

2.7.3 Kink-antikink interaction in dissipative ϕ^4 model

Considering now the addition of dissipation in the ϕ^4 field equation, that is

$$\partial_{tt}\phi = \varepsilon\phi - \phi^3 + \partial_{xx}\phi - \mu\partial_t\phi, \tag{2.24}$$

where $\mu > 0$ accounts for the dissipation, we will study the kink-antikink interaction in the limit of small dissipation and large distance of separation. To start, we propose the following ansatz

$$\phi(x,t) = \phi_{\rm k}(x - x_-(t)) + \phi_{\rm ak}(x - x_+(t)) - \sqrt{\varepsilon} + W(x, x_+, x_-), \tag{2.25}$$

where $\phi_{\rm k}$ and $\phi_{\rm ak}$ corresponds to a kink and antikink solution of the stationary Eq. (2.24), respectively. Therefore

$$\phi_{\rm k}(x - x_-(t)) = \sqrt{\varepsilon}\tanh\left(\sqrt{\frac{\varepsilon}{2}}(x - x_-(t))\right)$$

and

$$\phi_{\rm ak}(x - x_+(t)) = -\sqrt{\varepsilon}\tanh\left(\sqrt{\frac{\varepsilon}{2}}(x - x_+(t))\right).$$

The function W accounts for the small nonlinear corrections of interaction between the solutions. Besides, x_- and x_+ corresponds to the center positions of the kink and antikink, respectively, that are promoted as functions of time. The spatial profile of this ansatz is illustrated in Fig. 2.16, where we have defined

$$\Delta(t) \equiv x_+(t) - x_-(t), \quad \delta(t) = \frac{x_-(t) + x_-(t)}{2},$$

as the distance of separation between the kinks and the center position, respectively.

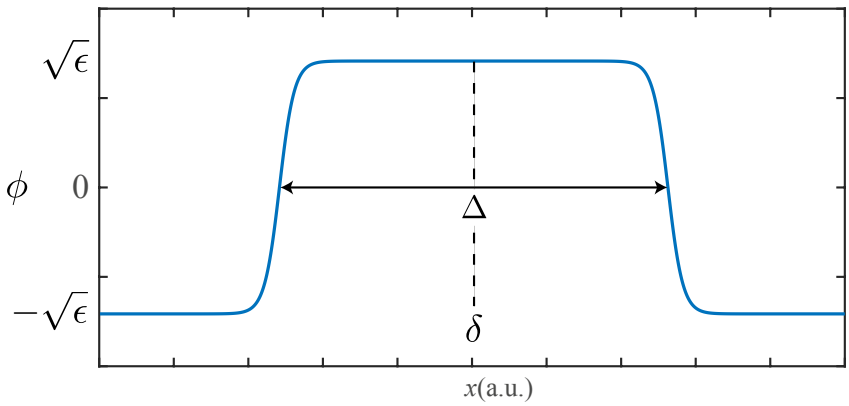

Figure 2.16: Spatial profile of the ansatz from Eq. (2.16).

It will be assumed that the kinks are located very far apart, implying that Δ will be much larger than the kink width $\sqrt{2/\varepsilon}$ ($\Delta \gg \sqrt{2/\varepsilon}$). As a consequence, since W accounts for the effects of interaction will be also small. In addition, it will be assumed that the kinks travel slowly, implying that the temporal derivatives of $x_-(t)$ and $x_+(t)$ are small, in such a way that terms proportional to the product of W with $\dot{x}_-$ or $\dot{x}_+$ will be neglected.

Taking into account the previous considerations, introducing the ansatz into Eq. (2.24) and linearizing in W, we obtain the following linear system

$$\mathcal{L}W = b,$$

where the linear operator $\mathcal{L}$ corresponds to

$$\mathcal{L} \equiv \varepsilon - 3(\phi_{\rm k} + \phi_{\rm ak} - \sqrt{\varepsilon})^2 + \partial_{xx},$$

and

$$\begin{aligned} b = \frac{1}{2}\left(\ddot{\Delta} + \mu\dot{\Delta}\right)(\partial_{z_-}\phi_{\rm k} - \partial_{z_+}\phi_{\rm ak}) - \left(\ddot{\delta} + \mu\dot{\delta}\right)(\partial_{z_-}\phi_{\rm k} + \partial_{z_+}\phi_{\rm ak}) \\ + \left(\dot{\delta}^2 + \frac{\dot{\Delta}^2}{4}\right)(\partial_{z_-z_-}\phi_{\rm k} + \partial_{z_+z_+}\phi_{\rm ak}) - \dot{\delta}\dot{\Delta}(\partial_{z_-z_-}\phi_{\rm k} - \partial_{z_+z_+}\phi_{\rm ak}) \\ - \left(3\phi_{\rm k}(\phi_{\rm ak} - \sqrt{\varepsilon})^2 + 3\phi_{\rm k}^2(\phi_{\rm ak} - \sqrt{\varepsilon}) - 3\sqrt{\varepsilon}\phi_{\rm ak}(\phi_{\rm ak} - \sqrt{\varepsilon})\right), \end{aligned} \tag{2.26}$$

where $z_\pm(t) = x - x_\pm(t)$.

Our goal to characterize the kink-antikink interaction is to find the dynamical equations for δ and Δ. Our strategy we will be to apply the Fredholm solvability condition introduced in Section 2.4. For that, we introduce the following inner product

$$\langle f|g\rangle = \int_{-\infty}^{+\infty} fg\,\mathrm{d}x,$$

thus $\mathcal{L}$ is a self-adjoint operator, i.e., $\mathcal{L}^\dagger = \mathcal{L}$, where $\mathcal{L}^\dagger$ is the adjoint operator. We require finding the elements of the Kernel of $\mathcal{L}^\dagger$. Nevertheless, given the fact that $\mathcal{L}^\dagger$ is not suitable to perform analytical calculations it is necessary to make some simplifications. Let us propose the followings *pseudo-eigenvectors*

$$\langle\tau| = \partial_{z_-}\phi_{\mathrm{k}} + \partial_{z_+}\phi_{\mathrm{ak}}, \tag{2.27}$$

$$\langle\chi| = \partial_{z_-}\phi_{\mathrm{k}} - \partial_{z_+}\phi_{\mathrm{ak}}, \tag{2.28}$$

meaning that both products $\langle\tau|\,\mathcal{L}^\dagger$ and $\langle\chi|\,\mathcal{L}^\dagger$ are exponentially close to zero [49]. To show this, notice that since the spatial derivative fulfills $\partial_{z_-}\phi_{\mathrm{k}}$

$$0 = \left[\varepsilon - 3\phi_{\mathrm{k}}^2 + \partial_{xx}\right]\partial_{z_-}\phi_{\mathrm{k}},$$

the terms that remain when we apply $\mathcal{L}^\dagger$ to $\partial_{z_-}\phi_{\mathrm{k}}$ are proportional to $\phi_{\mathrm{k}}(\phi_{\mathrm{ak}} - \sqrt{\varepsilon})\partial_{z_-}\phi_{\mathrm{k}}$, which in the limit of large distance of separation Δ is small. This comes from the fact that

$$\lim_{x\to x_1\gg x_0}\phi_{\mathrm{ak}}(x) - \sqrt{\varepsilon} = 2\sqrt{\varepsilon}\,\mathrm{e}^{-2\sqrt{\frac{\varepsilon}{2}}(x_1-x_0)}, \tag{2.29}$$

and because $\partial_{z_-}\phi_{\mathrm{k}}$ is a localized function around x_-. The same analysis can be applied to the product of $\mathcal{L}^\dagger$ with $\partial_{z_+}\phi_{\mathrm{ak}}$, obtaining the same result. Then, the products $\langle\tau|\,\mathcal{L}^\dagger$ and $\langle\chi|\,\mathcal{L}^\dagger$ are exponentially close to zero and we can consider τ and χ as pseudo-eigenvectors. In Fig. 2.17 we show the spatial profile of these functions. We will name τ and χ as the *translational* and *interaction* mode.

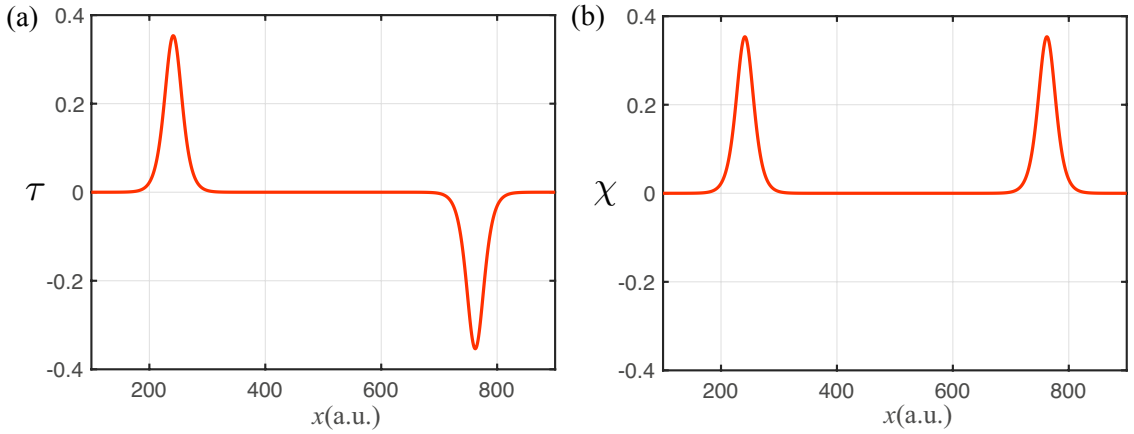

Figure 2.17: Profile of translation and interaction modes τ and χ defined in Eq. (2.27) and (2.28). We have used $\varepsilon = 0.5$.

Applying the Fredholm solvability condition we impose that

$$\langle\tau|b\rangle = 0, \quad \text{and} \quad \langle\chi|b\rangle = 0.$$

Translational mode

Integrating numerically the inner product $\langle\tau|b\rangle$ we see that the term proportional to the expression $\left(\ddot{\delta}+\mu\dot{\delta}\right)$ is the only relevant in b. In fact, setting $\varepsilon=1$, $x_-=-100$ and $x_+=100$, the inner product of τ with this term is more than 10^{10} larger than the others terms b. Thus, from Eq. (2.26) we can conclude that at dominant order

$$\ddot{\delta}+\mu\dot{\delta}=0,$$

which means that the central position of the localized structures is constant, keeping motionless. This behavior is expected since the system must keep its spatial symmetry because there is no external forcing.

Interaction mode

On the other hand, applying the same analysis to the inner product $\langle\chi|b\rangle$, we observe that the relevant terms are

$$\frac{1}{2}\left(\ddot{\Delta}+\mu\dot{\Delta}\right)\langle\chi|\chi\rangle+\left\langle\partial_{z_-}\phi_{\rm k}\middle|3\sqrt{\varepsilon}\phi_{\rm ak}(\phi_{\rm ak}-\sqrt{\varepsilon})\right\rangle-\left\langle\partial_{z_+}\phi_{\rm ak}\middle|3\sqrt{\varepsilon}\phi_{\rm k}(\phi_{\rm k}-\sqrt{\varepsilon})\right\rangle=0, \quad (2.30)$$

where we have used the fact that

$$\begin{aligned}&3\phi_{\rm k}(\phi_{\rm ak}-\sqrt{\varepsilon})^2+3\phi_{\rm k}^2(\phi_{\rm ak}-\sqrt{\varepsilon})-3\sqrt{\varepsilon}\phi_{\rm ak}(\phi_{\rm ak}-\sqrt{\varepsilon})=\\&3\phi_{\rm ak}(\phi_{\rm k}-\sqrt{\varepsilon})^2+3\phi_{\rm ak}^2(\phi_{\rm k}-\sqrt{\varepsilon})-3\sqrt{\varepsilon}\phi_{\rm k}(\phi_{\rm k}-\sqrt{\varepsilon}).\end{aligned}$$

The third inner product in Eq. (2.30) can be approximated analytically. For that, let us rewrite this integral using the variable $y=x-x_+$

$$\left\langle\partial_{z_+}\phi_{\rm ak}\middle|3\sqrt{\varepsilon}\phi_{\rm k}(\phi_{\rm k}-\sqrt{\varepsilon})\right\rangle=3\sqrt{\varepsilon}\int_{-\infty}^{+\infty}\partial_{z_+}\phi_{\rm ak}(y)\,\phi_{\rm k}(y+\Delta)\,(\phi_{\rm k}(y+\Delta)-\sqrt{\varepsilon})\mathrm{d}y.$$

The integrand of this expression is zero in the whole integration region, except where y is close to zero. Given the fact that we are considering Δ very large, we can use the approximation (2.29) to write

$$\begin{aligned}\left\langle\partial_{z_+}\phi_{\rm ak}\middle|3\sqrt{\varepsilon}\phi_{\rm k}(\phi_{\rm k}-\sqrt{\varepsilon})\right\rangle&\approx 3\sqrt{\varepsilon}\int_{-\infty}^{+\infty}\partial_{z_+}\phi_{\rm ak}(y)\,\sqrt{\varepsilon}\,(-2\sqrt{\varepsilon})\,\mathrm{e}^{-2\sqrt{\frac{\varepsilon}{2}}(y+\Delta)}\mathrm{d}y\\&=6\varepsilon\sqrt{\varepsilon}\,\mathrm{e}^{-2\sqrt{\frac{\varepsilon}{2}}\Delta}I_{\rm ak},\end{aligned}$$

where $I_{\rm ak}=-\int_{-\infty}^{+\infty}\partial_{z_+}\phi_{\rm ak}(y)\mathrm{e}^{-2\sqrt{\frac{\varepsilon}{2}}y}\mathrm{d}y$. The same analysis applied the second inner product in (2.30) yields to

$$\left\langle\partial_{z_-}\phi_{\rm k}\middle|3\sqrt{\varepsilon}\phi_{\rm ak}(\phi_{\rm ak}-\sqrt{\varepsilon})\right\rangle=-6\varepsilon\sqrt{\varepsilon}\,\mathrm{e}^{-2\sqrt{\frac{\varepsilon}{2}}\Delta}I_{\rm k},$$

with $I_{\rm k}=\int_{-\infty}^{+\infty}\partial_{z_-}\phi_{\rm k}(y)\mathrm{e}^{-2\sqrt{\frac{\varepsilon}{2}}y}\mathrm{d}y$. It is easy to see that $I_{\rm ak}=I_{\rm k}$ and that they are positive. These integrals will be labeled simply as I.

Finally, replacing in (2.30) we obtain the kink-antikink interaction law

$$\ddot{\Delta} + \mu\dot{\Delta} = -24\frac{I}{\langle\chi|\chi\rangle}\varepsilon\sqrt{\varepsilon}\,\mathrm{e}^{-2\sqrt{\frac{\varepsilon}{2}}\Delta},$$

which predicts that the kink-antikink interaction is attractive and lead to an eventual *annihilation*. Moreover, this equation predicts that there are not width equilibriums, that is, in this model there are not *localized stable structures*. Nevertheless, one of the topics that this thesis will cover is the effect of the parametric forcing in this model, where it will be demonstrated the existence of localized structures.

2.8 Localized structures in vegetation

Let us turn now to the study of particle-like solutions in a context of current relevance, the vegetation, particularly focused on localized structures in semi-arid or arid climates. It is important to note that due to the climatic change observed in the last decades, the arid and semi-arid zones of the planet are growing. In this section, we will introduce a model for the dynamics of vast classes of vegetation communities. As far as this thesis is concerned, we are interested in the interaction between localized structures that corresponds to vegetation surrounded by bare soil. We will discuss how these structures can lead to pattern formation in Chapter 4.

2.8.1 Mean-field model of vegetation evolution

When we talk of semi-arid or arid climates, we refer to climatic conditions with scarce water resources. In these climates is common to encounter different non-uniform structures in vegetation, generically called *vegetation patterns* [44, 72]. These structures are a consequence of how the hydric stress (insufficiency of water) can cause clustering effects to take advantage of water resources that benefit the vegetation domains, affecting the plants survivability and growth rate and leading to vegetation patches. It is understood that this hydric stress implicates a symmetry-breaking instability or Turing instability [62, 63, 65], predicting periodic configurations and the sequence of symmetry-breaking transitions that the patterns experiment, as the aridity is increased. A well-known example of this type are the *tiger bush*, which are banded periodic vegetation covers (see Fig. 2.18 a)), present in regions of Australia, West Africa, and North America. On the other hand, the same mechanism predicts the existence of aperiodic, randomly distributed patches of vegetation on bare soil [64, 73], or localized spots of bare soil, surrounded by uniform vegetation cover [90]. One example of this latter type are the *fairy circles*, discovered in Namib desert (see Fig. 2.18 b)).

The model that will be considered is a modified version of the integro-differential equation, interaction-redistribution model, introduced in 1997 by Lefever and Lejeune to explain the apparition of tiger bush [62]. In this model we define $b(\mathbf{r}, t) = m_p(\mathbf{r}, t)/m_{\max}$, where $m_p(\mathbf{r}, t)$ is the bio-mass contained per unit area in a given position $\mathbf{r}$ and time t and $m_{\max}$ the maximum

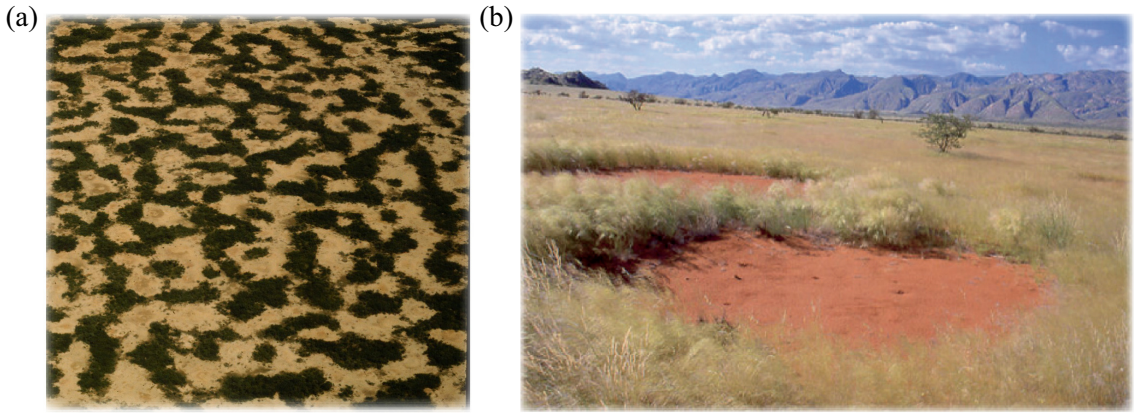

Figure 2.18: Examples of vegetation patterns in nature: a) tiger bush [1] and b) fairly circles [90].

amount that the species can produce. The spatiotemporal evolution of the normalized biomass $b(\mathbf{r},t)$ is modeled by the following non-local logistic equation

$$\partial_t b(\mathbf{r},t) = k_1 b(\mathbf{r},t) - k_2 b(\mathbf{r},t) + D\int [\Phi_{\text{in}}(|\mathbf{r}'|)b(\mathbf{r}+\mathbf{r}',t) - \Phi_{\text{out}}(|\mathbf{r}'|)b(\mathbf{r},t)]\mathrm{d}\mathbf{r}', \qquad (2.31)$$

where the first two terms account for the biomass gain and losses due to the natural growth and decay of plants. The integral in the third term is extended to the whole space and involves the ingoing and outgoing seed fluxes between neighbors, named as Φ_{in} and Φ_{out}, respectively. The factor D is a phenomenological constant. Moreover, k_1 and k_2 are factors that take into account the facilitation and competition mechanisms of the plant-to-plant feedbacks, respectively. They are modeled as

$$k_1 = [1 - b(\mathbf{r},t)]\mathscr{M}_{\text{f}}(\mathbf{r},t), \quad k_2 = \mu\mathscr{M}_{\text{c}}(\mathbf{r},t),$$

where μ is a phenomenological constant, accounting for the aridity. The terms $\mathscr{M}_{\text{f}}$ and $\mathscr{M}_{\text{c}}$ are mean-fields factors describing facilitation and competition mechanisms, expressed as

$$\mathscr{M}_{\text{f,c}}(\mathbf{r},t) = \exp\left(\chi_{\text{f,c}}\int \Phi_{\text{f,c}}(|\mathbf{r}'|)b(\mathbf{r}+\mathbf{r}',t)\right),$$

where χ_f and χ_c are positive parameters which fix the strength of the interactions. The kernels Φ_{f} and Φ_{c} describes the spatial extension of feedback effects, where in the case of facilitation processes are associated with the overground canopy, and in competition processes with the root sphere size.

The homogeneous and stationary states of Eq. (2.31) are given by

$$\mu = (1-b)\exp(\Lambda b),$$

where $\Lambda = \chi_{\text{f}} - \chi_{\text{c}}$ is named as *feedback balance*, and corresponds to the difference between the strengths of facilitative and competitive feedbacks. This parameter controls the stability of the homogeneous states. In fact, for $\Lambda > 1$ the system exhibits a saddle-node transition point.

Considering that the kernels and the seed fluxes are Gaussian fields and performing an expansion of the system dynamics in the neighborhood of the critical point $\Lambda = 1$ and small bio-mass b, the Eq. (2.31) can be put in the form of a partial differential equation [90]. Defining a new variable $b(\mathbf{r}, t) = \xi^{1/2} u(\mathbf{r}, t)$, where ξ is a *smallness parameter* which is part of the expansion, this equation reads (local interaction-redistribution model)

$$\partial_t u = -u[\eta - \kappa u + u^2] + [\Delta - \Gamma u]\nabla^2 u - \alpha u \nabla^4 u, \tag{2.32}$$

where η accounts for the aridity (like μ); κ is the facilitation-to-competition susceptibility ratio, which controls the stability of the homogeneous states (like Λ); Δ, Γ and α are linear and nonlinear diffusion coefficients. It can be proved that this equation can also be derived not only using Gaussian kernels and seed fluxes. It is required however that these functions do not diverge for $r \to \infty$ and to be radially symmetric. We will not demonstrate this here. Hence, close to super and subcritical transition the system is described by the Nagumo nonlinearity [22, 23] with linear and nonlinear diffusion.

This equation predicts the same solutions aforementioned (tiger bush and fairy circles) and more besides [90]. Moreover, since it is simpler than Eq. (2.31), it is more suitable to perform analytical calculations. For these reasons, we will restrict ourselves to use this equation for our analysis. In the next sections, we will introduce some solutions predicted by this model.

2.8.2 Periodic vegetation patterns

The homogeneous and stationary states of (2.32) are given by

$$u_0 = 0, \quad u_\pm = \left[\kappa \pm \sqrt{\kappa^2 - 4\eta}\right]/2, \tag{2.33}$$

where u_0 and u_+ are the only physically acceptable solutions, due that it is required $u \geq 0$. The solution u_- is positive for certain values of η and κ, but always unstable. Besides, the solution u_0 is stable for $\eta > 0$ and unstable for $\eta < 0$.

On the other hand, performing a linear stability analysis for u_+, it is possible to predict the formation of periodic configurations that invade the whole available territory. For such purpose, let us propose the following ansatz $u(\vec{x}, t) = u_+ + A e^{\sigma t + \vec{k}\cdot\vec{x}}$. Introducing it into Eq. (2.32), linearizing in A and after straightforward calculations, one gets the following relation between the growth rate σ and wavenumber modulus k

$$\sigma = u_+(\kappa - 2u_+) - (\Delta - \Gamma u_+)k^2 - \alpha u_+ k^4.$$

Since this is a quartic equation in k, there exists a wavenumber k_c for which the stability of the state u_+ become marginal, i.e., $\sigma(k_c) = 0$. The conditions to fulfill this are

$$\sigma(k = k_c) = 0, \quad \frac{\mathrm{d}\sigma}{\mathrm{d}k}(k = k_c) = 0, \quad \frac{\mathrm{d}^2\sigma}{\mathrm{d}k^2}(k = k_c) < 0,$$

which are nothing but to impose that the maximum of $\sigma(k)$ be equal to zero and to occur at k_c. Thus, the critical wavelength, corresponding to the distance between two maxima or

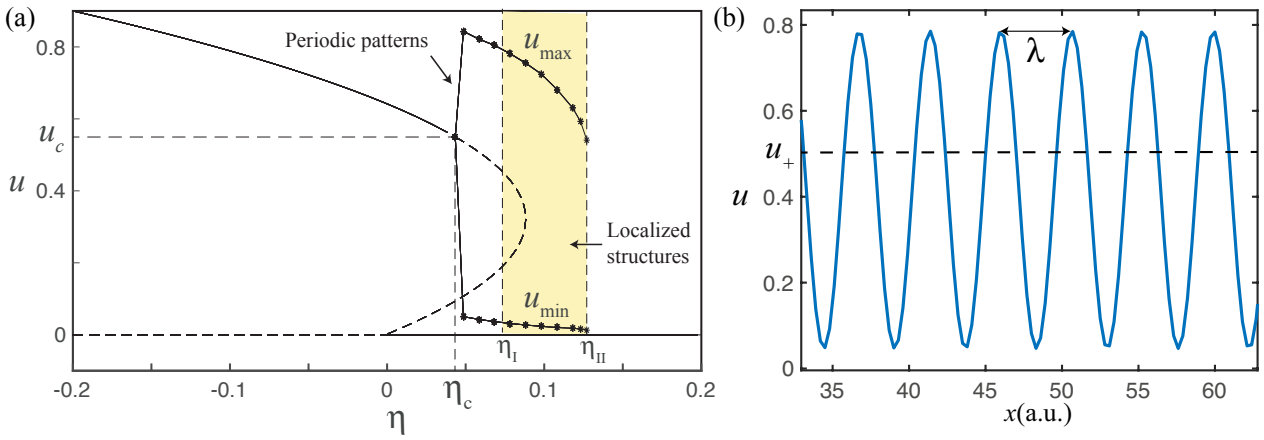

Figure 2.19: a) One dimensional stability diagram of steady states for parameters $\kappa = 0.6, \Delta = 0.02, \Gamma = 0.5, \alpha = 0.125$. The dotted lines represent unstable states. In η_c the periodic patterns emerge with wavelength λ, with maximum and minimum values $u_{\max}$ and $u_{\min}$, respectively. The yellow stripe stands for the region where the localized patches can be found. b) Periodic pattern with wavelength given by Eq. (2.34), using $\eta = 0.05$.

minima of the plant distribution, is given by

$$\lambda = 2\pi\sqrt{\frac{2\alpha}{\Gamma - \Delta/u_L}}, \tag{2.34}$$

where u_L is solution of the cubic equation

$$4\alpha u_L^2(2u_L - \kappa) = (\Gamma u_L - \Delta)^2,$$

and corresponds to the steady state threshold where stability changes. We discard imaginary solutions since they do not have physical meaning. In Fig. 2.19 (a) it is shown the corresponding stability diagram for $\kappa > 0$ for the one-dimensional case when there is only one critical threshold u_L (notice that through Eq. (2.33) we can calculate the aridity threshold η_L). Here the dotted lines represent unstable states. In η_c periodic states emerge with wavelength λ given by Eq. (2.34), which extend until η_{II}. This kind of instability that lead to pattern formation is usually referred as *Turing instability* [92], which was studied in Sec. 2.3.

2.8.3 Localized structures

Localized vegetation patterns are composed of spatially localized structures, in the sense that they are stable elemental structures with a well-defined size. In contrast with the periodic patterns, apparently, they do not have a tendency to spread and invade the whole territory, but rather to form isolated groups. As we have mentioned before, the interaction-redistribution vegetation model predicts the formation of localized patches (or localized structures) of vegetation surrounded by bare soil. In this section we will introduce them.

The interaction-redistribution model predicts that for $\kappa > 0$, it is possible to find stable localized patches (LPs) [13,64,73,90], in a certain range of positive η values beyond the saddle-

node point. This range is represented in the yellow stripe between η_{I} and η_{II} showed Fig. 2.19 a). In general, this region is different in one and two dimensions. The corresponding spatial profile of these radially symmetric LPs is illustrated in Fig. 2.20 for the two-dimensional case. In Fig. 2.20 d) we show an example from nature of LPs surrounded by desert soil, located in Western Australia. As it is shown, they seem to be randomly distributed and the size is not variable.

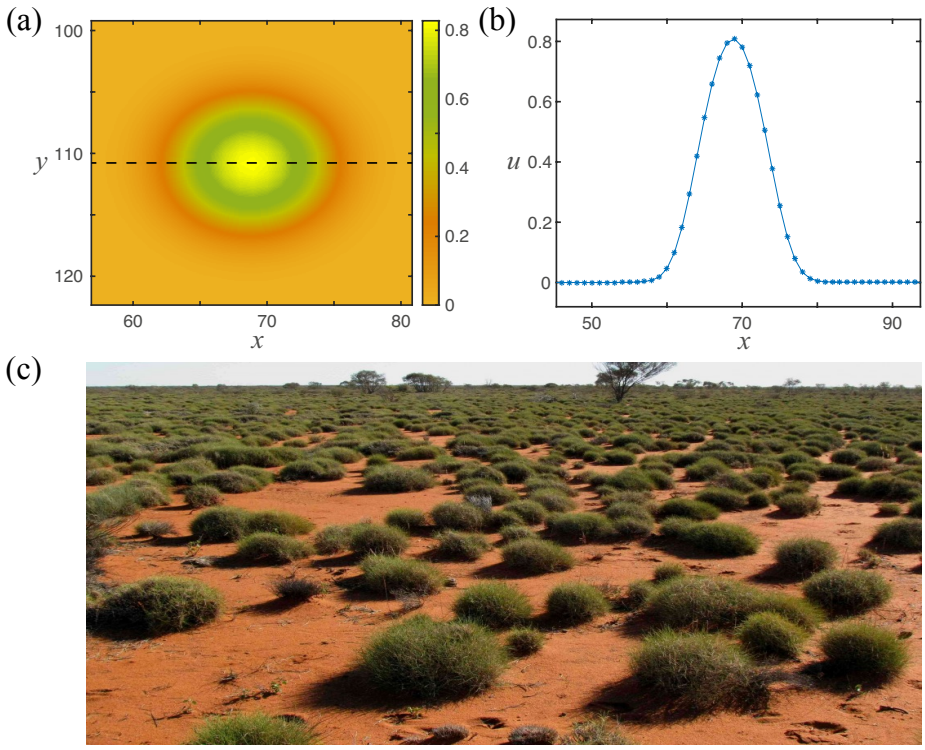

Figure 2.20: a) Localized structure profile in 2 dimensions, using $\kappa = 0.6, \Delta = 0.02, \Gamma = 0.5, \alpha = 0.125$ and $\eta = 0.05$. b) Spatial profile of a LP from the two dimensional Eq (2.32). The dashed line stands for the spatial profile shown in c). d) Spinifex grassland, Yakabindi station, Western Australia (courtesy of Vilis Nams, Dalhousie University, Canada) [2].

2.9 Diffraction theory

This and the next section serves as a brief theoretical background of the results discussed in Chapter 5, where we will study a diffraction grating, resulting of applying a laser beam to a nematic liquid crystal cell. This cell is characterized by exhibiting a zigzag wall lattice when a voltage is applied. We consider this lattice as the natural extension to two dimensions of the study of particle-like solutions.

In this section we will introduce the main aspects of *Fraunhofer diffraction patterns*, which will be crucial for later discussions.

2.9.1 Fraunhofer diffraction

When an emitting light point source is intersected by an obstacle, it will be deviate from its rectilinear propagation. Roughly speaking, the wave will bend around it and form dark fringe patterns. This can happen for example after a light passes through a very small aperture, like a narrow slit, as in *Young's experiment*. This phenomenon is named as *diffraction* [37].

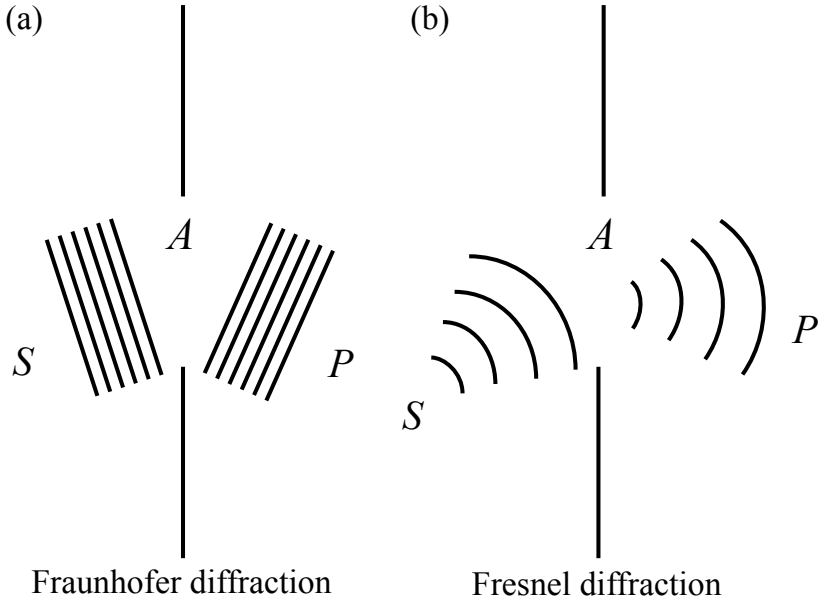

Figure 2.21: Wave diffracted by an aperture A. S and P are the source and receiving points, respectively. (a) Fraunhofer diffraction: Incident and diffracted waves are planes. (b) Fresnel diffraction: The waves curvature is significant.

The simplest way to analyze diffraction patterns is based on the *Huygens-Fresnel principle*, which states that every point of the wavefront acts as the source of a second spherical wave, of the same frequency, that spreads out in all directions [8,37,47]. The optical field at a point beyond an obstacle will be the superposition of all such wavelets reaching that point.

We distinguish between two general cases of diffraction, known as *Fraunhofer diffraction* and *Fresnel diffraction*. To illustrate their qualitative properties, let us consider the case when a light source intersects an aperture, as shown in Fig. 2.21.

The Fraunhofer diffraction occurs when the source and the receiving point, represented as S and P in Fig. 2.21(a), respectively, are far away from the aperture[6]. It is considered that if $w^2/(f\lambda) \ll 1$ the Fraunhofer diffraction occurs, where w is the aperture size, f the distance from the aperture to the plane of observation and λ the light wavelength. If this is true, the waves curvature can be neglected and the waves can be approximated as plane waves.

The mathematical expression for the pattern intensity profile comes from the *Fresnel-Kirchhoff formula*, which gives the diffraction pattern of a monochromatic spherical wave passing through an aperture. In the limit when S and P are at a large distance from the

[6]For this reason is also known as *far field diffraction*.

aperture, this formula can be approximated by [37, 78]

$$U_p(x,y) = \int\int t(x',y')\, \mathrm{e}^{-2\pi \mathrm{i}(ux'+vy')} \mathrm{d}x'\, \mathrm{d}y', \tag{2.35}$$

where

$$u = \frac{x}{\lambda f} \quad \text{and} \quad v = \frac{y}{\lambda f},$$

are called the *spatial frequencies*, λ is the light wavelength and f the distance between the aperture and the observation plane. The variables $\{x', y'\}$ integrate in the aperture plane, marked as A in Fig. 2.22. The variables $\{x, y\}$ are located in the plane of observation. The function $t(x', y')$ is called the *transmission coefficient* or *aperture function*, and tells how much light passes through the aperture. Thereby $t = 1$ is when there is no obstruction and light passes completely, while $t = 0$ is when there is an obstruction and no light passes. The *irradiance* or *intensity* of the diffraction pattern is defined as $I = |U_p|^2$.

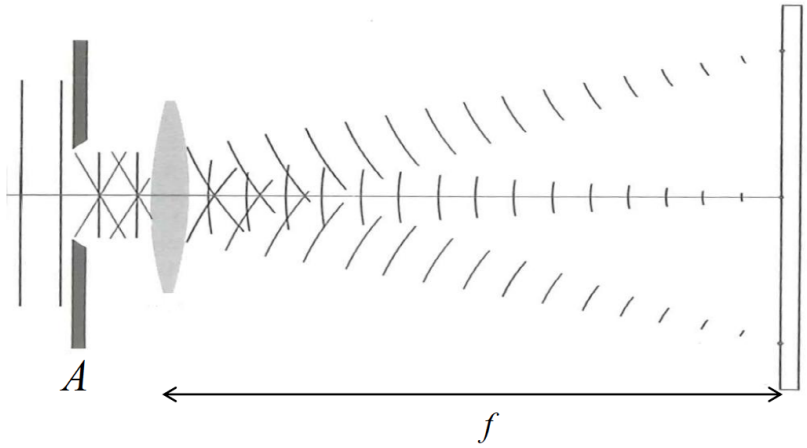

Figure 2.22: Schematic representation of a the Fraunhofer diffraction using positive lens. Here A is the aperture plane and f the focal distance.

To visualize the Fraunhofer diffraction patterns it is common to use positive lens to focalize the incident plane wave since this is equivalent to view the plane wave at infinity. Then f in those cases correspond to the *lens focal distance*. A schematic representation of this case is shown in Fig. 2.22. The peaks of the diffraction profile are called *diffraction orders*.

2.9.2 Multiple slits diffraction

Let us consider a simple case of Fraunhofer diffraction, composed by N slits of width b, separated by a distance h as showed in Fig. 2.23. In this case, we only restrict our calculations to one dimension. The transmission function is given by

$$t(x) = \begin{cases} 1 & nh < x < nh + b \quad \text{for} \quad 0 \leq n \leq N-1 \\ 0 & \text{otherwise,} \end{cases}$$

which replacing in Eq. (2.35) and after straightforward calculations, yields to

$$I = |U_p|^2 = I_0 \left(\frac{\sin\beta}{\beta}\right)^2 \left(\frac{\sin N\gamma}{N\sin\gamma}\right)^2, \tag{2.36}$$

with $\beta = \frac{1}{2}kb\sin\theta$ and $\gamma = \frac{1}{2}kh\sin\theta$, where k is the light wavenumber and θ is the angle defined in Fig. 2.23 (a). This diffraction grating is plotted in Fig. 2.23 (b).

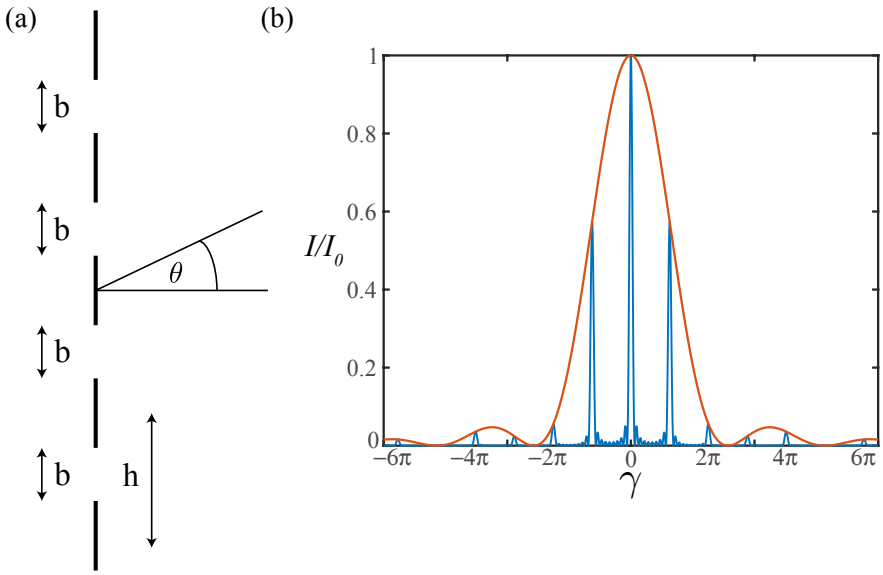

Figure 2.23: (a) Schematic representation of N slits of width b, separated by h. (b) Corresponding diffraction grating expressed in Eq. (2.36), with $h = 2.5$, $b = 1$ and $N = 10$. The red line corresponds to the factor $(\sin\beta/\beta)^2$.

2.10 Liquid crystals

Although there are four popular categories for the states of matter, namely, solid, liquid, gas and plasma, the borders or intersections between them are not always clear. There exists a huge number of intermediate states, that is to say, states that have properties of two or more of these states. A well known example are the *liquid crystals* [28], which exhibit properties from both solid and fluid state. They have properties of solid, but also of liquids, e.g., they may flow like a liquid, but their molecules exhibit orientational order [19]. They were first described systematically by the Austrian botanical physiologist Friedrich Reinitzer in 1888 when he prepared cholesteryl benzoate. He found an anomalous opalescence behavior.

Liquid crystals are composed of molecules which tend to be elongated. They can be divided into different phases, like *thermotropic, lyotropic, met allotropic, polymeric and coloidal* [19, 51]. We are particularly interested in thermotropic liquid crystals, which present different phases depending on the temperature. We distinguish three principal cases: *nematic, smectic* and *cholesteric*, classified by Georges Friedel in 1922 [39], represented schematically in Fig. 2.24.

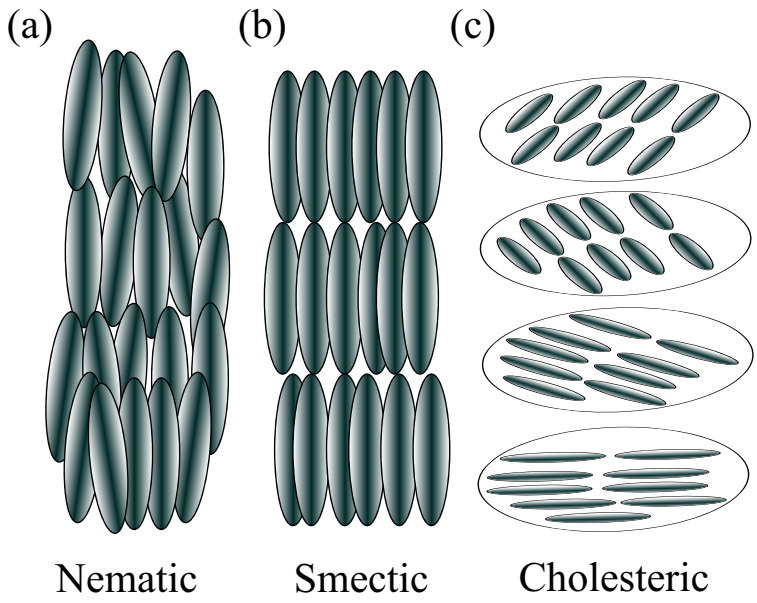

Figure 2.24: Different liquid crystal phases: nematic, smectic and cholesteric.

The nematic liquid crystals are by far the most important phase for applications. In this phase, all the molecules are aligned approximately parallel to each other at long distances (orientational order). In the cholesteric phase, the molecules have an additional property, chirality, implying that the molecules have a twisting, forming a macroscopic helical structure. In the smectic phase, the molecules have orientational and positional order, having them ordered in layers [19].

The liquid crystals have also the property to exhibit complex behaviors in presence of electromagnetic fields, where can exhibit phenomena such as pattern formation, spatiotemporal chaos, turbulences, etc. Moreover, their optical properties have been used for technological applications such as the widely known Liquid Crystal Displays (LCD) [99].

2.10.1 Zigzag instability

As far as this thesis is concerned, we are interested in studying nematic liquid crystals filled in a *in-plane switching (IPS) cell*, as the one illustrated in Fig. 2.25 (a). As it is shown, this cell consists of two glass plates, separated by a few micrometers, where the liquid crystal is injected by capillarity. The molecules have *planar anchoring*, meaning that they are fixed at the borders and parallel to the glass plates. In contact with each surface of glass there are located a patterned thin films made of *indium tin oxide* (ITO), which is a transparent conductor (green in the figure). In addition, these films are connected to a generator, which generates an electric field that will change the orientation of the molecules.

It has been reported [6] that in a certain region of parameters, the liquid crystal molecules exhibit a zigzag instability in this IPS cell, as shown in Fig. 2.25 (b). In Chapter 5 we will discuss the diffraction grating, formed because of applying a laser beam to this zigzag configuration.

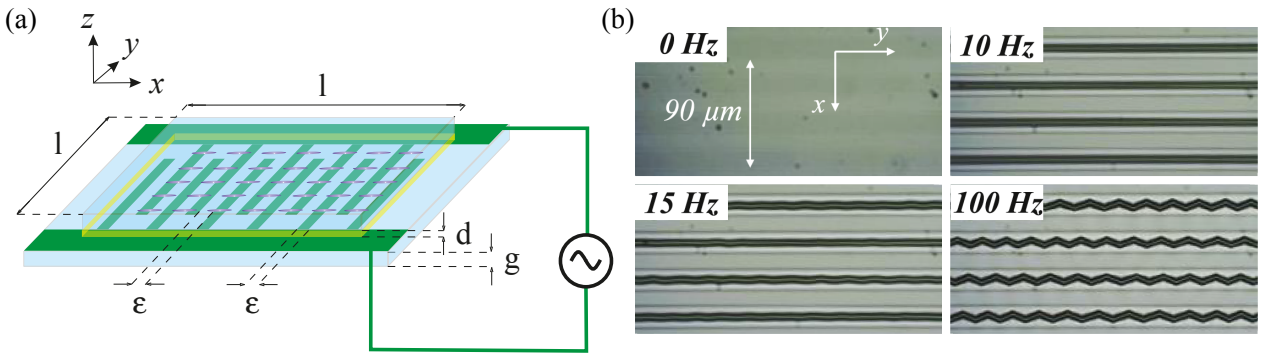

Figure 2.25: (a) Schematic representation of the liquid crystal IPS cell, connected to a generator. (b) Zig-zag instability exhibited by a nematic liquid crystal filled in this cell.

2.11 Numerical methods for integrating partial differential equations

It is common to encounter problems from different disciplines, like physics, economics, engineering, biology, etc., where is necessary the use of numerical methods to find a solution, that allows to figure out the phenomenon under study. This is due to the nonintegrability of these problems when they are put into mathematical form. The choice of a numerical method depends, among other things, on its error (how precise they are) and the time it takes to integrate. In some way, a numerical method is similar to perform an experiment, since it is used to corroborate theoretical predictions and to discover new behaviors, in some cases unexpected.

Some of the methods developed to integrate differential equations are the *Runge-Kutta* methods, the *Richardson extrapolation* method and the *predictor-corrector* method [35]. As far as this thesis is concerned, we will use the *fourth-order Runge-Kutta* (RK4) method to integrate every equation, which though is usually used to solve ordinary differential equations can be used to solve partial differential equations [76]. We will approximate the spatial partial derivatives using the *finite differences method* [86].

In general, the Runge-Kutta method propagates a solution over an interval by combining the information from several Euler-method steps [35]. Then, it is performed a Taylor expansion to some order to match with the information obtained. The advantage of this method is that, since it calculates step by step and does not need previous information, the discretization step can be adjusted as the integration advances.

2.11.1 Fourth-order Runge-Kutta method

Let us consider the following first-order differential equation

$$\frac{\mathrm{d}\mathbf{u}}{\mathrm{d}t} = \mathbf{f}(\mathbf{u}, t),$$

where $\mathbf{u}$ and $\mathbf{f}$ are N-dimensional vectors[7]. The function $\mathbf{f}$ is known. Let the time be discrete, with a discretization step $\mathrm{d}t \equiv t_{n+1} - t_n$. Then, $\mathbf{u}(t_n) \equiv \mathbf{u}_n$, is the discrete solution. The RK4 method advances to the next step $\mathbf{u}_{n+1}$ in the following way

$$\mathbf{u}_{n+1} = \mathbf{u}_n + \frac{1}{6}\left(\mathbf{k}_1 + 2\mathbf{k}_2 + 2\mathbf{k}_3 + \mathbf{k}_4\right) + \mathcal{O}(\mathrm{d}t^5),$$

where

$$\begin{aligned}
\mathbf{k}_1 &= \mathrm{d}t\, \mathbf{f}(\mathbf{u}_n, t_n), \\
\mathbf{k}_2 &= \mathrm{d}t\, \mathbf{f}(\mathbf{u}_n + \mathbf{k}_1/2, t_n + \mathrm{d}t/2), \\
\mathbf{k}_3 &= \mathrm{d}t\, \mathbf{f}(\mathbf{u}_n + \mathbf{k}_2/2, t_n + \mathrm{d}t/2), \\
\mathbf{k}_4 &= \mathrm{d}t\, \mathbf{f}(\mathbf{u}_n + \mathbf{k}_3, t_n + \mathrm{d}t).
\end{aligned}$$

One disadvantage of this method is that it calls the function $\mathbf{f}$ four times, which makes it slower than other methods. However, since the error is of order $\mathrm{d}t^5$, this is a precise and stable method.

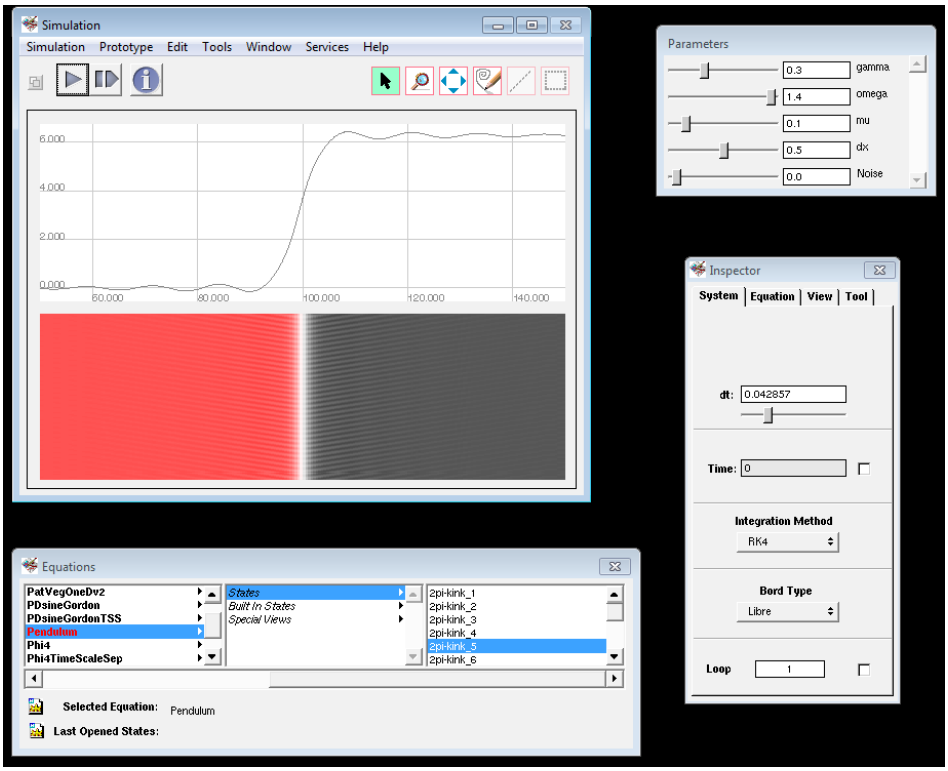

Figure 2.26: Screenshot of the software *DimX*, showing a real time simulation of the parametrically driven and damped sine-Gordon equation.

2.11.2 Interactive simulations

This thesis has been complemented by interactive simulations, by using the software *DimX* developed by Pierre Coullet and collaborators, at the laboratory *Institut Non Linéaire de*

[7]This is the same scenario introduced in Eq. (2.1)

Nice. This software has allowed us to appreciate in real time simulation the temporal evolution of the equations under study, with the possibility to change its parameters as the integration progresses. Fig. 2.26 shows a screenshot of this software.

Chapter 3

Flaming kinks

In this chapter we will discuss and provide further analysis of the results presented in articles included in Appendix A and Appendix B. In these works we reported and studied a new type of kinks termed as *flaming kinks*, which are solutions of the sine-Gordon and ϕ^4 equation under dissipation and parametric forcing. What characterizes them is the emission of evanescent (or damped) waves that start from the kink center position and travel in counterparts directions. Moreover, the interaction between a flaming kink and a *flaming antikink* allows the formation of stable localized structures.

In the manuscript from Appendix A we explored the main properties of flaming kinks, applied to a chain of coupled pendulums and a magnetic wire. We also studied the formation of localized structures, characterising their phase space width numerically. Furthermore, in the manuscript from Appendix B we characterized analytically the flaming kink-antikink interaction, showing good agreement with numerical findings. Throughout next sections, we will also cover aspects that were not treated in these articles.

3.1 Flaming kinks in the parametrically driven and damped sine-Gordon equation

In this section we will briefly review and discuss some properties of *flaming kinks* introduced in Appendix A, in the context of the parametrically driven and damped sine-Gordon equation.

3.1.1 Main properties

In Sec. 2.7.1 we studied kink solutions from the sine-Gordon equation, in the context of a chain of coupled pendulums. On the other hand, in Sec. 2.6.2 we studied the main properties of parametric forcing in the context of a simple damped and driven pendulum with a vertical oscillatory point. Let us now then introduce the sine-Gordon equation in presence of dissipation and the same kind of parametric forcing, that is, the chain of pendulums support

now is forced to oscillate vertically. The equation that describes the vertical deviation angle $\theta(x,t)$ now is

$$\partial_{tt}\theta = -(\omega_0^2 + \gamma \sin\omega t)\sin\theta + \kappa^2\partial_{xx}\theta - \mu\partial_t\theta, \tag{3.1}$$

with each parameter having the same physical meaning as in the aforementioned sections. Notice now that unlike the sine-Gordon equation, this equation is not Lorentz invariant and does not have analytical solutions. However, notice that since the sine-Gordon equation appears in many physical fields, this equation gives a good description of the effect of parametric forcing on these systems. One example is the case of a magnetic wire under oscillatory external electromagnetic fields in a particular limit.

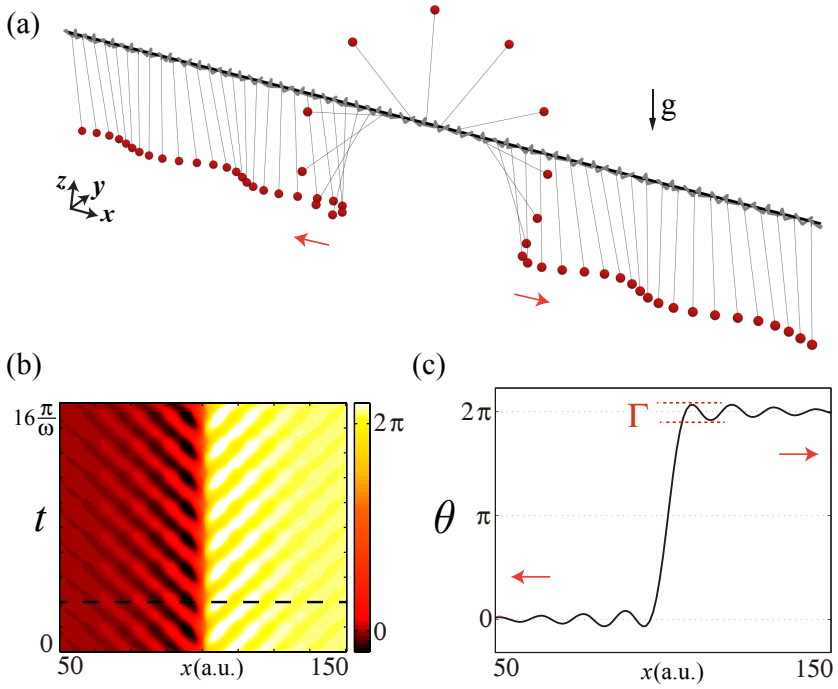

Figure 3.1: Flaming kinks obtained from numerical integration of Eq. (3.1) with $\omega_0 = 1.0, \gamma = 0.3, \omega = 1.4, \mu = 0.1, \kappa = 1.0, \mathrm{d}x = 0.5$ and $\mathrm{d}t = 0.1$. (a) Schematic representation of a flaming kink. (b) Spatiotemporal evolution. (c) Spatial profile of the solution at a certain instant marked with a dashed line in (b).

If we integrate numerically this equation, giving as an initial condition the kink solution from the sine-Gordon equation (see Sec. 2.7.1), we will observe two main changes:

1. The kink speed decreases over time until the kink reaches a fixed position. This is a consequence of the presence of dissipation.
2. Evanescent waves appear from the center position, traveling in opposite directions towards $x = \pm\infty$, along the $\theta = 0$ and $\theta = 2\pi$ state. This phenomenon is due to the parametric forcing.

We consider that the waves propagation resembles the emission of flames, or, more specifically, resembles a *hopping pattern* behavior observed in combustion under controlled conditions [11, 50]. For this reason, these kinks have termed as *flaming kinks*. Their profile is showed in Fig. 3.1. Moreover, as in the conservative case, this system admits *flaming antikinks*, where the pendulums rotate from $\theta = 2\pi$ to $\theta = 0$ as x increases.

3.1.2 Resonant properties

As we discussed in Sec. 2.6.2, one of the properties of parametric forcing is that the amplitude reaches its maximum value at different frequencies, not only at the natural frequency. However, although the system considered here contains a parametric forcing, the flaming kinks present *resonant* properties, that is, the amplitude of the waves reaches its maximum value when ω approaches ω_0. In Fig. 3.2 we illustrate this behavior. The tendency showed when the dissipation is changed is similar to the one showed in Fig. 2.5, when we studied the driven and damped harmonic oscillator. Besides, it has been demonstrated that the flaming kinks evolve periodically in time, with period $2\pi/\omega$, which is also a resonant property.

The region of parameters where flaming kinks can be found in the Ince-Strutt diagram (see Sec. 2.6.2) is showed in Fig. 3.2 (c). Notice that in this region the flaming kinks waves have a bigger amplitude. For higher or lower frequencies than ω_0, this amplitude is remarkably smaller.

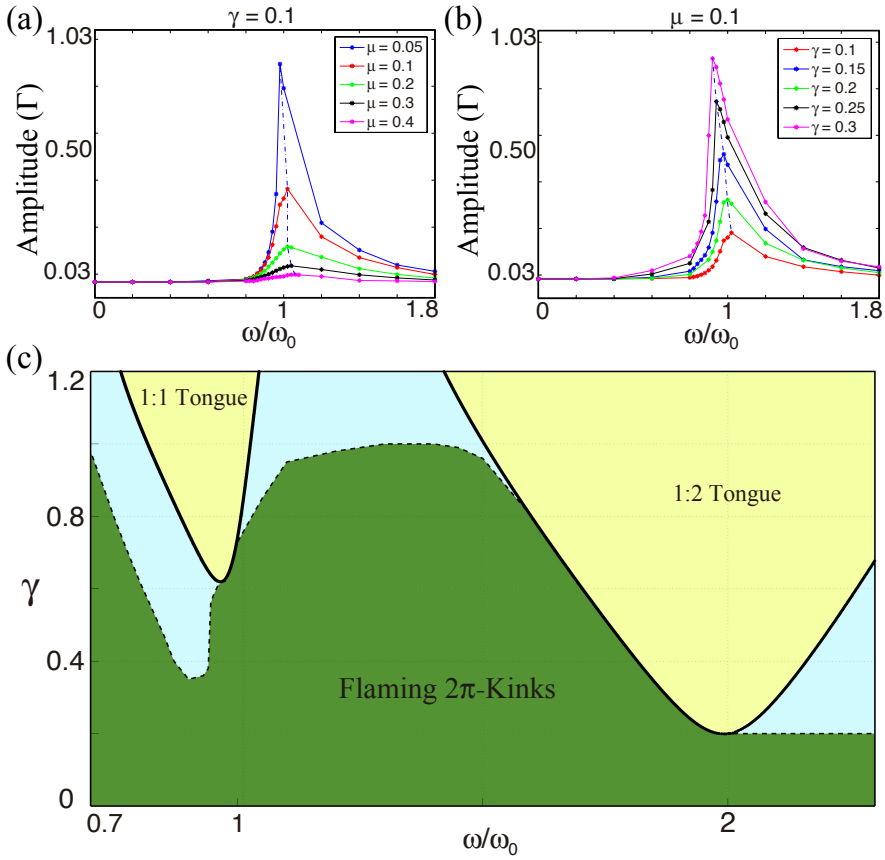

Figure 3.2: Waves amplitude in function of the forcing frequency ω for: (a) constant $\gamma = 0.1$ and different values of the damping coefficient μ. (b) constant $\mu = 0.1$ and different values of the forcing amplitude γ. (c) Phase space as a function of frequency and amplitude of the forcing with $\mu = 0.1$. The green zone accounts for the region where flaming kinks are observed.

One way to understand this resonant property is studying the dynamics of a small perturbation around de kink solution of the conservative sine-Gordon equation. Thus, we propose

$\theta(x,t) = \theta_k(x,t) + \varphi(x,t)$, where θ_k is the kink solution and φ a small perturbation. Then, replacing it in Eq. (3.1), linearizing in φ. After straigthforward calculations we obtain

$$\partial_{tt}\varphi = -\omega_0^2\varphi\cos\theta_k - \gamma\varphi\cos\theta_k\sin\omega t - \gamma\sin\theta_k\sin\omega t + \partial_{xx}\varphi - \mu(\partial_t\theta_k + \partial_t\varphi),$$

where the first two terms of the right-hand side tell us that φ reaches its maximum value at the natural frequency ω_0. The variable φ is nothing but the amplitude of the waves of a flaming kink.

3.1.3 Localized structures

In Section IV of the manuscript included in Appendix A we discussed that the interaction between a flaming kink and a flaming antikink allows the formation of stable localized structures. Their profile is showed in Fig. 3.3. As it is shown in the spatiotemporal diagram, the superposition of evanescent waves creates stationary waves between the kinks. Besides, the distance of separation Δ is stable and oscillates in time.

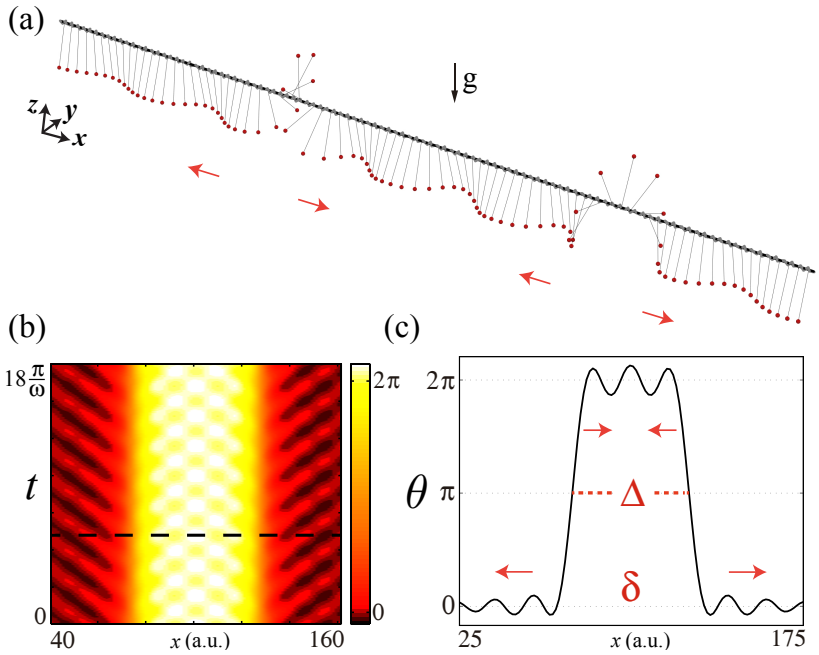

Figure 3.3: Localized structures formed due to the flaming kink-antikink interaction. (a) Schematic representation of the solution. (b) Spatiotemporal evolution. (c) Spatial profile of the solution at a certain instant marked with a dashed line in (b). The parameters δ and Δ account for the width and position of the localized structure, respectively.

Temporal width evolution

The width Δ determines an integer number of stationary waves between a flaming kink and a flaming antikink. If we perturb a localized structure increasing the width with a large

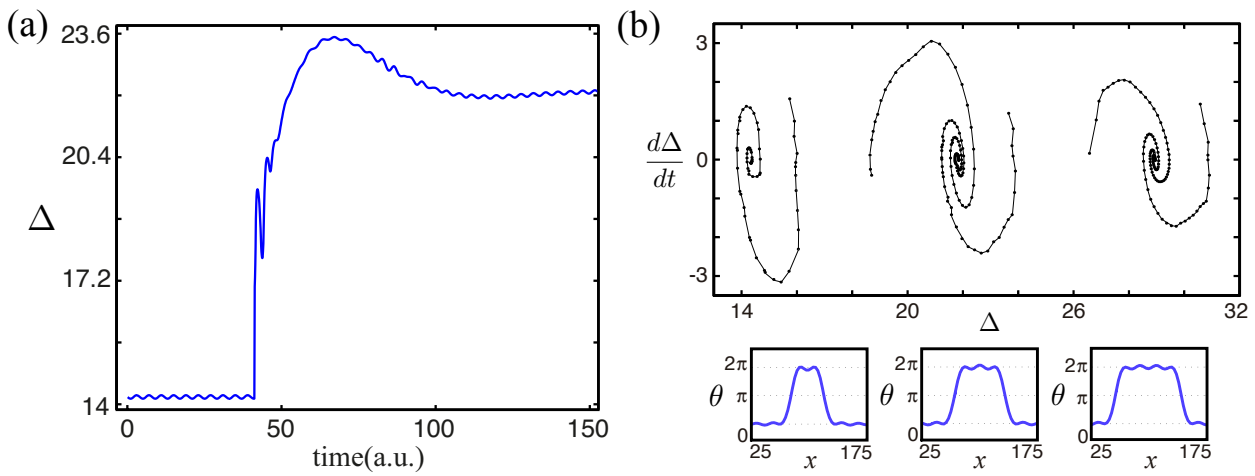

Figure 3.4: (a) Temporal width evolution under a perturbation. Notice that it reaches a new equilibrium. (b) Phase space $\{\dot{\Delta}, \Delta\}$ of the localized structures, obtained monitoring periodically the width evolution. The lower panels show the respective profiles of equilibrium widths.

enough perturbation, the width can reach a new equilibrium. This behavior is shown in Fig. 3.4 (a). Notice from this figure that the width oscillates in time.

Since the flaming kinks are periodic in time, if we monitor the width over one period $2\pi/\omega$, we will see a frozen localized structure, that is, with no oscillation in Δ (stroboscopic monitoring). Using this strategy we have constructed the phase space diagram showed in Fig. 3.4 (b).

Interaction law

The dynamical equation that Δ follows was proposed in Appendix A article as a phenomenological model. This one reads

$$\ddot{\Delta} + \mu\dot{\Delta} = -a\Gamma e^{-\lambda\Delta} \sin\left(\frac{2\pi\Delta}{\sigma} + \varphi_0\right), \tag{3.2}$$

where $a, \Gamma, \lambda, \sigma$ and φ_0 can be computed numerically. This equation predicts the existence of widths equilibriums, as the ones showed in Fig. 3.4 (b). In the manuscript from Appendix B we derived this equation from a perturbative analysis, considering the flaming kinks from the ϕ^4 scalar field equation under parametric forcing and dissipation.

3.2 Flaming kinks in a ferromagnetic wire

In Section II of the manuscript presented in Appendix A, we introduced a ferromagnetic wire under oscillatory external electromagnetic fields and showed that this system admits flaming

kink solutions. We also illustrated how in certain limit the dynamics of this system can be described by the sine-Gordon. In this section, we will make in detail this derivation.

As we discussed in the manuscript, the ferromagnetic wire is described by the normalized magnetization $\mathbf{m}(z,t)$, where z and t correspond to the spatial coordinate along the wire and time (see Fig. 3.5). The dynamics of $\mathbf{m}(z,t)$ is described by the Landau-Lifshitz-Gilbert equation [69], which in Cartesian coordinates reads

$$\partial_t \mathbf{m} = -\mathbf{m} \times (h\hat{x} - \beta m_z \hat{z} + \partial_{zz}\mathbf{m} - \alpha \partial_t \mathbf{m}), \tag{3.3}$$

where $\{\hat{x}, \hat{y}, \hat{z}\}$ are the Cartesian unit vectors, h is the electromagnetic external field intensity applied in the x direction, $\beta > 0$ accounts for the anisotropy of the wire, favouring configurations where the magnetization lies in the xy plane, the term $\partial_{zz}\mathbf{m}$ corresponds to the Laplacian operator accounting for short-range magnetic interactions, and the term proportional to α is a Rayleigh-like dissipation function known as Gilbert damping, and it accounts for energy losses [69]. The dynamics of this equation is characterized by preserving the norm of magnetization.

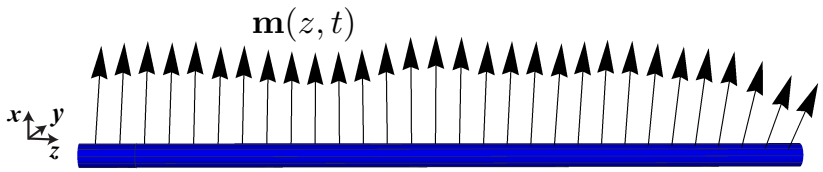

Figure 3.5: Schematic representation of the magnetization vector.

Let us consider a spherical representation of $\mathbf{m}(z,t)$,

$$\mathbf{m} = \sin\theta[\cos\phi\,\hat{x} + \sin\phi\,\hat{y}] + \cos\theta\hat{z},$$

where $\theta(z,t)$ and $\phi(z,t)$ are the polar and azimuthal angle, respectively. Introducing this expression into Eq. (3.3), we can derive the following relations

$$\begin{aligned}\partial_t\theta = &-h\sin\phi + \alpha h\cos\phi\cos\theta + \frac{\alpha\beta}{2}\sin 2\theta + 2\cos\theta\,\vec{\nabla}\phi\cdot\vec{\nabla}\theta \\ &+ \sin\theta\vec{\nabla}^2\phi + \alpha\vec{\nabla}^2\theta - \frac{\alpha}{2}\sin 2\theta\,(\vec{\nabla}\phi)^2\end{aligned} \tag{3.4}$$

and

$$\begin{aligned}\sin\theta\,\partial_t\phi = &-\alpha h\sin\phi - h\cos\phi\cos\theta - \frac{\beta}{2}\sin 2\theta + 2\alpha\cos\theta\,\vec{\nabla}\phi\cdot\vec{\nabla}\theta \\ &+ \alpha\sin\theta\vec{\nabla}^2\phi - \vec{\nabla}^2\theta + \frac{1}{2}\sin 2\theta(\vec{\nabla}\phi)^2.\end{aligned} \tag{3.5}$$

Considering the following scaling expansions

$$\theta = \frac{\pi}{2} + \varepsilon\delta\theta_0, \quad h = \varepsilon h_0, \quad \partial_{zz} = \varepsilon\partial_{\tilde{z}\tilde{z}}, \quad \alpha = \varepsilon\alpha_0 \quad \text{and} \quad \beta = \frac{\beta_0}{\varepsilon}, \tag{3.6}$$

where ε is a small parameter, we notice that Eq. (4.8) yields to

$$\sin\theta\,\partial_t\phi = \beta_0\sin\theta\delta\theta_0 + \mathcal{O}(\varepsilon^2),$$

which combining with the first and last relations in Eq. (3.6), gives us at leading order

$$\theta = \frac{\pi}{2} + \frac{\partial_t \phi}{\beta},$$

i.e., the polar angle becomes a slave variable of ϕ in this limit. Therefore, introducing it into Eq. (3.4) and using the aforementioned relations, we can obtain a dynamical equation for ϕ

$$\frac{\varepsilon \partial_{tt}\phi}{\beta_0} = -\varepsilon h_0 \sin\phi - \varepsilon \alpha_0 \beta_0 \delta\theta_0 + \varepsilon \partial_{\tilde{z}\tilde{z}}\phi + \mathcal{O}(\varepsilon^2),$$

$$\Rightarrow \partial_{tt}\phi = -h_0\beta_0 \sin\phi - \alpha_0\beta_0\partial_t\phi + \beta_0\partial_{\tilde{z}\tilde{z}}\phi + \mathcal{O}(\varepsilon^2),$$

which at leading order can be written as the dissipative sine-Gordon equation [74]

$$\partial_{tt}\phi = -\omega_0^2 \sin\phi - \mu\partial_t\phi + \kappa^2\partial_{\tilde{z}\tilde{z}}\phi, \tag{3.7}$$

if we set $\omega_0 = \sqrt{h_0\beta_0}$, $\mu = \alpha_0\beta_0$ and $\kappa = \sqrt{\beta_0}$.

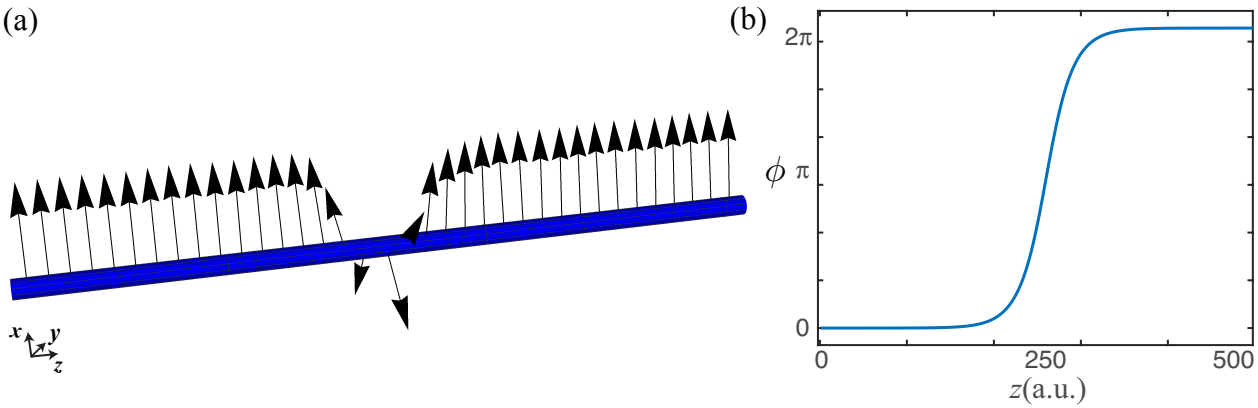

Figure 3.6: Schematic representation of a kink solution in the ferromagnetic wire, obtained by integrating numerically Eq. (3.3), using $h = 0.8$, $\beta = 10$ and $\alpha = 0.02$.

This means that in the limit when the anisotropy β is large compared to the other parameters, that is, when the magnetization is mostly restricted to the xy plane ($\theta \approx \pi/2$), the azimuthal angle ϕ satisfies, at leading order, the sine-Gordon equation in presence of dissipation. Then, it is expected that this system admits kink solutions, as the one showed in Fig. 3.6.

If the electromagnetic external field h_0 varies over time like $h_0 = H_0/\beta_0 + \gamma/\beta_0 \sin\omega t$, namely, if it is composed by a constant component H_0 and a oscillatory part, the Eq. (3.7) will contain a parametric forcing like the one discussed in the previous section, i.e., the dynamics of the azimuthal angle ϕ will be described by the parametrically driven and damped sine-Gordon equation. Therefore, as we showed in Section II of the Appendix A article, this system admits flaming kinks.

3.3 Flaming kinks in the parametrically driven and damped ϕ^4 equation

In Sec. 2.7.2 we introduced the analytical kink solution of the conservative ϕ^4 scalar field equation. Let us now add parametric forcing and dissipation to this system, following the same idea of how were introduced into the sine-Gordon equation. Thus, the ϕ^4 equation under these conditions reads

$$\partial_{tt}\phi = (\varepsilon\phi - \phi^3)(1 - \gamma \sin \omega t) + \partial_{xx}\phi - \mu\partial_t\phi,$$

where γ and ω are the effective forcing amplitude and frequency, respectively, as before.

In this equation we can also observe flaming kinks, showing that this phenomenon is robust, that is, it can be observed in different physical contexts. Their properties are essentially the same as in the sine-Gordon equation, namely, they evolve periodically in time and exhibit resonant properties. Notice however that unlike the sine-Gordon equation, the resonance occurs when[1] $\omega \approx \sqrt{2\varepsilon}$.

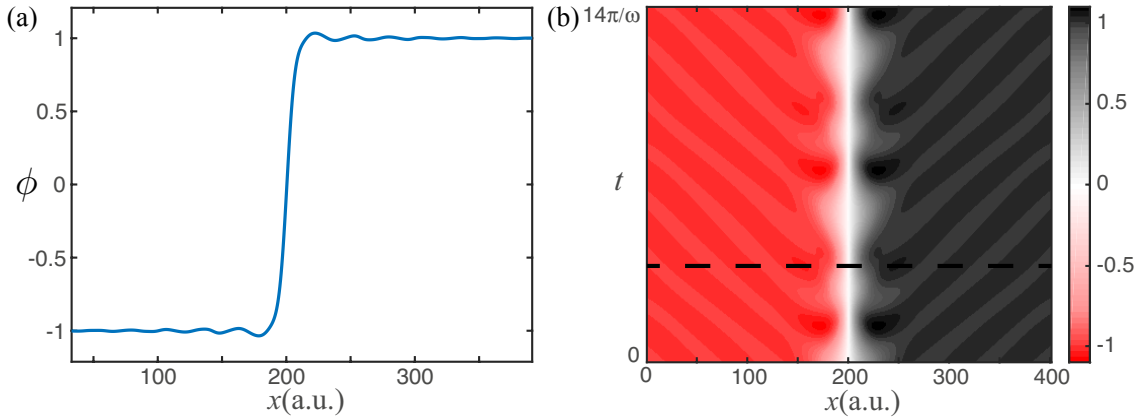

Figure 3.7: Flaming kinks in the parametrically and damped ϕ^4 scalar field equation. In (a) we show the spatial profile at one instant, marked with a dashed line in the spatiotemporal diagram in (b). We have used $\varepsilon = 1$, $\gamma = 0.5$, $\omega = 1$ and $\mu = 0.1$.

3.3.1 Flaming kink-antikink interaction

As we studied in Sec. 2.7.3, the ϕ^4 scalar field equation in presence of dissipation, does not admit localized structures. The kink-antikink interaction turns out to be attractive and leads to an eventual annihilation. However, as we have shown in the parametrically driven and damped sine-Gordon equation, the interaction between a flaming kink and a flaming antikink allows the formation of a family of localized structures. Then, since the parametrically driven and damped ϕ^4 equation admits flaming kinks, it is expected that this system contains localized structures.

[1] This condition can be obtained by performing a linear expansion around the equilibria $\pm\sqrt{\varepsilon}$.

As it is detailed in Section 2 in the manuscript from Appendix B, using a strategy of time-scale separation, similar to the one proposed by Kapitza to study the stability of the upside-down pendulum (see Sec. 2.6.3), we can derive an effective equation independent of time, which admits *frozen* flaming kinks solutions. In other words, this equation describes the dynamics of an average variable $u(x,t)$, representing kinks with stationary oscillatory profiles. This equation is indeed

$$\partial_{tt}u = \left(1 - \frac{\gamma^2}{2\omega^2}(\varepsilon - 3u^2)\left(1 - \frac{1}{\omega^2}\partial_{xx} + \frac{1}{\omega^4}\partial_{xxxx}\right)\right)(\varepsilon u - u^3) - \mu\partial_t u + \partial_{xx}u.$$

Notice that it contains spatial derivatives of fourth order, which ensure the presence of evanescent waves.

The procedure to derive the dynamical equation for Δ is essentially the same as in the dissipative ϕ^4 equation (see Sec. 2.7.3), but with the difference that the kinks now have oscillatory tails. Because of this is that we propose the following asymptotic behavior

$$\lim_{x\to x_1 \gg x_0} u_{\mathrm{k}}(x) - \sqrt{\varepsilon} = -2\sqrt{\varepsilon}\,\mathrm{e}^{-2\sqrt{\frac{\varepsilon}{2}}(x_1 - x_0)}\cos\left(\kappa(x_1 - x_0) + \delta_0\right),$$

with κ and δ_0 constants, to take into account this property. Since this is the main change made when we add parametric forcing, it is fair to say that what allows the possibility of creating localized structures is the interaction of the evanescent waves from the flaming kinks. The detailed derivation of the dynamical equation of Δ (see Eq. (3.2)) can be found in Section 3.2 of Appendix B.

3.4 Perturbative analysis using Inverse Scattering Transform method

3.4.1 General framework of the IST method

The Inverse Scattering Transform (IST) method is a useful technique to obtain analytical solutions of integrable systems under small perturbations [3,4,52]. Some well-known examples where this method is used are the Korteweg-de Vries equation, the nonlinear Schrödinger equation, the sine-Gordon equation and the Toda lattice equation.

To apply this method it is necessary to represent a nonlinear equation for the function $u(x,t)$ in the form of the *Lax's representation* [60],

$$\frac{\mathrm{d}\mathcal{L}}{\mathrm{d}t} + [\mathcal{L}, \mathcal{A}] = 0,$$

where the operators $\mathcal{L}$ and $\mathcal{A}$ are the so-called *Lax pair*, which depend on $u(x,t)$ and its derivatives, and $[\mathcal{L}, \mathcal{A}] = \mathcal{L}\mathcal{A} - \mathcal{A}\mathcal{L}$ is the commutator. These operators satisfy

$$\mathcal{L}\Psi = \lambda\Psi \quad \text{and} \quad \frac{\mathrm{d}\Psi}{\mathrm{d}t} = \mathcal{A}\Psi,$$

where Ψ is an unknown function usually referred as the *Jost function*. The basic idea of IST is to find the time evolution of the eigenvalues λ and eigenfunctions Ψ of this problem, or in other words, to find *scattering data*. The problem is solved by performing the *inverse scattering* procedure by solving the *Gelfand-Levitan-Marchenko integral equation* [67].

3.4.2 IST method applied to the sine-Gordon equation

This section is not intended to provide a detailed derivation of the equations obtained by the IST method. We will restrict ourselves to apply it to the sine-Gordon equation, considering as perturbation the dissipation and parametric forcing. For that, let us write the parametrically driven and damped sine-Gordon equation as

$$\partial_{tt}\theta + \sin\theta - \partial_{xx}\theta = \varepsilon P[\theta],$$

where

$$P[\theta] = -\mu\partial_t\theta - \gamma \sin\omega t \sin\theta \tag{3.8}$$

and ε is a small parameter. Remind from Sec. 2.7.1 that the SG equation admits analytical kink solutions of the form

$$\theta_k(x,t) = 4\arctan\left(\mathrm{e}^{\sigma z}\right),$$

with

$$z = -\gamma(v)(x - x_0 - vt),$$

where

$$\gamma(v) = \frac{1}{\sqrt{1-v^2}}$$

and $\sigma = \pm 1$, depending if it is a kink or antikink solution, respectively. Through the IST method, it is possible to obtain dynamical equations for v and x_0, which now are considered as functions of time. These equations are indeed [52]

$$\frac{\mathrm{d}v}{\mathrm{d}t} = -\frac{\varepsilon\sigma}{4}(1-v^2)^{3/2}\int_{-\infty}^{+\infty} P[\theta_k(z)]\,\mathrm{sech}\,z\,\mathrm{d}z$$

and

$$\frac{\mathrm{d}x_0}{\mathrm{d}t} = -\frac{\varepsilon\sigma}{4}v(1-v^2)\int_{-\infty}^{+\infty} P[\theta_k(z)]z\,\mathrm{sech}\,z\,\mathrm{d}z.$$

Note that the perturbation P is evaluated in the θ_k solution from the unperturbed SG equation. Likewise, the same expressions can also be obtained by means of applying a perturbative analysis, as showed in [71].

To calculate the integrals from these equations, let us first to express $P[\theta_k(z)]$ as a function of z. Notice that since θ_k is the solution of the unperturbed SG equation, the time derivative present in $P[\theta_k(z)]$ does not affect v and x_0. After straightforward calculations, we obtain

$$P[\theta_k(z)] = \frac{2\mu\sigma v}{\sqrt{1-v^2}}\,\mathrm{sech}\,z + 2\,\gamma\sin\omega t\,\sinh\left(\sigma z\right)\mathrm{sech}^2\left(\sigma z\right).$$

However, since $\sinh(\cdot)$ is an odd function and $\operatorname{sech}^2(\cdot)$ is even, it is satisfied that

$$\sinh(\sigma z)\operatorname{sech}^2(\sigma z) = \sigma \sinh z \operatorname{sech}^2 z,$$

and therefore, after solving the integrals, the equations for v and x_0 result in

$$\frac{\mathrm{d}v}{\mathrm{d}t} = -\varepsilon\sigma^2\mu v(1-v^2)$$

and

$$\frac{\mathrm{d}x_0}{\mathrm{d}t} = -\frac{\varepsilon\sigma^2\gamma}{2}v(1-v^2)\sin\omega t.$$

It is easy to realize that $\sigma^2 = 1$.

The analytical solution for the velocity is

$$v(t) = \pm v_0 \frac{1}{\sqrt{v_0^2 + \mathrm{e}^{2\varepsilon\mu t}(1-v_0^2)}},$$

which, as mentioned in past sections, decays to zero because of the presence of dissipation μ. The term v_0 is the velocity in $t = 0$. On the other hand, the analytical solution for x_0 is not easy to calculate, but we can still predict its behavior by writing

$$\frac{\mathrm{d}x_0}{\mathrm{d}t} = \frac{\gamma \sin\omega t}{2\mu}\frac{\mathrm{d}v}{\mathrm{d}t},$$

i.e., its temporal derivative is proportional to $\mathrm{d}v/\mathrm{d}t$, which tends to zero as time grows up. Thus, the position x_0 tends to a constant value, as also mentioned in past sections.

In conclusion, the IST method predicts that the kink solution from the SG equation tends to be static under dissipation and parametric forcing. But, unfortunately, it does not predict the emergence of the evanescent waves. The reason for the previous result is that the validity of this method is in the neighborhood of the integrable system. However, the flaming kinks are observed far from this limit.

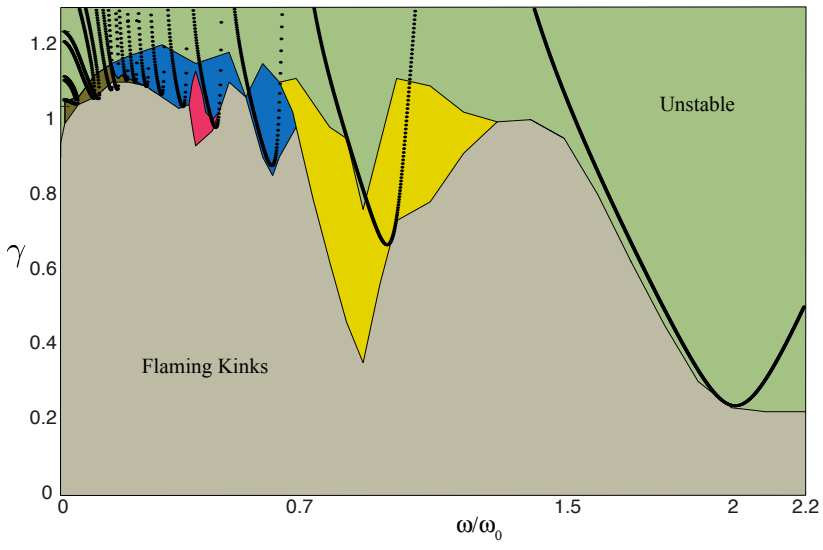

Figure 3.8: Phase diagram of the flaming kinks instabilities in the Ince-Stutt diagram for $\mu = 0.1$. The colors account for the different instabilities observed. In the region marked as unstable, we do not observe kink solutions.

3.5 Flaming kinks instabilities

The region where the flaming kinks can be found was presented in Fig. 3.2 (c). In this region, the flaming kinks share some properties in common, although they present differences in the amplitude and steepness of the waves. For instance, their central position does not move and their evolution in time is periodic, with the period of the parametric forcing. However, as we approach the Arnold tongues in the space of parameters $\{\omega, \gamma\}$, the flaming kinks exhibit some instabilities, characterized by not present the aforementioned properties, namely, their position could star to move and they could do not evolve periodically in time.

In this section, we present some flaming kinks instabilities found numerically by simulating the parametrically driven and damped sine-Gordon equation (see Eq. 3.1). We will restrict ourselves to present the main properties. Study in this direction is still in progress.

Let us start by presenting the phase diagram of these instabilities. In Fig. 3.8 we show the different regions where they can be found in the Ince-Stutt diagram (see section 2.6.2) for $\mu = 0.1$. As we can see, these instabilities emerge near the Arnold tongues. In the region marked as unstable, the system becomes highly complex and the kinks no longer exist.

We will name the different regions showed in the figure simply as the *yellow region*, *blue region*, *purple region* and *green region*.

Yellow region

In this region, the flaming kinks center position starts to move erratically and the waves propagation is not symmetric. We have not determined yet if the nature of the position dynamics (that clearly is of complex nature), namely, if it follows a chaotic rule, semi-periodic, etc.

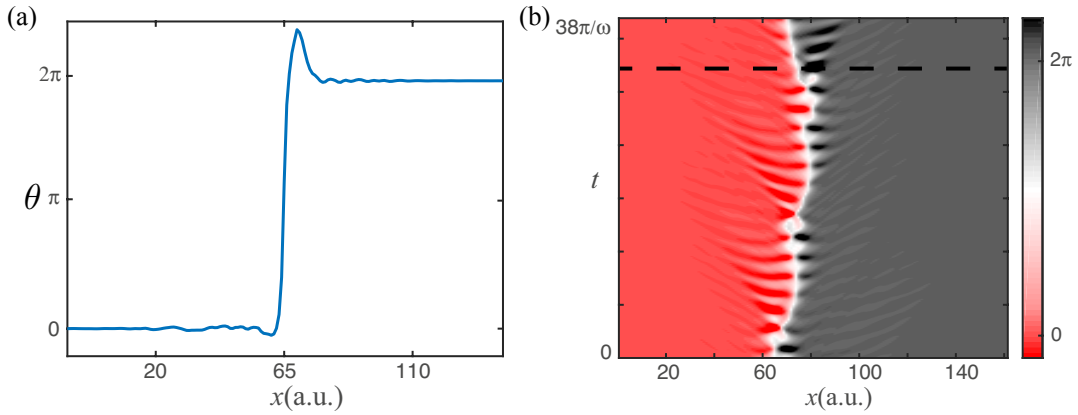

Figure 3.9: (a) Spatial profile of the solutions from yellow region. (b) Spatiotemporal evolution. The dashed line corresponds to the profile showed in (a).

Blue region

In the blue region, the states $\theta = 0$ and $\theta = 2\pi$ turn unstable, exhibiting irregular oscillatory patterns, which are not symmetric with respect to the center position. There not propagating waves, but irregular stationary waves. Besides, the kink position does not move.

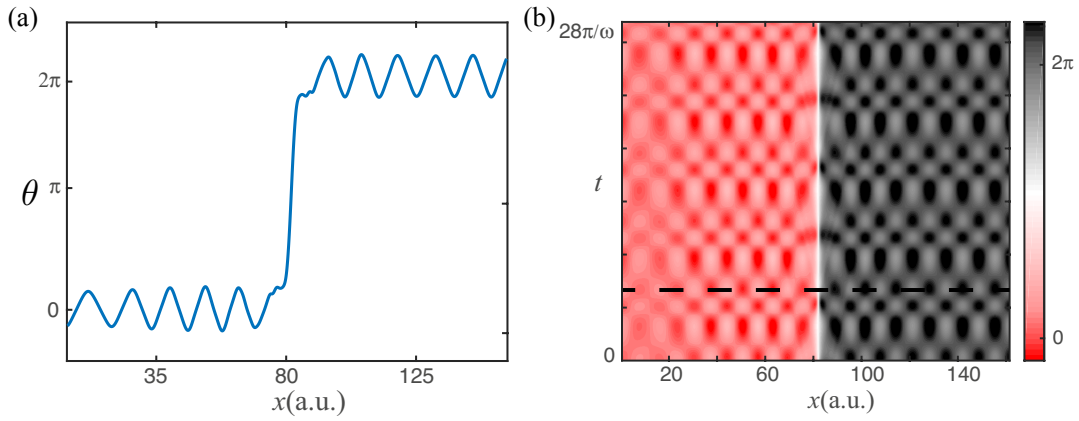

Figure 3.10: (a) Spatial profile of the solutions from blue region. (b) Spatiotemporal evolution. The dashed line corresponds to the profile showed in (a).

Purple region

Here the flaming kinks position moves, but in a more ordered way than in the yellow region. The flaming kinks emit waves in an asymmetrical form, that is, sometimes to $+x$ and sometimes to $-x$.

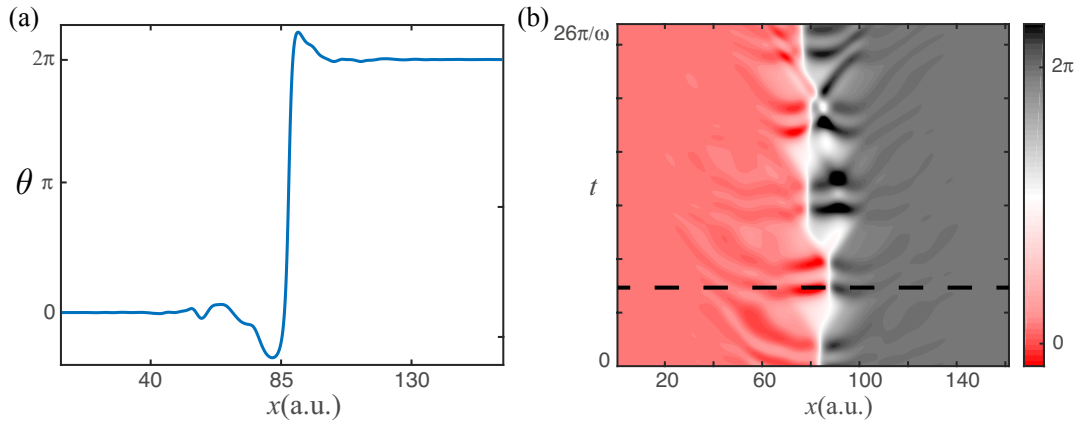

Figure 3.11: (a) Spatial profile of the solutions from purple region. (b) Spatiotemporal evolution. The dashed line corresponds to the profile showed in (a).

Green region

In this region, the flaming kinks do not move. The particular feature of this region is that the kink width widens periodically, and returns to its original value. When the kink returns to its original shape some waves emerge from the center and also to the center, that is, there are waves propagating in opposite directions in $\theta = 0$ and $\theta = 2\pi$.

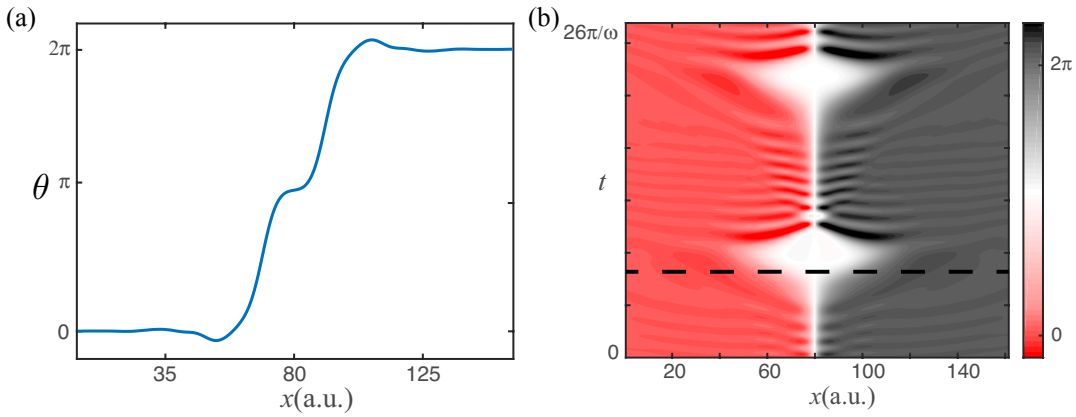

Figure 3.12: (a) Spatial profile of the solutions from green region. (b) Spatiotemporal evolution. The dashed line corresponds to the profile showed in (a).

3.6 Flaming kinks in two dimensions

In this section, we will extend our study of flaming kinks considering now two spatial dimensions. We will discuss the emergence of an interface instability formed in the kink center position. Study in this direction is still in progress.

Sine-Gordon in two dimensions

Let us start considering the two dimensional extension of the sine-Gordon equation,

$$\partial_{tt}\theta = -\sin\theta + \nabla^2\theta,$$

where now $\theta = \theta(x, y, t)$ and ∇^2 is the two dimensional Laplacian. This equation admits the same analytical kink solutions of the one dimension case

$$\theta(x, y, t) = 4\arctan\left(\exp\{-\sigma\gamma(v)(x - x_0 - vt)\}\right) \quad \text{with} \quad \gamma(v) = \frac{1}{\sqrt{1 - v^2}},$$

that is, their profile does not change in the y direction. Besides, as in the one-dimensional case, these solutions can travel with a constant velocity in the x direction. Fig. 3.13 shows their profile in one and two dimensions.

What motivates us to study the sine-Gordon in two dimensions is because it models systems more realistic and suitable for applications. One example of this are the Josephson

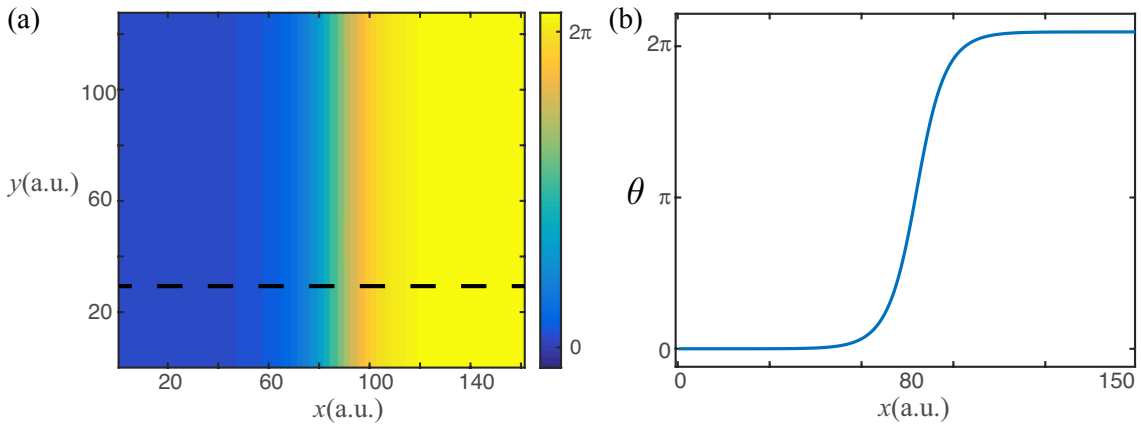

Figure 3.13: (a) Spatial profile of two dimensional sine-Gordon kinks. The dashed line corresponds to the one dimensional profile shown in (b).

junctions, composed of two superconducting layers separated by a nonsuperconducting material (see Fig. 3.14 (a)). These devices are named after Brian Josephson, who in 1962 predicted that pairs of superconducting electrons could travel through the nonsuperconducting barrier by *tunneling effect*. When these layers are large (y direction in the figure), the phase difference of the macroscopic wavefunctions in every superconductor is described by the sine-Gordon equation [26, 83]. Then, it is expected that this system admits kink solutions[2] as the one showed in Fig. 3.14 (b).

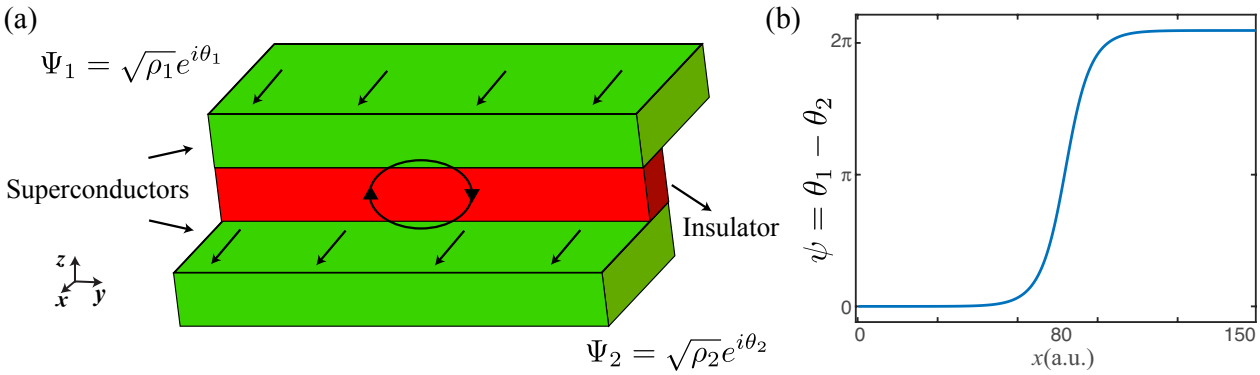

Figure 3.14: (a) Schematic representation of a Josephson junction. The green layers represent superconductors and the red one an insulator material. The terms Ψ_1 and Ψ_2 account for the macroscopic wavefunctions in every layer. (b) Kink (or fluxon) solution of the phase difference $\psi = \theta_1 - \theta_2$.

Other examples that could be well described by the two-dimensional sine-Gordon equation are a two-dimensional array of magnetic wire or crystal dislocations. In each one of these systems, the parametric forcing needs to be reinterpreted.

[2]It is usual to name as *fluxons* to the kink solutions in this context.

Two dimensional parametrically driven and damped sine-Gordon equation

If we now add dissipation and parametric forcing, the equation reads

$$\partial_{tt}\theta = -(1 + \gamma \sin \omega t) \sin \theta + \nabla^2 \theta - \mu \partial_t \theta,$$

with γ and μ the forcing amplitude and damping coefficient, respectively, as before. Under these conditions, it is not surprising to expect the same behavior as in the one-dimensional case. Namely, the kink speed should tend to zero due to dissipation, and evanescent waves traveling in opposite directions should appear from the center position line (red line in the figure) because of the parametric forcing. However, in addition to these features, we observe another phenomenon: The flaming kinks exhibit an interface instability on its center line position, that is, where $\theta(x, y, t) = \pi$ (red line in the figure). We illustrate this in Fig. 3.15, where it can be observed that this line exhibits an oscillatory profile, both in space and time. We have not determined yet the region of parameters where this feature can be observed.

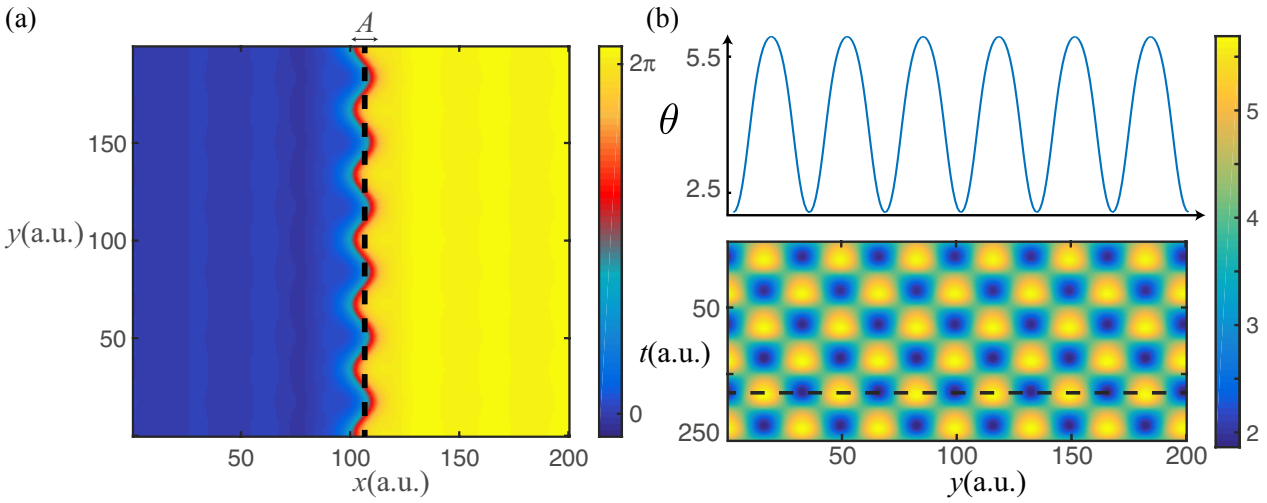

Figure 3.15: (a) Flaming kink spatial profile in two dimensions. (b) The upper figure corresponds to the dotted line showed in (a). The lower figure is the spacetime evolution of this profile, illustrating a typical stationary waves profile.

Hysteresis in the interface amplitude

The traveling evanescent waves exhibit the same properties as in one dimension, that is, they exhibit resonant properties. Nevertheless, the center kink position now oscillates due to the interface instability. Its frequency of oscillation is half the forcing frequency, which makes us understand that this is a parametric resonance. Moreover, the amplitude of oscillation of this interface exhibits hysteresis as we change the forcing frequency. We illustrate this behavior in Fig. 3.16.

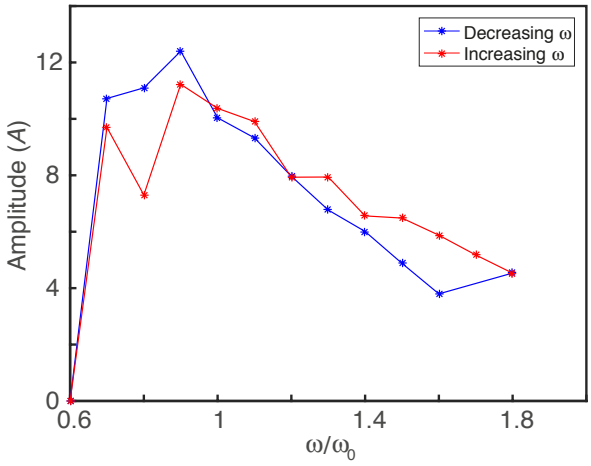

Figure 3.16: Interface amplitude in function of the forcing frequency. The blue (red) line corresponds to the amplitude when the forcing frequency is decreased (increased).

Localized structures in two dimensions

This system also admits localized structures, resulting from the interaction of a flaming kink with a flaming antikink, shown in Fig. 3.17 (a). As in the one-dimensional case, they also exhibit stationary waves between the kinks. Until now we have not found localized structures with other forms, as circular for instance.

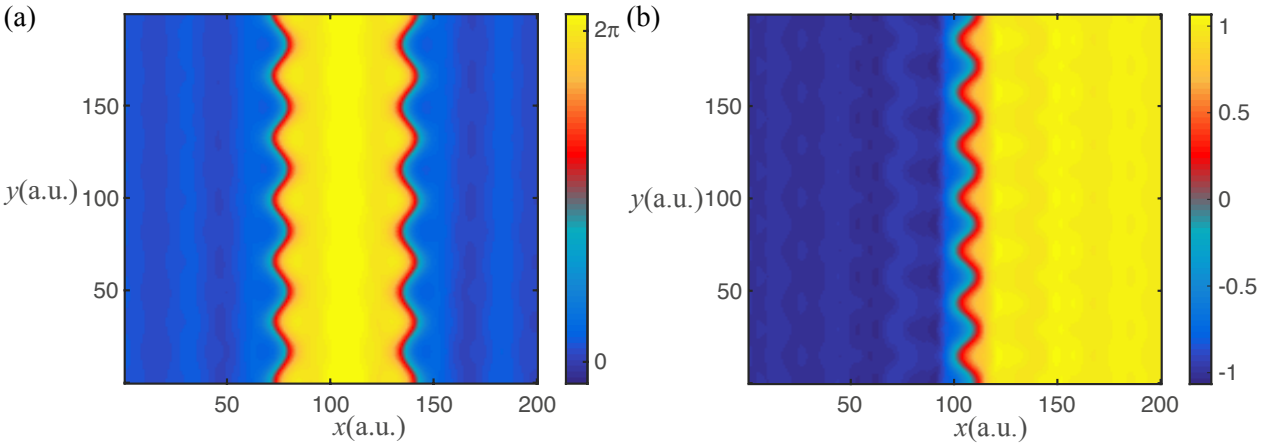

Figure 3.17: (a) Localized structure profile, resulting from the two dimensional flaming kink-antikink interaction. (b) Flaming kink spatial profile for the two dimensional driven and damped ϕ^4 equation. We have set $\varepsilon = 1, \mu = 0.1, \omega = 0.5$ and $\gamma = 0.8$.

Two dimensional ϕ^4 scalar field equation

We would like to specify that these two-dimensional flaming kinks are not restricted only to the sine-Gordon equation. They are also present in the ϕ^4 scalar field equation in two

dimensions, submitted to the same kind dissipation and parametric forcing

$$\partial_{tt}\phi = \varepsilon\phi - \phi^3 + \nabla^2\phi - \mu\partial_t\phi, \tag{3.9}$$

where $\phi = \phi(x, y, t)$ and ∇^2 is the two dimensional Laplacian. Their profile can be seen in Fig. 3.17 (b). The same properties aforementioned can be found in this equation.

Experimental motivation

To conclude this chapter, we would like to show some experimental data that resembles the interface instability found, particularly an experiment that consists of vertically vibrated granular layers. The details of this experiment can be found in Ref. [94]. In Figure 3.18 we show a figure of this work, illustrating the different pattern observed when the forcing amplitude and frequency are varied. As it is shown, for certain values there is a regime where the granular layers reorganize, in such a way that form a zigzag instability, similar to the one observed in our simulations. Moreover, this instability can derive in different forms, as circular for instance. We have not found this behavior yet. Similar patterns can also be found in [10, 46].

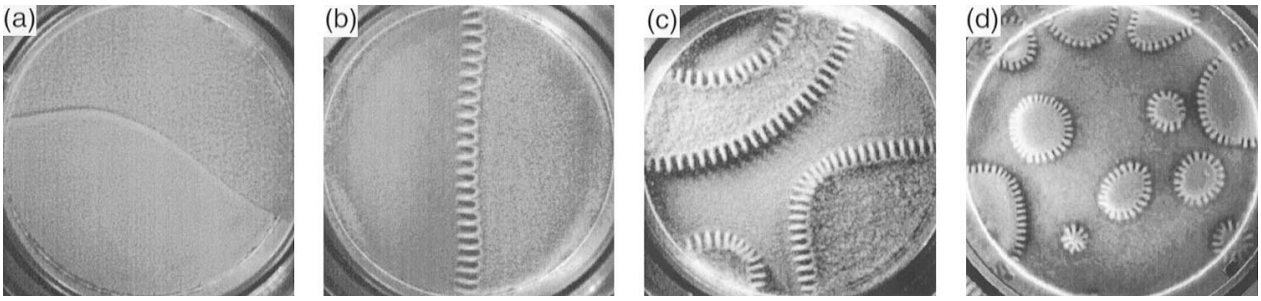

Figure 3.18: Fronts between domains with opposite phase in a 7-particle deep layer for different values of the forcing amplitude and frequency. This picture was taken from [94].

Chapter 4

Localized structures lattices in vegetation

In this chapter, we will discuss how the interaction between the localized structures introduced in Sec. 2.8.3 can lead to the formation of stable localized structure lattices. We will analyze both one-dimensional and two-dimensional cases, deriving in each case the interaction law between localized structures. As we will see, their interaction is repulsive, that is, they tend to move away. This feature is crucial for the formation of stable lattices.

4.1 Lattices in one dimension

4.1.1 Properties of one dimensional localized structures

In Sec. 2.8.1 we discussed a model for the dynamics of vegetation in semi-arid climates, which in one dimension writes (interaction-redistribution local model)

$$\partial_t u = -u[\eta - \kappa u + u^2] + [\Delta - \Gamma u]\partial_{xx} u - \alpha u \partial_{xxxx} u, \tag{4.1}$$

where $u(x,t)$ accounts for the normalized phytomass at the spatial position x in an instant t. We discussed that when $\kappa > 0$, between some range of η values it is possible to find localized structures surrounded by bare soil, which in one dimension have the profile shown in Fig. 4.1. This profile corresponds to the steady state, reached after a transient evolution.

Asymptotic behavior

As we can see from the figure, the tails seem to tend to zero exponentially. To probe if this is true or not, we perform a linear analysis around $u = 0$ of the stationary equation ($\partial_t u = 0$). Then, linearizing in u we get

$$0 = -u\eta + \Delta \partial_{xx} u, \tag{4.2}$$

which confirms the exponential behavior of a localized structure u_{LS}

$$u_{LS}(|x - x_0| \to \infty) \propto \mathrm{e}^{-\gamma|x-x_0|} \quad \text{with} \quad \gamma = \sqrt{\eta/\Delta}, \tag{4.3}$$

where x_0 is the center position (see Fig. 4.1). This feature can be confirmed numerically by performing a curve fitting in the tails. The details of the fitting are presented in the figure.

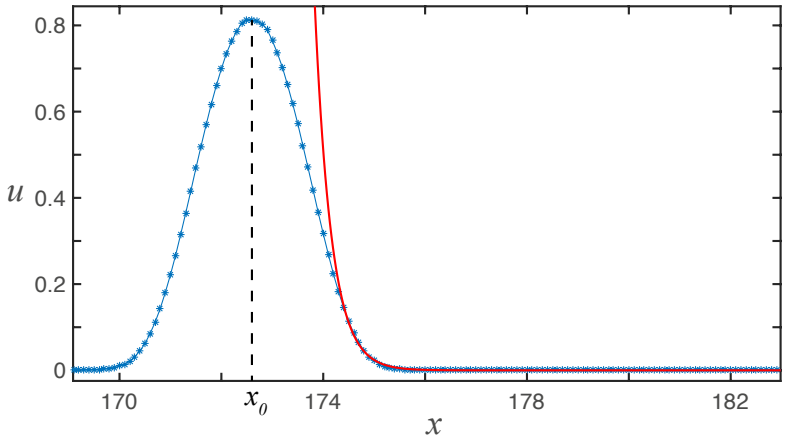

Figure 4.1: One dimensional localized structure profile. The parameters used are $\eta = 0.17, \kappa = 0.8, \Delta = 0.02, \Gamma = 0.5$ and $\alpha = 0.13$. The red line corresponds to the exponential fitting, using Eq. (4.3). For this case the theoretical value of γ is 2.91 and from the fitting 3.06. The coefficient of determination results $R^2 = 0.9978$.

Localized structures repulsion

A single localized structure will remain static after reaching the equilibrium. Due to the spatial symmetries in Eq. (4.1), it will remain axially symmetric. However, if we put an additional localized structure at a certain distance, we will see that they start to move, repelling each other. This repulsion initially is quick, i.e., the LSs start to move fast, but as time goes by they will move slower. This evolution is presented in Fig. 4.2 (b), where we have measured numerically the distance of separation $r(t)$ in function of time. We have considered r as the distance between the center positions.

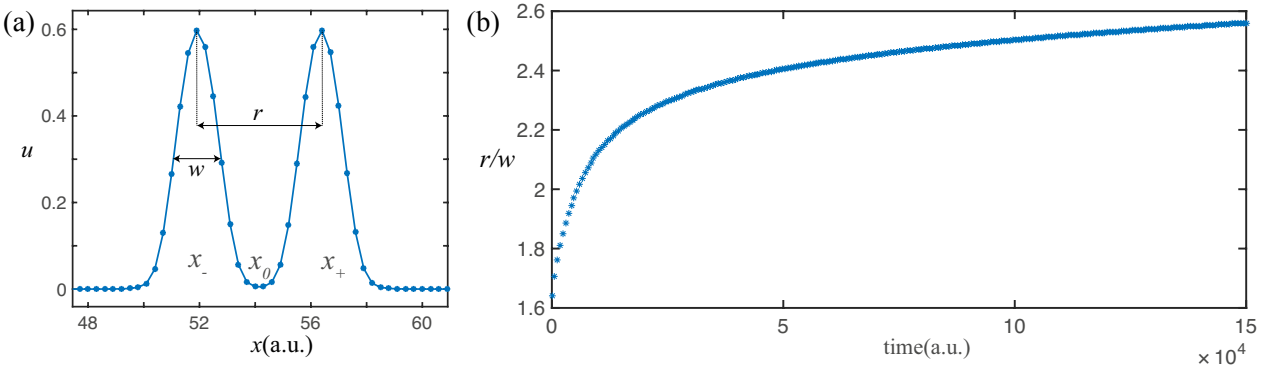

Figure 4.2: (a) Two localized structures separated by a distance r. (b) Numerical data of r in function of time, showing the repulsion between LSs. The parameters used are $\eta = 0.12, \kappa = 0.6, \Delta = 0.02, \Gamma = 0.5, \alpha = 0.125$ and $\mathrm{d}x = 0.4$.

The time evolution of r seems to follow a logarithmic rule, implying that its temporal derivative follows an exponential law in r ($\dot{r} \propto \mathrm{e}^{-Ar}$), which makes sense since the asymptotic

behavior of the LSs tails is exponential. In the next section, we will derive analytically the dynamic equation that r satisfies in a particular limit and will compare with numerical data.

4.1.2 Interaction between two localized structures

In this section, we will derive the interaction dynamics between two localized structures, following a similar strategy used for the kink-antikink interaction from the ϕ^4 model equation (see Sec. 2.7.3) and for the flaming kink-antikink interaction (see Appendix B).

To start, we propose the following ansatz,

$$u(x,t) = u_{LS}^{-}(x - x_{-}(t)) + u_{LS}^{+}(x - x_{+}(t)) + W(x_{-}(t), x_{+}(t), x), \tag{4.4}$$

which accounts for the interaction dynamics between two localized structures, u_{LS}^{-} and u_{LS}^{+}, with central positions $x_{-}(t)$ and $x_{+}(t)$, respectively, as it is illustrated in Fig. 4.2(a). These positions have been promoted as functions of time. Moreover, the function W accounts for the corrections of the profile due to the interaction dynamics, which will be assumed small, i.e., nonlinear terms will be neglected. The terms proportional to the product of W with $\dot{x}_{-}(t)$ or $\dot{x}_{+}(t)$ also will be neglected, since it will be considered that the LSs travel slow.

To simplify our calculations, we define

$$r(t) \equiv x_{+}(t) - x_{-}(t) \quad \text{and} \quad x_0(t) \equiv \frac{x_{+}(t) - x_{-}(t)}{2}, \tag{4.5}$$

as the distance and central position between the LSs, respectively, and

$$z_{\pm}(t) \equiv x - x_{\pm}(t). \tag{4.6}$$

We will also assume that the distance r is large compared to the size of the localized structures. Therefore, introducing this ansatz into Eq. (4.1) and after straightforward calculations, we get the following linear system

$$\mathcal{L}W = b, \tag{4.7}$$

where the linear operator is

$$\begin{aligned}\mathcal{L} = &-\eta + 2\kappa(u_{LS}^{-} + u_{LS}^{+}) - 3(u_{LS}^{-} + u_{LS}^{+})^2 + \Delta\partial_{xx} \\ &- \Gamma\left[(u_{LS}^{-} + u_{LS}^{+})\partial_{xx} + \partial_{xx}(u_{LS}^{-} + u_{LS}^{+})\right] \\ &- \alpha\left[(u_{LS}^{-} + u_{LS}^{+})\partial_{xxxx} + \partial_{xxxx}(u_{LS}^{-} + u_{LS}^{+})\right]\end{aligned} \tag{4.8}$$

and

$$\begin{aligned}b = &\frac{\dot{r}}{2}\left(\partial_{z_-}u_{LS}^{-} - \partial_{z_+}u_{LS}^{+}\right) - \dot{x}_0\left(\partial_{z_-}u_{LS}^{-} + \partial_{z_+}u_{LS}^{+}\right) \\ &- 2\kappa u_{LS}^{-}u_{LS}^{+} + 3u_{LS}^{-}u_{LS}^{+}\left(u_{LS}^{-} + u_{LS}^{+}\right) \\ &+ \Gamma\left(u_{LS}^{-}\partial_{xx}u_{LS}^{+} + u_{LS}^{+}\partial_{xx}u_{LS}^{-}\right) \\ &+ \alpha\left(u_{LS}^{-}\partial_{xxxx}u_{LS}^{+} + u_{LS}^{+}\partial_{xxxx}u_{LS}^{-}\right).\end{aligned} \tag{4.9}$$

Adjoint operator

As we have discussed in previous sections, this linear system has solution if the Fredholm solvability condition is fulfilled (see Sec. 2.4). This condition will help us to determine the dynamical equations for $r(t)$ and $x_0(t)$. To apply it, we define the following inner product

$$\langle f|g\rangle = \int_{-\infty}^{+\infty} fg \, \mathrm{d}x, \tag{4.10}$$

through which the adjoint operator $\mathcal{L}^\dagger$ can be obtained. Since this is defined as $\langle \mathcal{L}^\dagger f | g\rangle = \langle f|\mathcal{L}g\rangle$, all the terms of $\mathcal{L}$ remain the same in $\mathcal{L}^\dagger$, expect

$$\Gamma(u_{LS}^- + u_{LS}^+)\partial_{xx} \quad \text{and} \quad \alpha(u_{LS}^- + u_{LS}^+)\partial_{xxxx}. \tag{4.11}$$

The adjoint of these terms can be obtained by integrating by parts two and four times, respectively. To illustrate this idea, let us consider the first of these terms

$$\left\langle f \middle| \Gamma(u_{LS}^- + u_{LS}^+)\partial_{xx} g \right\rangle = \int_{-\infty}^{+\infty} f \, \Gamma(u_{LS}^- + u_{LS}^+)\partial_{xx} g \, \mathrm{d}x, \tag{4.12}$$

which under one integration by parts reads

$$f \, \Gamma(u_{LS}^- + u_{LS}^+)\partial_x g \Big|_{-\infty}^{\infty} - \int_{-\infty}^{+\infty} \partial_x [f \, \Gamma(u_{LS}^- + u_{LS}^+)]\partial_x g \, \mathrm{d}x. \tag{4.13}$$

Notice that the first term vanishes, since $(u_{LS}^- + u_{LS}^+)$ is zero in $\pm\infty$. Applying again integration by parts we get

$$\partial_x [f \, \Gamma(u_{LS}^- + u_{LS}^+)] g \Big|_{-\infty}^{\infty} - \int_{-\infty}^{+\infty} \partial_{xx} [f \, \Gamma(u_{LS}^- + u_{LS}^+)] g \, \mathrm{d}x. \tag{4.14}$$

And therefore,

$$\left\langle f \middle| \Gamma(u_{LS}^- + u_{LS}^+)\partial_{xx} g \right\rangle = \left\langle \partial_{xx} [f \, \Gamma(u_{LS}^- + u_{LS}^+)] \middle| g \right\rangle, \tag{4.15}$$

gives us the term applied to f, which will be write as $\partial_{xx}[\Gamma(u_{LS}^- + u_{LS}^+)\cdot]$. This term is the adjoint of the first term in (4.11). Proceeding in the same way with the second term, we finally obtain the adjoint operator

$$\begin{aligned} \mathcal{L}^\dagger = & -\eta + 2\kappa(u_{LS}^- + u_{LS}^+) - 3(u_{LS}^- + u_{LS}^+)^2 + \Delta\partial_{xx} \\ & - \Gamma\left\{(u_{LS}^- + u_{LS}^+)\partial_{xx} + \partial_{xx}\left[(u_{LS}^- + u_{LS}^+)\cdot\right]\right\} \\ & - \alpha\left\{(u_{LS}^- + u_{LS}^+)\partial_{xxxx} + \partial_{xxxx}\left[(u_{LS}^- + u_{LS}^+)\cdot\right]\right\}, \end{aligned} \tag{4.16}$$

which is different to $\mathcal{L}$.

Kernel of $\mathcal{L}^\dagger$

Remind that to apply the Fredholm solvability condition we need to calculate the Kernel components of $\mathcal{L}^\dagger$, that is, the elements that fulfill $\langle f| \, \mathcal{L}^\dagger = 0$. However, due to the complexity

of $\mathcal{L}^\dagger$, is preferable to obtain them numerically. To do that, let us discretize the derivatives in $f(x)$ when we apply $\langle f|\,\mathcal{L}^\dagger$, using central differencing with the 4 nearest neighbors. Thus, defining

$$\begin{aligned}
c_0 =& -\eta + 2\kappa U - 3U^2 - 2\Gamma\partial_{xx}U - 2\alpha\partial_{xxxx}U,\\
c_1 =& -2\Gamma\partial_x U - 4\alpha\partial_{xxx}U,\\
c_2 =& \Delta - \Gamma U - 6\alpha\partial_{xx}U,\\
c_3 =& -4\alpha\partial_x U,\\
c_4 =& -\alpha U\partial_{xxxx},
\end{aligned} \tag{4.17}$$

where $U = u^-_{LS} + u^+_{LS}$, the result of applying $\mathcal{L}^\dagger$ to $\langle f_j|$, with $f_j \equiv f(x = \mathrm{d}xj)$, is

$$\begin{aligned}
\langle f_j|\,\mathcal{L}^\dagger =& \left(\frac{7c_4}{240\mathrm{dx}^4} - \frac{7c_3}{240\mathrm{dx}^3} - \frac{c_2}{560\mathrm{dx}^2} + \frac{c_1}{280\mathrm{dx}}\right) f_{j-4}\\
&+ \left(-\frac{2c_4}{5\mathrm{dx}^4} + \frac{3c_3}{10\mathrm{dx}^3} + \frac{8c_2}{315\mathrm{dx}^2} - \frac{4c_1}{105\mathrm{dx}}\right) f_{j-3}\\
&+ \left(\frac{169c_4}{60\mathrm{dx}^4} - \frac{169c_3}{120\mathrm{dx}^3} - \frac{c_2}{5\mathrm{dx}^2} + \frac{c_1}{5\mathrm{dx}}\right) f_{j-2}\\
&+ \left(-\frac{122c_4}{15\mathrm{dx}^4} + \frac{61c_3}{30\mathrm{dx}^3} + \frac{8c_2}{5\mathrm{dx}^2} - \frac{4c_1}{5\mathrm{dx}}\right) f_{j-1}\\
&+ \left(\frac{91c_4}{8\mathrm{dx}^4} - \frac{205c_2}{72\mathrm{dx}^2} + c_0\right) f_j\\
&+ \left(-\frac{122c_4}{15\mathrm{dx}^4} - \frac{61c_3}{30\mathrm{dx}^3} + \frac{8c_2}{5\mathrm{dx}^2} + \frac{4c_1}{5\mathrm{dx}}\right) f_{j+1}\\
&+ \left(\frac{169c_4}{60\mathrm{dx}^4} + \frac{169c_3}{120\mathrm{dx}^3} - \frac{c_2}{5\mathrm{dx}^2} - \frac{c_1}{5\mathrm{dx}}\right) f_{j+2}\\
&+ \left(-\frac{2c_4}{5\mathrm{dx}^4} - \frac{3c_3}{10\mathrm{dx}^3} + \frac{8c_2}{315\mathrm{dx}^2} + \frac{4c_1}{105\mathrm{dx}}\right) f_{j+3}\\
&+ \left(\frac{7c_4}{240\mathrm{dx}^4} + \frac{7c_3}{240\mathrm{dx}^3} - \frac{c_2}{560\mathrm{dx}^2} - \frac{c_1}{280\mathrm{dx}}\right) f_{j+4},
\end{aligned} \tag{4.18}$$

where $\mathrm{d}x$ is the discretization used. Then, using this system of equations we can construct a matrix M that satisfies

$$M\vec{f} = \vec{0} \quad \text{with} \quad \vec{f} = \begin{pmatrix} f_1 \\ \vdots \\ f_{j-1} \\ f_j \\ f_{j+1} \\ \vdots \\ f_N \end{pmatrix}, \tag{4.19}$$

where N is the number of points considered. Notice that to obtain the Kernel of $\mathcal{L}^\dagger$, we only need to calculate the null eigenvectors of M. The advantage of this procedure is that it this is not a difficult task, even if the dimension of M is large. Nevertheless, let us first take a look at the eigenvalues spectrum of M.

Using the same parameters as in Fig. 4.1, $\mathrm{d}x = 0.1$ and $N = 30$, and setting u_{LS}^{-} and u_{LS}^{+} at a distance of 150 points, we got the eigenvalues spectrum showed in Fig. 4.3, where we confirm the stability of the localized structures since every eigenvalue has real part negative. Moreover, the lowest eigenvalues, in this case, are -0.022 and -0.024, which decrease as the distance r increases. These eigenvalues are the null eigenvalue that we are looking for, although they are not equal to zero due to the numerical approximation made.

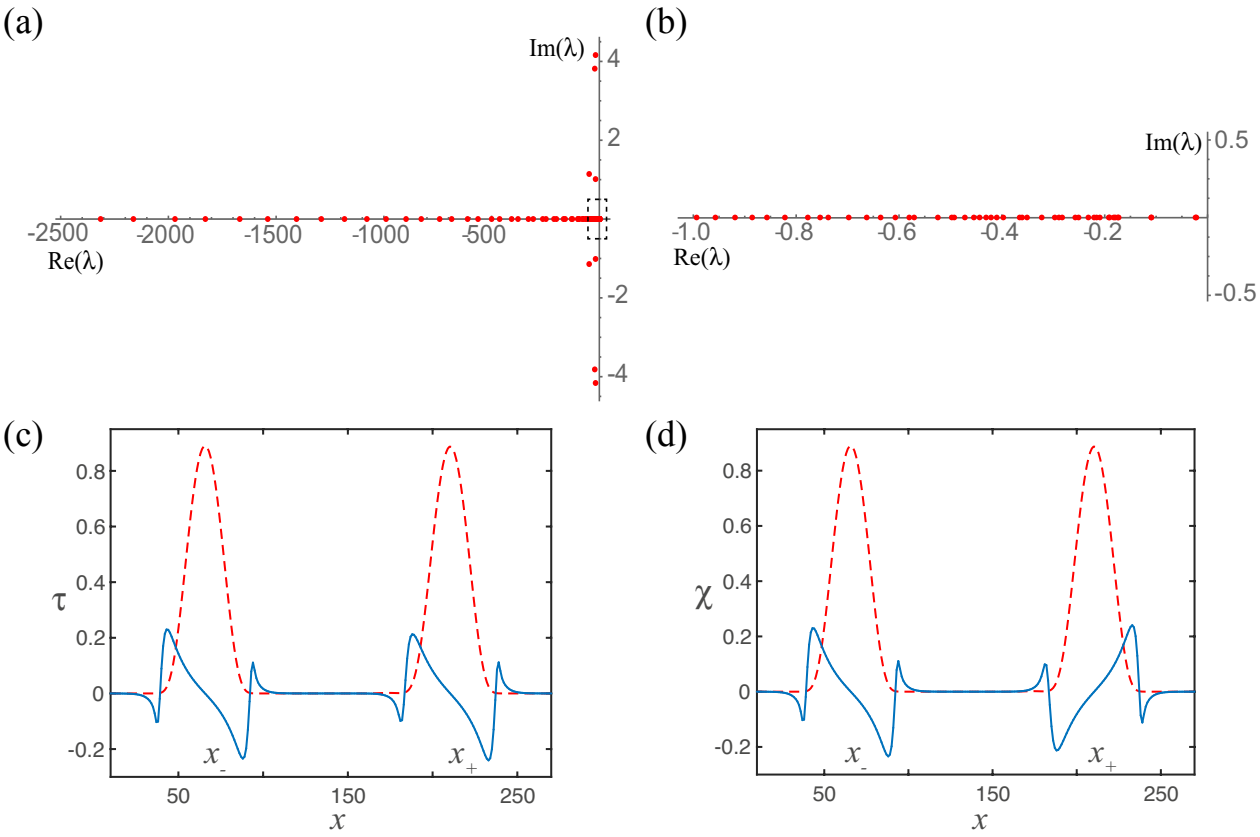

Figure 4.3: (a) Eigenvalues spectrum of matrix M, defined in Eq. 4.19, using the same parameters from Fig. 4.1, $\mathrm{d}x = 0.1$ and $N = 30$. (b) Zoom of the dashed region marked in (a). (c) Null eigenvector τ. (c) Null eigenvector χ.

Finally, the linear combination of the eigenvectors associated with the null eigenvalues calculated gives us the elements of the Kernel of $\mathcal{L}^{\dagger}$. These will be labeled as $\langle\tau|$ and $\langle\chi|$, shown in Fig. 4.3.

Interaction dynamical equations

Now that we have the Kernel of $\mathcal{L}^{\dagger}$, the dynamical equations of r and x_0 are determined by applying the Fredholm solvability condition, which reads

$$\langle\tau|b\rangle = 0 \tag{4.20}$$

and

$$\langle\chi|b\rangle = 0. \tag{4.21}$$

In the first of these products, because τ is odd around x_0, the only term that remains is

$$\left\langle \tau \middle| \dot{x}_0 \left(\partial_{z_-} u_{LS}^- + \partial_{z_+} u_{LS}^+ \right) \right\rangle = 0, \tag{4.22}$$

implying that

$$\dot{x}_0 = 0, \tag{4.23}$$

i.e., the central position of the LSs does not move. This result is obtained from the numerical simulations, which is expected due to the symmetries of the equation. On the other hand, in the product from Eq. (4.21) the terms that remain are

$$\begin{aligned} &\left\langle \chi \middle| \frac{\dot{r}}{2} \left(\partial_{z_-} u_{LS}^- - \partial_{z_+} u_{LS}^+ \right) \right\rangle + \\ &\langle \chi | - 2\kappa u_{LS}^- u_{LS}^+ + 3 u_{LS}^- u_{LS}^+ \left(u_{LS}^- + u_{LS}^+ \right) \\ &+ \Gamma \left(u_{LS}^- \partial_{xx} u_{LS}^+ + u_{LS}^+ \partial_{xx} u_{LS}^- \right) \\ &+ \alpha \left(u_{LS}^- \partial_{xxxx} u_{LS}^+ + u_{LS}^+ \partial_{xxxx} u_{LS}^- \right) \rangle = 0. \end{aligned} \tag{4.24}$$

The integrals involved in this equation can be approximated analytically. For that, it is convenient to write

$$\chi(x) = \chi_-(x - x_-) + \chi_+(x - x_+), \tag{4.25}$$

that is, we divide χ into to parts, one localized around x_- and other around x_+. To illustrate how to approximate analytically, let us take a look at the second product of this equation

$$\begin{aligned} \left\langle \chi \middle| 2\kappa u_{LS}^- u_{LS}^+ \right\rangle &= 2\kappa \int_{-\infty}^{\infty} \left[\chi^-(x - x_-) + \chi^+(x - x_+) \right] u_{LS}^-(x - x_-) u_{LS}^+(x - x_+) \mathrm{d}x \\ &= 2\kappa \left[\int_{-\infty}^{\infty} \chi^-(z_-) u_{LS}^-(z_-) u_{LS}^+(z_- - r) \mathrm{d}z_- + \int_{-\infty}^{\infty} \chi^+(z_+) u_{LS}^-(z_+ + r) u_{LS}^+(z_+) \mathrm{d}z_+ \right]. \end{aligned} \tag{4.26}$$

In the second equality we have changed our variables to $z_- = x - x_-$ in the first integral and to $z_+ = x - x_+$ in the second one. We have also used $r = x_+ - x_-$. These integrals are exponentially close to zero in the whole region of integration, except when they are evaluated near zero. Therefore, we approximate them by setting the integral limits from $-r/2$ to $r/2$. Moreover, since r is large, the terms $u_{LS}^+(z_- - r)$ and $u_{LS}^-(z_+ + r)$ are exponentially small in the region of integration. Thus, it is valid to use the asymptotic behavior of u_{LS}^- and u_{LS}^+ (see Eq. (4.3)) and write

$$\begin{aligned} &\left\langle \chi \middle| 2\kappa u_{LS}^- u_{LS}^+ \right\rangle \approx \\ &2\kappa \left[\int_{-r/2}^{r/2} \chi^-(z_-) u_{LS}^-(z_-) \mathrm{e}^{-\gamma |z_- - r|} \mathrm{d}z_- + \int_{-r/2}^{r/2} \chi^+(z_+) \mathrm{e}^{-\gamma |z_+ + r|} u_{LS}^+(z_+) \mathrm{d}z_+ \right]. \end{aligned} \tag{4.27}$$

where $|z_- - r| = r - z_-$ and $|z_+ + r| = z_+ + r$ in this region of integration. Therefore,

$$\left\langle \chi \middle| -2\kappa u_{LS}^- u_{LS}^+ \right\rangle \approx -2\kappa \mathrm{e}^{-\gamma r} I_1, \tag{4.28}$$

where

$$I_1 = -\left[\int_{-r/2}^{r/2} \chi^-(z_-) u_{LS}^-(z_-) \mathrm{e}^{\gamma z_-} \mathrm{d}z_- + \int_{-r/2}^{r/2} \chi^+(z_+) \mathrm{e}^{-\gamma z_+} u_{LS}^+(z_+) \mathrm{d}z_+ \right]. \tag{4.29}$$

Proceeding in the same way with the others integral in Eq (4.24), we finally obtain the dynamical equation for r

$$\dot{r} = A\mathrm{e}^{-\gamma r} + B\mathrm{e}^{-2\gamma r}, \tag{4.30}$$

where

$$A = \frac{2\left[(\alpha\gamma^4 + \Gamma\gamma^2 - 2\kappa)I_1 + 3I_2 + \Gamma I_4 + \alpha I_5\right]}{\left\langle\chi\middle|\partial_{z_-}u^-_{LS} - \partial_{z_+}u^+_{LS}\right\rangle} \tag{4.31}$$

and

$$B = \frac{6I_3}{\left\langle\chi\middle|\partial_{z_-}u^-_{LS} - \partial_{z_+}u^+_{LS}\right\rangle}, \tag{4.32}$$

with

$$I_2 = -\left[\int_{-r/2}^{r/2}\chi^-(z_-)(u^-_{LS}(z_-))^2\mathrm{e}^{\gamma z_-}\mathrm{d}z_- + \int_{-r/2}^{r/2}\chi^+(z_+)\mathrm{e}^{-\gamma z_+}(u^+_{LS}(z_+))^2\mathrm{d}z_+\right], \tag{4.33}$$

$$I_3 = -\left[\int_{-r/2}^{r/2}\chi^-(z_-)u^-_{LS}(z_-)\mathrm{e}^{2\gamma z_-}\mathrm{d}z_- + \int_{-r/2}^{r/2}\chi^+(z_+)\mathrm{e}^{-2\gamma z_+}u^+_{LS}(z_+)\mathrm{d}z_+\right], \tag{4.34}$$

$$I_4 = -\left[\int_{-r/2}^{r/2}\chi^-(z_-)\partial_{z_-z_-}u^-_{LS}(z_-)\mathrm{e}^{\gamma z_-}\mathrm{d}z_- + \int_{-r/2}^{r/2}\chi^+(z_+)\mathrm{e}^{-\gamma z_+}\partial_{z_+z_+}u^+_{LS}(z_+)\mathrm{d}z_+\right] \tag{4.35}$$

and

$$I_5 = -\left[\int_{-r/2}^{r/2}\chi^-(z_-)\partial^{(4)}_{z_-}u^-_{LS}(z_-)\mathrm{e}^{\gamma z_-}\mathrm{d}z_- + \int_{-r/2}^{r/2}\chi^+(z_+)\mathrm{e}^{-\gamma z_+}\partial^{(4)}_{z_+}u^+_{LS}(z_+)\mathrm{d}z_+\right]. \tag{4.36}$$

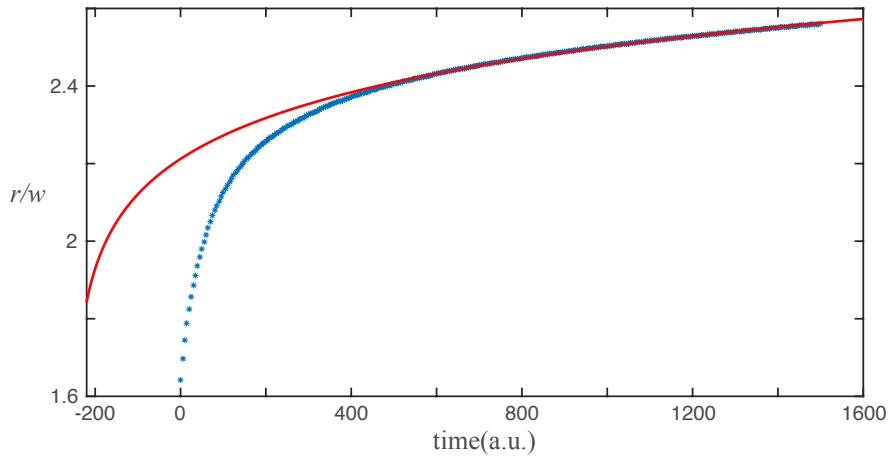

Figure 4.4: Curve fitting of numerical data of $r(t)$. The red curve is the fitting obtained using Eq. (4.38). The parameters used were $\eta = 0.12, \kappa = 0.6, \Delta = 0.02, \Gamma = 0.5$, $\alpha = 0.125$, $\mathrm{d}t = 0.01$ and $\mathrm{d}x = 0.4$. The γ obtained was 2.40, which is close to the theoretical gamma $\gamma = \sqrt{\eta/\Delta} = 2.45$. The R^2 of the fitting is 0.9977.

We have checked numerically that the factors A and B are positive. In addition, because r is large, we can neglect the $\mathrm{e}^{-2\gamma r}$ term in Eq. (4.30) and write

$$\dot{r} = A\mathrm{e}^{-\gamma r}, \tag{4.37}$$

from where we can derive the temporal dependence of r

$$r(t) = \frac{1}{\gamma}\ln(t - t_0) + \frac{1}{\gamma}\ln(A\gamma), \tag{4.38}$$

which agrees with numerical data, as shown in the curve fitting in Fig. 4.4, for large r. In fact, the fitting is better when the distance of separation is more than 2.3 times the LSs width w. The γ factor obtained from the fitting is close to the theoretical prediction.

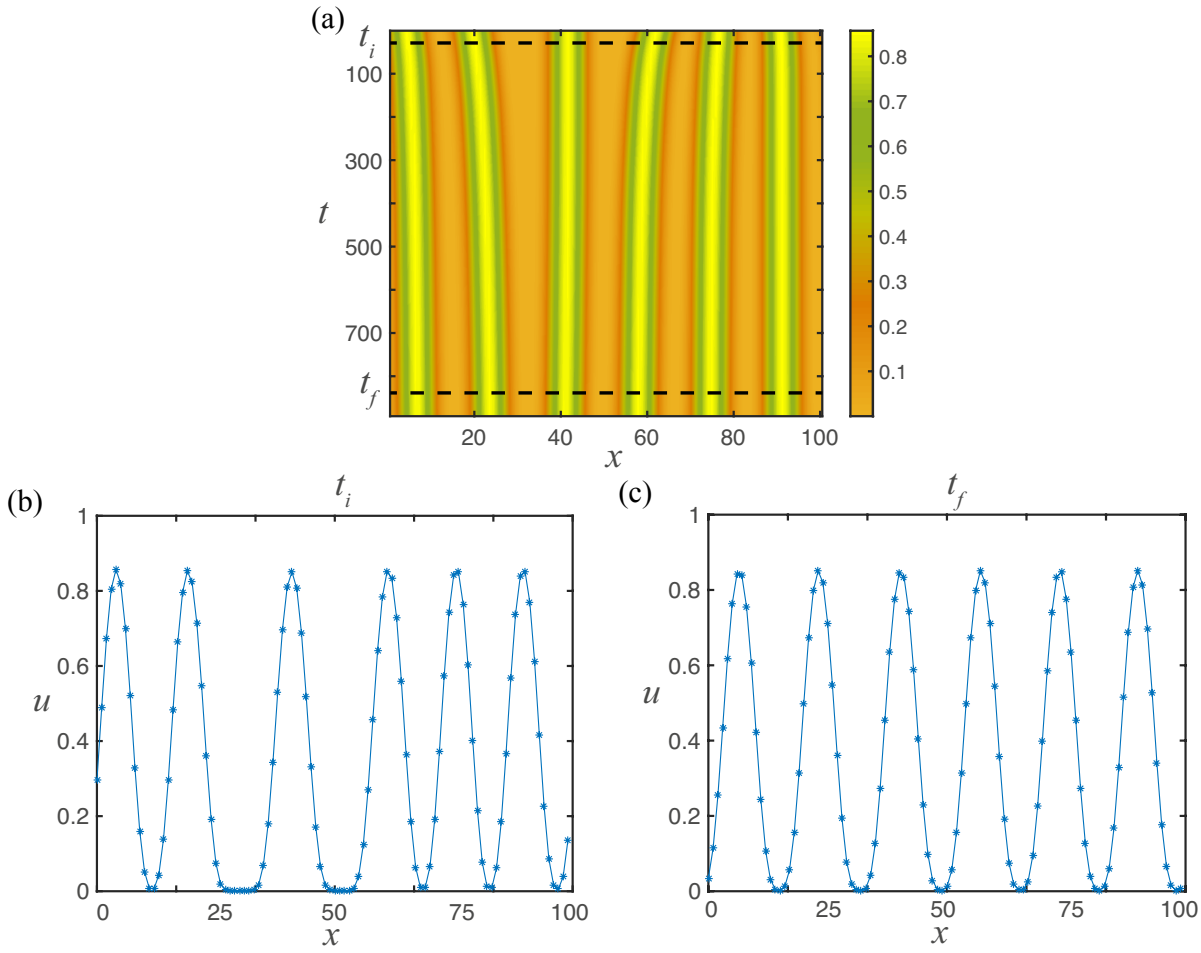

Figure 4.5: (a) Spatiotemporal diagram of the evolution of multiple LSs at different distances. After some time they reach an equilibrium with constant distance of separation between them. The boundary conditions have been set as periodic. The dashed lines correspond to the instant t_i and t_f, showed in (b) and (c), respectively. The parameters used were $\eta = 0.13, \kappa = 0.7, \Delta = 0.01, \Gamma = 0.5, \alpha = 0.1, \mathrm{d}x = 0.3$ and $\mathrm{d}t = 0.01$.

4.1.3 Multiple localized structures

Now that we have derived the interaction law between two LSs, let us analyze the case when multiple LSs interact. Note that since the interaction between them is repulsive, we can consider this system as particles interacting with repulsive forces. Then, it is expected that they will reach an equilibrium when the sum of these forces be equal to zero. In Fig.

4.5 we show what the evolution of an initial condition of LSs at different distances, with periodic boundary conditions. As we can see, they reorganize and reach an equilibrium with a constant distance of separation.

Moreover, the previous situation shows us that if we remove one LS of a periodic configuration, the LSs will reorganize again to a new distance of separation between them. We illustrate this situation in Fig. 4.6.

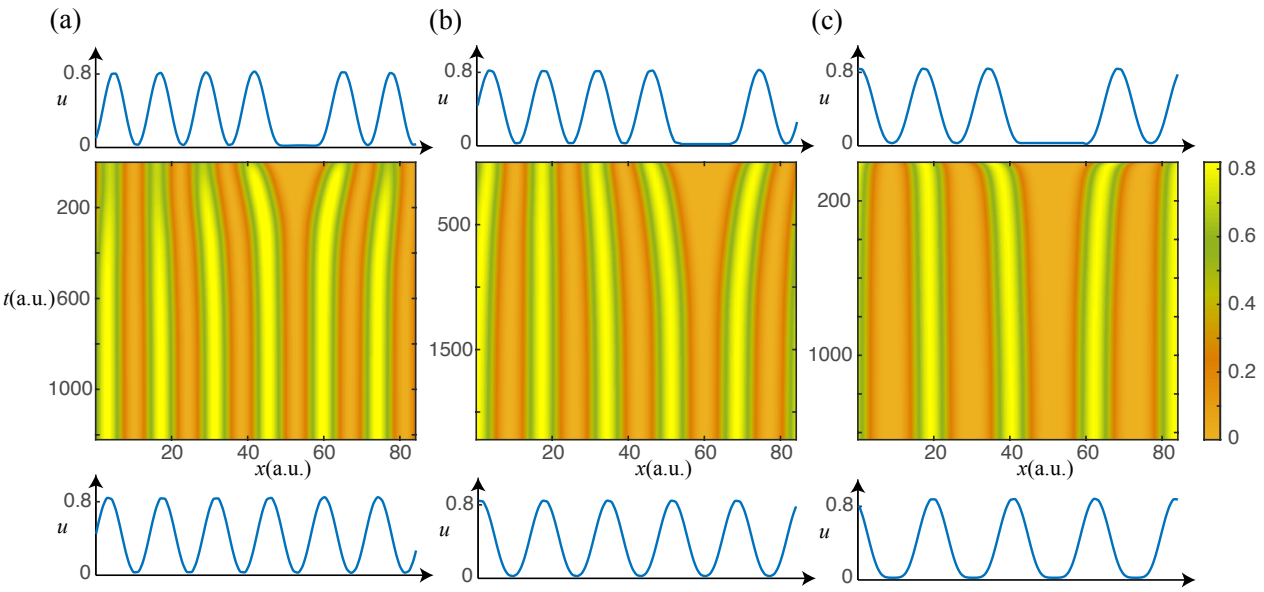

Figure 4.6: Evolution of periodic one-dimensional configurations, after removing one localized structure. The figures (a), (b) and (c) show the evolution of a seven, six, and five LSs periodic profile evolution, after removing one LS. The upper and lower profiles show the initial and final profile of each case, respectively. In all cases the LSs rearrange, reaching a new periodic profile with a larger wavelength. The parameters used were $\eta = 0.13, \kappa = 0.7, \Delta = 0.01, \Gamma = 0.5, \alpha = 0.1, \mathrm{d}x = 0.26$ and $\mathrm{d}t = 0.01$.

Thus, the mechanism of pattern formation that we have presented here differs from the one discussed in Sec. 2.8.2, the Turing instability. In the Turing instability, the wavelength of a periodic pattern is intrinsic to the system, meaning that the wavelength formed does not depend on the size of the system. Otherwise, if we remove a wavelength, another will emerge to maintain the initial wavelength.

4.2 Lattices in two dimensions

Let us now follow the same strategy to study lattices in two dimensions.

4.2.1 Asymptotic behavior of two dimensional localized structures

In the previous section, we showed that the asymptotic behavior of one-dimensional localized structures follows an exponential law for large distances. However, this is not true in two spatial dimensions. To prove that, let us consider the two-dimensional model

$$\partial_t u = -u[\eta - \kappa u + u^2] + [\Delta - \Gamma u]\nabla^2 u - \alpha u \nabla^4 u, \tag{4.39}$$

where ∇^2 is the two dimensional Laplacian. Linearizing around $u = 0$ in the stationary equation ($\partial_t u = 0$), we obtain

$$0 = -u\eta + \Delta\nabla^2 u, \tag{4.40}$$

which in spherical coordinates reads

$$0 = -u\eta + \Delta\left(\frac{\partial^2}{\partial r^2} + \frac{1}{r}\frac{\partial}{\partial r}\right)u, \tag{4.41}$$

since the localized structures are radially symmetric ($\partial_\theta u = 0$). This equation admits analytical solution, which is

$$u(r) = AK_0(\gamma r), \tag{4.42}$$

where $A > 0$ is a constant, $\gamma = \sqrt{\eta/\Delta}$ and K_0 is the modified Bessel function of second kind, which is a real function for $r > 0$. For large values of r we can approximate this function by

$$K_0(r) \approx \sqrt{\frac{\pi}{2}}\frac{\mathrm{e}^{-r}}{\sqrt{r}} \tag{4.43}$$

and then,

$$u_{LS}(r \to \infty) \propto \frac{\mathrm{e}^{-\gamma r}}{\sqrt{r}} \tag{4.44}$$

is the asymptotic behavior of the two dimensional localized structures.

4.2.2 Interaction dynamical equations

To derive the dynamical equations of the interaction between two localized structures, we will follow a similar strategy used in the one-dimensional case. We will restrict our calculations to the x axis that passes through the center of the localized structures, as shown in Fig. 4.7. This is justified if we assume that the LSs are located at a very large distance r, that we can neglect the interactions in other directions. Therefore, we approximate the Laplacian and Bi-Laplacian as one-dimensional operators

$$\nabla^2 = \partial_{xx} \quad \text{and} \quad \nabla^4 = \partial_{xxxx}. \tag{4.45}$$

The ansatz we propose for the two LSs interacting at a distance r is

$$u_{LS}(x) = u^-_{LS}(x + r/2) + u^+_{LS}(x - r/2) + W(r, x), \tag{4.46}$$

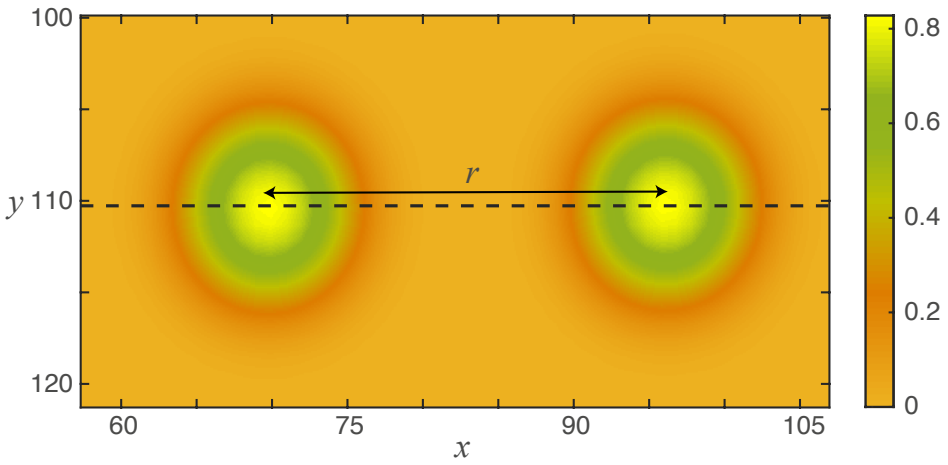

Figure 4.7: Two-dimensional structures located at a distance r. The dashed line passes through the centers and will be the axis where we restrict our calculations.

because the origin is located in the middle of the LSs. Since it was showed in one dimension that the center position does not have dynamics, we will assume the same here.

Notice that the procedure to obtain the dynamical equation for $r(t)$ is essentially the same as in one dimension, due to our restriction to the x axis. The only difference is the asymptotic behavior of the localized structures. In fact, the linear system obtained after replacing the ansatz will be

$$\mathcal{L}W = b, \tag{4.47}$$

with the same operator $\mathcal{L}$ as in one dimension, and

$$\begin{aligned} b =& \frac{\dot{r}}{2}\left(\partial_{z_-}u^-_{LS} - \partial_{z_+}u^+_{LS}\right) \\ & - 2\kappa u^-_{LS}u^+_{LS} + 3u^-_{LS}u^+_{LS}\left(u^-_{LS} + u^+_{LS}\right) \\ & + \Gamma\left(u^-_{LS}\partial_{xx}u^+_{LS} + u^+_{LS}\partial_{xx}u^-_{LS}\right) \\ & + \alpha\left(u^-_{LS}\partial_{xxxx}u^+_{LS} + u^+_{LS}\partial_{xxxx}u^-_{LS}\right), \end{aligned} \tag{4.48}$$

with $z_\pm = x \mp r/2$. We choose the same inner product as in one dimension, and in consequence, the Kernel of $\mathcal{L}^\dagger$ remains the same. The Fredholm solvability condition reads $\langle\chi|b\rangle = 0$, from where we derive the dynamical equation for r. The analytical approximations that we do are slightly different than in one dimension. To illustrate them, let us consider the inner product between χ and $2\kappa u^-_{LS}u^+_{LS}$, as in Eq. (4.26)

$$\begin{aligned} &\left\langle\chi\middle|2\kappa u^-_{LS}u^+_{LS}\right\rangle \\ &= 2\kappa\left[\int_{-\infty}^{\infty}\chi^-(z_-)u^-_{LS}(z_-)u^+_{LS}(z_- - r)\mathrm{d}z_- + \int_{-\infty}^{\infty}\chi^+(z_+)u^-_{LS}(z_+ + r)u^+_{LS}(z_+)\mathrm{d}z_+\right]. \end{aligned} \tag{4.49}$$

Again, we restrict the integral limits only from $-r/2$ to $r/2$ and replace $u^+_{LS}(z_- - r)$ and $u^-_{LS}(z_+ + r)$ by their asymptotic behavior . Since now we have restricted to the x axis, using Eq. (4.44) the asymptotic behavior reads

$$u_{LS}(|x - x_0| \to \infty) \propto \frac{\mathrm{e}^{-\gamma|x-x_0|}}{\sqrt{|x-x_0|}}, \tag{4.50}$$

where x_0 is the LSs central position, thus,

$$\langle\chi|2\kappa u_{LS}^{-}u_{LS}^{+}\rangle \approx$$
$$2\kappa\left[\int_{-r/2}^{r/2}\chi^{-}(z_{-})u_{LS}^{-}(z_{-})\frac{\mathrm{e}^{-\gamma|z_{-}-r|}}{\sqrt{|z_{-}-r|}}\mathrm{d}z_{-}+\int_{-r/2}^{r/2}\chi^{+}(z_{+})\frac{\mathrm{e}^{-\gamma|z_{+}+r|}}{\sqrt{|z_{+}+r|}}u_{LS}^{+}(z_{+})\mathrm{d}z_{+}\right]. \tag{4.51}$$

Notice that $|z_{-}-r|=r-z_{-}$ and $|z_{+}+r|=z_{+}+r$ in this region of integration. Moreover, performing a Taylor expansion we get

$$\frac{1}{\sqrt{z_{\pm}\pm r}}\approx\frac{1}{\sqrt{r}}\pm\frac{z_{\pm}}{2r^{3/2}}. \tag{4.52}$$

The second term of this expansion can be neglected because r is large. Therefore,

$$\langle\chi|2\kappa u_{LS}^{-}u_{LS}^{+}\rangle \approx$$
$$2\kappa\frac{\mathrm{e}^{-\gamma r}}{\sqrt{r}}\left[\int_{-r/2}^{r/2}\chi^{-}(z_{-})u_{LS}^{-}(z_{-})\mathrm{e}^{\gamma z_{-}}\mathrm{d}z_{-}+\int_{-r/2}^{r/2}\chi^{+}(z_{+})\mathrm{e}^{-\gamma z_{+}}u_{LS}^{+}(z_{+})\mathrm{d}z_{+}\right], \tag{4.53}$$

i.e., $\langle\chi|2\kappa u_{LS}^{-}u_{LS}^{+}\rangle\approx 2\kappa\frac{\mathrm{e}^{-\gamma r}}{\sqrt{r}}I_1$, with I_1 as it was defined in the previous section. Proceeding in the same way with the other integrals from $\langle\chi|b\rangle=0$, we get

$$\dot{r}=A\frac{\mathrm{e}^{-\gamma r}}{\sqrt{r}}+B\frac{\mathrm{e}^{-2\gamma r}}{r}, \tag{4.54}$$

with A and B as in the previous section.

In Fig. 4.8 we present a curve fitting of $\dot{r}$ in function of r obtained numerically. The fitting was performed only considering the first term in Eq. (4.54), assuming that r is large.

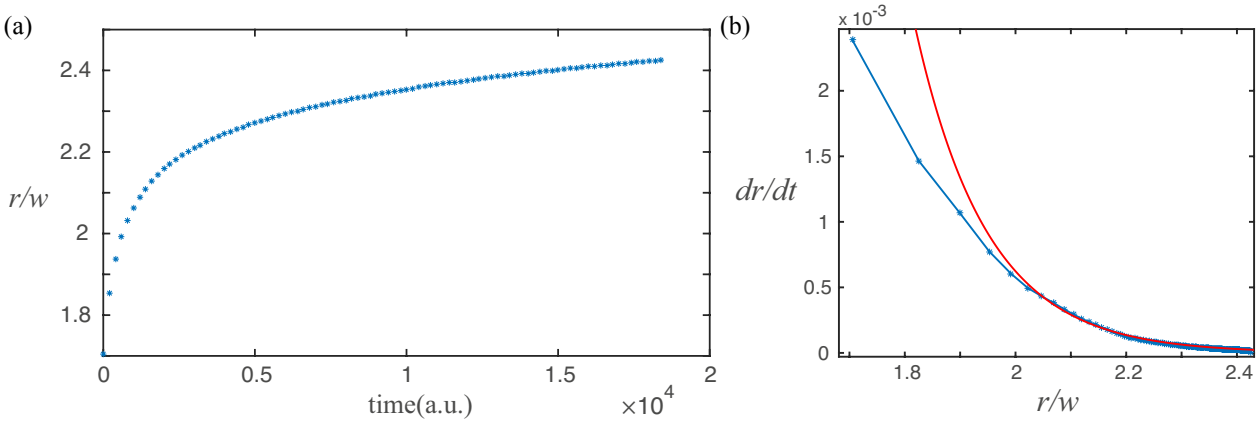

Figure 4.8: (a) Numerical data of the distance of separation r in function of time, in units of the width w. (b) Curve fitting of numerical data of $\dot{r}$ in function of r, using first term of Eq. (4.54). The distance r is normalized with the LSs width. The parameters used in simulations were $\eta=0.12,\kappa=0.6,\Delta=0.02,\Gamma=0.5,\alpha=0.125$, $\mathrm{d}x=\mathrm{d}y=0.3$ and $\mathrm{d}t=0.001$. The R^2 obtained was 0.9924.

4.2.3 Lattices of multiple two dimensional localized structures

Let us now study the evolution of multiple two-dimensional LSs. As in the one-dimensional case, the equilibrium is reached when the sum of the interactions acting on a LS is equal to zero. We consider this as particles interacting with repulsive forces decaying exponentially with the distance, and then, the equilibrium is reached when the sum of these forces vanish. In Fig. 4.9 we present some possible configurations in equilibrium.

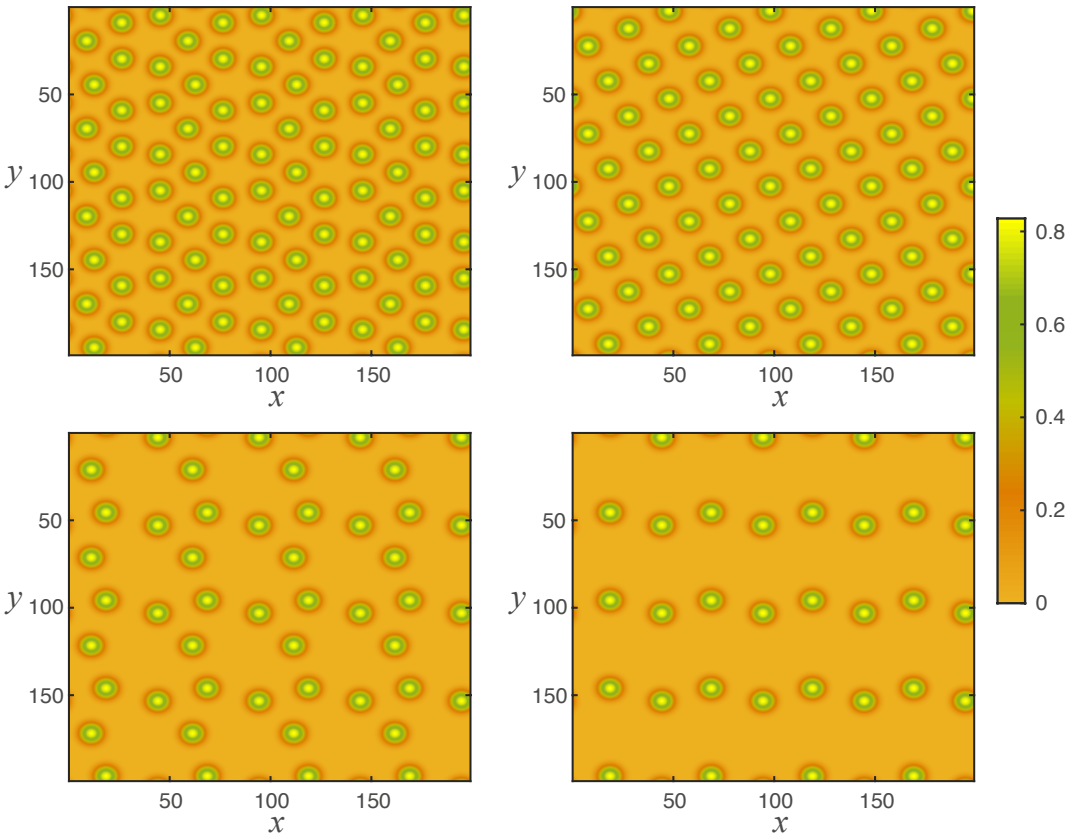

Figure 4.9: Different equilibrium configuration of two dimensional localized structures. We have used periodic boundary conditions. The parameters used were $\eta = 0.12, \kappa = 0.6, \Delta = 0.02, \Gamma = 0.5, \alpha = 0.125, \mathrm{d}x = \mathrm{d}y = 0.3$ and $\mathrm{d}t = 0.001$, with periodic boundary conditions.

Chapter 5

Diffraction grating in a zigzag lattice in nematic liquid crystals

This chapter serves as a complement of the calculations from the manuscript presented in Appendix D. In this work, we analyzed the diffraction grating produced by applying a laser beam to a nematic liquid crystal cell submitted to a voltage, which exhibits a zigzag instability (see Sec. 2.10.1) that varies with the applied signal. We investigated a theoretical model, based on Fraunhofer diffraction theory, to predict the different patterns observed. Our findings are in good agreement with experimental data.

5.1 Diffraction grating in an empty in-plane switching cell

In this section, we will derive in detail the diffraction profile of applying a laser beam to an empty IPS cell (without liquid crystal) presented in Section 3A of the manuscript. We will base our calculations on the Fraunhofer diffraction theory discussed in Sec. 2.9.

To start, let us consider the empty IPS cell (see Fig. 2.25 (a)) from the experiment. A sketch of its different components is shown in Fig. 5.1 (a). As a simple approximation, we consider the transmission coefficient of this cell as a periodic function, with its maximum value normalized to 1 ($t_{\max} = 1$) and restricted only to one dimension. This has the form[1]

$$t(x) = \begin{cases} \alpha & n\gamma < x < n\gamma + \frac{\gamma-\varepsilon}{2}, \\ 1 & n\gamma + \frac{\gamma-\varepsilon}{2} < x < n\gamma + \frac{\gamma+\varepsilon}{2}, \\ \alpha & n\gamma + \frac{\gamma+\varepsilon}{2} < x < (n+1)\gamma, \end{cases} \tag{5.1}$$

that is, it has period γ, which is the electrodes width. The zones where its value is α correspond where the electrodes are located. We consider a lattice composed by N electrodes, meaning that $0 \leq n \leq N-1$.

[1]Notice that the origin is different than in Appendix D article.

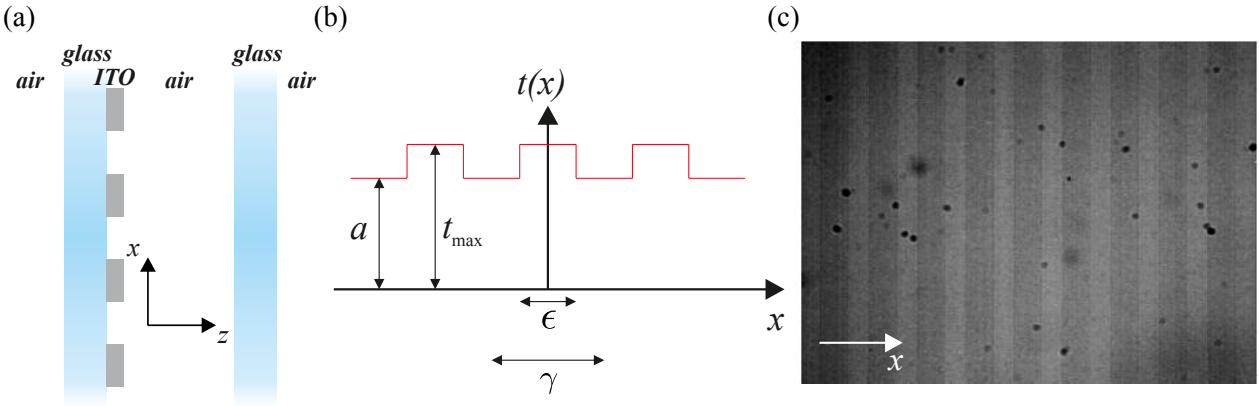

Figure 5.1: (a) Schematic representation of the different zones of the empty IPS cell. (b) One dimensional transmission coefficient model in x direction. (c) Cell picture taken from a microscope.

As we discussed in Sec. 2.9, the diffraction profile intensity is given by

$$I(u) = |E(u)|^2 = \left| \int_0^{N\gamma} t(x)\, \mathrm{e}^{-2\pi \mathrm{i} u x} \mathrm{d}x \right|^2 . \tag{5.2}$$

The integration includes the N electrodes. Since $t(x)$ is periodic, it is convenient to use Eq. (5.1) to write

$$\begin{aligned} E(u) &= \sum_{n=0}^{N-1} \left(\alpha \int_{\gamma n}^{n\gamma+\frac{\gamma-\varepsilon}{2}} + \int_{n\gamma+\frac{\gamma-\varepsilon}{2}}^{n\gamma+\frac{\gamma+\varepsilon}{2}} + \alpha \int_{n\gamma+\frac{\gamma+\varepsilon}{2}}^{(n+1)\gamma} \right) \mathrm{e}^{-2\pi \mathrm{i} u x} \mathrm{d}x \\ &= \sum_{n=0}^{N-1} \left(\alpha \int_{\gamma n}^{(n+1)\gamma} + (1-\alpha) \int_{n\gamma+\frac{\gamma-\varepsilon}{2}}^{n\gamma+\frac{\gamma+\varepsilon}{2}} \right) \mathrm{e}^{-2\pi \mathrm{i} u x} \mathrm{d}x. \end{aligned} \tag{5.3}$$

Then, solving the integrals, without performing the summation, we obtain

$$\begin{aligned} E(u) &= \sum_{n=0}^{N-1} \mathrm{e}^{-\pi \mathrm{i} u \gamma (2n+1)} \left(\alpha \frac{\sin \pi u \gamma}{\pi u} + (1-\alpha) \frac{\sin \pi u \varepsilon}{\pi u} \right) \\ &= \left(\alpha \frac{\sin \pi u \gamma}{\pi u} + (1-\alpha) \frac{\sin \pi u \varepsilon}{\pi u} \right) \mathrm{e}^{-\pi \mathrm{i} u \gamma} \sum_{n=0}^{N-1} \left(\mathrm{e}^{-\pi \mathrm{i} u \gamma 2} \right)^n . \end{aligned} \tag{5.4}$$

The last summation can be solved using $\sum_{n=0}^{N-1} x^n = (1-x^N)/(1-x)$. Therefore, after straightforward calculations we get

$$E(u) = \mathrm{e}^{-\pi \mathrm{i} u \gamma N} \frac{\sin \pi u \gamma N}{\sin \pi u \gamma} \left(\alpha \frac{\sin \pi u \gamma}{\pi u} + (1-\alpha) \frac{\sin \pi u \varepsilon}{\pi u} \right), \tag{5.5}$$

and so,

$$I(u) = \frac{\sin^2 \pi u \gamma N}{\sin^2 \pi u \gamma} \left[\alpha \gamma \,\mathrm{sinc}(\pi u \gamma) + (1-\alpha) \varepsilon \,\mathrm{sinc}(\pi u \varepsilon) \right]^2 , \tag{5.6}$$

where $\mathrm{sinc}(x) = \sin(x)/x$.

Notice that the exponential factor that appears in Eq. (5.5) is not relevant in $I(u)$ after applying the modulus. In fact, depending on the origin of our spatial system this factor can change, without affecting the final result. Also notice that if we set $\alpha = 0$, we recover the result from Sec. 2.9.2, the diffraction grating of N slits, as expected.

5.1.1 Diffraction orders

The diffraction orders correspond to the peaks of the irradiance $I(u)$. These are obtained by evaluating this function in $u = m/\gamma$, with m an integer number. However, remind that $u = \frac{\mathrm{d}}{\lambda f}$, where d is the spatial variable in the diffraction profile. Hence, the position of the mth diffraction order, with the origin at order 0, is given by

$$\mathrm{d}_m = m\frac{\lambda f}{\gamma}, \tag{5.7}$$

and so, the distance between them is

$$\Delta = \frac{\lambda f}{\gamma}. \tag{5.8}$$

Therefore, the diffraction orders distance increases with the light wavelength of the laser beam and the focal distance but decreases for higher values of α, the transmission coefficient of the cell ITO sections. This value is typically about some millimeters and coincides with experimental observations.

5.2 Diffraction grating in a perfect zigzag liquid crystal lattice

Let us now turn to analyze the case when the cell is filled with nematic liquid crystal and exhibits the zigzag instability. Using Fraunhofer diffraction theory we will derive in detail the two-dimensional irradiance $I(u, v)$ of a *perfect zigzag lattice*, that is, periodic in x and y directions, with constant amplitude and wavelength. This result was presented in Section 4A from Appendix D.

The perfect zigzag lattice at issue is shown in Fig. 5.2 (a), with c the period in the x direction and $2b$ in y direction. For simplicity, it will be assumed that the transmission coefficient $t(x, y)$ is 0 in the black zones, where the zigzag is formed, and normalized to 1 in the remaining area. Moreover, the white zones width will be a and θ the angle of the zigzag lines with the vertical axis y, as shown in the figure.

The transmission coefficient, as expected, will be periodic like the zigzag lattice, with the same periods in x and y. We choose our coordinate system origin in such a way that $t(x, y)$ be

$$t(x,y) = \begin{cases} 1, & cn - a/2 + |y - 2m|\tan\theta \leq x \leq cn + a/2 + |y - 2m|\tan\theta \\ & \qquad -b + 2bm \leq y \leq b + 2bm \\ 0, & \text{otherwise} \end{cases} \tag{5.9}$$

where $0 \leq n \leq N-1$ and $0 \leq m \leq M-1$. For some fixed $\{n, m\}$ values, the $t(x, y)$ profile is illustrated in Fig. 5.2 (b). This region is repeated along the zigzag lattice.

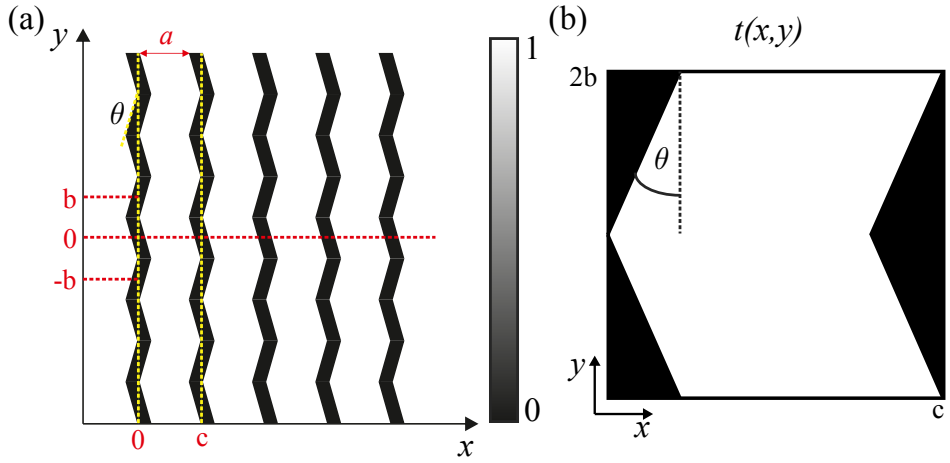

Figure 5.2: (a) Sketch of a perfect zigzag lattice, with constant amplitude and wavelength. (b) Transmission coefficient $t(x, y)$ values for some $\{n, m\}$ values.

As we have discussed, the diffraction grating profile is given by $I(u, v) = |E(u, v)|^2$, where

$$\begin{aligned} E(u,v) &= \int\int t(x,y)\mathrm{e}^{-2\pi\mathrm{i}(ux+vy)}\mathrm{d}x\mathrm{d}y \\ &= \sum_{n=0}^{N-1}\sum_{m=0}^{M-1}\int_{-b+2bm}^{b+2bm}\int_{cn-a/2+|y-2m|\tan\theta}^{cn+a/2+|y-2m|\tan\theta}\mathrm{e}^{-2\pi\mathrm{i}(ux+vy)}\mathrm{d}x\mathrm{d}y. \end{aligned} \tag{5.10}$$

The integral limits are the limits of Eq. (5.9). Performing the integration in x, yields to

$$E(u,v) = \sum_{n=0}^{N-1}\sum_{m=0}^{M-1}\mathrm{e}^{-2\pi\mathrm{i}ucn}\left(\frac{\sin\pi ua}{\pi u}\right)\int_{-b+2bm}^{b+2bm}\mathrm{e}^{-2\pi\mathrm{i}(vy+u|y-2m|\tan\theta)}\mathrm{d}y. \tag{5.11}$$

Then, under the change of variables $y' = y - 2bm$, we obtain

$$E(u,v) = \sum_{n=0}^{N-1}\sum_{m=0}^{M-1}\mathrm{e}^{-2\pi\mathrm{i}ucn}\left(\frac{\sin\pi ua}{\pi u}\right)\mathrm{e}^{-2\pi\mathrm{i}v2bm}\int_{-b}^{b}\mathrm{e}^{-2\pi\mathrm{i}(vy'+u|y'|\tan\theta)}\mathrm{d}y', \tag{5.12}$$

and performing the summations,

$$E(u,v) = \left(\frac{\sin\pi cuN}{\sin\pi cu}\right)\left(\frac{\sin\pi v2bM}{\sin\pi v2b}\right)\left(\frac{\sin\pi ua}{\pi u}\right)\int_{-b}^{b}\mathrm{e}^{-2\pi\mathrm{i}(vy'+u|y'|\tan\theta)}\mathrm{d}y'. \tag{5.13}$$

To remove the absolute value in y' of the remaining integral, we split it into two parts

$$\begin{aligned} &\int_{-b}^{b}\mathrm{e}^{-2\pi\mathrm{i}(vy'+u|y'|\tan\theta)}\mathrm{d}y' = \int_{-b}^{0}\mathrm{e}^{-2\pi\mathrm{i}y'(v-u\tan\theta)}\mathrm{d}y' + \int_{0}^{b}\mathrm{e}^{-2\pi\mathrm{i}y'(v+u\tan\theta)}\mathrm{d}y' \\ &= \mathrm{e}^{-b\pi\mathrm{i}u\tan\theta}\left(\mathrm{e}^{b\pi\mathrm{i}v}\frac{\sin(\pi b(v-u\tan\theta))}{\pi(v-u\tan\theta)} + \mathrm{e}^{-b\pi\mathrm{i}v}\frac{\sin(\pi b(v+u\tan\theta))}{\pi(v+u\tan\theta)}\right), \end{aligned} \tag{5.14}$$

finally obtaining,

$$
\begin{aligned}
E(u,v) =& ab\left(\frac{\sin\pi cuN}{\sin\pi cu}\right)\left(\frac{\sin\pi v2bM}{\sin\pi v2b}\right)\operatorname{sinc}(\pi ua) \\
&\times \mathrm{e}^{-b\pi \mathrm{i}u\tan\theta}\left(\mathrm{e}^{b\pi \mathrm{i}v}\operatorname{sinc}(\pi b(v-u\tan\theta)) + \mathrm{e}^{-b\pi \mathrm{i}v}\operatorname{sinc}(\pi b(v+u\tan\theta))\right)
\end{aligned}
\tag{5.15}
$$

and

$$
\begin{aligned}
I(u,v) = & \left[ab\left(\frac{\sin\pi cuN}{\sin\pi cu}\right)\left(\frac{\sin\pi v2bM}{\sin\pi v2b}\right)\operatorname{sinc}(\pi ua)\right]^2 \\
&\times [\operatorname{sinc}^2(\pi b(v-u\tan\theta)) + \operatorname{sinc}^2(\pi b(v+u\tan\theta)) \\
&+ 2\cos(\pi v2b)\operatorname{sinc}(\pi b(v-u\tan\theta))\operatorname{sinc}(\pi b(v+u\tan\theta))].
\end{aligned}
\tag{5.16}
$$

This formula predicts that in the Fourier space $\{u, v\}$ there are lines at θ degrees, as in the zigzag lattice.

The zigzag instability exhibits variations in amplitude and wavelength, depending on the voltage tension and frequency applied to the cell [6]. Then, the perfect zigzag lattice will not predict the observed patterns. To carry out this problem, in section 4B of the manuscript from Appendix D we consider an *imperfect zigzag lattice*, by perturbing the constant zigzag wavelength and width with randoms functions. Since it is not possible to obtain an analytical solution, in this case, we have obtained the diffraction grating by applying the $2D$ Fourier Transform to the imperfect zigzag lattice. The results are presented and discussed in Section 5 of Appendix D, concluding that this approximation based on the Fraunhofer diffraction theory allows us to explain qualitatively the different diffraction profiles.

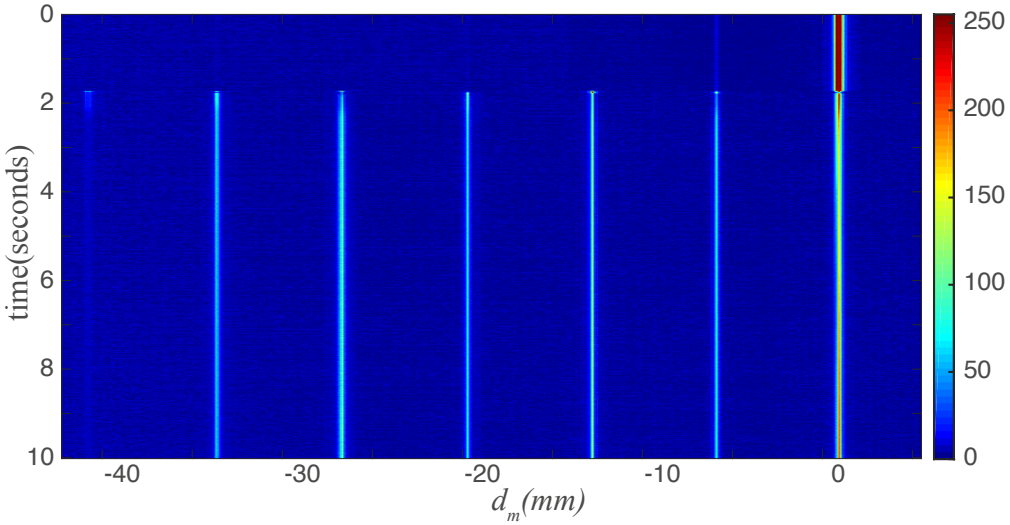

Figure 5.3: Spatiotemporal diagram of the diffraction grating for a square signal of 16 V_{pp} and 1 kHz. Around $t = 1.5$ seconds the generator is turned on. The distance is measured from the order 0. The intensity variation is notorious in order 0 and 6.

5.3 Diffraction grating temporal evolution

To conclude this chapter, let us complement our study by presenting how the light intensity of the diffraction grating changes over time when the generator is turned on.

When the generator connected to the IPS liquid crystal cell is turned on, we observe a temporal evolution in the diffraction grating intensity. This evolution is barely noticeable to the human eye. Processing the diffraction images, we observe that the diffraction orders intensity evolves in time tending to a constant value, in average, which depends on the generator signal features. In Fig. 5.3 we show the spatiotemporal evolution when the generator is turned on. We recognize two general behaviors presented in Figure 5.4 (b) and (c): the intensity can decrease or increase from its original value. Moreover, just when the signal is turned on, both cases show that the intensity performs a peak of short time before relaxing to a constant value. The noise showed in the intensities are attributed mainly to fluctuations in the laser beam.

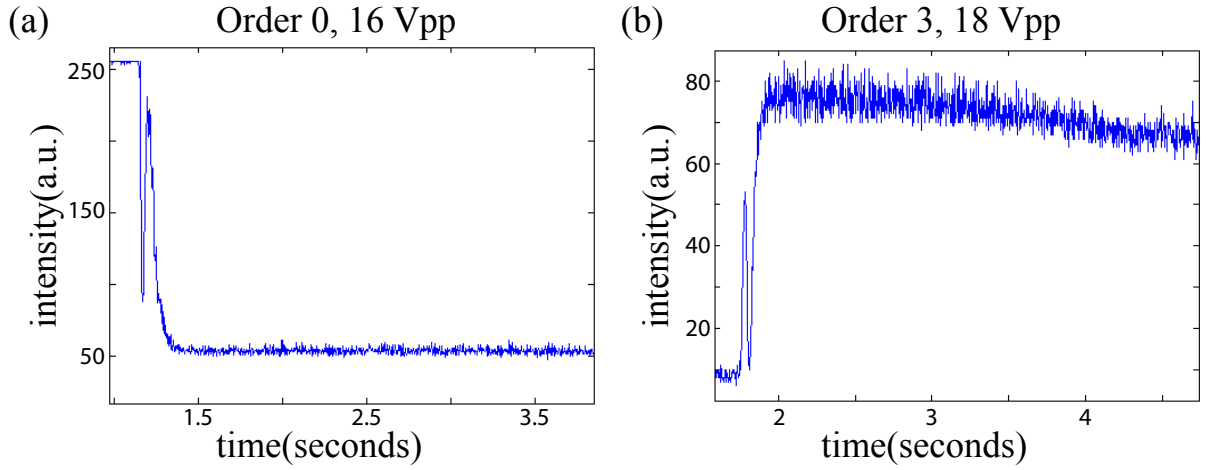

Figure 5.4: Plots (a) and (b) show the light intensity of diffraction orders 0 and 3 in function of time, for a applied signal of 16 V_{pp} and 18 V_{pp}, respectively. In both cases the signal is sinusoidal, with a frequency of 1 kHz.

Chapter 6

Conclusions

In the last three decades, considerable progress has been made in the understanding of localized structures. Thanks to fast computers, numerical simulations have allowed studying more deeply their properties, which has motivated the realization of many experiments for their observation and manipulation in a wide range of physical contexts. Several interesting behaviors of these structures have been discovered, with potential applications.

In this thesis, we have studied localized structures with particle-like properties in different contexts: coupled oscillators, vegetation, and optics. Our main goal has not been the understanding of their formation, but in the properties that arise because of their interaction or due to the presence of an external factor.

In the first context, coupled oscillators, we studied the effect of an external oscillatory parametric forcing and dissipation in kink solutions of the sine-Gordon equation, finding a new type of kinks, the *flaming kinks*. For simplicity the physical system considered was a chain of pendulums, with each pendulum coupled to its nearest neighbor with a linear spring. We found that these solutions are persistent under this forcing and that, contrary to our expectations, they exhibit resonant properties instead of parametric resonance. We demonstrate that the interaction between a flaming kink and a flaming antikink allows the formation of a family localized structures, with well-defined equilibrium widths. Furthermore, we also found that the flaming kinks are present in the ϕ^4 scalar field equation under the same kind of dissipation and parametric forcing, meaning that they correspond to a robust phenomenon. Using a perturbative analysis in this system we derived the dynamical equation that follows the width of the localized structures, with qualitatively good agreement with numerical observations. Moreover, we applied our results to a magnetic wire submitted to an external oscillatory magnetic field, which its magnetization is described by the Landau-Lifshitz-Gilbert equation. By simulating this equation, in a certain limit in the parameters, we verified the presence of flaming kinks. This is explained since this system is described by the parametrically driven and damped sine-Gordon equation in this limit.

In the second context under study, vegetation, we studied the interaction between particle-like localized structures, consisting in a localized amount of vegetation surrounded by bare soil. We were focused on studying the formation of stable lattices, i.e., arranges composed of

these structures. For that purpose we characterized the interaction dynamics between them through a perturbative analysis, finding good agreement with numerical data. We found that this interaction is indeed repulsive, that is, they tend to repel each other, which motivated us to consider this system as particles interacting by repulsive forces. Thus, the equilibrium of several localized structures located arbitrarily is reached when the sum of these forces is zero. We showed that in one dimension the equilibrium corresponds to periodic profiles, while in two dimensions it can take configuration with nontrivial symmetries. This can be understood since the interaction forces decay exponentially to zero with the distance, which makes more complex the possible equilibrium configurations. In every analysis performed we considered the one and two-dimensional cases. Furthermore, we showed that when a stable configuration is reached, and we remove a single localized structure, the system will rearrange to another stable configuration. This mechanism differs from the Turing instability used to explain pattern formation since in this case, a new localized structure appears after it is removed. We consider that the mechanism presented here is a more realistic view of the dynamics of localized patches in vegetation.

Finally, in the third context considered in this thesis, optics, we were focused on studying the effect of light applied to a zigzag interface instability, or more precisely, a transverse particle-like solution. This zigzag instability is produced in a nematic liquid crystal in-plane switching cell submitted to a generator, which is modified as the frequency and voltage tension are varied. We studied the diffraction grating produced by applying a laser beam to this interface, finding rich complex diffraction patterns. To explain the different profiles observed experimentally, we proposed a simple theoretical model based on the Fraunhofer diffraction theory. To test our model we first considered an empty cell, finding good agreement with experimental observations. Then, as a first approximation, we proposed a model for a perfect zigzag instability, that is, with constant width and wavelength, deriving analytically the diffraction intensity profile. As expected, it does not explain the diffraction grating observed. To carry out this problem we modified the perfect zigzag by adding aleatory functions to its wavelength and width. Since is not possible to make analytical calculations, in this case, the diffraction grating was calculated numerically by applying a two dimensional Fourier Transform, finding good agreement with the patterns observed. We consider that this work is a proof of concept of manipulable diffraction gratings, which could open the possibility of new optical data processing.

Bibliography

[1] http://geoblog.weebly.com/environmental-sciences-blog/announcement-plants-patterns-and-climate-change.

[2] http://maginams.ca/australia-spinifex/.

[3] Mark J Ablowitz and Peter A Clarkson. *Solitons, nonlinear evolution equations and inverse scattering*, volume 149. Cambridge university press, 1991.

[4] Mark J Ablowitz and Harvey Segur. *Solitons and the inverse scattering transform*. SIAM, 1981.

[5] Thorsten Ackemann, WilliamJ Firth, and Gian-Luca Oppo. Fundamentals and applications of spatial dissipative solitons in photonic devices. *Advances in atomic, molecular, and optical physics*, 57:323–421, 2009.

[6] I Andrade-Silva, MG Clerc, and Vincent Odent. Zig-zag wall lattice in a nematic liquid crystal with an in-plane switching configuration. *Physical Review E*, 90(2):022504, 2014.

[7] Aleksandr Aleksandrovich Andronov, Semen Emmanuilovich Khaikin, and Aleksandr Adolfovich Vitt. *Theory of oscillators*. Dover, 1966.

[8] Bevan B Baker and Edward Thomas Copson. *The mathematical theory of Huygens' principle*, volume 329. American Mathematical Soc., 2003.

[9] Carl M Bender and Steven A Orszag. *Advanced mathematical methods for scientists and engineers I: Asymptotic methods and perturbation theory*. Springer Science & Business Media, 2013.

[10] D Blair, IS Aranson, GW Crabtree, V Vinokur, LS Tsimring, and C Josserand. Patterns in thin vibrated granular layers: Interfaces, hexagons, and superoscillons. *Physical Review E*, 61(5):5600, 2000.

[11] Peter Blomgren, Scott Gasner, and Antonio Palacios. Hopping behavior in the kuramoto–sivashinsky equation. *Chaos: An Interdisciplinary Journal of Nonlinear Science*, 15(1):013706, 2005.

[12] Immanuel M Bomze. Lotka-volterra equation and replicator dynamics: a two-dimensional classification. *Biological cybernetics*, 48(3):201–211, 1983.

[13] Ignacio Bordeu, Marcel G Clerc, Piere Couteron, René Lefever, and Mustapha Tlidi. Self-replication of localized vegetation patches in scarce environments. *Scientific Reports*, 6, 2016.

[14] Edmond Bour. *Théorie de la déformation des surfaces*. 1861.

[15] Oleg M Braun and Yuri Kivshar. *The Frenkel-Kontorova model: concepts, methods, and applications*. Springer Science & Business Media, 2013.

[16] Eugene I Butikov. On the dynamic stabilization of an inverted pendulum. *American Journal of Physics*, 69(7):755–768, 2001.

[17] Eugene I Butikov. Subharmonic resonances of the parametrically driven pendulum. *Journal of Physics A: Mathematical and General*, 35(30):6209, 2002.

[18] David K Campbell, Jonathan F Schonfeld, and Charles A Wingate. Resonance structure in kink-antikink interactions in $\varphi 4$ theory. *Physica D: Nonlinear Phenomena*, 9(1-2):1–32, 1983.

[19] Sivaramakrishna Chandrasekhar. Liquid crystals. 1977.

[20] S-N Chow and Jack K Hale. *Methods of bifurcation theory*, volume 251. Springer Science & Business Media, 2012.

[21] Marcel G Clerc, Pablo C Encina, and Enrique Tirapegui. Shilnikov bifurcation: stationary quasi-reversal bifurcation. *International Journal of Bifurcation and Chaos*, 18(07):1905–1915, 2008.

[22] MG Clerc, D Escaff, and VM Kenkre. Patterns and localized structures in population dynamics. *Physical Review E*, 72(5):056217, 2005.

[23] MG Clerc, D Escaff, and VM Kenkre. Analytical studies of fronts, colonies, and patterns: combination of the allee effect and nonlocal competition interactions. *Physical Review E*, 82(3):036210, 2010.

[24] P Coullet, C Riera, and Ch Tresser. Stable static localized structures in one dimension. *Physical review letters*, 84(14):3069, 2000.

[25] Mark C Cross and Pierre C Hohenberg. Pattern formation outside of equilibrium. *Reviews of modern physics*, 65(3):851, 1993.

[26] Jesús Cuevas-Maraver, Panayotis Kevrekidis, and Floyd Williams. *The sine-Gordon model and its applications: From pendula and Josephson Junctions to Gravity and High-Energy Physics*, volume 10. Springer, 2014.

[27] Jonathan HP Dawes. After 1952: The later development of alan turing's ideas on the mathematics of pattern formation. *Historia Mathematica*, 43(1):49–64, 2016.

[28] Pierre-Gilles De Gennes and Richard Alben. The physics of liquid crystals, 1975.

[29] Orazio Descalzi, Mederic Argentina, and Enrique Tirapegui. Saddle-node bifurcation: Appearance mechanism of pulses in the subcritical complex ginzburg-landau equation. *Physical Review E*, 67(1):015601, 2003.

[30] Orazio Descalzi, Marcel G Clerc, Stefania Residori, and Gaetano Assanto. *Localized states in physics: solitons and patterns*. Springer Science & Business Media, 2011.

[31] Orazio Descalzi, Pablo Gutiérrez, and Enrique Tirapegui. Localized structures in nonequilibrium systems. *International Journal of Modern Physics C*, 16(12):1909–1916, 2005.

[32] Peter Deuflhard. *Newton methods for nonlinear problems: affine invariance and adaptive algorithms*, volume 35. Springer Science & Business Media, 2011.

[33] C Elphick, E Tirapegui, ME Brachet, P Coullet, and G Iooss. A simple global characterization for normal forms of singular vector fields. *Physica D: Nonlinear Phenomena*, 29(1-2):95–127, 1987.

[34] Leonhard Euler. De novo genere oscillationum. *Comment. acad. sc. Petrop*, 11(1739):128–149, 1750.

[35] Brian P Flannery, William H Press, Saul A Teukolsky, and William Vetterling. Numerical recipes in c. *Press Syndicate of the University of Cambridge, New York*, 24, 1992.

[36] Thor Fossen and Henk Nijmeijer. *Parametric resonance in dynamical systems*. Springer Science & Business Media, 2011.

[37] Grant R Fowles. *Introduction to modern optics*. Courier Corporation, 1975.

[38] Ivar Fredholm. Sur une classe d?équations fonctionnelles. *Acta mathematica*, 27(1):365–390, 1903.

[39] MG Friedel. *Les États Mésamorphes de la matière*. 1922.

[40] Galileo Galilei, Andrea Frova, and Mariapiera Marenzana. *Thus spoke Galileo: the great scientist's ideas and their relevance to the present day*. Oxford University Press, 2006.

[41] George Francis Gause. *The struggle for existence*. Courier Corporation, 2003.

[42] VB Glasko, F Leriust, Ia P Terletskii, and SF Shushurin. An investigation of particle-like solutions of a nonlinear scalar field equation. *SOVIET PHYSICS JETP-USSR*, 8(2):312–315, 1959.

[43] Roy H Goodman and Richard Haberman. Kink-antikink collisions in the phi^ 4 equation: The n-bounce resonance and the separatrix map. *SIAM Journal on Applied Dynamical Systems*, 4(4):1195–1228, 2005.

[44] P Greig-Smith. Pattern in vegetation. *The Journal of Ecology*, pages 755–779, 1979.

[45] Eugene P Gross. Particle-like solutions in field theory. *Annals of Physics*, 19(2):219–233, 1962.

[46] A Hagberg, A Yochelis, H Yizhaq, C Elphick, L Pismen, and E Meron. Linear and nonlinear front instabilities in bistable systems. *Physica D: Nonlinear Phenomena*, 217(2):186–192, 2006.

[47] Eugene Hecht. Optics, schaum's outline series, 1975.

[48] PL Kapitza. Collected papers of pl kapitza, edited by d. terharr, 1965.

[49] Tosio Kato. *Perturbation theory for linear operators*, volume 132. Springer Science & Business Media, 2013.

[50] JD Kelley, GH Gunaratne, A Palacios, and J Shulman. Modal decomposition and normal form for hydrodynamic flows: Examples from cellular flame patterns. *The European Physical Journal Special Topics*, 204(1):119–131, 2012.

[51] Iam-Choon Khoo. *Liquid crystals: physical properties and nonlinear optical phenomena*, volume 64. John Wiley & Sons, 2007.

[52] Yuri S Kivshar and Boris A Malomed. Dynamics of solitons in nearly integrable systems. *Reviews of Modern Physics*, 61(4):763, 1989.

[53] E Knobloch and KA Wiesenfeld. Bifurcations in fluctuating systems: The center-manifold approach. *Journal of Statistical Physics*, 33(3):611–637, 1983.

[54] T Kontorova and J Frenkel. On the theory of plastic deformation and twinning. ii. *Zh. Eksp. Teor. Fiz.*, 8:1340–1348, 1938.

[55] Krishna Kumar. Linear theory of faraday instability in viscous liquids. In *Proceedings of the Royal Society of London A: Mathematical, Physical and Engineering Sciences*, volume 452, pages 1113–1126. The Royal Society, 1996.

[56] Yuri A Kuznetsov. *Elements of applied bifurcation theory*, volume 112. Springer Science & Business Media, 2013.

[57] GL Lamb. Analytical descriptions of ultrashort optical pulse propagation in a resonant medium. *Reviews of Modern Physics*, 43:99–124, 1971.

[58] George L Lamb Jr. Elements of soliton theory. *New York, Wiley-Interscience, 1980. 300 p.*, 1980.

[59] LD Landau and EM Lifshitz. Mechanics, vol. 1. *Course of theoretical physics*, pages 84–93, 1976.

[60] Peter D Lax. Integrals of nonlinear equations of evolution and solitary waves. *Communications on pure and applied mathematics*, 21(5):467–490, 1968.

[61] René Lefever, Nicolas Barbier, Pierre Couteron, and Olivier Lejeune. Deeply gapped vegetation patterns: on crown/root allometry, criticality and desertification. *Journal of Theoretical Biology*, 261(2):194–209, 2009.

[62] René Lefever and Olivier Lejeune. On the origin of tiger bush. *Bulletin of Mathematical biology*, 59(2):263–294, 1997.

[63] Olivier Lejeune, Pierre Couteron, and René Lefever. Short range co-operativity competing with long range inhibition explains vegetation patterns. *Acta Oecologica*, 20(3):171–183, 1999.

[64] Olivier Lejeune, Mustapha Tlidi, and Pierre Couteron. Localized vegetation patches: a self-organized response to resource scarcity. *Physical Review E*, 66(1):010901, 2002.

[65] Philip K Maini, Hans G Othmer, et al. *Mathematical models for biological pattern formation*. Springer, 2001.

[66] Nicholas Manton and Paul Sutcliffe. *Topological solitons*. Cambridge University Press, 2004.

[67] Vladimir Aleksandrovich Marchenko. *Sturm-Liouville operators and applications*, volume 373. American Mathematical Soc., 2011.

[68] Jerry B Marion. *Classical dynamics of particles and systems*. Academic Press, 2013.

[69] Isaak D Mayergoyz, Giorgio Bertotti, and Claudio Serpico. *Nonlinear magnetization dynamics in nanosystems*. Elsevier, 2009.

[70] Norman W McLachlan. Theory and application of mathieu functions. 1951.

[71] David W McLaughlin and Alwyn C Scott. Perturbation analysis of fluxon dynamics. *Physical Review A*, 18(4):1652, 1978.

[72] J-C Menaut, B Walker, David J Tongway, Christian Valentin, and Josiane Seghieri. *Banded vegetation patterning in arid and semiarid environments: ecological processes and consequences for management*, volume 149. Springer Science & Business Media, 2001.

[73] Ehud Meron, Erez Gilad, Jost von Hardenberg, Moshe Shachak, and Yair Zarmi. Vegetation patterns along a rainfall gradient. *Chaos, Solitons & Fractals*, 19(2):367–376, 2004.

[74] HJ Mikeska. Solitons in a one-dimensional magnet with an easy plane. *Journal of Physics C: Solid State Physics*, 11(1):L29, 1978.

[75] M Nakhla and Jiri Vlach. A piecewise harmonic balance technique for determination of periodic response of nonlinear systems. *IEEE Transactions on Circuits and Systems*, 23(2):85–91, 1976.

[76] A Ostermann and M Roche. Runge-kutta methods for partial differential equations and fractional orders of convergence. *Mathematics of computation*, 59(200):403–420, 1992.

[77] Edward Ott. *Chaos in dynamical systems*. Cambridge university press, 2002.

[78] José-Philippe Pérez and Maurice Françon. *Optique: fondements et applications avec 200 exercices et problèmes résolus/J.-P. Pérez; préf. de Maurice Françon*. Masson, 2000.

[79] Michael E Peskin, Daniel V Schroeder, and Emil Martinec. An introduction to quantum field theory, 1996.

[80] Len M Pismen. *Patterns and interfaces in dissipative dynamics*. Springer Science & Business Media, 2006.

[81] Henri Poincaré. Sur l'équilibre d'une masse fluide animée d'un mouvement de rotation. *Acta mathematica*, 7(1):259–380, 1885.

[82] S Neil Rasband. *Chaotic dynamics of nonlinear systems*. Courier Dover Publications, 2015.

[83] Michel Remoissenet. *Waves called solitons: concepts and experiments*. Springer Science & Business Media, 2013.

[84] Reinhard Richter and IV Barashenkov. Two-dimensional solitons on the surface of magnetic fluids. *Physical review letters*, 94(18):184503, 2005.

[85] Juan R Sanmartin. O botafumeiro: Parametric pumping in the middle ages. *American Journal of Physics*, 52(10):937–945, 1984.

[86] Gordon D Smith. *Numerical solution of partial differential equations: finite difference methods*. Oxford university press, 1985.

[87] Steven H Strogatz. *Nonlinear dynamics and chaos: with applications to physics, biology, chemistry, and engineering*. Westview press, 2014.

[88] Ju Swift and Pierre C Hohenberg. Hydrodynamic fluctuations at the convective instability. *Physical Review A*, 15(1):319, 1977.

[89] Mustapha Tlidi, Miltos Georgiou, and Paul Mandel. Transverse patterns in nascent optical bistability. *Physical Review A*, 48(6):4605, 1993.

[90] Mustapha Tlidi, René Lefever, and Andrei Vladimirov. On vegetation clustering, localized bare soil spots and fairy circles. In *Dissipative Solitons: From Optics to Biology and Medicine*, pages 1–22. Springer, 2008.

[91] Mustapha Tlidi, Majid Taki, and Theodore Kolokolnikov. Introduction: Dissipative localized structures in extended systems, 2007.

[92] Alan Mathison Turing. The chemical basis of morphogenesis. *Bulletin of mathematical biology*, 52(1-2):153–197, 1990.

[93] Paul B Umbanhowar, Francisco Melo, and Harry L Swinney. Localized excitations in a vertically vibrated granular layer. *Nature*, 382(6594):793, 1996.

[94] Paul B Umbanhowar, Francisco Melo, and Harry L Swinney. Periodic, aperiodic, and transient patterns in vibrated granular layers. *Physica A: Statistical Mechanics and its Applications*, 249(1):1–9, 1998.

[95] Tanmay Vachaspati. *Kinks and domain walls: An introduction to classical and quantum solitons*. Cambridge University Press, 2006.

[96] Balth van der Pol and MJO Strutt. Ii. on the stability of the solutions of mathieu's equation. *The London, Edinburgh, and Dublin Philosophical Magazine and Journal of Science*, 5(27):18–38, 1928.

[97] Alexander Vilenkin. Cosmic strings and domain walls. *Physics reports*, 121(5):263–315, 1985.

[98] Herbert Weigel. *Chiral soliton models for baryons*, volume 743. Springer, 2007.

[99] Pochi Yeh and Claire Gu. *Optics of liquid crystal displays*, volume 67. John Wiley & Sons, 2010.

[100] Konstantin G Zloshchastiev. Nonminimal particle-like solutions in cubic scalar field theory. *Physics Letters B*, 450(4):397–404, 1999.

Appendix A

Flaming 2π kinks in parametrically driven systems

In this appendix we introduce flaming kinks in the sine-Gordon equation in the context of driven coupled oscillators and driven magnetic wire.

Publication details:

- Title: Flaming 2π kinks in parametrically driven systems.
- Authors: E. Berrios-Caro, M. G. Clerc and A. O. León.
- Publication date: 23 November 2016.
- Published in Physical Review E.
- DOI: https://journals.aps.org/pre/abstract/10.1103/PhysRevE.94.052217

Flaming 2π kinks in parametrically driven systems

E. Berrios-Caro,[1] M. G. Clerc,[1] and A. O. Leon[2]
[1]*Departamento de Física, Facultad de Ciencias Físicas y Matemáticas, Universidad de Chile, Casilla 487-3, Santiago, Chile*
[2]*Institute for Materials Research, Tohoku University, Sendai 980-8577, Japan*
(Received 10 July 2016; revised manuscript received 25 October 2016; published 23 November 2016)

Macroscopic extended systems with dissipation and injection of energy can exhibit particlelike solutions. Dissipative kinks with an oscillatory cloak and a family of localized states that connect uniform symmetric states in a magnetic wire forced with a transversal oscillatory magnetic field and in a parametrically driven damped pendula chain are studied. The oscillatory cloak is composed of evanescent waves emitted at the kink position and generated by a resonant mechanism. These waves mediate the kink interaction and generate a family of localized states.

DOI: 10.1103/PhysRevE.94.052217

I. INTRODUCTION

Macroscopic particlelike solutions in extended dissipative systems have been observed in different fields, such as domains in magnetic materials, chiral bubbles in liquid crystals, interfaces in chemical reactions, kinks in granular media, fronts in populations dynamics, liquid crystals, and nonlinear optics, among others [1–3]. Hence, one can infer the universality of particlelike solutions in nonequilibrium systems [4]. Although these states are spatially extended, they exhibit properties typically associated with particles. Consequently, one can characterize them with a family of continuous parameters such as the position and the core width. A natural strategy to obtain these solutions would be to integrate the systems under small variations corresponding to energy dissipation [5]. These types of systems are termed "quasireversible" [6]. Since integrable systems exhibit natural frequencies, a way to force these systems is through temporal modulation of parameters that characterize the system under study. This type of forcing is called parametric [7]. In the past few decades, scientific efforts were focused on improving our understanding of kinks [8]. These solutions are characterized by connecting two equivalent symmetric states. Methods such as variation of parameters and inverse scattering have played a key role in understanding the dynamics of particlelike solutions. However, for dissipative systems—with large injection and dissipation of energy—the dynamic characterization of particlelike solutions remains an open question.

The aim of this article is to study dissipative kinks with an oscillatory cloak and a family of localized states that connect uniform symmetric states. We consider two physical systems that exhibit these structures, namely a magnetic wire forced with a transversal oscillatory magnetic field, and a parametrically driven damped pendula chain. These kink solutions are characterized by the emission of evanescent waves from the front position (cf. Fig. 1). Using an analogy of hopping pattern behavior observable in combustion carried out under controlled conditions [9,10], we consider that propagation of evanescent waves observed in our simulations could be, for want of a more descriptive name, referred to as "*flaming* 2π *kinks*." The oscillatory cloaks are generated by a resonance mechanism between the natural frequency and external forcing. These evanescent waves mediate the kink interaction and generate a family of localized states.

II. FLAMING 2π KINKS IN PARAMETRICALLY DRIVEN MAGNETIC WIRE

The dynamics of ferromagnetic wires are characterized by the normalized magnetization $\mathbf{m}(t,z)$ [11], where $\{z,t\}$ account for the spatial coordinate along the wire and time, respectively. A one-dimensional easy-plane ferromagnetic macroscopic wire is described by the dimensionless Landau-Lifshitz-Gilbert equation [11],

$$\partial_t \mathbf{m} = -\mathbf{m} \times (h\mathbf{e}_x - \beta m_z \mathbf{e}_z + \partial_{zz}\mathbf{m} - \alpha \partial_t \mathbf{m}), \qquad (1)$$

where $\{\mathbf{e}_x,\mathbf{e}_y,\mathbf{e}_z\}$ are the unit vectors along the respective Cartesian axes, $\beta > 0$ accounts for the anisotropy of the wire and it favors configurations where the magnetization lies on the xy plane, the term proportional to α is a Rayleigh-like dissipation function known as Gilbert damping, and it accounts for energy losses, h is the dimensionless intensity of the external magnetic field in the x direction, and the term $\partial_{zz}\mathbf{m}$ corresponds to the Laplacian operator accounting for short-range magnetic interactions [11]. To get an idea of the magnitude of the parameters, for example for $CsNiF_3$, $|\mathbf{m}| \approx 2.2 \times 10^5$ A/m, $\beta \approx 39$, temporal and spatial scales are around 20 ps and 5 nm, and the dissipation parameter is of the order $\alpha \approx 0.02$ [12].

For a positive external field, $h > 0$, the stable equilibrium of the system is the magnetization pointing along the magnetic field, $\mathbf{m} = \mathbf{e}_x$, a magnetization vector aligned with the vertical axis [see Fig. 1(a)]. Perturbations around this equilibrium are characterized by a natural frequency $\omega_0 = \sqrt{h\beta}$ [13]. The dissipation can be counterbalanced by considering a combination of a constant and an oscillatory external magnetic field, $h(t) = H_0 + h_0 \cos(\omega t)$. Notice that the dynamics of the above model (1) conserve the norm of $\mathbf{m}$. Hence, spherical coordinates are an adequate representation to describe the magnetic dynamics of the driven wire. This system has kink solutions. The orientation of magnetization vectors creates a marked spatial pattern: at the left and right ends of the chain, magnetization vectors are predominantly directed along the external field, while at the central part of the chain they undergo a complete rotation, clearly revealing the presence of a kink solution [8]. Figure 1 shows a schematic representation of the magnetic kink solution. Here the spatiotemporal evolution and magnetization components of this particlelike solution were obtained from numerical simulations of Eq. (1). Numerical

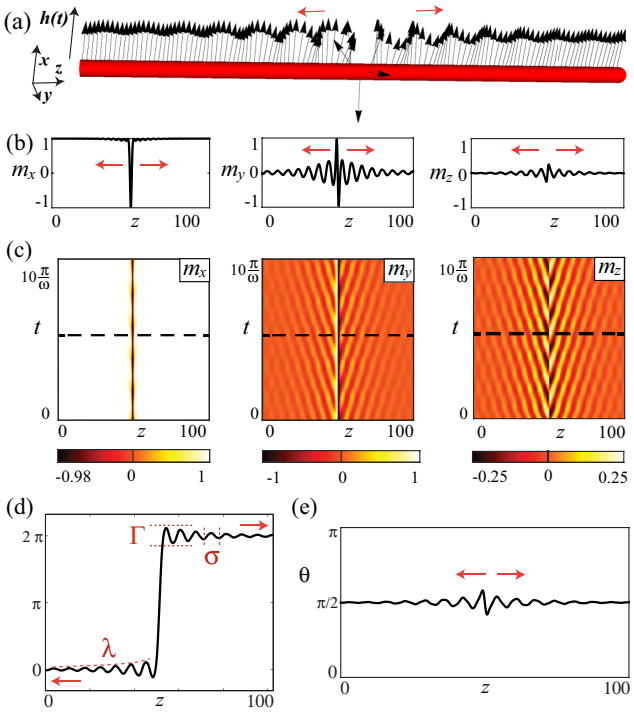

FIG. 1. Flaming 2π kink in a parametrically driven magnetic wire obtained from numerical simulation of Eq. (1) with $h(t) = H_0 + h_0\cos(\omega t)$, $H_0 = 2$, $h_0 = 0.8$, $\omega = 6$, $\beta = 10$, and $\alpha = 0.02$. (a) Schematic representation of magnetization $\mathbf{m}(z)$ upon a driven magnetic wire. (b) Magnetization components of the flaming magnetic kink. (c) Spatiotemporal evolution of the flaming kink. The horizontal dashed line in the diagrams shows the time when the images of (b) were obtained. (d) Corresponding ϕ profile in the spherical representation of the magnetization. $\{\Gamma,\sigma,\lambda\}$ are the amplitude, wavelength, and steepness of the evanescent wave, respectively. (e) Corresponding θ profile in the spherical representation of the magnetization.

simulations were conducted using the fifth-order Runge-Kutta method scheme for temporal integration, finite differences of sixth order for spatial discretization, and Neumann boundary conditions ($\partial_z m = 0$ at the borders). From the spatiotemporal evolution, we can infer that the kink solution is characterized by the emission of evanescent waves from the front position (see Fig. 1). In the quasireversible limit, these waves disappear [5].

To study in detail the flaming kinks, we consider the following spherical representation for magnetization vector $\mathbf{m} = \sin(\theta)[\cos(\phi)\mathbf{e}_x + \sin(\phi)\mathbf{e}_y] + \cos(\theta)\mathbf{e}_z$. In this representation, the magnetization is described by the polar $\theta(t,z)$ and azimuthal $\phi(t,z)$ angles [see Figs. 1(d) and Fig. 1(e)]. When the magnetic anisotropy coefficient is large enough ($\beta \gg 1$), the magnetization vector is located mainly in the xy plane, and the magnetic field acts in the same way as gravity for coupled mechanical oscillators [14,15]. In addition, let us consider small dissipation, an external field, and the scaling relations $|\theta - \pi/2| \sim \alpha \sim h \sim \partial_{zz}\phi \sim 1/\beta \ll 1$ and $\phi \sim \partial_t\phi \sim 1$. Using a spherical representation and this scaling in Eq. (1), one finds at leading order that the polar angle becomes a slave variable $\theta[\phi] \approx \pi/2 + \partial_t\phi/\beta$, and the

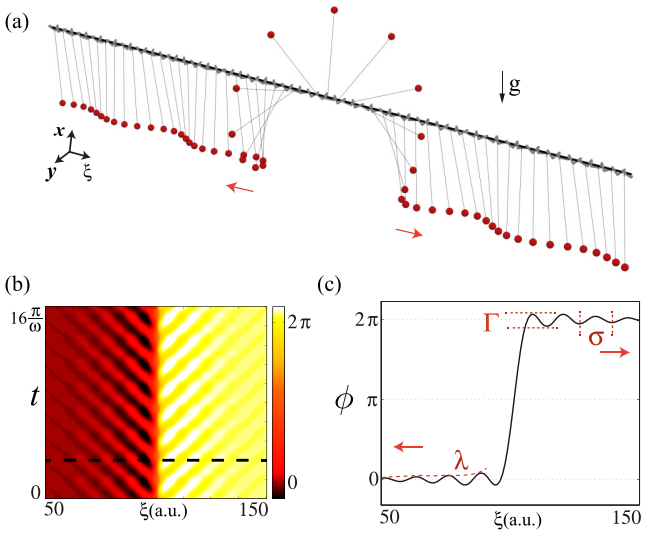

FIG. 2. Flaming 2π kink in a vertically driven chain of coupled pendula obtained from numerical simulation of Eq. (2) with $\omega_0^2(t) = \omega_0^2 + \gamma\cos(\omega t)$, $\omega_0^2 = 1$, $\gamma = 0.3$, $\omega = 1.4$, and $\mu = 0.1$. (a) Schematic representation of a vertically driven dissipative chain of coupled pendula. (b) Spatiotemporal evolution of a motionless flaming kink. (c) Profile of a flaming kink; $\{\Gamma,\sigma,\lambda\}$ are the amplitude, wavelength, and steepness of the evanescent wave, respectively.

azimuthal angle satisfies [14]

$$\partial_{tt}\phi = -\omega_0^2(t)\sin(\phi) + \partial_{\xi\xi}\phi - \mu\partial_t\phi, \tag{2}$$

where $\mu \equiv \alpha\beta$, $\xi \equiv z/\beta^{1/2}$ is a normalized spatial coordinate, and $\omega_0^2(t) = \beta H_0 + \beta h_0\cos(\omega t)$. The aforementioned model stands for a vertically driven dissipative chain of coupled pendula [16]. The parameters $\{\omega_0 \equiv \beta H_0, \gamma \equiv \beta h_0, \mu\}$ account for the natural frequency, the amplitude of the applied force, and the oscillation damping coefficient. Hence, the parametric-driven dissipative sine-Gordon model produces results that considerably resemble the magnetization dynamics in a magnetic chain described with the Landau-Lifshitz-Gilbert equation.

In the next section, we introduce a pendula chain. This set of coupled oscillators is well-described by the sine-Gordon model.

III. FLAMING 2π KINKS IN A PARAMETRICALLY DRIVEN PENDULA CHAIN

Let us consider a plane pendulum of length l_0. The pendulum oscillates in the x-y plane in the presence of gravitation acceleration g pointing along $-\mathbf{e}_x$, as illustrated in Fig. 2. The mechanical motion is governed by $d_{tt}\phi = -\omega_0^2\sin(\phi) - \mu d_t\phi$, where the natural frequency is $\omega_0^2 = g/l_0$, and the damping parameter μ accounts for dissipation. Notice that the above equation is the same as Eq. (2) when the magnetization is uniform, $\partial_{zz}\mathbf{m} = \mathbf{0}$. In the pendulum, as well as in the magnetic system, the angle ϕ accounts for the dynamics in the xy plane. On the other hand, the polar angle of the magnetization vector, $\theta = \arccos(m_z)$, is related to the angular velocity of the pendulum, $\beta(\theta - \pi/2) \approx \partial_t\phi$.

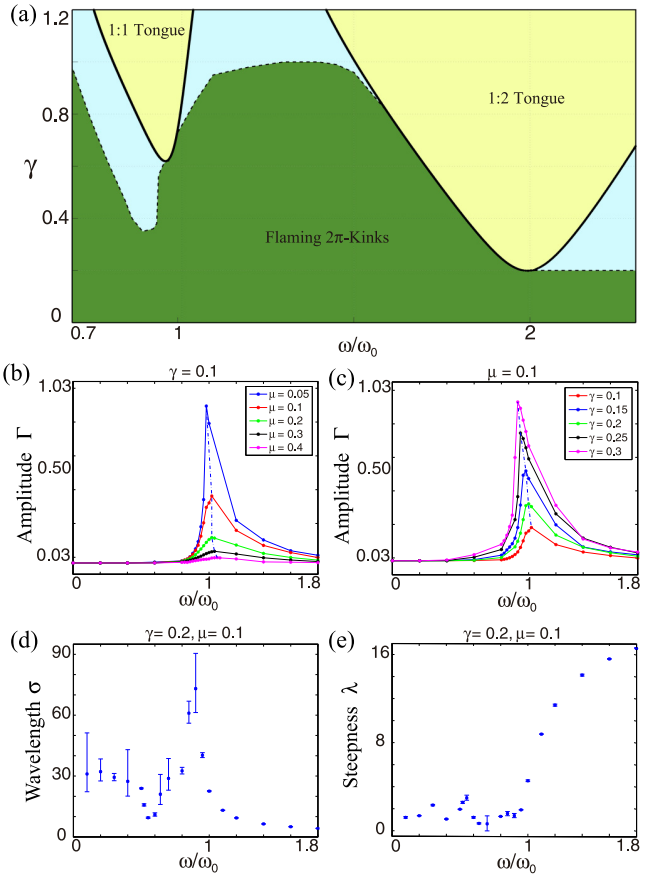

FIG. 3. Characterization of a flaming 2π kink for a vertically driven chain of pendula with $\beta H_0 = 1$. (a) Phase space as a function of frequency and amplitude forcing with $\mu = 0.1$. The tongues account for the strong resonances (1 : 1 and 1 : 2). The flaming 2π kinks are observed in the dark region. (b) Amplitude of evanescent waves Γ as a function of forcing frequency by different dissipation coefficients and forcing intensities (c). Wavelength σ (d) and steepness λ (e) of evanescent waves as a function of frequency forcing ω.

A pendula chain is a system composed of several of the oscillators described above, where each one of them couples to its neighbors by torsion springs, as shown in Fig. 2(a). In the continuum limit, the linear coupling between a pendulum and its neighborhood is written in terms of a Laplacian operator, $\partial_{\xi\xi}\phi$. The torsion spring mechanism is equivalent to the short-range magnetic interaction that couples magnetic moments in ferromagnetic materials. This system in the continuum limit is described by the sine-Gordon model Eq. (2).

Numerical simulations of the sine-Gordon Eq. (2), for small forcing intensities and large dissipation, exhibit 2π kink solutions, that is, the zero equilibrium is connected with the 2π state [8]. Figure 2 shows a schematic representation, a spatiotemporal evolution, and a profile of a flaming 2π kink observed in a vertically driven dissipative chain of coupled pendula. The evanescent waves are well characterized by an amplitude Γ, a steepness λ, and a wavelength σ [see Fig. 2(b)]. Notice there is a good agreement between flaming 2π kinks observed in a forced magnetic wire and a forced chain of pendula. Figure 3(a) illustrates the region of parameter space where the flaming 2π kinks are observed. This region was obtained numerically from Eq. (2) by the persistence of the flaming 2π kink under the small modification of the parameters. From this figure, one can conclude that the flaming 2π kinks are observed in a wide range of frequencies and forcing amplitudes.

To identify the mechanism of flaming 2π kinks, we have computed the amplitude Γ, the wavelength σ, and the spatial damping λ (steepness) [see Figs. 1(d) and 2(c)] of the evanescent waves as a function of the dissipation, frequency, and amplitude of the forcing. The lower panels of Fig. 3 show these results. The amplitude of evanescent waves as a function of the forcing frequency exhibits a resonance when the forcing frequency coincides with the natural frequency ($\omega/\omega_0 \approx 1$). Figure 3 shows this resonance for different dissipation and intensity forcing coefficients. The behavior of these curves is not well described by linear or weakly nonlinear resonance [7,17]. Therefore, one can conclude that the appearance of evanescent waves is the result of a resonance between the parametric forcing and the natural frequency of the pendula. That is, at close to 1 : 1 resonance, the amplitude of the evanescent wave is large ($\omega/\omega_0 \approx 1$), which is disclosed in Figs. 3(b) and 3(c). Moreover, in the quasireversal limit ($\{\gamma,\mu\} \ll 1$), the amplitude of the evanescent waves is negligible, and the flaming 2π kinks and 2π kinks are indistinguishable. Likewise, we have characterized the wavelength σ and steepness λ of the evanescent waves as a function of frequency forcing (see the bottom panels of Fig. 3). The steepness increases with frequency higher than the natural frequency. The wavelength exhibits a resonance when the forcing frequency coincides with the natural frequency. This wavelength does not match with the wavelength of the dispersion relation obtained from linear theory around a vertical state. Hence, from the above observations, the properties of evanescent waves are of a nonlinear type.

IV. LOCALIZED FLAMING STATES

Due to the space reflection invariance $\xi \to -\xi$, both kinks connecting 0-2π and 2π-0 exist. The last state is usually termed "antikink." Both states correspond to a front solution connecting two symmetric states. The interaction between spatially monotone fronts in one-dimensional dynamical systems is attractive [18,19], i.e., the fronts attract and eventually annihilate. This scenario changes when fronts exhibit stationary spatial damped oscillations, the front interaction decays at large distance, and it alternates between attractive and repulsive [19]. Therefore, under these conditions, the system under study shows a family of localized structures characterized by having a collapsed snaking bifurcation diagram [19,20]. Namely, in the parameter region that corresponds to the coexistence of localized states, one can clearly see that localized states characterized with a shorter width occur in a wider range of parameters; in contrast, the localized structures of considerable length require precise parameter fine-tuning. In the case of fronts connecting two standing waves (not evanescent), the interaction does not decay quickly with distance, alternating between attractive and repulsive modes. Hence, a family of localized structures with a homoclinic snaking bifurcation diagram is expected [21]. At variance with

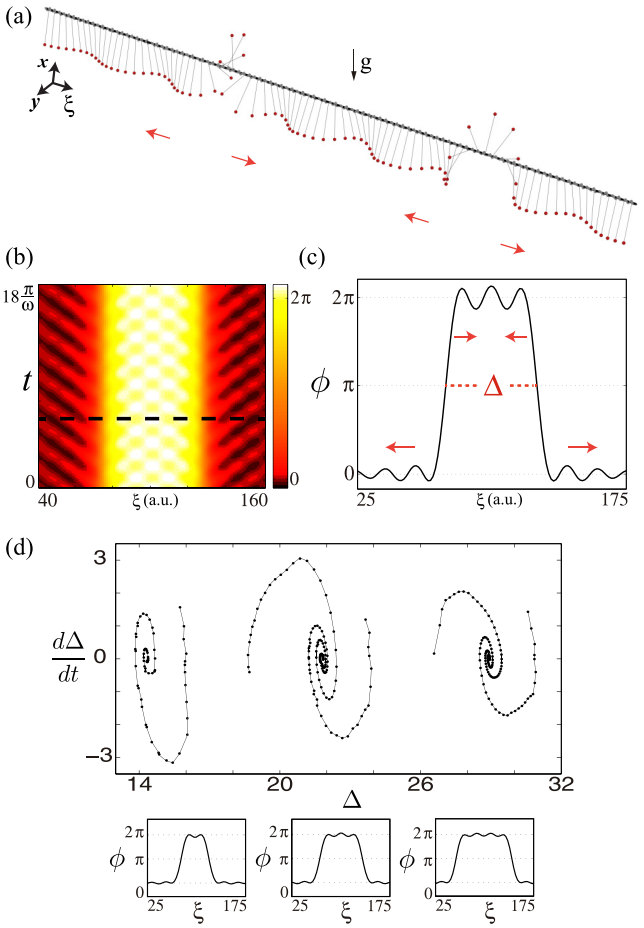

FIG. 4. Localized flaming states in a vertically driven chain of coupled pendula obtained from numerical simulation of Eq. (2) with the same parameters as in Fig. 2. (a) Schematic representation of a bound state composed of a flaming 2π kink and a 2π antikink. Profile at a given time (b) and spatiotemporal temporal evolution (c) of a localized flaming structure. (d) Phase space of the flaming 2π kink position $\{\Delta,\dot{\Delta}\}$ and their stationary localized flaming states, respectively.

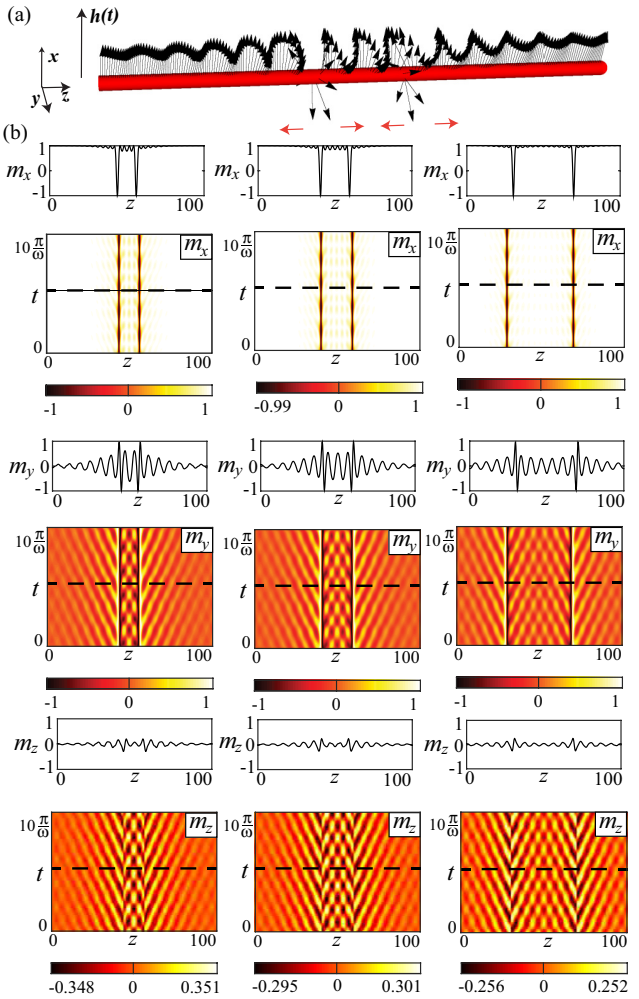

FIG. 5. Flaming localized states in a magnetic wire forced with a transversal oscillatory magnetic field. (a) Arrow representation of a bound state composed of a flaming 2π kink and a flaming 2π antikink at a given time. (b) Cartesian components of the magnetization for three particlelike states with different widths. For every magnetization component, the magnetization profile is shown above the corresponding spatiotemporal diagram. The horizontal line in the diagram shows the instant when the profiles were obtained. For this figure, we used the same parameters as in Fig. 1.

the previous description, localized structures obtained from kink interaction coexist simultaneously.

In our case of flaming 2π kinks, the interaction is governed by evanescent waves. Figure 4 shows a localized structured composed of a flaming 2π kink and a flaming 2π antikink observed in a vertically driven chain of coupled pendula. Monitoring periodically the flaming 2π kink with forcing frequency ω (extended Poincaré section), the flaming 2π kinks are motionless. Indeed, in the extended Poincaré section, the flaming 2π kinks are stationary and characterized with spatial damping oscillations [similar to that shown in Fig. 2(b)], that is, in the extended Poincaré section $\phi(x \to \pm\infty) \to \phi_0 e^{\mp\lambda x} \sin(\frac{2\pi x}{\sigma})$. Hence, it is natural to expect that the interaction between the kinks will be dominated by contributions from the oscillation tails. To prove this, let us consider a pair of a kink and an antikink, located a considerable distance from each other. Let Δ be the distance between the positions of each kink [see Fig. 4(b)]. Using the general theory of kink interaction [19] and assuming a temporal scale separation, for systems with inertia upon the extended Poincaré section, the dynamics between the kink could be described by

$$\ddot{\Delta} + \mu\dot{\Delta} = -a\Gamma e^{\mp\lambda\Delta} \sin\left(\frac{2\pi\Delta}{\sigma} + \varphi_o\right), \qquad (3)$$

where the phenomenological coefficients $\{a,\varphi_o,\Gamma\}$ are numerically computed. The dynamics of the kink interaction satisfies a Newton-type equation with a force that decays exponentially with distance and alternates between positive and negative values. Hence, the system has a family of steady states of the form $\Delta_n = (\pi n - \varphi_o)/\sigma$ for large enough $n = \{1,2,\dots\}$, which alternate between node and saddle

equilibria. Figure 4(d) illustrates in its lower panels three stable localized structures with different sizes. To confirm the dynamics predicted by the previous phenomenological model, Eq. (3), we have reconstructed the phase space for the flaming kink interaction by numerically measuring the evolution of the position $\Delta(t)$ and the rate of change $\dot{\Delta}(t)$ of a pair of kinks. Figure 4(d) shows the phase space of the flaming 2π kink position and its stationary localized flaming states, respectively. This phase space presents a quite good agreement with the phenomenological model Eq. (3). Then the results extracted from the extended Poincaré section are consistent.

We can infer that the interaction between flaming kinks is mediated by the evanescent waves, which permits the generation of bound states (cf. Fig. 4). To verify the robustness of this property, we have conducted numerical simulations of magnetic wire forced with a transversal oscillatory magnetic field. Figure 5 shows three of the flaming localized states obtained for the same parameters used in Fig. 1. Those figures were obtained using the following type of initial condition: $\mathbf{m} = \cos[\phi_k(z - z_k) + \phi_{ak}(z - z_{ak})]\mathbf{e}_x + \sin[\phi_k(z - z_k) + \phi_{ak}(z - z_{ak})]\mathbf{e}_y$, where $\{\phi_k(z - z_{ak}), \phi_{ak}(z - z_{ak})\}$ are, respectively, the flaming 2π kink and the flaming 2π antikink solution of sine-Gordon, and the coordinates $\{z_k, z_{ak}\}$ stand for the positions of the flaming kinks. These numerical simulations show that the family of localized states formed by the flaming kinks are a common phenomenon of parametric systems that exhibit kinks. Note that for small bound states there is a standing wave connecting the kink positions [see Fig. 5(c)]. However, as the width of the flaming localized states becomes larger, a standing wave is observed in the center only, while propagative waves are observed near kink positions. This structure is a direct consequence of the evanescent nature of the waves emitted by the flaming kinks.

V. CONCLUSIONS AND REMARKS

We have studied dissipative kinks with an oscillatory cloak and a family of flaming localized states that connect uniform symmetrical states in a magnetic wire forced with a transversal oscillatory magnetic field and in a parametrically driven damped pendula chain. We have termed these particlelike solutions "flaming kinks." The oscillatory cloak is composed of evanescent waves from the kink position and is generated by a resonant mechanism between the frequency of parametric forcing and the natural frequency of the extended oscillator. These evanescent waves mediate the kink interaction and generate a family of localized states. Using an extended Poincaré section and numerical simulations, we have inferred the flaming kink interaction. Numerical simulations of a magnetic wire forced with a transversal oscillatory magnetic field and a parametrically driven damped pendula chain show quite fair agreement with our findings.

We have characterized the parameter space for a parametrically driven damped pendula chain where the flaming 2π kinks are observed. However, elucidating the mechanisms by which these flaming 2π kinks disappear is in progress. Localized particles in two dimensions with evanescent waves have been observed in droplets on a vertically driven fluid [22]. The dynamics of these two-dimensional particles is similar to those seen in the flaming kinks. Study in this direction is in progress.

ACKNOWLEDGMENTS

We acknowledge the referee for valuable suggestions. M.G.C. gratefully acknowledges the financial support of FONDECYT projects 1150507. E.B.-C. gratefully acknowledges the financial support of CONICYT through Becas Magister Nacional 2015, Contract No. 22151824. A.O.L. gratefully acknowledges the JSPS KAKENHI Grant No. 26103006.

[1] L. M. Pismen, *Patterns and Interfaces in Dissipative Dynamics* (Springer, Berlin, 2006).

[2] M. Cross and H. Greenside, *Pattern Formation and Dynamics in Nonequilibrium Systems* (Cambridge University Press, New York, 2009).

[3] *Localized States in Physics: Solitons and Patterns*, edited by O. Descalzi, M. G. Clerc, R. Residori, and G. Assanto (Springer Science & Business Media, Berlin, 2011).

[4] G. Nicolis and I. Prigogine, *Self-organization in Nonequilibrium Systems* (Wiley, New York, 1977).

[5] Y. S. Kivshar and B. A. Malomed, Dynamics of solitons in nearly integrable systems, Rev. Mod. Phys. **61**, 763 (1989).

[6] M. Clerc, P. Coullet, and E. Tirapegui, Lorenz bifurcation: Instabilities in quasireversible systems, Phys. Rev. Lett. **83**, 3820 (1999); The stationary instability in quasi-reversible systems and the Lorenz pendulum, Int. J. Bifurcation Chaos **11**, 591 (2001).

[7] L. D. Landau and E. M. Lifshiftz, *Mechanics*, Course of Theoretical Physics Vol. 1 (Pergamon, Oxford, 1976).

[8] O. M. Braun and Y. Kivshar, *The Frenkel-Kontorova Model: Concepts, Methods, and Applications* (Springer Science & Business Media, Berlin, 2013).

[9] J. D. Kelley, G. H. Gunaratne, A. Palacios, and J. Shulman, Modal decomposition and normal form for hydrodynamic flows: Examples from cellular flame patterns, Eur. Phys. J. Spec. Top. **204**, 119 (2012).

[10] P. Blomgren, S. Gasner, and A. Palacios, Hopping behavior in the Kuramoto-Sivashinsky equation, Chaos **15**, 013706 (2005).

[11] I. D. Mayergoyz, G. Bertotti, and C. Serpico, *Nonlinear Magnetization Dynamics in Nanosystems* (Elsevier, Oxford, 2009).

[12] D. Urzagasti, D. Laroze, M. G. Clerc, and H. Pleiner, Breather soliton solutions in a parametrically driven magnetic wire, Europhys. Lett. **104**, 40001 (2013).

[13] M. G. Clerc, S. Coulibaly, and D. Laroze, Localized states and non-variational Ising-Bloch transition of a parametrically driven easy-plane ferromagnetic wire, Physica D **239**, 72 (2010).

[14] H. J. Mikeska, Solitons in a one-dimensional magnet with an easy plane, J. Phys. C **11**, L29 (1978).

[15] K. M. Leung, Mechanical properties of double-sine-Gordon solitons and the application to anisotropic Heisenberg ferromagnetic chains, Phys. Rev. B **27**, 2877 (1983).

[16] M. G. Clerc, S. Coulibaly, and D. Laroze, Parametrically driven instabilities in quasi-reversal systems, Int. J. Bifurcation Chaos **19**, 3525 (2009).

[17] N. N Bogoliubov and Y. A. Mitropolski, *Asymptotic Methods in the Theory of Non-Linear Oscillations* (Gordon and Breach, New York, 1961).

[18] K. Kawasaki and T. Otha, Kink dynamics in one-dimensional nonlinear systems, Physica (Amsterdam) **116A**, 573 (1982).

[19] P. Coullet, Localized patterns and fronts in nonequilibrium systems, Int. J. Bifurcation Chaos **12**, 2445 (2002).

[20] P. Coullet, L. Gil, and D. Repaux, Defects and Subcritical Bifurcations, Phys. Rev. Lett. **62**, 2957 (1989).

[21] M. G. Clerc, C. Fernández-Oto, and S. Coulibaly, Pinning-depinning transition of fronts between standing waves, Phys. Rev. E **87**, 012901 (2013).

[22] S. Protiere, A. Boudaoud, and Y. Couder, Particle-wave association on a fluid interface, J. Fluid Mech. **554**, 85 (2006).

Appendix B

Flaming kink-antikink interaction in parametrically driven systems

In this appendix we derive in detail the flaming kink-antikink interaction law analytically, using the driven and damped ϕ^4 scalar field equation.

Publication details:

- Title: Flaming kink-antikink interaction in parametrically driven systems.
- Author: E. Berrios-Caro.
- Submitted to Journal of Physics: Conference Series.
- Conference: XX Simposio de la Sociedad Chilena de Física, 2016.

Flaming kink-antikink interaction in parametrically driven systems

E. Berrios-Caro

Departamento de Física, Facultad de Ciencias Físicas y Matemáticas, Universidad de Chile, Casilla 487-3, Santiago, Chile

E-mail: ernesto.berrios@ug.uchile.cl

Abstract. Particle-like solutions are of great importance to explain complex dynamics in several physical systems. Of particular interest are the so-called kink solutions, characterized by connecting two symmetric states. Recently a new type of kink solutions was reported, the flaming kinks, which are solutions of the sine-Gordon and ϕ^4 model equations under dissipation and parametric oscillatory forcing. They are characterized by the emission of evanescent waves from the center position in two counterparts directions. Besides, their interaction allows the formation of stable localized structures. In this work the flaming kink-antikink interaction is studied both numerically and analytically, characterizing the dynamics of the distance of separation between the kinks. Numerical simulations show fair agreement with our theoretical findings.

1. Introduction

The sine-Gordon equation has attracted attention in many fields of physics due to its modeling of, e.g., dislocations in crystals, domain walls in ferromagnets, flux in Josephson transmission lines, among others [1–4]. One of the interesting properties of this equation is the presence of kink soliton solutions [1]. These solutions are particle-like states for classical field equations, that is, they are solutions that can be characterized by a finite number of parameters such as position, width, charge, and so forth.

The ϕ^4 model equation also admits kink soliton solutions and it is often used as a prototype model [5] for more complex configurations of the field theory, in areas like particle physics [6] and cosmology [7, 8]. One particular interest of particle-like dynamics is the possibility to make quantum analogies, as the kink-antikink interaction, due to its similarity with particle-antiparticle behavior.

Both sine-Gordon and ϕ^4 model equation admit analytical kink solutions that travel with a constant speed [1–8]. The interaction between them shows some interesting features: the kink-kink collision results in a change of direction in the velocity of each kink, while the kink-antikink collision is perfectly permeable, since they pass through each other [9, 10].

The above scenario changes drastically in presence of dissipation and oscillatory parametric forcing [11], i.e., when a parameter of the system is modulated in time [12]. Firstly, as it is expected, the speed drops to zero because of the damping. Besides, because of the parametric forcing, evanescent waves appear from the center position of the kinks, moving in opposite directions. To illustrate this phenomenon, let us consider a simple mechanical model of a parametrically driven and damped chain of pendulums connected by linear springs to their first

neighbors. In the conservative continuous limit the dynamics of the vertical deviation angle of the chain of pendulums is described by the sine-Gordon equation [13]. The kink solutions in this case correspond to a localized rotation of pendulums in 2π, since the system has multi stability due to the degeneracy of the angle. Moreover, the pendulums interaction with air causes dissipation and the parametric forcing considered corresponds to a vertical synchronized oscillation of the chain support, at a certain frequency and amplitude. The corresponding equation of this system writes [14]

$$\partial_{tt}\theta = -(\omega_0^2 + \gamma \sin \omega t) \sin \theta - \mu \partial_t \theta + \kappa^2 \partial_{xx} \theta, \tag{1}$$

where $\theta(x,t)$ accounts for the vertical deviation in position x and time t, ω_0 is the natural frequency of a single pendulum, $\gamma \equiv a\omega^2/l$ where a and ω account for the amplitude and forcing frequency, respectively. Besides, l is the length of every pendulum, μ account for the dissipation and κ is the coupling constant of springs. Figure 1 shows the solution obtained from the numerical integration, clearly revealing the presence of traveling waves in opposite directions from the kink center position. All numerical simulations of this work have been performed with the fourth-order Runge-Kutta method with Neumann boundary conditions ($\partial_x \theta = 0$ at the borders).

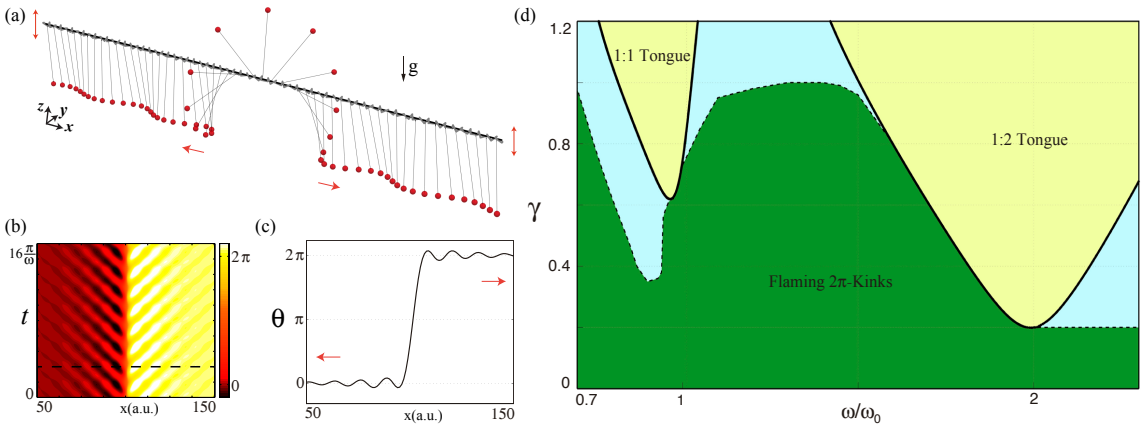

Figure 1. Flaming kinks of a chain of coupled pendulums, under dissipation and parametric forcing, obtained from numerical integration of Eq. (1) with $\omega_0 = 1.0, \gamma = 0.3, \omega = 1.4, \mu = 0.1, \kappa = 1.0, dx = 0.5$ and $dt = 0.1$. (a) Schematic representation of a flaming kink. (b) Spatiotemporal evolution. (c) Spatial profile of the solution at a certain instant marked with a dashed line in (b). (d) Phase space as a function of frequency and amplitude of the forcing with $\mu = 0.1$. The green zone accounts for the region where flaming kinks are observed.

In a recent previous work [15], these solutions have been named as *flaming kinks*, since the propagation of waves resembles a hopping pattern behavior observed in combustion under controlled conditions [16, 17]. Additionally, it has been demonstrated that the amplitude of the traveling waves is maximum when the frequency of the forcing coincides with the natural frequency, and that the system evolves periodically to the same state at a time $2\pi/\omega$. This implies that this phenomenon has a *resonant* nature. Furthermore, it has been established the region of parameters where these solutions exist as it is illustrated in phases space of Fig. 1(d), obtained numerically by means of looking for the persistence of the flaming kink solutions. The $1:1$ and $1:2$ tongues specify the region where the solution $\theta = 0$ is unstable. This stability chart is known as the Ince-Strutt diagram [18].

The flaming kinks are a robust phenomenon, that is, they can be observed in different contexts such as the ϕ^4 model equation under the same kinds of dissipation and parametric forcing. This equation writes

$$\partial_{tt}\phi = (\epsilon\phi - \phi^3)(1 - \gamma \sin \omega t) - \mu\partial_t\phi + \partial_{xx}\phi, \tag{2}$$

where $\phi(x,t)$ is a scalar field and ϵ is a parameter which controls the size of the kink.

1.1. Localized structures

Let us first show some properties of the flaming kink-antikink interaction which allows the formation of a family of localized structures.

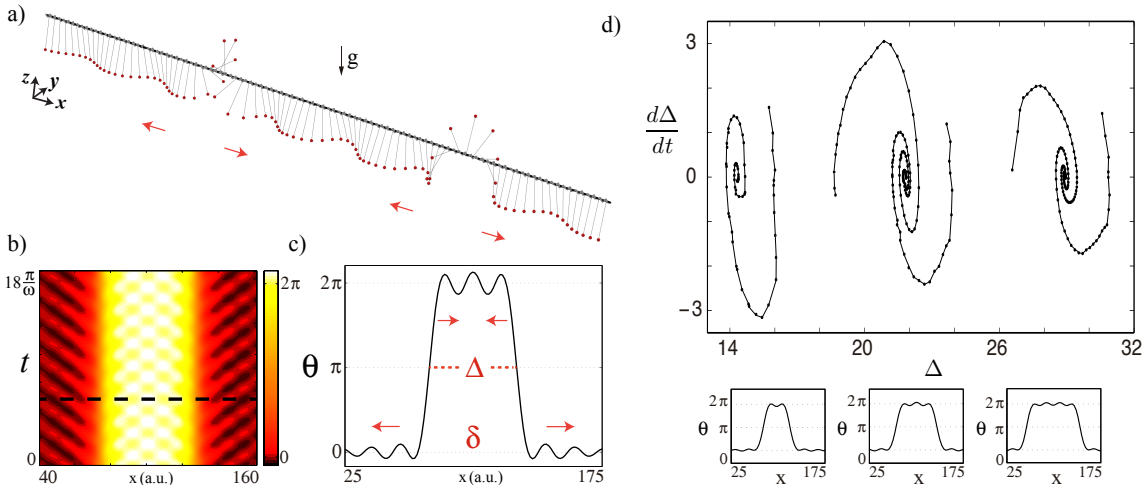

Figure 2. Flaming localized structures of a chain of coupled pendulums, under dissipation and parametric forcing, obtained from numerical integration of Eq. (1) with the same parameters as in Figure 1. (a) Schematic representation of the solution. (b) Spatiotemporal evolution. (c) Spatial profile of the solution at a certain instant marked with a dashed line in (b). The parameters Δ and δ account for the width and position of the localized structure, respectively. (d) Phase space $\{\Delta, \dot{\Delta}\}$ of the localized structures. The lower panels show the respective profiles of equilibrium widths.

Since the flaming kinks are characterized by the emission of waves, their interaction is governed by the superposition of contributions from the oscillatory tails. As a consequence, numerical simulations show the presence of stationary waves between a flaming kink and a flaming antikink [15]. In Fig. 2 it is shown a typical profile of these *flaming localized structures* in the chain of coupled pendulums obtained through numerical integration of Eq. (1). As the spatiotemporal diagram illustrates, there are stationary waves between the kinks.

Moreover, it has been observed that the distance of separation between the kinks is stable. However, the most interesting fact of these structures is shown in the phase space in Fig. 2(d). It reveals the presence of equilibrium widths, with a length determined by a integer number of the stationary waves formed. It also shows how the width evolves under a perturbation, with the possibility to reach a new equilibrium. A detailed study of this behavior has not been done.

The aim of this article is to study numerically and analytically in detail the interaction between a flaming kink and a flaming antikink. To carry out this study we will perform a time-scale analysis in the dissipative ϕ^4 equation under parametric forcing to derive a time

independent equation. From this equation we will study the interaction law of these kinks, i.e. the dynamics of the position and distance of separation, by performing a perturbative analysis.

2. Time-scale separation in dissipative ϕ^4 model under parametric forcing

Since the flaming kink-antikink interaction evolves slower compared to the dynamics of the waves, which is of the order of the period of the forcing, it is expected that at certain limit the system exhibits a separation of scales in time. Then, following a similar strategy proposed by Kapitza [19], we propose that the flaming kink solutions in Eq. (2) can be written as

$$\phi(x,t) = u(x,t) + \xi(x,t), \tag{3}$$

where u accounts for the average shape of the flaming kink solution and ξ for the traveling waves, such that

$$u(x,t) \gg \xi(x,t),$$

due to the smallness of the waves compared to the kink. Furthermore, we will impose that

$$\partial_{tt} u(x,t) \ll \partial_{tt} \xi(x,t),$$

to take into account the different time-scales. Replacing (3) in (2) and linearizing in ξ we obtain

$$\begin{aligned} \partial_{tt} u + \partial_{tt} \xi = &\left(\epsilon u - u^3 + \xi(\epsilon - 3u^2)\right)(1 - \gamma \sin \omega t) \\ &- \mu(\partial_t u + \partial_t \xi) + \partial_{xx} u + \partial_{xx} \xi. \end{aligned} \tag{4}$$

Considering the limit when $\mu \ll \omega$ the dominant terms of this equation are

$$\partial_{tt} \xi = -(\epsilon u - u^3)\gamma \sin \omega t + \partial_{xx} \xi, \tag{5}$$

because gamma accounts for the acceleration of the support bar of the chain of pendulums, i.e. $\gamma \propto \omega^2$. Since ξ is a fast time-scale variable, the spatial derivatives can be put out of the integration. Using the Laplace method [20] for the time integration, we obtain

$$\xi \approx (\epsilon u - u^3)\frac{\gamma}{\omega^2} \sin \omega t + \varphi, \tag{6}$$

where φ is a correction that accounts for the spatial dependence of ξ spatial derivative. Thus, replacing (6) in (5) we derive

$$\partial_{tt} \varphi = -\partial_{xx}(\epsilon u - u^3)\gamma \sin \omega t + \partial_{xx} \varphi,$$

and integrating in time again as before, we get

$$\varphi \approx -\partial_{xx}(\epsilon u - u^3)\frac{\gamma}{\omega^4} \sin \omega t + \psi,$$

with ψ also a correction.

If we repeat the same procedure and after some straightforward calculations we can derive the following approximation for ξ

$$\xi = \frac{\gamma}{\omega^2} \sin \omega t \mathcal{F}(\epsilon u - u^3),$$

where the operator $\mathcal{F}$ is defined as

$$\mathcal{F} = \left(1 - \frac{1}{\omega^2}\partial_{xx} + \frac{1}{\omega^4}\partial_{xxxx}\right).$$

Since the variable ξ takes into consideration the propagation of waves, which are periodic in time, it is expected that its temporal average over one or few periods vanish. Moreover, the variable u does not change significantly in this scale and can be considered unaffected by taking the temporal average. Then, defining the temporal average as

$$\langle f(t)\rangle = \frac{\omega}{2\pi}\int_0^{2\pi/\omega} f(t)dt,$$

over one period $2\pi/\omega$ and applying it in (4) results in

$$\partial_{tt}u = (\epsilon u - u^3) - \gamma(\epsilon - 3u^2)\langle \xi \sin\omega t\rangle - \mu\partial_t u + \partial_{xx}u, \tag{7}$$

and because $\langle \sin^2 \omega t\rangle = 1/2$, it is straightforward that this equation becomes

$$\partial_{tt}u = \left(1 - \frac{\gamma^2}{2\omega^2}(\epsilon - 3u^2)\mathcal{F}\right)(\epsilon u - u^3) - \mu\partial_t u + \partial_{xx}u, \tag{8}$$

which is an effective equation of the slow variable u. Since it contains fourth-order derivatives in space, it ensures the presence of damped waves. Notice that this equation does not depend on time explicitly. Also note that the terms contained in $\mathcal{F}$ become smaller as ω grows. Hence, the scaling method allow us to obtain an effective time independent equation. In Fig. 3 it is shown the spatial profile of a stationary solution of this equation, illustrating the presence of evanescent waves.

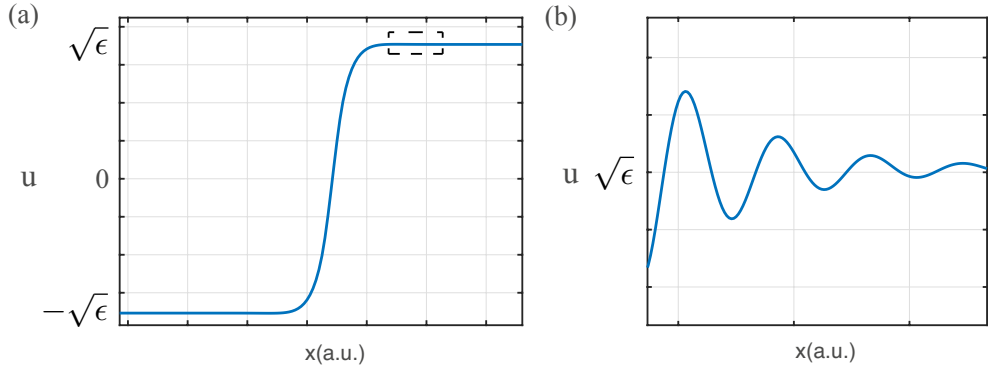

Figure 3. (a) Profile of the stationary flaming kink solution of equation (8). The dashed rectangle corresponds to a zoom showed in (b). (b) Stationary evanescent waves present in the kink solution.

3. Flaming kink-antikink interaction

3.1. Asymptotic approximations

The analytical kink solution of the stationary ϕ^4 model equation is [8]

$$\phi_{\rm k}(x) = \sqrt{\epsilon}\tanh\left(\sqrt{\frac{\epsilon}{2}}(x - x_0)\right) \tag{9}$$

where x_0 is the center position. The width of this kink is defined as $\sqrt{\frac{2}{\epsilon}}$. Its spatial profile is shown in Fig. 4(a).

Performing a Taylor expansion it is straightforward that at dominant order is fulfilled that

$$\lim_{x\to x_1\gg x_0} \phi_{\rm k}(x) - \sqrt{\epsilon} = -2\sqrt{\epsilon}\, e^{-2\sqrt{\frac{\epsilon}{2}}(x_1-x_0)},$$

i.e., the solutions decays exponentially far away from the center position.

However, to take into account the evanescent waves of solutions of Eq. (8), we propose the following limit

$$\lim_{x\to x_1\gg x_0} u_{\rm k}(x) - \sqrt{\epsilon} = -2\sqrt{\epsilon}\, e^{-2\sqrt{\frac{\epsilon}{2}}(x_1-x_0)} \cos\left(\kappa(x_1-x_0)+\delta_0\right), \tag{10}$$

where κ and δ_0 can be computed numerically.

The same analysis can be applied to the antikink solution, after a change of sign since $\phi_{\rm k} = -\phi_{\rm ak}$.

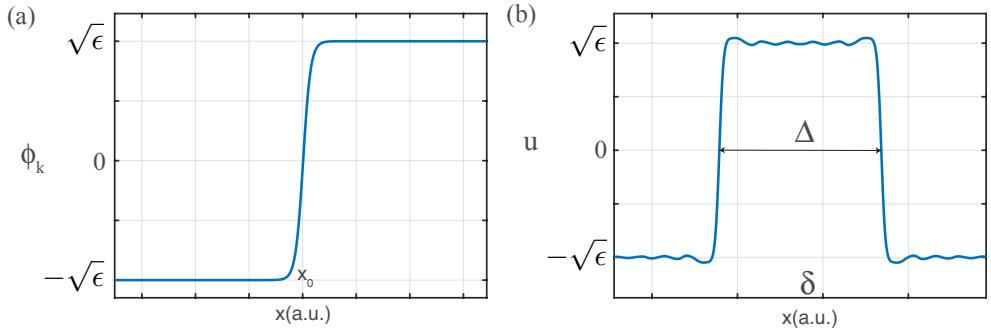

Figure 4. (a) Profile of the analytical kink solution of the ϕ^4 equation expressed in Eq. (9). (b) Profile of the ansatz $u_{\rm loc}$ proposed in Eq. (11). The position and width are labeled as δ and Δ, respectively.

3.2. Interaction dynamics

Now let us propose the following ansatz for the localized structures [21]

$$u_{\rm loc}(x,t) = u_{\rm k}(x-x_-(t)) + u_{\rm ak}(x-x_+(t)) - \sqrt{\epsilon} + W(x,x_+,x_-), \tag{11}$$

where $x_-(t)$ and $x_+(t)$ are the central positions of the kinks. We define

$$\Delta(t) \equiv x_+(t) - x_-(t)$$

as the width of the localized structure, which is promoted as a function of time. It will be assumed that the kinks are very far apart, implying that Δ will be much larger than the kink width. On the other hand, the function W accounts for the effect of the parametric forcing, which we assume small, and the deformation of the kink as result of the presence of the other one. In addition, it will be assumed that the kinks travel slowly, implying that the temporal derivatives of $x_-(t)$ and $x_+(t)$ are small compared with the speed of propagation of waves. The spatial profile of this ansatz at a certain instant is illustrated in Fig. 4 (b).

In order to take into account all these considerations, the non linear terms in W will be neglected, as well as the terms proportional to the product of W with $\dot{x}_-$ or $\dot{x}_+$.

Let us define the following interaction variables to simplify our calculations

$$\delta(t) = \frac{x_-(t) + x_-(t)}{2},$$

$$z_\pm(t) = x - x_\pm(t).$$

Notice that δ is the central position of the localized structures.

Therefore, introducing the ansatz (11) into Eq. (2), after linearizing in W and performing straightforward calculations we obtain

$$\mathcal{L}W = b,$$

with the linear operator

$$\mathcal{L} = \epsilon - 3v^2 + \partial_{xx} + \frac{\gamma^2}{2\omega^2}\left[6v\mathcal{F}(\epsilon v - v^3) - (\epsilon - 3v^2)\mathcal{F}(\epsilon - 3v^2)\right],$$

where

$$v = u_\mathrm{k} + u_\mathrm{ak} - \sqrt{\epsilon}.$$

On the other hand,

$$\begin{aligned} b = {} & \frac{1}{2}\left(\ddot{\Delta} + \mu\dot{\Delta}\right)(\partial_{z_-}u_\mathrm{k} - \partial_{z_+}u_\mathrm{ak}) - \left(\ddot{\delta} + \mu\dot{\delta}\right)(\partial_{z_-}u_\mathrm{k} + \partial_{z_+}u_\mathrm{ak}) \\ & + \left(\dot{\delta}^2 + \frac{\dot{\Delta}^2}{4}\right)(\partial_{z_-z_-}u_\mathrm{k} + \partial_{z_+z_+}u_\mathrm{ak}) - \dot{\delta}\dot{\Delta}(\partial_{z_-z_-}u_\mathrm{k} - \partial_{z_+z_+}u_\mathrm{ak}) \\ & - \left(1 - \frac{\gamma^2}{2\omega^2}\mathcal{F}\right)\left(3u_\mathrm{k}(u_\mathrm{ak} - \sqrt{\epsilon})^2 + 3u_\mathrm{k}^2(u_\mathrm{ak} - \sqrt{\epsilon}) - 3\sqrt{\epsilon}u_\mathrm{ak}(u_\mathrm{ak} - \sqrt{\epsilon})\right). \end{aligned} \tag{12}$$

Defining the following inner product

$$\langle f|g\rangle = \int_{-\infty}^{+\infty} fg\,\mathrm{d}x,$$

we can see that the operator $\mathcal{L}$ is self-adjoint, i.e., $\mathcal{L}^\dagger = \mathcal{L}$, where $\mathcal{L}^\dagger$ is the adjoint operator.

To derive the equations for δ and Δ we can apply the Fredholm solvability condition to this linear system. This condition establishes that the system has solution if the inner product between the elements of the Kernel of $\mathcal{L}^\dagger$, the eigenvectors that satisfy $\langle v|\,\mathcal{L}^\dagger = 0$, with b is zero, i.e, $\langle v|b\rangle = 0$ [22]. Nevertheless, given the fact that $\mathcal{L}^\dagger$ is not suitable to perform analytical calculations it is necessary to make some simplifications. Let us propose the followings *pseudo-eigenvectors* [23]

$$\tau = \partial_{z_-}u_\mathrm{k} + \partial_{z_+}u_\mathrm{ak}, \tag{13}$$

$$\chi = \partial_{z_-}u_\mathrm{k} - \partial_{z_+}u_\mathrm{ak}, \tag{14}$$

meaning that both products $\langle\tau|\,\mathcal{L}^\dagger$ and $\langle\chi|\,\mathcal{L}^\dagger$ are exponentially close to zero. To show this notice that since u_k satisfy the stationary Eq. (7), its spatial derivatives fulfil

$$0 = \left[\epsilon - 3u_\mathrm{k}^2 + \partial_{xx} + \frac{\gamma^2}{2\omega^2}6u_\mathrm{k}\mathcal{F}(\epsilon u_\mathrm{k} - u_\mathrm{k}^3) - (\epsilon - 3u_\mathrm{k}^2)\mathcal{F}(\epsilon - 3u_\mathrm{k}^2)\right]\partial_{z_-}u_\mathrm{k}.$$

The terms that remain when we apply $\mathcal{L}^\dagger$ to $\partial_{z_-}u_\mathrm{k}$ are proportional to $u_\mathrm{k}(u_\mathrm{ak} - \sqrt{\epsilon})\partial_{z_-}u_\mathrm{k}$, which in the limit of large Δ is very close to zero according to (10). Similarly, applying the same analysis to u_ak, it is straightforward that the remaining terms of $\mathcal{L}^\dagger$ applied to $\partial_{z_+}u_\mathrm{ak}$ are

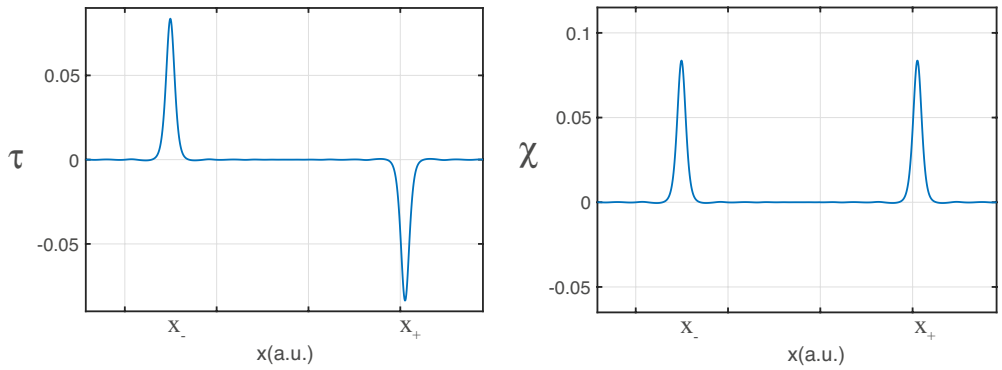

Figure 5. Profile of translation and interaction modes τ and χ defined in Eqs. (13) and (14). We have used $\epsilon = 0.5$ and $\mu = 0.1$.

also small. Then, applying $\mathcal{L}^\dagger$ to τ and χ result in a exponentially small number and can be considered as pseudo-eigenvectors. They will be named as translation and interaction modes, respectively. Their spatial profile is showed in Fig. 5.

Using that τ and χ are pseudo-eigenvectors, we can now apply the Fredholm solvability condition. Thus, we impose that

$$\langle \tau | b \rangle = 0, \tag{15}$$

and

$$\langle \chi | b \rangle = 0. \tag{16}$$

Performing numerical integration of the inner product $\langle \tau | b \rangle$ using formula (12), we observe that the term proportional to the expression $\left(\ddot{\delta} + \mu\dot{\delta}\right)$ is the only relevant in b and that the other can be neglected. In fact, setting $\epsilon = 1$, $x_- = -100$ and $x_+ = 100$, the inner product of τ with this term is more than 10^{10} larger than the others terms in b. Therefore, from (15) we can conclude that

$$\ddot{\delta} + \mu\dot{\delta} = 0,$$

which means that the central position of the localized structures tends to a constant value. This behavior is expected since the system must keep its spatial symmetry.

On the other hand, applying the same analysis to the inner product $\langle \chi | b \rangle$, we observe that the relevant terms are

$$\frac{1}{2}\left(\ddot{\Delta} + \mu\dot{\Delta}\right)\langle \chi | \chi \rangle - \left\langle \chi \middle| 3u_{\rm k}(u_{\rm ak} - \sqrt{\epsilon})^2 + 3u_{\rm k}^2(u_{\rm ak} - \sqrt{\epsilon}) - 3\sqrt{\epsilon}u_{\rm ak}(u_{\rm ak} - \sqrt{\epsilon}) \right\rangle = 0, \tag{17}$$

which can be approximated analytically. Let us first consider the fact that

$$\begin{aligned} &3u_{\rm k}(u_{\rm ak} - \sqrt{\epsilon})^2 + 3u_{\rm k}^2(u_{\rm ak} - \sqrt{\epsilon}) - 3\sqrt{\epsilon}u_{\rm ak}(u_{\rm ak} - \sqrt{\epsilon}) = \\ &3u_{\rm ak}(u_{\rm k} - \sqrt{\epsilon})^2 + 3u_{\rm ak}^2(u_{\rm k} - \sqrt{\epsilon}) - 3\sqrt{\epsilon}u_{\rm k}(u_{\rm k} - \sqrt{\epsilon}). \end{aligned}$$

Then, the second inner product of (17) can be written as

$$\begin{aligned} &\left\langle \partial_{z_-} u_{\rm k} \middle| 3u_{\rm k}(u_{\rm ak} - \sqrt{\epsilon})^2 + 3u_{\rm k}^2(u_{\rm ak} - \sqrt{\epsilon}) - 3\sqrt{\epsilon}u_{\rm ak}(u_{\rm ak} - \sqrt{\epsilon}) \right\rangle \\ &- \left\langle \partial_{z_+} u_{\rm ak} \middle| 3u_{\rm ak}(u_{\rm k} - \sqrt{\epsilon})^2 + 3u_{\rm ak}^2(u_{\rm k} - \sqrt{\epsilon}) - 3\sqrt{\epsilon}u_{\rm k}(u_{\rm k} - \sqrt{\epsilon}) \right\rangle. \end{aligned}$$

Here, the dominant inner products are

$$-\left\langle \partial_{z_-} u_{\rm k} \middle| 3\sqrt{\epsilon} u_{\rm ak}(u_{\rm ak}-\sqrt{\epsilon}) \right\rangle + \left\langle \partial_{z_+} u_{\rm ak} \middle| 3\sqrt{\epsilon} u_{\rm k}(u_{\rm k}-\sqrt{\epsilon}) \right\rangle . \tag{18}$$

Let us expand the second of these inner products using the change of variables $y = x - x_+$ and $\Delta = x_+ - x_-$. We obtain

$$\left\langle \partial_{z_+} u_{\rm ak} \middle| 3\sqrt{\epsilon} u_{\rm k}(u_{\rm k}-\sqrt{\epsilon}) \right\rangle = 3\sqrt{\epsilon} \int_{-\infty}^{+\infty} \partial_{z_+} u_{\rm ak}(y)\, u_{\rm k}(y+\Delta)\, (u_{\rm k}(y+\Delta)-\sqrt{\epsilon}) {\rm d}y.$$

The integrand of this expression is zero in the whole integration region, except where y is close to zero. Given the fact that we are considering Δ very large, we can use the approximation (10) to write

$$\begin{aligned}\left\langle \partial_{z_+} u_{\rm ak} \middle| 3\sqrt{\epsilon} u_{\rm k}(u_{\rm k}-\sqrt{\epsilon}) \right\rangle &\approx 3\sqrt{\epsilon} \int_{-\infty}^{+\infty} \partial_{z_+} u_{\rm ak}(y)\, \sqrt{\epsilon}\, (-2\sqrt{\epsilon})\, e^{-2\sqrt{\frac{\epsilon}{2}}(y+\Delta)} \cos\left(\kappa\Delta+\delta_0\right) {\rm d}y \\ &= 6\epsilon\sqrt{\epsilon}\, e^{-2\sqrt{\frac{\epsilon}{2}}\Delta} \cos\left(\kappa\Delta+\delta_0\right) I_{\rm ak},\end{aligned}$$

where $I_{\rm ak} = -\int_{-\infty}^{+\infty} \partial_{z_+} u_{\rm ak}(y) e^{-2\sqrt{\frac{\epsilon}{2}}y} {\rm d}y$. Performing the same analysis to the first inner product in (18) we obtain

$$\left\langle \partial_{z_-} u_{\rm k} \middle| 3\sqrt{\epsilon} u_{\rm ak}(u_{\rm ak}-\sqrt{\epsilon}) \right\rangle \approx -6\epsilon\sqrt{\epsilon}\, e^{-2\sqrt{\frac{\epsilon}{2}}\Delta} \cos\left(\kappa\Delta+\delta_0\right) I_{\rm k},$$

where $I_{\rm k} = \int_{-\infty}^{+\infty} \partial_{z_-} u_{\rm k}(y) e^{-2\sqrt{\frac{\epsilon}{2}}y} {\rm d}y$. It is easy to see that $I_{\rm ak} = I_{\rm k}$ and that they are positive. These integrals will be labeled simply as I.

Finally, replacing in (17) it is obtained the kink-antikink interaction law

$$\ddot{\Delta} + \mu\dot{\Delta} = -24\frac{I}{\langle\chi|\chi\rangle}\epsilon\, \sqrt{\epsilon}\, e^{-2\sqrt{\frac{\epsilon}{2}}\Delta} \cos\left(\kappa\Delta+\delta_0\right),$$

which has the form a Newton-type equation with dissipation and a force that decays exponentially with the distance, alternating between positive and negative values. Notice that it predicts the existence of equilibriums of the form $\Delta_n = \frac{(2n+1)\pi/2-\delta_0}{\kappa}$, as showed in the zeros of Fig. 2(d). Moreover, it predicts how the width evolves to an equilibrium, performing spirals in the phase space. This means that the width oscillates around an equilibrium before reaching it. Also, the equation predicts that under a larger perturbation these is a possibility to reach a new equilibrium, with a larger width.

4. Conclusions

In this work, the flaming kink-antikink interaction was studied analytically and numerically by means of applying perturbative theory to an effective time independent equation in a particular limit, when the frequency of the forcing is large. The findings showed good agreement with numerical results. Although the calculations were derived in the large frequency limit, they can predict the general behavior observed numerically.

Acknowledgements

I gratefully acknowledge to Marcel Clerc and Alejandro León for their valuable comments and suggestions during the realization of this work. Also, to the the financial support of CONICYT though Becas Magíster Nacional 2015, Contract No. 22151824.

Appendix C

Pattern formation mediated by repulsive interaction between localized structures

In this appendix we include our results of formation of stable lattices, composed by localized structures surrounded by bare soil.

Publication details:

- Title: Pattern formation mediated by repulsive interaction between localized structures.
- Authors: E. Berrios-Caro, M. G. Clerc, D. Escaff, C. Sandivari and M. Tlidi.
- In preparation for being submitted to Scientific Reports.

Pattern formation mediated by repulsive interaction between localized structures

E. Berrios-Caro,[1] M.G. Clerc,[1] D. Escaff,[2] C. Sandivari,[1] and M. Tlidi[3]

[1] *Departamento de Física, Facultad de Ciencias Físicas y Matemáticas, Universidad de Chile, Casilla 487-3, Santiago, Chile*

[2] *Complex Systems Group, Facultad de Ingeniería y Ciencias Aplicadas, Universidad de los Andes, Avenida Monseñor Álvaro del Portillo No 12.455 Las Condes, Santiago, Chile*

[3] *Optique Nonlinéaire Théorique, Université Libre de Bruxelles (U.L.B.), CP 231, Campus Plaine, B-1050 Bruxelles, Belgium*

Non-equilibrium processes often lead to the formation of spatial periodic structures developed from a homogeneous state through the spontaneous breaking of symmetries. Based on the difference in transport or coupling processes in chemical reactions, Turing established the first mechanism of pattern formation. Here, we show that the pattern formation process conducted by repulsive localized vegetation patches produces pattern formation. The observed patterns unlike those predicted by the Turing mechanism do not have an intrinsic length. The characteristic length and type of the pattern depend on the number of the initial localized states. Pair interaction law of localized patches allows us to understand all these behaviors.

PACS numbers: 75.78.-n, 89.75.-k, 05.45.-a

Macroscopic systems maintained out of equilibrium, under the influence of injection and dissipation of energy and momenta, are characterized by exhibiting self-structuring phenomena [1–5]. This phenomenon is characterized by the formation of spatial periodic structures, *patterns*. In the course of the last decades, much effort has been devoted to the study of pattern formation or dissipative structures arising in natural sciences (see the textbooks [5, 6] and the references therein). In many physical systems, these structures emerge as a spatial instability of a uniform state when a control parameter is changed and surpasses a critical value, which usually corresponds to a force imbalance or transport optimization of energy, momenta and/or particles. Indeed, these bifurcations correspond to spontaneous symmetry breaking [1–4]. The first mechanism proposed to understand the pattern formation is based on the difference in transport or coupling processes in chemical reactions, known as *Turing instability* [7]. The patterns based on this

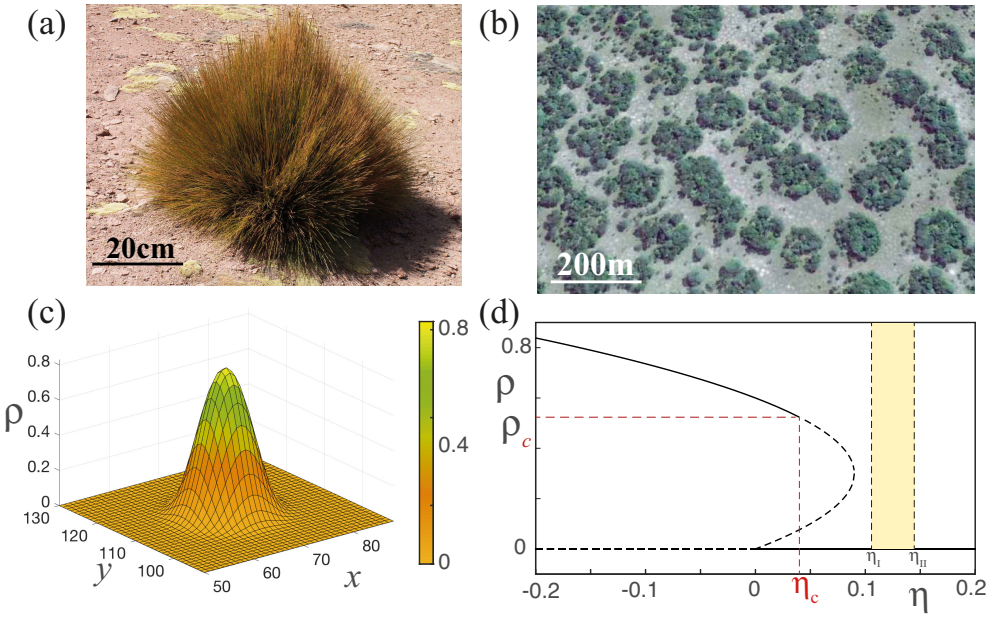

Figure 1. (color online) Localized vegetation patches. (a) snapshot of a typical tussocks of Festuca orthohylla in the north of Chile (courtesy of Luis Faúndez Yancas, Universidad de Chile). (b) Satellite images of localized vegetation patches in Zambia [15]. (c) A numerical localized vegetation patch of the interaction-redistribution model Eq. (1). (d) Bifurcation diagram, showing homogeneous states of model Eq. (1). Full (dotted) lines represent stable (unstable) states. The localized structures can be found for aridities between η_I and η_{II}.

mechanism are characterized by having an intrinsic wavelength that does not depend on the edge conditions and

system size. The origin of this intrinsic length is due to the different transport or coupling processes. This mechanism has been applied from biology to optics, passing through chemistry and physics [4–6, 8]. Likewise, macroscopic systems under the influence of injection and dissipation of energy, often lead to the formation of localized spatial structures [9–11]. Localized structures in dissipative media have been observed in various fields of nonlinear science such as fluid dynamics, optics, laser physics, chemistry, and plant ecology. Localized structures consist of isolated or randomly distributed spots surrounded by regions in the uniform state. Their main feature is to allow the confinement of energy, chemical concentration, light or phytomass density, etc [12]. They may consist of dips embedded in the homogeneous background. They are often called spatial solitons, dissipative solitons, localized patterns, cavity solitons, or auto-solitons, depending on the physical contexts in which theirs were observed. Coexistence between extended states is a prerequisite condition for localized structures formation. However, in the presence of a symmetry breaking instability, the coexistence between a single uniform solution and a patterned state allows for the stabilization of localized state [9–11].

Although localized states are spatially extended, they exhibit properties typically associated with particles. Consequently, one can characterize them with a family of continuous parameters such as position, amplitude, and width. A characteristic property of particle-like solutions is that their interaction can be described simply in terms of continuous parameters describing the localized states. Usually, the interaction of localized structures in two dimensions is attractive or alternates between repulsive and attractive [13, 14]. In the latter case, the system can display bounded states.

The aim of this letter is to show that the pattern formation process conducted by repulsive localized vegetation patches produces pattern formation. Based on an interaction-redistribution local model for vegetation, we show that localized vegetation patches are repulsive. Using an asymptotic method, we characterize the repulsive pair interaction law of localized patches. This type of interaction allows us to infer the possibility of inducing patterns. The observed patterns, unlike those predicted by the Turing mechanism, do not have an intrinsic length. The characteristic length and type of the pattern depend on the number, initial and boundary conditions of the localized states. Numerically, we observe hexagonal, square, and superlattice patterns when the density of localized patches is decreasing.

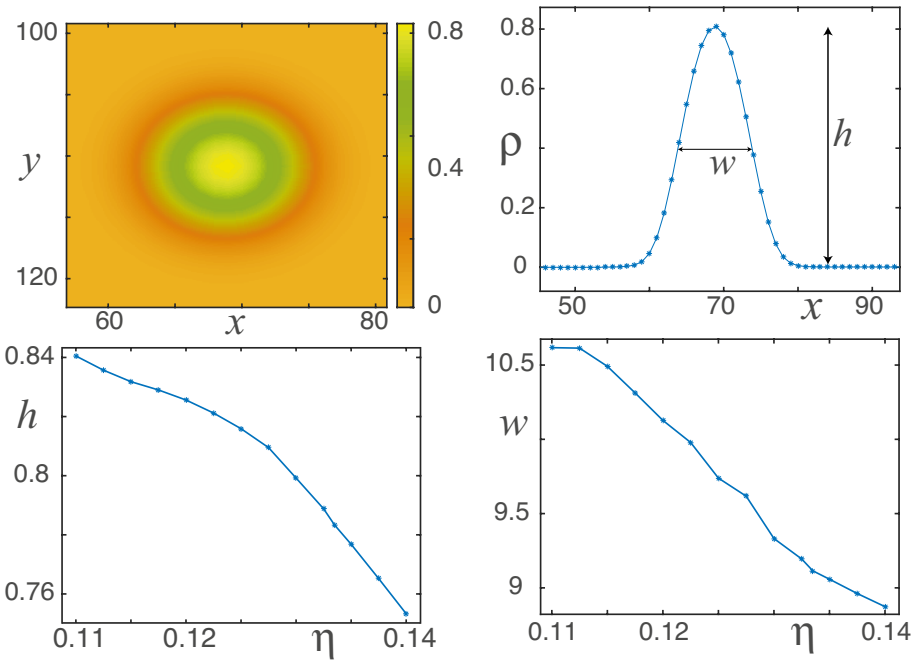

Figure 2. (color online) Localized patches of the interaction-redistribution model Eq. (1) with $\kappa = 0.6$, $\Delta = 0.02$, $\Gamma = 0.5$, and $\alpha = 0.125$. Top panels account for tridimensional and profile representation of localized patches for $\eta = 0.12$. The parameters h and w stand for the high and the waist of the localized patch, respectively. Bottom panels present the variation of the high and the waist of the localized patch as function of aridity.

Theoretical description.- Pattern formation in vegetated environments has attracted the interest of the community in the last decades [16, 17]. The competition for resources, such as water and nutrients can lead to spatial self-organization. Several models describing vegetation patterns and self-organization in arid and semiarid landscapes have been proposed. They can be classified into three types: interaction-redistribution models that are based on the

relationship between the structure of individual plants and the facilitation-competition interactions existing within plant communities [18–22], reaction-diffusion type of models that take into account the influence of water transport by below ground diffusion and/or above ground run-off [17, 23–25], and stochastic models focuses on the role of environmental randomness as a source of noise-induced symmetry breaking transitions [26]. Considering the first of the description strategies, for the idealized situation of a strictly isotropic and homogeneous environment, the phytomass density $\rho(r,t)$ evolves according to the dimensionless kinetic equation (*the interaction-redistribution model*) [27, 28]

$$\partial_t \rho = \rho(\eta + \kappa\rho - \rho^2) + (\Delta - \Gamma\rho)\nabla^2\rho - \alpha\rho\nabla^4\rho \tag{1}$$

where η accounts for the aridity, κ stands for the difference between the interaction strengths associated with the competitive and facilitative process, *susceptibility*, Δ is the rate at which plants diffuse, the parameters Γ and α are, respectively, the nonlinear diffusion coefficients. Γ and α are determined by the difference of the second moments of competition and facilitation kernel of vegetation coupling and the fourth moment of the competition kernel [27].

Depending on aridity, model (1) may exhibit monostability or bistability of uniform solutions. For large aridity the only homogeneous state is non-vegetation or bare state ($\rho = 0$). When the aridity is decreasing the bare state exhibits a subcritical bifurcation, given rise the emergence of a vegetation uniform states $\rho_v \equiv (\kappa + \sqrt{\kappa^2 - 4\eta})/2$. This vegetation state extends up to the limit point $\rho_v^c = \kappa/2$ and $\eta_{sn} = \kappa^2/4$. At this point, the system has a saddle-node bifurcation. Figure 1 shows the typical bifurcation diagram of model (1). The vegetation state undergoes a spatial instability characterized by a wavelength $\lambda = 2\pi\sqrt{2\alpha}/\sqrt{\Gamma - \Delta/\rho_L}$, where ρ_L is solution of the cubic equation $4\alpha\rho_L^2(2\rho_L - \kappa) = (\Gamma\rho_L - \Delta)^2$. Hence, model Eq. (1) has coexistence between the bare and periodic state. This coexistence is a prerequisite condition to observe localized structure states [9–11]. These states correspond to localized patches of vegetation. Figure 1 illustrates a typical localized patches observed in model Eq. (1) and in nature. These localized states are observed in the shadow region in the bifurcation diagram between $\eta_I < \eta < \eta_{II}$ (cf. Fig. 1). These solutions appear by saddle-node bifurcation at $\eta = \eta_{II}$ and disappear by curvature instability at $\eta = \eta_I$ [29]. There is not an analytical characterization of the localized patches. Figure 2 shows a numerical characterization of the high and the waist of localized patches as function of the aridity parameter. From this figure, we can infer that when aridity is increasing the phytomass of a localized patch decreases.

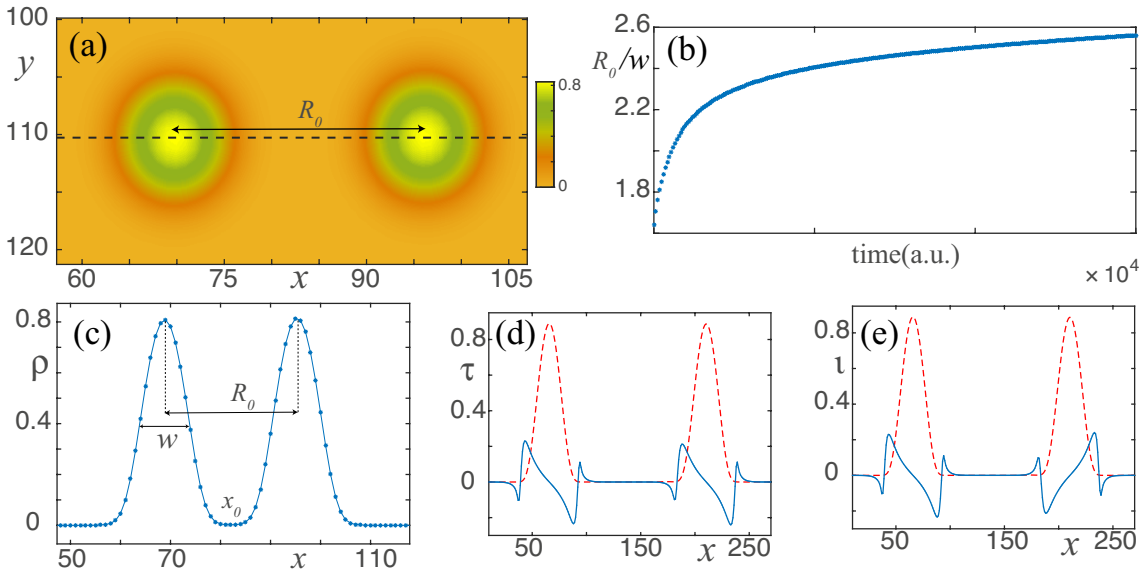

Figure 3. (color online) Interaction of two localized patches of the interaction-redistribution model Eq. (1) with $\eta = 0.12$, $\kappa = 0.6$, $\Delta = 0.02$, $\Gamma = 0.5$, and $\alpha = 0.125$. (a) Two localized patches separates by a R_0 distances. (b) Temporal evolution of the distance between localized patches $R_0(t)$, points and solid line account for numerical evolution of model eq. (1) and analytical temporal evolution using Eq. (4). (c) Profile of interacting localized patches. (d) and (e) profile of the translation and the interaction mode of $\mathcal{L}^\dagger$.

Interaction of localized patches.- Field observations show a rich self-organization of vegetation mediated by localized patches as is illustrated in Fig. 1. To figure out this complex dynamics is indispensable to grasp the interaction between a pair of localized patches. Figure 3 depicts the repulsive interaction of two localized patches. Indeed, to optimize the scare resource localized patches segregate one state to the other one. Let's consider the following ansatz to pair

interaction dynamics [13, 14]

$$\rho(\vec{r},t) = \rho^{-}\left(\vec{r} + \frac{R_0(t)}{2}\hat{r}\right) + \rho^{+}\left(\vec{r} - \frac{R_0}{2}\hat{r}\right) + W, \tag{2}$$

where $\rho^{\pm}(\vec{r} \mp R_0/2\hat{r})$ is a localized patch of vegetation places at $\pm R_0/2\hat{r}$, $\vec{r} = r\hat{r}$ accounts to spatial coordinates with origin at the left localized patch, $\hat{r}$ and $R_0(t)$ are, respectively, the unitary vector in the direction and the distance between localized patches, and $W(\vec{r}, R_0(t))$ is a small correction function. Introducing the above ansatz in Eq. (1), linearizing in W and after straight forward calculations, one gets

$$\begin{aligned}\mathcal{L}W = &\frac{\dot{R}_0}{2}(\partial_r\rho^{-} - \partial_r\rho^{+}) - 2\kappa\rho^{+}\rho^{-} + 3\rho^{+}\rho^{-}\bar{\rho} + \\ &\Gamma(\rho^{+}\partial_r\rho^{-} + \rho^{-}\partial_r\rho^{+}) + \alpha(\rho^{+}\partial_r\rho^{-} + \rho^{-}\partial_r\rho^{+}),\end{aligned} \tag{3}$$

where the linear operator $\mathcal{L} \equiv \eta + 2\kappa\bar{\rho} - 3\bar{\rho}^2 + \Delta\partial_{rr} - \Gamma(\bar{\rho}\partial_r^2 + \partial_r^2\bar{\rho}) - \alpha(\bar{\rho}\partial_r^4 + \partial_r^4\bar{\rho})$ and $\bar{\rho} \equiv \rho_{LP}^{-} + \rho_{LP}^{+}$. To solve the above linear equation, we consider that the localized patches are separate enough ($R_0/w \gg 1$ and w is the localized patch waist) and the tail of localized patches can be approach by a modified Bessel function of second kind, $\rho^{\pm}(|r| \to \infty) \to K_0(r) = e^{\sqrt{\eta/\Delta}r}/\sqrt{r}$. Introducing, the inner product $\langle f|g\rangle = \int fgdr$, the linear operator $\mathcal{L}$ is not self-adjoint ($\mathcal{L} \neq \mathcal{L}^{\dagger}$). Numerically, we have characterized the two kernel elements of $\mathcal{L}^{\dagger}$, which are related to the translation ($|\tau\rangle$) and the interaction mode ($|\iota\rangle$). Figure 3 shows these modes. Applying solvability condition in the linear Eq. (3) with respect to interaction mode [30] and at dominate order we obtain (pair interaction law)

$$\dot{R}_0 = A\frac{e^{-\sqrt{\eta/\Delta}R_0}}{\sqrt{R_0}}, \tag{4}$$

where A is a positive constant determined by numerical integration. Therefore, the pair interaction law of localized patches is isotropic, of repulsive nature, and decaes exponentially with the distance of localized states. Indeed, the interaction is of short range type.

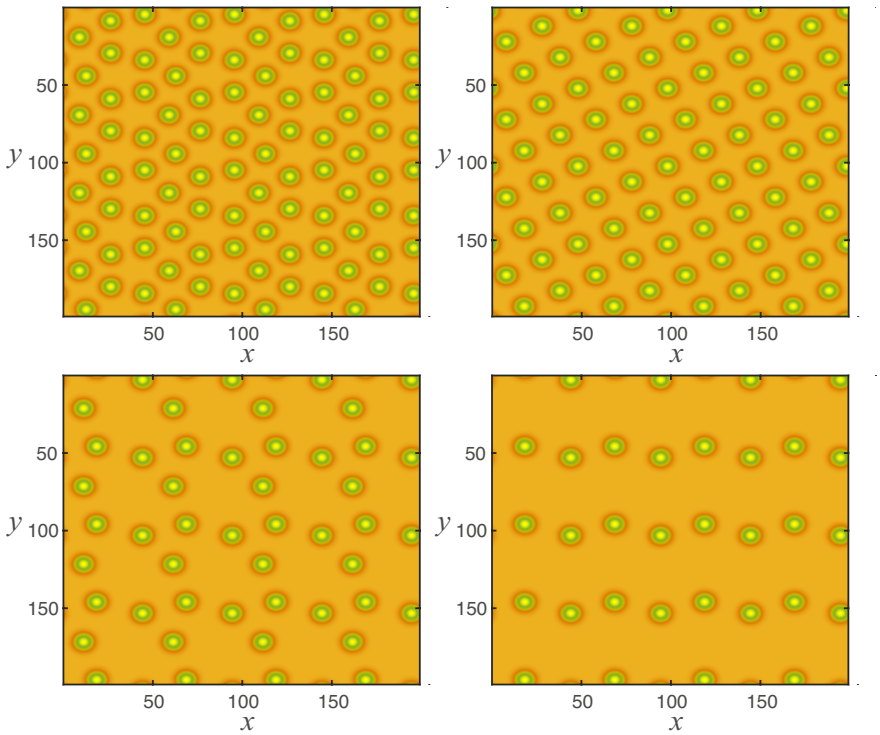

Figure 4. (color online) Localized patches lattice of the interaction-redistribution model Eq (1) with periodic boundary conditions, $\kappa = 0.6$, $\Delta = 0.02$, $\Gamma = 0.5$, and $\alpha = 0.125$ and different quantity of vegetation localized patches 96 (a), 72 (b), 48 (c), and 32 (d).

Self-assembling of localized patches.- From pair interaction law, we can describe the dynamics of several vegetation localized patches. As a matter of fact, due to the exponential decay of interaction, the dynamics of localized patches is ruled by nearest localized patch neighbors. From this dynamics, one expects as equilibrium a regular pattern or lattice. When the density of localized patches is high, we observe as equilibrium hexagonal pattern (cf. Fig. 4a). This type of pattern is expected because it corresponds to close packing of isotropic particles. However, when the density of localized patches is decreased, the equilibrium state changes to other lattices type. Figure 4 shows hexagonal, square, and two superlattice dissipative structures obtained numerically from the interaction-redistribution model Eq (1) changing the density of localized patches. Hence, the pattern formation is mediated by the localized structure interaction. At variance of Turing patterns, the observed lattice of vegetation localized patches does not have an intrinsic wavelength. The characteristic wavelength depends on the localized patches density and the initial conditions. Namely, when one deletes or adds a localized state the characteristic wavelength adapts to a novel value. To emphasize this mechanism of pattern formation, we have conducted numerical simulations of the interaction-redistribution model (1) in one-dimension with periodic boundary conditions, in the region of parameters where localized states are observed. Analogously to the previous analysis, one can calculate and characterize the pair interaction law of localized structures. In this case, the interaction is of repulsive nature and is characterized by decaying exponentially with the distance between localized states. Figure 5 illustrates the pattern formation process mediated by localized structures interaction. Numerically, we observe that from a set of disorder initially localized structures (see top profile Fig. 5a) begin to repel until the system finds a pattern state as equilibrium (see bottom profile Fig. 5a). The wavelength of this pattern is the system size L divided by the number of localized structure N ($\lambda_N \equiv L/N = 85/6$). Subsequently, a localized structure is eliminated and the system evolves to its novel equilibrium with wavelength $\lambda_N = 85/5$ (cf. Fig. 5b). This process is repeated once again and the system finds another periodic structure with $\lambda_N = 85/4$. It is important to note that a similar dynamical behavior observed with Neumann boundary conditions. Therefore, the observed pattern does not have a characteristic wavelength. Indeed, the wavelength is determined by the initial conditions as is illustrated by Fig. 5.

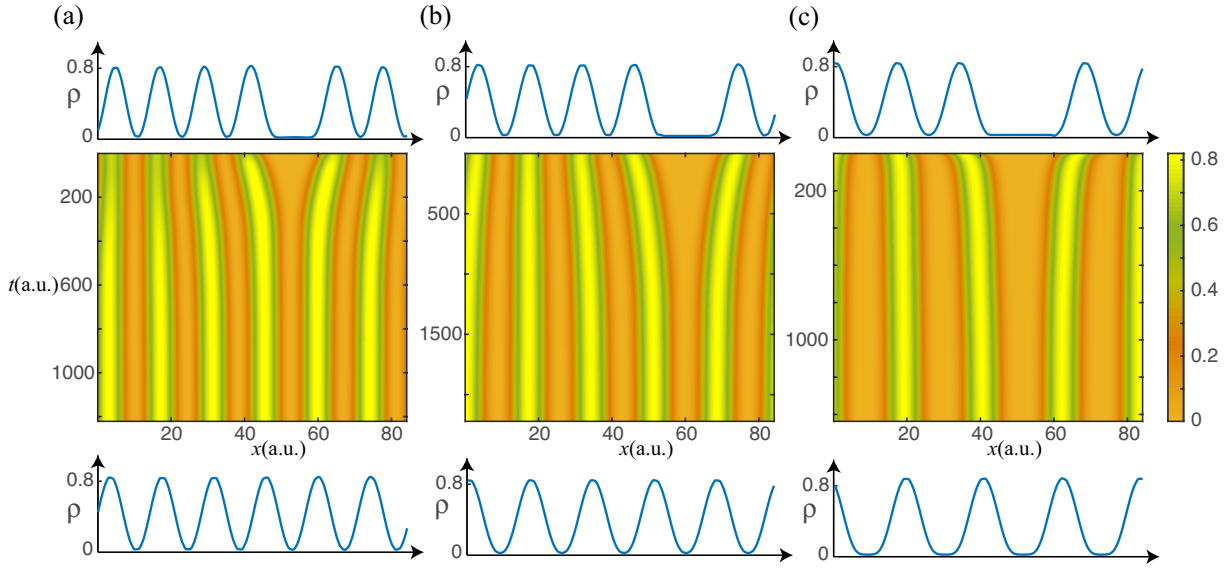

Figure 5. (color online) Pattern formation process mediated by localized structures, obtained from one-dimension interaction-redistribution model with periodic boundary conditions. Spatiotemporal evolution with different initial conditions (top profile) and the final states are represented in the bottom profiles.

In conclusions, we have shown that the pattern formation process conducted by repulsive localized vegetation patches produces pattern formation. The patterns, unlike those predicted by the Turing mechanism, do not have an intrinsic length. The characteristic length and type of the pattern depend on the number, initial and boundary conditions of the localized states. Numerically, we observe hexagonal, square, and superlattice patterns when the density of localized patches is decreasing.

M. G. C. thanks for the financial support of FONDECYT projects 1150507. E. B-C thanks the financial support of CONICYT though Becas Magister Nacional 2015, Contract nº 22151824.

[1] P. Glansdorff and I. Prigogine, Thermodynamic theory of structures. Stability and fluctuations (Wiley, New York 1971).
[2] G. Nicolis and I. Prigogine, *Self-organization in nonequilibrium systems*, (J.Wiley & Sons, New York 1977).
[3] L.M. Pismen, *Patterns and interfaces in dissipative dynamics.* (Springer, Berlin Heidelberg 2006).
[4] M. Cross and H. Greenside, *Pattern Formation and Dynamics in Nonequilibrium Systems*, (Cambridge University Press, New York, 2009).
[5] M. I. Rabinovich, A. B. Ezersky, and P. D. Weidman, *The Dynamics of Patterns* (World Scientic, Singapore, 2000).
[6] P. Ball, *The Self-Made Tapestry: Pattern Formation in Nature* (Oxford University Press, New York, 1999).
[7] A. Turing, The chemical basis of morphogenesis, Phil. Trans. R. Soc. B **237**, 37 (1952).
[8] J.D. Murray, *Mathematical Biology, II Spatial Models and Biomedical Applications* (Springer-Verlag, New York, 2001).
[9] *Localized states in physics: solitons and patterns*, edited by O. Descalzi, M.G. Clerc, R. Residori, and G. Assanto (Springer Science & Business Media, Berlin Heidelberg, 2011).
[10] H. G. Purwins, H. U. Bodeker, and S. Amiranashvili, *Dissipative solitons*, Adv. Phys. **59**, 485 (2010).
[11] M. Tlidi, K. Staliunas, K. Panajotov, A. G. Vladimiorv, and M. G. Clerc, Localized structures in dissipative media: from optics to plant ecology, Phil. Trans. R. Soc., A **372**, 20140101 (2014).
[12] M. Tlidi, M. Taki, & T. Kolokolnikov. Introduction: Dissipative localized structures in extended systems, Chaos **17**, 037101 (2007).
[13] I.S. Aranson, K.A. Gorshkov, A.S. Lomov, and M.I. Rabinovich, Stable particle-like solutions of multidimensional nonlinear fields, Physica D **43**, 435 (1990).
[14] M.G. Clerc, S. Coulibaly and D. Laroze, Interaction law of 2D localized precession states, EPL, **90**, 38005 (2010).
[15] Image of Google Earth Pro in the Mufumbwe district in the north-western province of Zambia, $13°46'39.83''$S, $25°16'39.59''$E.
[16] A. S. Watt, Pattern and process in the plant community, J. ecology, **35**, 1 (1947).
[17] E. Meron, *Nonlinear Physics of Ecosystems?*, (CRC Press, Boca Raton, 2015).
[18] R. Lefever, and O. Lejeune, On the origin of tiger bush. Bulletin of Mathematical Biology **59**, 263 (1997).
[19] O. Lejeune, amd M. Tlidi, M. A model for the explanation of vegetation stripes (tiger bush). J. Vegetation science **10**, 201 (1999).
[20] E. Gilad, J. Von Hardenberg, A. Provenzale, M., Shachak, and E. Meron, Ecosystem engineers: from pattern formation to habitat creation. Phys. Rev. Lett. **93**, 098105 (2004).
[21] P. Couteron, F. Anthelme, M.G. Clerc, D., Escaff, C. Fernandez-Oto, and M. Tlidi, Plant clonal morphologies and spatial patterns as self-organized responses to resource-limited environments. Philosophical Transactions of the Royal Society A **372**, 20140102 (2014).
[22] M.W. van Rooyen, G.K. Theron, N. van Rooyen, W. J. Jankowitz, and W.S. Matthews, Mysterious circles in the Namib Desert: review of hypotheses on their origin. Journal of Arid Environments 57, 467 (2004).
[23] C. A. Klausmeier, Regular and irregular patterns in semiarid vegetation. Science **284**, 1826 (1999).
[24] J. Von Hardenberg, E., Meron, M., Shachak, and Y. Zarmi, Diversity of vegetation patterns and desertification. Phys. Rev. Lett. **87**, 198101 (2001).
[25] M. Rietkerk, S.C. Dekker, P. C. de Ruiter, and J. van de Koppel, Self-organized patchiness and catastrophic shifts in ecosystems, Science **305**, 1926 (2004).
[26] L. Ridol , P. D'Odorico, P. and F. Laio, Noise-induced phenomena in the environmental sciences, (Cambridge University Press, 2011).
[27] O. Lejeune, and M. Tlidi, A model for the explanation of vegetation stripes (tiger bush), J. Vegetation science, **10**, 201 (1999).
[28] M. Tlidi, R., Lefever, and A. Vladimirov, On vegetation clustering, localized bare soil spots and fairy circles. In Dissipative Solitons: From Optics to Biology and Medicine (pp. 1-22). Edited by A. Ankiewicz and N Akhmediev (Springer, Berlin Heidelberg, 2008).
[29] I. Bordeu, M. Clerc, P. Couteron, R. Lefever, M. Tlidi, Self-replication of localized vegetation patches in scarce environments, Scientific Reports **6**, 33703 (2016).
[30] Ivar Fredholm. Sur une classe d'equations fonctionnelles. Acta mathematica, **27**,365 (1903).

Appendix D

Harnessing diffraction grating in an in-plane switching cell submitted to zigzag lattice

In this appendix we include our results of an experiment consisting in applying a laser beam to an in-plane switching liquid crystal cell, submitted to a generator.

Publication details:

- Title: Harnessing diffraction grating in an in-plane switching cell submitted to zigzag lattice.
- Authors: V. Odent, E. Berrios-Caro and M. G. Clerc.
- Publication date: 1 October 2016.
- Published in Applied Optics.
- DOI: https://www.osapublishing.org/ao/abstract.cfm?uri=ao-55-28-7803

applied optics

Harnessing diffraction grating in an in-plane switching cell submitted to zigzag lattice

VINCENT ODENT,[1,2,*] ERNESTO BERRIOS-CARO,[1] AND MARCEL G. CLERC[1]

[1]Departamento de Física, Facultad de Ciencias Físicas y Matemáticas, Universidad de Chile, Casilla 487-3, Santiago, Chile
[2]Université Lille 1, Laboratoire de Physique des Lasers, Atomes et Molécules, CNRS UMR8523 59655 Villeneuve d'Ascq Cedex, France
*Corresponding author: vincent.odent@phlam.univ-lille1.fr

Received 9 June 2016; revised 27 July 2016; accepted 30 August 2016; posted 30 August 2016 (Doc. ID 267941); published 22 September 2016

Programmable diffraction gratings are relevant in optical data processing. One of the adequate device candidates is the in-plane switching liquid crystal cell. This technology, developed initially for liquid crystal screens, has also been studied with two inter-digital electrodes as a diffraction grating. Recently, the apparition of programmable zigzag wall lattices in an in-plane switching configuration has been reported. Here, we report a theoretical and experimental study of programmable diffraction grating in an in-plane switching cell.

OCIS codes: (230.1950) Diffraction gratings; (230.3720) Liquid-crystal devices; (260.1960) Diffraction theory.

http://dx.doi.org/10.1364/AO.55.007803

1. INTRODUCTION

In-plane-switching (IPS) technology was developed initially for liquid crystal displays (LCD) to solve the twisted nematic (TN) field limitations. Since its introduction in 1996 [1,2], this technology has allowed for the improvement of screen qualities, especially color contrast and vision angles [3]. Moreover, IPS technology was also used as inter-digital electrodes, combined with liquid crystals, for switchable optical diffraction. A lot of liquid crystal phase grating designs have been reported that use this electrode configuration [4–7]. Their applications range from optical data processing and beam steering [8] to optical communication networking devices [9], which emphasize the relevance to controlling and understanding the different mechanisms existing in this kind of diffraction grating. Some works have studied the high voltage impact on the diffracted grating [10] or tested a new configuration with carbon nanotubes [11]. Latterly, the apparition of zigzag lattice in an IPS cell filled with nematic liquid crystal beyond a certain voltage threshold has been reported [12]. Recently, we have studied in detail, theoretically and experimentally, the zigzag instability of a wall lattice in a nematic liquid crystal with an IPS configuration [13]. We have also evidenced the importance of the liquid crystal molecule anchoring on their own dynamics when they are submitted to an external electrical forcing [14,15].

The aim of this paper is to investigate the zigzag wall lattice influence on the diffraction grating. We study an IPS cell used without liquid crystal. We confirm the diffractive nature of the empty cell, which works as diffraction grating with a low contrast. This property changes when we consider this cell filled with a nematic liquid crystal subjected to a given voltage. We propose an analytical model to reproduce a zigzag lattice, which gives us the typical x signature of the diffraction image. Numerical simulations of a more realistic/imperfect zigzag lattice, taking into account the different experimental properties, show quite good agreement with the experimental observations. This method allows us make evident a dispersion of the amplitude and the wavelength of the zigzag lattice inside the sample.

2. EXPERIMENTAL SETUP

The experimental setup is depicted in Fig. 1. We use two identical cells, one empty (without liquid) and the second one filled with a nematic liquid crystal. We consider IPS cells with a homogeneous planar alignment [following the x-axis, cf. Fig. 1(a)] and a parallel rubbing to the electric field (Instec, *IPS02A89uX90*). The indium tin oxide (ITO) electrode width and the gap width are the same; $\epsilon = 15$ μm. The height of the electrodes is negligible (∼25 nm) compared to the cell thickness ($d = 8.9 \pm 0.2$ μm). The active zone is a square of side $l = 1$ cm. Under these settings, we can consider the cell in a good approximation as an infinite media. The liquid crystal cell is composed of a layer of *E7* nematic liquid crystal, which is inserted between two glass plates (thickness $g = 1.1$ mm). The elastic constants of the liquid crystal are, respectively, $K_1 = 11.2$, $K_2 = 6.8$, and $K_3 = 18.6(\times 10^{-12}$ N). The parallel and the perpendicular dielectrical constants are $\varepsilon_{\parallel} = 18.96$ and $\varepsilon_{\perp} = 5.16$ [16,17]. The cell electrodes are connected to a function generator. The typical parameter range for the frequency is ∼200 mHz – 2 MHz and for the amplitude ∼10 V_{pp} – 20 V_{pp} (volt peak-to-peak). We illuminate

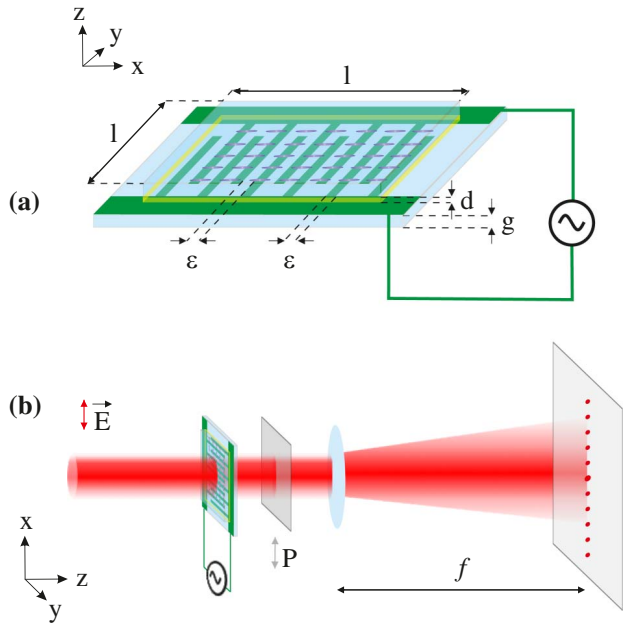

Fig. 1. (a) Schematic representation of the liquid crystal IPS cell, connected to a generator. Thickness between the two glass plates, $d = 8.8 \pm 0.2$ μm. Thickness of a glass plate, $g = 1$ mm. Active zone, $l \times l = 1$ cm^2. Gap between two electrodes, $\epsilon = 15$ μm. (b) Sketch of the experimental setup: $\vec{E}$, vertically polarized collimated beam; P, vertical linear polarizer; f, focal distance of the imaging lens.

the cell with a vertically polarized helium–neon laser beam at 632.8 nm, as shown in Fig. 1(b). The beam is previously collimated, using a telescope, in order to consider the Fraunhofer approximation valid. The beam waist is $w = 1.1$ mm. The laser power is sufficiently weak to prevent the molecular reorientation, which is typically $P_0 = 1$ mW. A linear polarizer is placed behind the cell. We generate, on a screen, the diffraction figure placed in the focal plane of a convergent lens. We record the diffusive light of the diffraction figure on the screen with a CCD monochrome camera. By replacing the screen by a power meter, we have the possibility of recording the power value of every diffracted order until the sixth one.

3. DIFFRACTION THEORY WITH AN EMPTY CELL

In the literature, there are several reports about liquid crystal phase grating based on IPS [9,10,18]. However, to the best of our knowledge, no works study the transmission of the empty cell. We propose a simple diffraction grating model, which evidences the ITO electrodes as a diffraction grating.

A. One-dimensional Frauhofer Diffraction Theory

We consider the most simple model to reproduce the Fraunhofer diffraction phenomenon with an empty IPS cell. The cell is constituted by two parallel glass layers and two electrode combs of ITO, which are stuck on one glass layer (inside the cell), as represented in Fig. 2(a).

One can calculate the diffraction figure from the intensity transmission function $t(x)$ (diffraction grating) [19,20]. This one is a crenel function, following the x axis, as represented

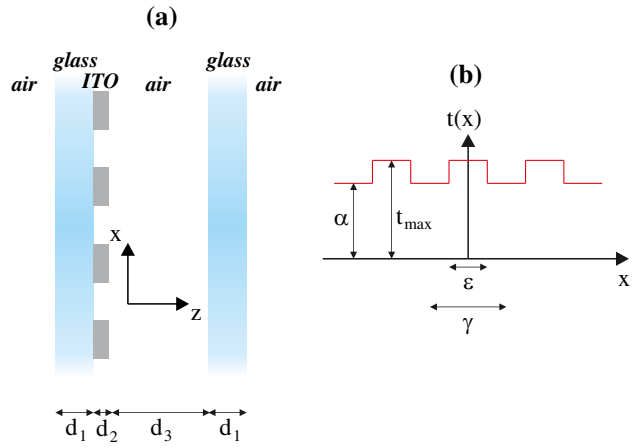

Fig. 2. (a) Sketch of an empty IPS cell that is constituted by two parallel glass layers and two electrode combs of ITO, and (b) the cell intensity transmission function.

in Fig. 2(b). To simplify, we evaluate $t_{max} = 1$, which is the light part that crosses only the two glass layers, and we consider α as the transmission coefficient in amplitude of the light which crosses the glass layers and the electrodes. ϵ is the electrode width, and γ is the distance between two electrodes. Hence,

$$t(x) = \begin{cases} 1, & -\frac{\epsilon}{2} + n\gamma < x < \frac{\epsilon}{2} + n\gamma \\ 1 - \alpha & \frac{\epsilon}{2} + n\gamma < x < \frac{3\epsilon}{2} + n\gamma. \end{cases} \quad (1)$$

The diffraction figure is given by

$$I(u) = |E|^2 = \left| \int_{-\gamma/2}^{\gamma/2} \sum_{n=0}^{N} t(x - x_n) e^{-2\pi i u x} dx \right|^2, \quad (2)$$

where N is the electrode numbers illuminated by the light source, $t(x)$ is the amplitude transmission function, and $2\pi u$ is the wavenumber. After the straightforward calculations from Eq. (2), we obtain the diffraction figure in the Fourier space.

$$I(u) = \frac{\sin^2(\pi u \gamma N)}{\sin^2(\pi u \gamma)} [\alpha\gamma \ \mathrm{sin}\ c(\pi u \gamma) + (1 - \alpha)\epsilon \ \mathrm{sin}\ c(\pi u \epsilon)]^2. \quad (3)$$

Considering the experimental electrode sizes, we have $\gamma = 2\epsilon$. We calculate the zero diffraction order from the equation above:

$$I(0) = N^2 \epsilon^2 [1 + \alpha]^2. \quad (4)$$

The other diffraction orders are given by

$$I(2m/\gamma) = 0, \quad (5)$$

and

$$I((2m + 1)/\gamma) = \frac{4N^2\epsilon^2}{\pi^2(2m + 1)^2} [1 - \alpha]^2, \quad (6)$$

where m is an integer number.

The experimental procedure to determine the coefficient α is done by measuring the different diffraction orders. Indeed, the theoretical α determination can be distorted by other phenomena, such as glass layer interferences, anchoring treatment, inhomogeneities, and imperfection, among others.

B. Experimental Transmission Coefficient Determination

The α value is determined experimentally by evaluating the diffraction order ratio. We consider the six first diffraction orders. The experimental values are reported in Table 1.

From Eqs. (4) and (6), we calculate the three following diffraction order ratios:

$$\frac{I(0)}{I(1/\gamma)_{\text{theo}}} = \frac{\pi^2}{4}\left[\frac{1+\alpha}{1-\alpha}\right]^2, \tag{7}$$

$$\frac{I(1/\gamma)}{I(3/\gamma)_{\text{theo}}} = 9, \tag{8}$$

$$\frac{I(1/\gamma)}{I(5/\gamma)_{\text{theo}}} = 25. \tag{9}$$

Note that the odd diffraction orders do not depend on the α value. The theoretical ratios from Eqs. (8) and (9) present a good agreement with their experimental observations:

$$\frac{I(1/\gamma)}{I(3/\gamma)_{\text{exp}}} = 9.9, \tag{10}$$

$$\frac{I(1/\gamma)}{I(5/\gamma)_{\text{exp}}} = 23.6. \tag{11}$$

By rewriting Eq. (7), we find

$$\alpha = \frac{2\sqrt{\frac{I(0)}{I(1/\gamma)}} - \pi}{2\sqrt{\frac{I(0)}{I(1/\gamma)}} + \pi}. \tag{12}$$

The experimental ratio $I(0)/I(1/\gamma)$ gives us $\alpha = 0.70$. Hence, the empty cell plays the role of a diffraction grating, however, with a lower efficiency (low contrast). Indeed, the visibility, for the empty cell is $V = 0.09$.

4. DIFFRACTION THEORY WITH A LIQUID CRYSTAL CELL

A lot of studies have evaluated the diffraction efficiency of the one-dimensional (1D) spot pattern [9,18,21,22]. In particular, Han has presented the diffraction efficiency, with a sample where the zigzag instability exists [12]. We complete this characterization by adding a frequency study. Figure 3 shows the diffraction efficiency of our sample depending on the voltage amplitude, between $T = 0$ V_{pp} and $T = 100$ V_{pp}, and the frequency, between $f = 10$ Hz and $f = 1$ MHz. The diffraction efficiency is defined as

Table 1. Experimental Intensity of the First Diffraction Orders of an Empty In-plane Switching Cell

Diffraction Order	Power Values (μW)
0	576
1	31.8
2	1.1
3	3.20
4	0.89
5	1.36

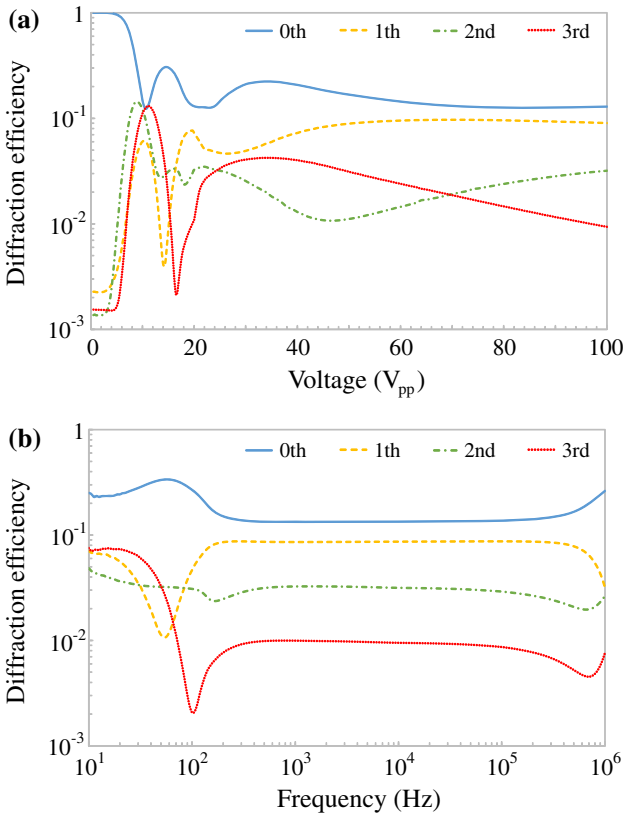

Fig. 3. Diffraction efficiencies of the zeroth to fourth order. (a) Voltage evolution for $f = 1$ kHz, and (b) frequency evolution for $T = 20$ V_{pp}.

$$D_e = I/I_0, \tag{13}$$

where I is the order of diffracted intensity, and I_0 is the total transmitted light. Figure 3(a) qualitatively gives the same results as the Han evaluation, given that the liquid crystal mixture is the same, $E7$, and the liquid crystal cells have a small difference around the electrode gaps. We observe in Fig. 3(a) a strong diffraction order modification between $T = 8$ V_{pp} and $T = 30$ V_{pp} for a fix frequency value of $f = 1$ kHz. For a fixed tension amplitude value $T = 20$ V_{pp}, we also observe, in Fig. 3(b), a strong modification of the diffraction orders between $f = 10$ Hz and $f = 1$ kHz. This information helps us evaluate the region of parameters, where the liquid crystal dynamics change a lot and, consequently, its diffraction figure.

Recently, we have observed that below a voltage threshold (amplitude or frequency), the cell filled with a liquid crystal exhibits an Ising wall lattice which becomes a zigzag instability [13]. To confirm these phenomena, we have used parallel polarizers and observe black bands (Ising wall lattice) and black zigzags (zigzag instability). We use this configuration to generate a programmable diffraction grating.

A. Perfect Zigzag Lattice: Two-dimensional Fraunhofer Diffraction Theory

In a first approximation, we assume to have a perfect two-dimensional (2D) diffraction mask, with a periodic black zigzag, as represented in Fig. 4(a). The zigzag pattern presents a constant amplitude and a constant wavelength. The lattice does not present a phase shift between the different zigzag instabilities. In this ideal case, we assume to have a visibility of V = 1, so $\alpha = 0$. θ is the angle between the y axis and the zigzag lines. The diffraction mask, represented in Fig. 4(a), gives the following diffraction figure in the Fourier space:

$$I(u,v) = \left| \int_{-b/2}^{b/2} \int_{-a/2-y\tan\alpha}^{a/2-y\tan\alpha} \sum_{n=0}^{N} \sum_{m=0}^{M} t(x-x_n, y-y_m) e^{-2\pi i(ux+vy)} \mathrm{d}x\mathrm{d}y \right|^2. \quad (14)$$

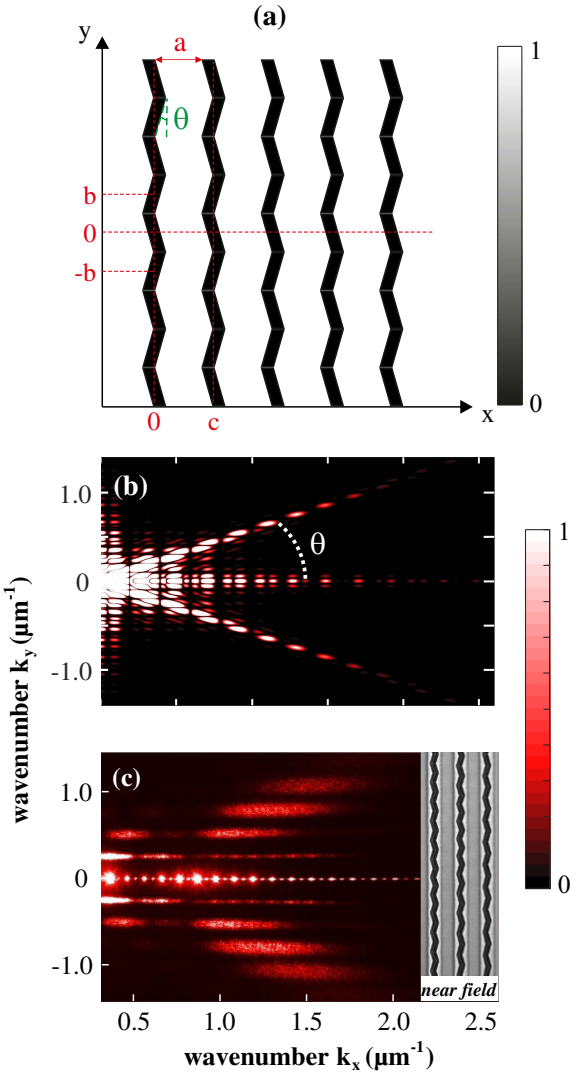

Fig. 4. (a) 2D perfect diffraction zigzag grating. (b) Diffraction image obtained from a 2D perfect diffraction zigzag grating using Eq. (15). (c) Experimental diffraction image obtained from an IPS cell with a zigzag lattice. Inset accounts for a snapshot of the cell, $f = 100$ Hz, and $T = 20$ V_{pp}.

After straightforward calculations, we obtain

$$I(u,v) = \frac{\sin(\pi ucN)}{\sin(\pi uc)} \frac{\sin(2\pi vbM)}{\sin(2\pi vb)} ab \sin c(\pi ua). [\sin c(\pi b(v - u\tan(\theta))) + \sin c(\pi b(v + u\tan(\theta)))], \quad (15)$$

where c is the period of the grating following the x axis. Its value is imposed by the distance between two electrodes in the cell ($c = \gamma$, cf. Fig. 2). a is the thickness of the white bands. We have the condition $a > \epsilon$. Physically, a represents the distance where liquid crystal molecules are not subjected to electro-reorientation [13]. $2b$ is the period of the zigzag instability. θ is the zigzag angle. N is the number of electrodes illuminated by the light, and cN is the transverse size of the illuminated cell following the x axis. M is the number of zigzags illuminated by the light, and bM is the transverse size of the illuminated cell following the y axis. With a Gaussian beam, we have the following equality: $bM = cN$.

The diffraction figure, obtained from Eq. (15), is depicted in Fig. 4(b). Notice the presence of two lines at θ degrees in the Fourier plane. Indeed, these two lines are a signature of the zigzag lattice.

However, the diffraction figure does not correspond exactly to the experimental diffraction figure, presented in Fig. 4(c). Indeed, the near field of the zigzag lattice presents some irregularities that are not taken into account in this perfect zigzag lattice. We will now consider a more realistic zigzag lattice.

B. Imperfect/Real Zigzag Lattice: 2D Fast Fourier Transform

To have an adequate description of the experimental findings, we consider an imperfect zigzag grating. We present a portion of the zigzag grating in Fig. 5, used as near field. The matrix used contains 8192 × 8192 pixels with a spatial resolution of $\Delta x = \Delta y = 0.1$ μm and a distance between two electrodes that is $\gamma = 30$ μm. The wavelength, $\lambda(x,y)$, and the thickness, $D(x,y)$, of the black zigzag lattice have a small variation depending on the location in the cell. We define for every

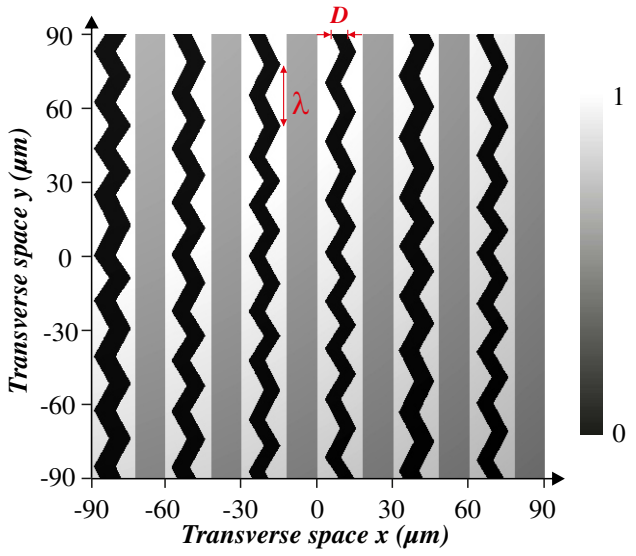

Fig. 5. Portion of the imperfect zigzag grating. λ_0 is the average wavelength, and D is the black zigzag average thickness.

period a wavelength $\lambda(x,y) = \lambda_0 \pm \delta\lambda(x,y)$, where $\delta\lambda(x,y) = \lambda_0\eta(x,y)/B_1$, and $\eta(x,y)$ is a random function giving a value between zero and one with a uniform distribution. In the same way, we define the thickness $D(x,y) = d \pm \delta d(x,y)$, where $\delta d(x,y) = d\eta(x,y)/B_2$. The observation on the experimental pictures of the sample by a microscope provides a more complex intensity profile than the crenel function, as presented in Fig. 2(b). Consequently, we had another grating on the zigzag grating. The cell is illuminated by a delimited laser source. We also take into account this effect in Fig. 5.

We calculate the diffraction image by using the 2D fast Fourier transform. We evaluate the parameters B_1 and B_2 by a quantitative comparison between the experimental (top) and numerical diffraction (bottom) figure presented in Fig. 6. Notice that we have chosen these parameters to obtain numerically diffractive images similar to those observed experimentally. Hence, experimental diffractive images can be reproduced qualitatively by the use of a simple model.

5. EXPERIMENTAL RESULTS

A. Low Frequency: $f = 10$ Hz

At $f = 10$ Hz and with a voltage tension of $T = 20\ V_{pp}$, the liquid crystal cell exhibits a roll lattice in the near field, see the inset in Fig. 6(a), which corresponds to a snapshot of the cell. The experimental image in the Fourier space is a 1D pattern with a wavenumber of $k_{10\,Hz} = 0.104\ \mu m^{-1}$. This wavenumber corresponds to a diffraction image with a diffraction step of $\lambda_{10\,Hz} = 60.4\ \mu m$. We explain the factor of 2 difference ($\lambda_{10\,Hz} = 2\gamma$, where γ is the diffraction grating step) by the fact that at this low frequency the black bands appear and disappear successively on the first electron comb and then on the second one. However, this temporal oscillation is not recorded on the near field image, which corresponds to a temporal average of the roll lattice dynamics. Considering this effect, the diffraction grating step is exactly 2γ, then we have a quite good agreement between the experimental and the numerical far field figure in Figs. 6(a) and 6(d).

B. Middle Frequency: $f = 100$ Hz

At $f = 100$ Hz with a voltage tension $T = 20\ V_{pp}$, the system presents a zigzag lattice. The zigzag signature in the Fourier space is the X structure with an angle $\pm\theta$. We note the presence of different bands. The band's thickness is directly linked to the λ dispersion. In this case, we evaluate $B_1 = 5$. The dispersion of D erases the vertical black lines due to destructive interferences. We evaluate $B_2 \simeq 7$. By taking into account these two dispersion parameters, we have a fairly good agreement between the experimental and the numerical diffraction figures, represented in Figs. 6(b) and 6(e).

C. High Frequency: $f = 1.3$ MHz

At $f = 1.3$ MHz with a voltage tension $T = 20\ V_{pp}$, we observe a sinusoidal lattice. We detect in the Fourier space two opposite (following $k_y = 0$) and intense lines. They represent the fundamental frequency of the sinusoidal functions. Some harmonics can also be seen. To confirm this observation, we modify the theoretical lattice with sinusoidal functions, and we evaluate $B_1 = 5$ and $B_2 \simeq 14$. We qualitatively obtain the same diffraction image.

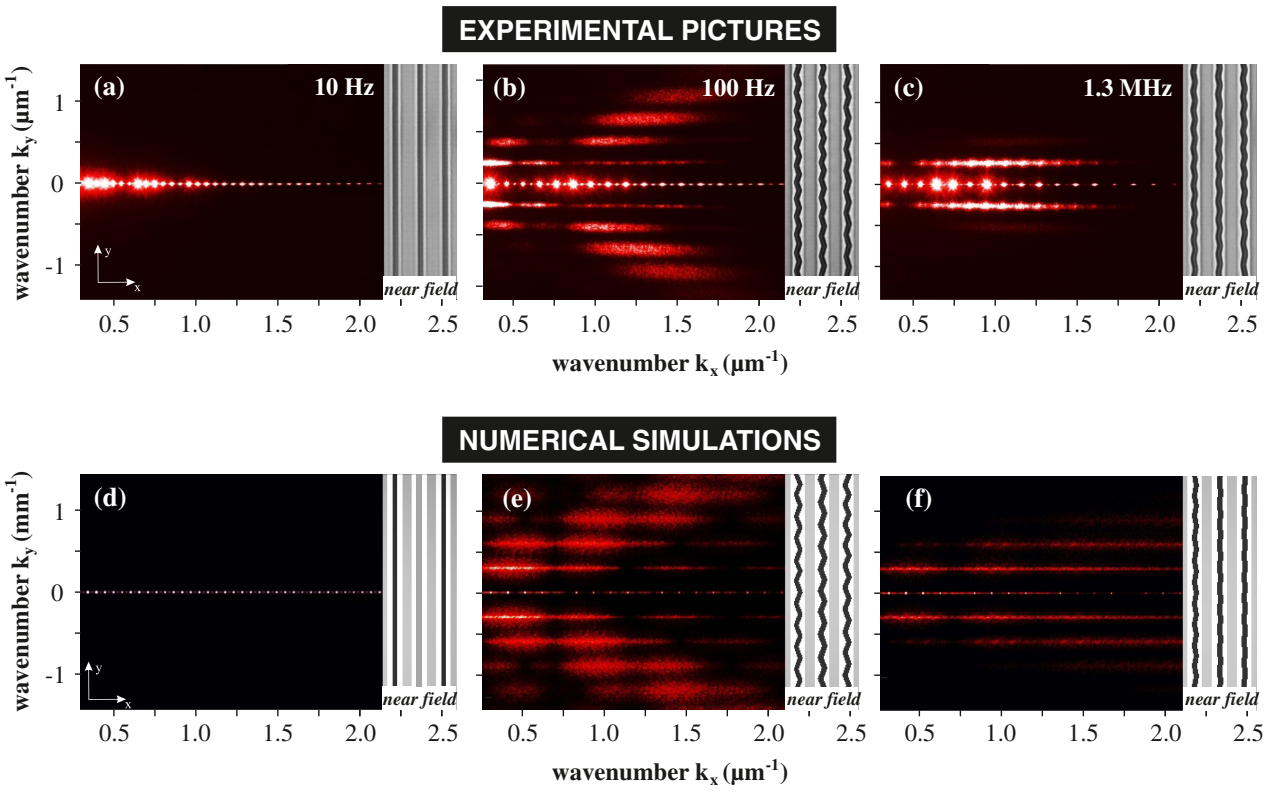

Fig. 6. Diffractive and near field images observed for different frequencies, (a) $f = 10$ Hz, (b) $f = 1.3$ MHz, and (c) $f = 10$ Hz, with a voltage of 20 V_{pp}. The top and bottom panels correspond to experimental and numerical observations, respectively.

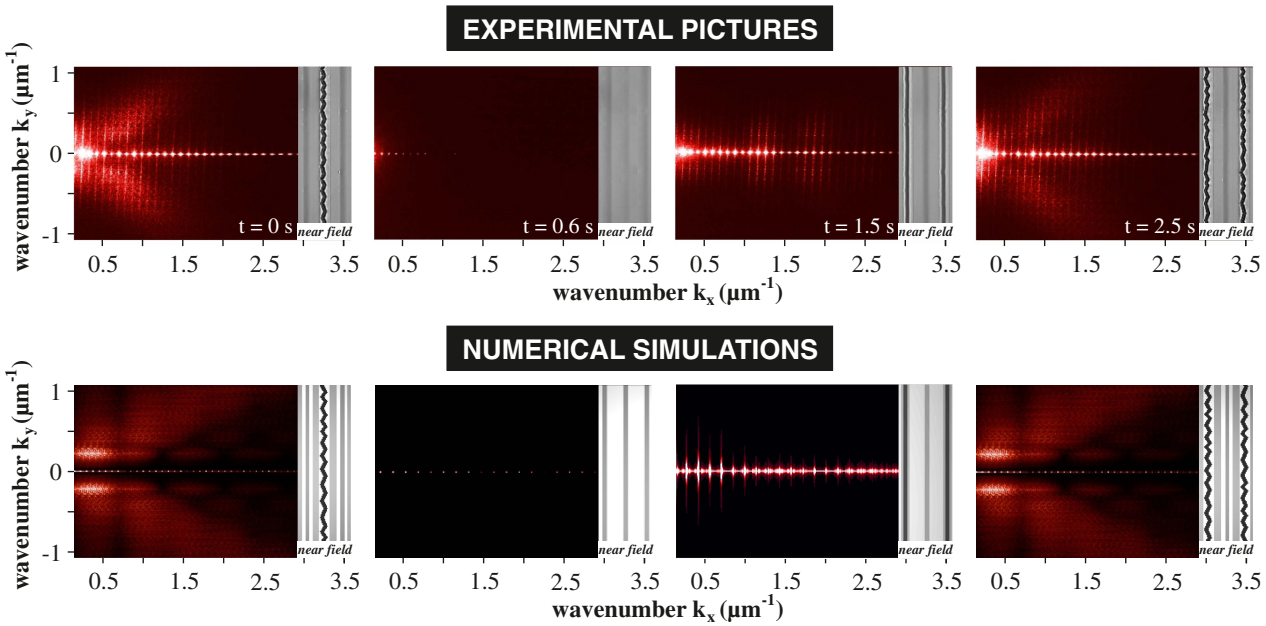

Fig. 7. Temporal sequence of diffractive figures observed for a semi temporal period with $f = 200$ mHz, and $T = 20$ V_{pp}. The top and bottom panels correspond to the experimental and numerical observations, respectively.

D. Very Low Frequency: $f = 200$ mHz

At a very low frequency of $f = 200$ mHz with the same voltage, the system cannot be considered stationary. The liquid crystal exhibits a conductive regime. The liquid crystal space charges oscillate with the electrical field. This phenomenon can be attributed to the gradient flexoelectric effects [23]. It has temporal dynamics directly linked to the voltage frequency. Figure 7 shows four pictures during the half period of the sinusoidal voltage. At $t = 0$ s, the central electrode in the near field presents a zigzag instability with a not well defined wavelength. Consequently, the diffraction image presents a X with large arms. We evaluate for our model $B_1 = 0.5$ and $B_2 \simeq 7$, which has a good agreement with the experimental observations.

E. Application

We have highlighted the results of programmable lattice that shows that one can generate more complex diffraction figures than those presented in the literature. First, these diffraction images give us some information about the molecular reorientation inside the cell, as well as the dispersion of the wavelength and the amplitude of the zigzag lattice. Second, the formation of a 2D diffraction image extends the possibility of beam steering and optical communication networking devices and the characterization of atomic spectra. Finally, this type of diffraction may allow for information about spatial structures of complex light sources.

6. CONCLUSION

Programmable diffraction gratings open the possibility of new optical data processing, characterization of atomic spectra with applications in astronomical observations, space flight instruments, and synchrotron spectrometers, among others. In this work, we have established the possibility of creating this kind of programmable grating. We have characterized an empty IPS cell and seen that it is like a bad diffraction grating. In contrast, an IPS cell filled with a nematic liquid crystal subjected to a given voltage exhibits a rich complex diffraction pattern. Applying a small voltage into a wide range of frequencies, the sample exhibits a stripe diffraction grating. Increasing the voltage, this diffractive pattern presents a spatial instability generating an undulating diffraction grating, and at higher voltages it becomes a zigzag type. We have analytically given a first approximation of the diffraction image obtained with a perfect zigzag lattice. Then, we have studied, experimentally and numerically, the diffractive image and observed a complex structure in the perpendicular direction to the "traditional 1D pattern" in the diffraction image. We have evidenced with this structure a variation/dispersion of the amplitude and the wavelength of the zigzag instability.

One of the limitations of our programmable diffraction gratings is that the time response of liquid crystals is slow on the order of milliseconds. However, this allows us to establish the proof of concept of manipulable diffraction grating. The possibility of faster programmable diffraction gratings using soft or solid materials is a still open question.

Funding. Fondo Nacional de Desarrollo Científico y Tecnológico (FONDECYT) (1150507); Comisión Nacional de Investigación Científica y Tecnológica (CONICYT) (22151824); Région Nord-Pas-de-Calais; Centre National de la Recherche Scientifique (CNRS); Ministère de l'Education Nationale, de l'Enseignement Superieur et de la Recherche (MESR); Nord-Pas-de-Calais Regional Council and European Regional Development Fund (ERDF) through the Contrat de Projets Etat-Région (CPER) 2007–2013; Agence Nationale de la Recherche (ANR) LABEX CEMPI (ANR-11-LABX-007).

Acknowledgment. M. G. C. thanks the financial support of the FONDECYT projects. E. B.-C. thanks the financial support of CONICYT through Becas Magister Nacional 2015. V. O. acknowledges the support of the Région Nord-Pas-de-Calais.

REFERENCES

1. M. Oh-e and K. Kondo, "Electro-optical characteristics and switching behavior of the in-plane switching mode," Appl. Phys. Lett. **67**, 3895–3897 (1995).
2. M. Oh-e, M. Ohta, S. Aratani, and K. Kondo, "Principles and characteristics of electro-optical behavior with in-plane switching mode," in *Proceedings of 15th International Display Research Conference* (Society for Information Display, 1995), pp. 577–580.
3. Y. Sun, Z. Zhang, H. Ma, X. Zhu, and S.-T. Wu, "Reflective in-plane switching liquid crystal displays," J. Appl. Phys. **93**, 3920–3925 (2003).
4. J. Chen, P. J. Bos, H. Vithana, and D. L. Johnson, "An electro-optically controlled liquid crystal diffraction grating," Appl. Phys. Lett. **67**, 2588–2590 (1995).
5. H. Murai, "Electro-optic properties of liquid crystal phase gratings and their simulation using a homogeneous alignment model," Liq. Cryst. **15**, 627–642 (1993).
6. R. Ramsey and S. C. Sharma, "Switchable holographic gratings formed in polymer-dispersed liquid-crystal cells by use of a He–Ne laser," Opt. Lett. **30**, 592–594 (2005).
7. C. W. Christenson, C. Greenlee, B. Lynn, J. Thomas, P. Blanche, R. Voorakaranam, P. S. Hilaire, L. J. Lacomb, R. A. Norwood, M. Yamamoto, and N. Peyghambarian, "Interdigitated coplanar electrodes for enhanced sensitivity in a photorefractive polymer," Opt. Lett. **36**, 3377–3379 (2011).
8. T. Scharf, M. Bouvier, and R. Dandliker, "Multilevel nematic liquid crystal phase grating," Proc. SPIE **4418**, 31–37 (2001).
9. I. Fujieda, O. Mikami, and A. Ozawa, "Active optical interconnect based on liquid-crystal grating," Appl. Opt. **42**, 1520–1525 (2003).
10. J.-W. Han, "Optical diffraction effects of grating cells fabricated using polymer-dispersed liquid crystals," Mol. Cryst. Liq. Cryst. **534**, 69–80 (2011).
11. K. Won, A. Palani, H. Butt, P. J. W. Hands, R. Rajeskharan, Q. Dai, A. A. Khan, G. J. Amaratunga, H. J. Coles, and T. D. Wilkinson, "Electrically switchable diffraction grating using a hybrid liquid crystal and carbon nanotube-based nanophotonic device," Adv. Opt. Mater. **1**, 368–373 (2013).
12. J. Han, "Comparison of optical diffraction gratings fabricated using in-plane switching cells," J. Korean Phys. Soc. **60**, 1361–1366 (2012).
13. I. Andrade-Silva, M. G. Clerc, and V. Odent, "Zig-zag wall lattice in a nematic liquid crystal with an in-plane switching configuration," Phys. Rev. E **90**, 022504 (2014).
14. I. Andrade-Silva, M. G. Clerc, and V. Odent, "Asymmetric counterpropagating fronts without flow," Phys. Rev. E **91**, 060501 (2015).
15. I. Andrade-Silva, M. G. Clerc, and V. Odent, "Asymmetric counter propagation of domain walls," Commun. Nonlinear Sci. Numer. Simul. **36**, 192–203 (2016).
16. P. Oswald and P. Pieranski, *Nematic and Cholesteric Liquid Crystals* (Taylor & Francis, 2005).
17. I. C. Khoo, *Liquid Crystals*, 2nd ed. (Wiley, 2007).
18. I. Fujieda, "Liquid-crystal phase grating based on in-plane switching," Appl. Opt. **40**, 6252–6259 (2001).
19. D. Rittenhouse, "An optical problem, proposed by Mr. Hopkinson, and solved by Mr. Rittenhouse," Trans. Am. Philos. Soc. **2**, 201–206 (1786).
20. J. Fraunhofer, "Neue Modifikation des Lichtes durch gegenseitige Einwirkung und Beugung der Strahlen, und Gesetze derselben," Denkschriften der Königlichen Akademie der Wissenschaften zu München **8**, 3–76 (1821).
21. C. Desimpel, K. Neyts, I. Janevska, A. Gjurcinovski, D. K. G. De Boer, and R. Cortie, "Polarization state of the diffraction peaks in in-plane switching cells," in *Proceedings of the 21st International Display Research Conference in Conjunction with the 8th International Display Workshops* (2001), pp. 161–164.
22. I. Drevensek-Olenik, M. Copic, M. E. Sousa, S. P. Gorkhali, and G. P. Crawford, "Optical diffraction properties of polymer dispersed liquid crystals switched by interdigitated electrodes," Mol. Cryst. Liq. Cryst. **438**, 251–261 (2005).
23. K. S. Krishnamurthy and P. Kumar, "Emergence of periodic order in electric-field-driven planar nematic liquid crystals: an exclusive ac effect absent in static fields," Phys. Rev. E **76**, 0517051 (2007).